Isolation of Fibrillar Elastin Gel (FEG) and its Application in Heart Valve Tissue Engineering

Sonia Iftekhar

Linacre College

University of Oxford

A thesis submitted for the degree of

Doctor of Philosophy

Michaelmas Term 2020

Isolation of Fibrillar Elastin Gel (FEG) and its Application in Heart Valve Tissue Engineering

Sonia Iftekhar, Linacre College

D.Phil. Thesis, Michaelmas Term 2020

Abstract

Elastin, although a small constituent of heart valves, plays a significant role in its functionality and the maintenance of tissue homeostasis. It is due to its low abundance that its significance has been overlooked in favour of collagen and glycosaminoglycans. However, repeatedly, the failure of biological prostheses has been associated with the disruption of elastic fibres. The incorporation of exogenous forms of elastin has been challenging due to the intrinsic insolubility and poor processability of polymeric forms. This has led to the precedence of applications of soluble forms of elastin, which, although are tailorable, do not offer sufficient structural integrity or bioactivity (once cross-linked).

This thesis reports a method for the isolation of a novel form of natural elastin, termed Fibrillar Elastin Gel (FEG), which was discovered during the course of the DPhil. A method was developed to modify polymeric elastin to a processable form with improved polymer-solvent interactions. FEG is a thermally induced aggregated gel, composed of rod-like fibres (4-6μm) with improved intermolecular interactions as shown by the appearance of a shoulder at 1618cm^{-1} by infrared spectroscopy. The material exhibits a low loss factor (~0.1 at 1Hz) and has been hypothesised to be applicable as a biomaterial for tissue engineering of heart valves.

Porous (>94%) scaffolds of multiple compositions were fabricated by freeze-casting. Swelling studies revealed a negative thermosensitivity and contraction of FEG above the inverse transition temperature (30°C). Tensile testing showed a strong positive correlation between the concentration of FEG and the strain-to-failure of composites which increased from 37% to 94% as the concentration increased. *In vitro* studies revealed FEG contains cell-binding sites and did not hinder the attachment or viability of induced pluripotent stem cell-derived cardiomyocytes. The elastogenic capability of FEG was assessed by studying the gene expression of lysyl oxidase (LOX), elastin (ELA), and fibrillin-1 (FIB-1) which upregulated significantly on scaffolds with higher FEG content, suggesting that FEG would be a suitable material to use to design templates that promote elastogenesis. In addition, layer-specific tri-layer scaffolds were shown to stimulate layer-specific gene expression of extracellular matrix markers such as collagen type I (COL), hyaluronan synthase-2 (HAS-2) and ELA. Tri-layer

scaffolds exhibited a non-linear mechanical response as well as bending anisotropy, a key deformation characteristic of native valves.

Preface

The research described in this thesis was carried out by the author at the Department of Materials, University of Oxford between October 2016 and February 2020, under the supervision of Prof. Jan T Czernuszka. It is original in its contents except where reference to the work of others is acknowledged in the text. No part/s of this thesis have been submitted or accepted for any other degree at this university or elsewhere.

Parts of the work in this thesis are the subject of a patent:

1. S. Iftekhar, J. T. Czernuszka, Oxford University Innovation Limited; Methods and Products, UK Patent Application Number: GB2004902.9. 2020 Apr 02.

Parts of the work in this thesis was presented at an international conference:

1. S. Iftekhar, C. Lopez, C. Carr, J. T. Czernuszka, "Novel Collagen and Elastin Composites for Heart Valve Tissue Engineering", 2018 MRS Fall Meeting, Boston, US.

Acknowledgements

Never in a million years would I have thought I would be writing my thesis during a pandemic. Although, my thesis is finally complete, the pandemic continues, and the world is still fighting and coming to terms with what the future holds. There are many people who I owe my gratitude to and without whom this thesis would not have come to be what it is today.

First and foremost, my supervisor, Prof. Jan Czernuszka. Thank you for providing me with this amazing opportunity (which I have absolutely relished from day one!) and allowing me to take my own decisions and steer the direction of my Ph.D., but also guiding me when it was needed. I would like to extend my sincerest thanks to Prof. Carolyn Carr for providing me with lab space to conduct the *in vitro* studies. I am also thankful to other members of the group in DPAG who were very helpful. A special thanks to Colleen Lopez and Ujang Purnama for training me and bearing with my questions.

I would also like to thank the Biomaterials group, specifically Jim (Yang) Xu, Rabia Nazir, Narjes Rashidi, Fangxin Li, Mu-Huan Lee, Sasza Nabilla, Ilayda Karadag, Hazal Gezmis for listening patiently to my frustrations and concerns when things didn't work out, which was a lot of the time!

I have to thank my siblings too, I'm not entirely sure what for, but I guess if you're reading this, you all helped me stay sane in your own unique ways!! Thank you, Selina, Onny, Shakline and Reema.

Last but by no means least, I would like to thank my parents, thank you for your boundless love, support, and encouragement in all I have strived to do.

Table of Contents

List of Abbreviations

ΔF	Interaction Free Energy
ΔG*	Activation Energy
ΔT	Change in Temperature
ΔV	Change in Volume
100C	100% Collagen - 0% FEG
25C-75E	25% Collagen - 75% FEG
50C-50E	50% Collagen - 50% FEG
75C-25E	75% Collagen - 25% FEG
AAA	Amino Acid Analysis
AB	AlamarBlue
AC	Against Curvature
ADH	Adipic Acid Dihydrazide
ANOVA	Analysis of Variance
ATR	Attenuated Total Reflectance
AV	Atrioventricular Valve
aVICs	Activated Valvular Interstitial Cells
BM-MSC	Bone Marrow-Mesenchymal Stem Cell
$C_2O_4^{2-}$	Oxalate Ions
CAVD	Calcific Aortic Valve Disease
cDNA	Complementary Deoxyribonucleic Acid
CH_2	Methyl Group
CM	Cardiomyocyte

COL	Collagen type I gene
COOH	Carboxyl Group
C_t	Cycle Threshold
CVD	Cardiovascular Disease
D_c	Diffusion Coefficient
DNA	Deoxyribonucleic acid
DPBS	Dulbecco’s Phosphate Buffered Saline
E	Young's Modulus from Storage Modulus
E_B	Bending Modulus
E_C	Compressive Modulus
ECM	Extracellular Matrix
EDC	(1-ethyl-3-(3-dimethylaminopropyl)carbodiimide hydrochloride)
EGDE	Ethylene Glycol Diglycidyl Ether
ELA	Elastin Gene
ELP	Elastin-Like-Polypeptides
EMT	Endothelial- to-Mesenchymal Transition
E_T	Young's Modulus
eVICs	Endothelial Valvular Interstitial Cells
FEG	Fibrillar Elastin Gel
FIB-1	Fibrillin-1 gene
FT-IR	Fourier Transform Infrared Spectroscopy
G	Osmotic Shear Modulus
G'	Storage Modulus
G"	Loss Modulus

G*	Complex Modulus
GAGs	Glycosaminoglycans
HA	Hyaluronic Acid
HAS	Hyaluronan Synthase gene
HAS-2	Hyaluronan Synthase 2 gene
HDMI	Hexamethylene Diisocyanate
HFP	1,1,1,3,3,3-Hexafluoro-2-propanol
hiPSC-CMs	human induced Pluripotent Stem Cells- derived cardiomyocytes
hiPSCs	human induced Pluripotent Stem Cells
HKG	Housekeeping Gene
HPVC	Human pre-valvular endocardial cells
HSD	Honestly Significant Difference
HUVEC	Human Umbilical Vein Endothelial Cells
HVTE	Heart Valve Tissue Engineering
IE	Insoluble Elastin
iPSC	induced Pluripotent Stem Cells
ISTE	In situ Tissue Engineering
ITT	Inverse Temperature Transition
k_b	Boltzmann's Constant
LC-MS	Liquid Chromatography–Mass Spectrometry
LCST	Lower Critical Solution Temperature
LOX	Lysyl Oxidase gene
LSCM	Laser Scanning Confocal Microscopy
M_c	Molecular Weight Between Cross-links

mRNA	Messenger Ribonucleic Acid
MSC	Mesenchymal Stem Cells
MW	Molecular Weight
n*	Number of Critical Nuclei
N/A	Not applicable
NaOH	Sodium Hydroxide
N_C	Crowding Factor
NH_2	Amino Group
NHS	N-Hydroxysuccinimide
NCMs	Non-cardiomyocytes
NR	Not reported
N_T	Total Charge
OH	Hydroxyl Group
oVICs	Osteoblastic Valvular Interstitial Cells
PBS	Phosphate Buffered Saline
PCL	Poly(Caprolactone)
PEG	Poly(Ethylene Glycol)
PEGDA	Polyethylene(Glycol) Diacrylate
PFA	Paraformaldehyde
PG	Proteoglycan
PGA	Poly(Glycolic Acid)
PGS	Poly(Glycerol Sebacate)
PHA	Poly(Hydroxyalkanoate)
pI	Isoelectric Point

PLA	Poly(Lactic Acid)
PLLA	Poly(-L-Lactic Acid)
PSC	Pluripotent Stem Cells
PTFE	Poly(Tetrafluoroethylene)
PVC	Polyvinyl Chloride
pVICs	Progenitor Valvular Interstitial Cells
Q_m	Water-Uptake Ratio
qPCR	Real-Time Quantitative Polymerase Chain Reaction
Q_v	Volumetric Swelling Ratio
qVICs	Quiescent Valvular Interstitial Cells
R	Hydrodynamic Radius
RGD	Arginine-Glycine-Aspartic Acid
RI	Rock Inhibitor
RPMI	Roswell Park Memorial Institute
SA/V	Surface Area-To-Volume Ratio
SE1	Soluble Elastin 1
SE2	Soluble Elastin 2
SE3	Soluble Elastin 3
SEM	Scanning Electron Microscopy
SV	Semilunar Valve
SVD	Structural Valve Deterioration
T	Temperature
tanδ	Loss Factor
TAVR	Transcatheter Aortic Valve Replacement

TBP	TATA-Box Binding Protein
TE	Tissue Engineering
TGF-β1	Transforming Growth Factor Beta-1
TNNT-2	Cardiac Muscle Troponin T
v	Specific Volume of Dry Polymer
V	Velocity
V_1	Molar Volume of Solvent
v_{2m}	Volume fraction from Volumetric swelling
V_c	Critical Velocity
v_e	Cross-linking Density
VEC	Valvular Endothelial Cells
VHD	Valvular Heart Disease
VICs	Valvular Interstitial Cells
V_o	Original Volume
VPGXG	Valine-Proline-Glycine-X-Glycine
WC	With Curvature
α	Volumetric Temperature Expansion Coefficient
α-SMA	Alpha Smooth Muscle Actin
γ	Shear Strain
δ	Phase Angle
η	Viscosity
η*	Complex Viscosity
ρ_p	Density of Polymer
ρ_s	Density of Solvent

σ	Shear Stress
σ^*	Interfacial Free Energy
Φ	Volume Fraction
χ	Polymer Solvent Interaction Parameter
ω	Frequency of Deformation

1

Scope of Thesis

Cardiovascular disease (CVD) is the largest contributor to morbidity and mortality in the world, resulting in 17.7 million deaths globally [1]. Degenerative diseases of the valves such as stenosis (valve stiffening) and regurgitation (insufficiently closing) contribute to CVD. Valvular heart disease (VHD) is becoming increasingly prevalent and can be either congenital or acquired [2]. The current treatment options are limited to two types, either a biological (autograft, allografts or xenografts) or mechanical valve. Both types of prostheses have been reported to be durable for up to ~15 years, however, biological valves are associated with structural deterioration and as mechanical valves are non-viable, reoperation is often necessary [3]. The failure of biological prostheses has been associated with the disruption of the extracellular matrix network, in particular the inability of adult cells to regenerate degraded elastin [4]. This is a major problem as the decrease in elastin alters the mechanical properties of valves, resulting in a decrease in its efficiency [5], [6]. Autologous valves have been shown to offer promise as they are inherently cellularised and therefore equivalent to native valves in terms of their ability to be remodelled and maintain long-term functionality [7]. However, the limited availability of autologous valves and the requirement of replacing one valve with another limits its feasibility.

Tissue engineering (TE) offers a promising alternative to current prostheses. It combines cells, scaffolds and biological signals to potentially mimic the extracellular matrix (ECM) of connective tissues and act as a bioactive replacement [8]. Although significant work has been carried out in the field, there is a need for constructs that can mimic the composition of native valves as this ultimately dictates the structural and mechanical properties. Substantial work has been conducted on synthetic and natural polymers as well as decellularised matrices, however, they lack the combination of

high stiffness and extensibility that valves exhibit due to their unique composition and architecture. An area which has received particularly little attention is the ventricularis layer of the valves which is composed of 13% elastin and is responsible for its high resilience and durability. This layer is particularly important as it is responsible for the long-term functionality of the valves. Approaches of fabricating scaffolds have been unsuccessful at simulating the mechanical properties of this layer sufficiently.

A possible method to do this is to incorporate a layer of elastin in scaffolds to mimic the ventricularis, however, endogenous forms of elastin are limited as biomaterials. Natural elastin-based materials are limited to two forms, one which is essentially unprocessable and another that is water-soluble and therefore requires extensive cross-linking [9]. The cross-linking of soluble elastins leads to scaffolds that no longer exhibit the physicochemical and mechanical properties of elastin [10]. Synthetic variants of elastin have become popular alternatives, however, questions that still need to be addressed include: (1) the compliance of elastin which gives its unique mechanical properties (a high strain-to-failure and resilience) and (2) the *in vitro* synthesis of elastin.

This thesis studies the isolation of a novel form of elastin which was identified during preliminary work by the author. After isolation of the material, characterisation of its properties as well as application of the material as a biomaterial for tissue engineering of heart valves will be evaluated. The main objectives of this thesis were to:

- Modify insoluble elastin by conducting limited hydrolysis to obtain a gel-like form of elastin. Evaluate the microstructure, infrared characteristics, rheological response, and the effect of pH on the gel to determine the extent of

polymer-solvent interactions and propose a model for the mechanism of isolation (Chapter 3).

- Fabricate elastin-only scaffolds as well as composites using freeze-casting with the new material to obtain porous structures. Evaluate the pore, swelling and degradation characteristics to understand the suitability of the material as a scaffold for tissue engineering applications. Identify a suitable composition to fabricate tri-layer scaffolds for application in heart valve tissue engineering (Chapter 4).
- Evaluate the compressive, tensile, and bending properties of scaffolds and understand the effect of the substitution of the material on the bulk mechanical properties (Chapter 5).
- Evaluate the biological properties of the scaffolds fabricated in terms of cell viability, adhesion, and gene expression. Particular attention is to be given to elastogenic markers that are involved in the synthesis of elastin as well as ECM markers that are layer-specific (Chapter 6).

2

Literature Review

2.1 Introduction

Tissue engineering (TE) offers the potential to engineer a viable autologous valve substitute that can overcome the limitations of implants. Heart valve TE (HVTE) is a multifactorial challenge that encompasses a scaffold (template for cells), cells and appropriate biological cues. This chapter presents the background to the structural and mechanical properties of valves as well as current strategies for HVTE. It aims to review the literature on potential scaffolds for TE with a focus on natural materials and discusses the importance of mimicking the native architecture of valves when designing scaffolds. This chapter emphasises the significance of elastin in the functionality of valves and the success of an engineered valve. It also highlights the little research on elastin-based scaffolds for HVTE applications and the need to integrate elastin in future research.

2.2. Heart Valves

2.2.1. Structure

The mammalian heart is an exceptionally complex organ. It is the first organ that forms in an embryo after conception and continuously grows through adolescence [11]. The heart beats approximately 2.5 billion times during an average human lifetime, primarily supplying the body with oxygen, essential nutrients, and disposing of metabolic waste [12]. The heart develops into a muscular four-chambered system from a single cardiac tube through a multifaceted process called cardiogenesis [13].

Cardiogenesis is a complex process that involves a cascade of simultaneously occurring events, it has been simplified in the following account to provide an overview of major events. The cardiac tube has a cellular outer layer called the myocardium and an inner layer called the endocardium, the layers are separated by the cardiac jelly, an acellular gelatinous matrix, predominantly composed of hyaluronic acid (HA) [14]. The cardiac jelly has been shown to act as a template and regulate cell migration, proliferation and differentiation [15]. Valvulogenesis is the process involved in heart valve development [16]. It begins with the formation of the endocardial cushions (from the cardiac jelly), they are swellings that are generated by the accumulation of ECM in the atrioventricular canal [17]. Endocardial cells surrounding the pre-valve cushions transform into mesenchymal cells by a process called the endothelial-to-mesenchymal transition (EMT) [18]. The cushions are invaded by mesenchymal cells and the cardiac jelly is remodelled, eventually replacing it with proteoglycans and structural proteins including collagen and elastin [19] to form the atrioventricular valves. The same process occurs at the outflow tract where the semilunar valves develop [20]. Morphogenesis of the valves from a gelatinous matrix to fibrous cusps occurs in a highly regulated and dynamic environment through sophisticated molecular and mechanical mechanisms [21], [22]. Four independent valves develop through this process. Two atrioventricular valves (AVs) which connect the atria to the ventricles, the bicuspid and tricuspid (also known as the mitral valve) valves; and two semilunar valves (SVs) which connect the ventricles to major blood vessels, these are the aortic and pulmonary valves. All except the bicuspid valve have three leaflets (or cusps). This thesis will focus on the properties of aortic valves.

The aortic valve is not an independent structure, it is part of a larger complex called the aortic root (Fig.2.1). The aortic root is part of the left ventricular outflow tract [23]. It is responsible for forming a boundary between the left ventricle and the aorta, as well as supporting the aortic valves and maintaining coronary perfusion and laminar flow [24]. The main components of the aortic root are the leaflets, the sinuses of Valsalva and the interleaflet triangles, it is necessary for all of these to be functioning properly to maintain the pressure of the heart [25]. The sinuses of Valsalva are dilated structures that sit behind the leaflets, they form vortices which enables them to close efficiently [26]. The interleaflet triangles are supportive structures that lie between the sinuses of Valsalva and the leaflets [27]. The three semilunar leaflets in the aortic valve are responsible for sealing the junction connecting the left ventricle to the ascending aorta [28]. The leaflets in the AV are attached in the shape of a hyperbolic curve, giving it its ability to bear high loads [29].

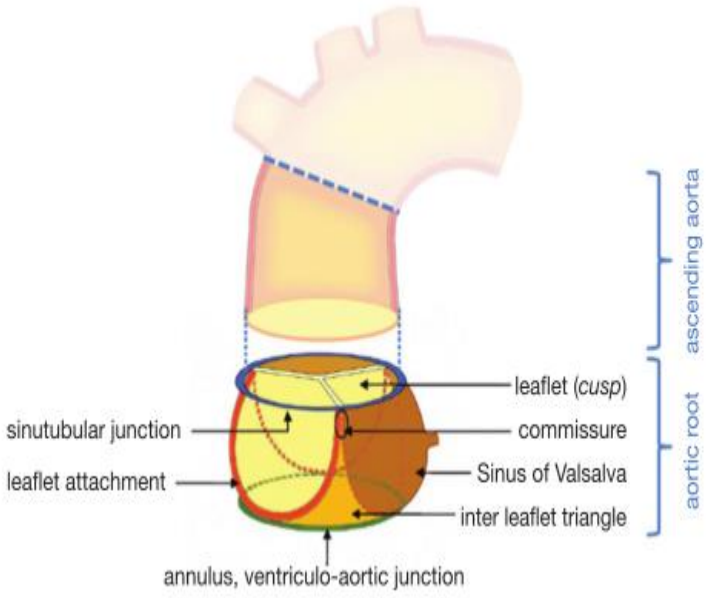

Figure 2.1: Illustration of the aortic root with its major components [24].

Heart valves are asymmetric connective tissues that adapt to their local environment by responding to physiological cues. They have a unique microstructure and are comprised of three major zones called the fibrosa, spongiosa and the ventricularis, illustrated for the aortic valve in Fig.2.2 [30]. Each of the layers has a specific composition and arrangement of extracellular matrix (ECM) components.

The fibrosa is the load bearing zone, it is made up of predominantly type I collagen fibres that are orientated in the circumferential direction and some elastic fibres. Collagen has a crimped structure which gives the fibrosa a corrugated shape when it is relaxed, under pressure the collagen fibres straighten, changing the shape of the valve to the closed position [31].

The spongiosa is a gelatinous zone which is sandwiched between the fibrosa and ventricularis. Its main function is to behave as a buffer and prevent delamination by allowing shearing between the outer zones during bending and stretching [32]. This layer is made up of loosely arranged collagen fibres, glycosaminoglycans (GAGs), proteoglycans (PGs) and water. The most abundant GAG is hyaluronan (HA) which forms approximately 60% of the spongiosa, other GAGs include dermatan sulphate and chondroitin sulphate [33].

The ventricularis layer is composed of randomly orientated collagen fibres and dense sheets of radially aligned elastin, this zone is much richer in elastin than the fibrosa [34]. It has the highest extensibility and enables the collagen to return to its original relaxed crimped configuration after extending by rapidly recoiling the elastic fibres [35].

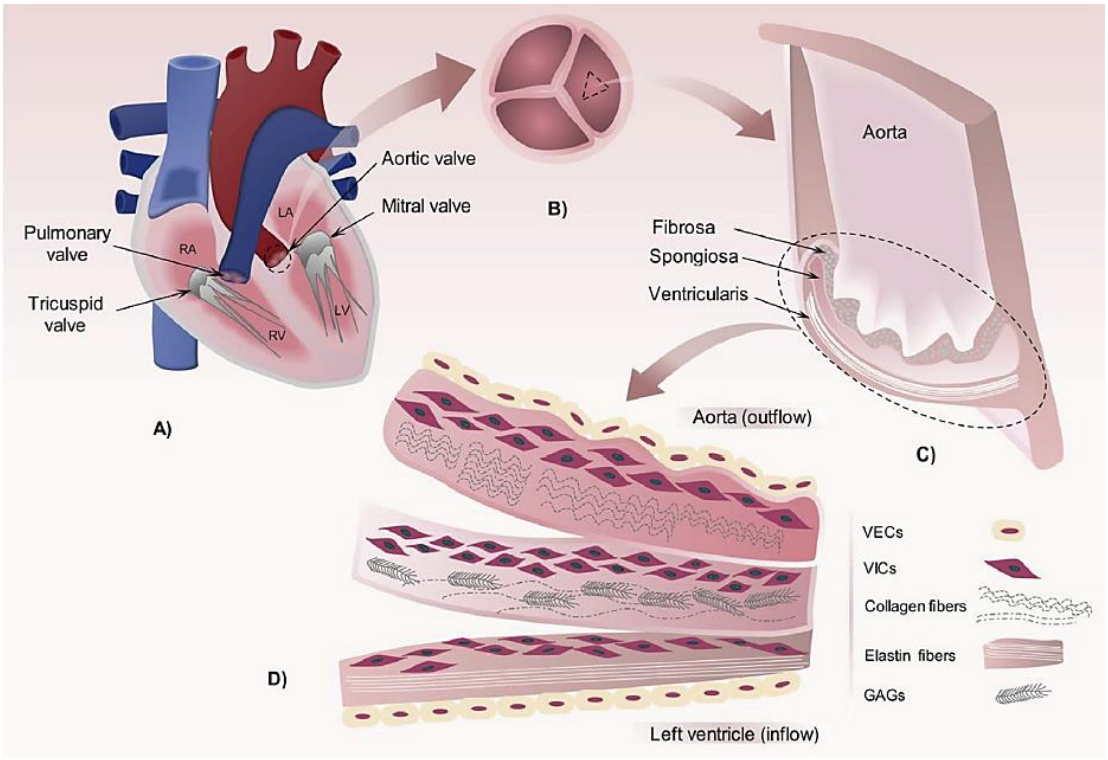

Figure 2.2: Illustration of tri-layer structure of aortic valve, showing the stratified zones in (D) collagen-rich fibrosa, spongiosa and the ventricularis, and the distribution of valvular interstitial cells (VICs) in all three layers and valvular endothelial cells (VECs) on the surface [36].

2.2.2. Composition

2.2.2.1. Collagen

Collagen is an insoluble protein that forms the basic structural element of all soft and hard connective tissues. It is the most abundant protein in humans and forms up to 30% of all proteins [37]. In the heart valves, collagen constitutes approximately 50% of the ECM, instilling it with adequate stiffness to carry out its function. There are 29 genetically different forms of collagen that have been identified as either fibrous or non-fibrous [38]. Valves are composed of three of these types: 74% type I, 24% type III and 2% type V collagen [39].

Procollagen, the precursor of collagen, is composed of three α-polypeptide chains that form a triple helix (Fig.2.3a). The primary structure of collagen contains over 1000 amino acids [40] and is a repeating sequence of $(G\text{-}X\text{-}Y)_n$ where G is glycine and X and Y can be any amino acid, but are frequently proline and hydroxyproline [41]. Glycine occurs at every third position of the polypeptide resulting in a tightly packed triple helix. The structure is stabilised by the formation of interchain hydrogen bonds.

Processing of procollagen occurs in the rough endoplasmic reticulum and involves glycosylation and hydroxylation of lysine and proline residues. Post-processing, tropocollagen is released into the extracellular space where the C- and N-terminals of procollagen are cleaved resulting in lateral aggregation of triple helices. Binding of helices occur at a periodicity of 67 nm resulting in a characteristic banding pattern called the D-period as shown in Fig.2.3b. The aggregated molecules are spontaneously cross-linked by lysyl oxidase (LOX) which oxidises hydroxylysine and lysine residues found at the end of collagen chains to form aldol cross-links.

Polymerisation of procollagen results in a hierarchically organised structure containing collagen fibres with a diameter of 1.5nm and length of 300nm [37]. The Young's modulus of collagen varies between 0.1-5.0GPa in connective tissues due to differences in structural arrangement [42]. Collagen has a low strain-to-failure (13%) but is very resilient (90%) [42] due to its highly packed structure which prevents sliding between helices.

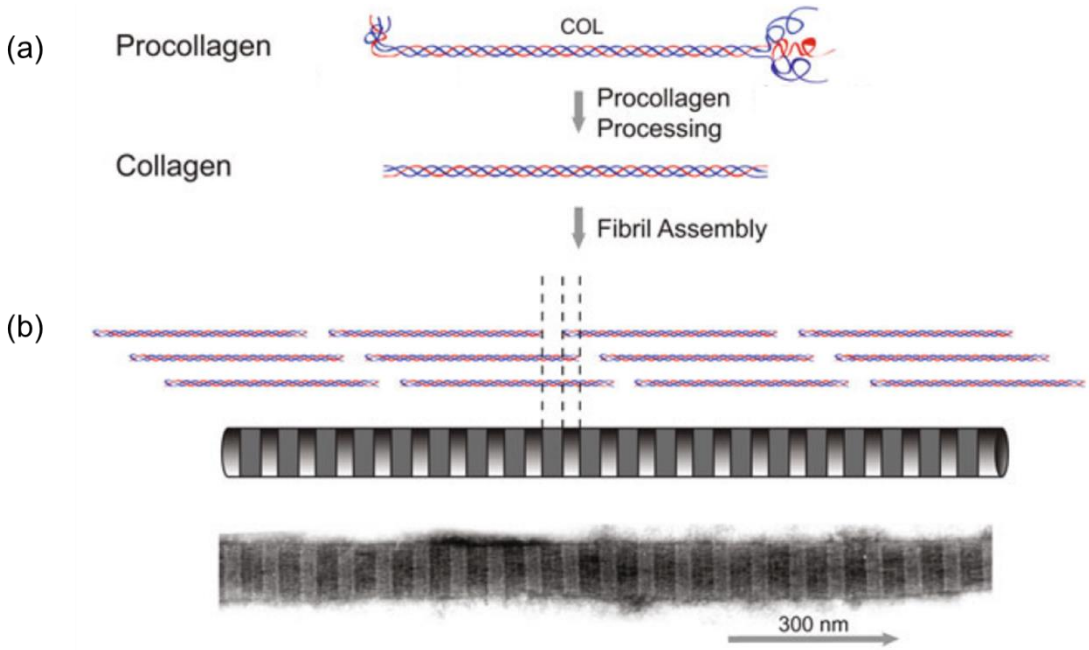

Figure 2.3: Assembly of collagen fibres involves (a) Procollagen molecules composed of three α-chains which are cleaved to result in aggregation of multiple helices into a striated fibrillar structure (b) with periodic banding of 67 nm and a length of 300 nm [43].

2.2.2.2. Glycosaminoglycans and Proteoglycans

Glycosaminoglycans (GAGs) and proteoglycans (PGs) are carbohydrate-based ECM components. GAGs are linear polysaccharides composed of repeating amino sugar and uronic acid disaccharide units. PGs are protein-saccharide complexes consisting of a core protein which is covalently bound to at least one GAG. PGs have multiple functions and vary in size, the primary PGs in the valves are versican, aggrecan, perlecan, decorin, biglycan [44].

Hyaluronic acid (HA) is the most prevalent GAG in the spongiosa as mentioned in 2.2.1. It is a large (10^6-10^7 Da [45]), hydrophilic, linear polysaccharide composed of two repeating monomeric sugars, N-acetyl-D-glucosamine and D-glucuronic (Fig.2.4)

[46]. HA can retain large volumes of water due to its anionic nature which makes it an ideal shock absorber.

HA is synthesised by three isoenzymes, known as hyaluronan synthases 1, 2 and 3 (HAS-1, HAS-2, and HAS-3). HAS-2 is the most common source of high molecular weight (MW) HA and its absence has been found to have detrimental effects on the EMT and cardiac morphogenesis [47]. Mutations in the HAS-2 gene lead to improper cardiac valve formation in mice and therefore HAS-2 is a crucial component for valve development [47].

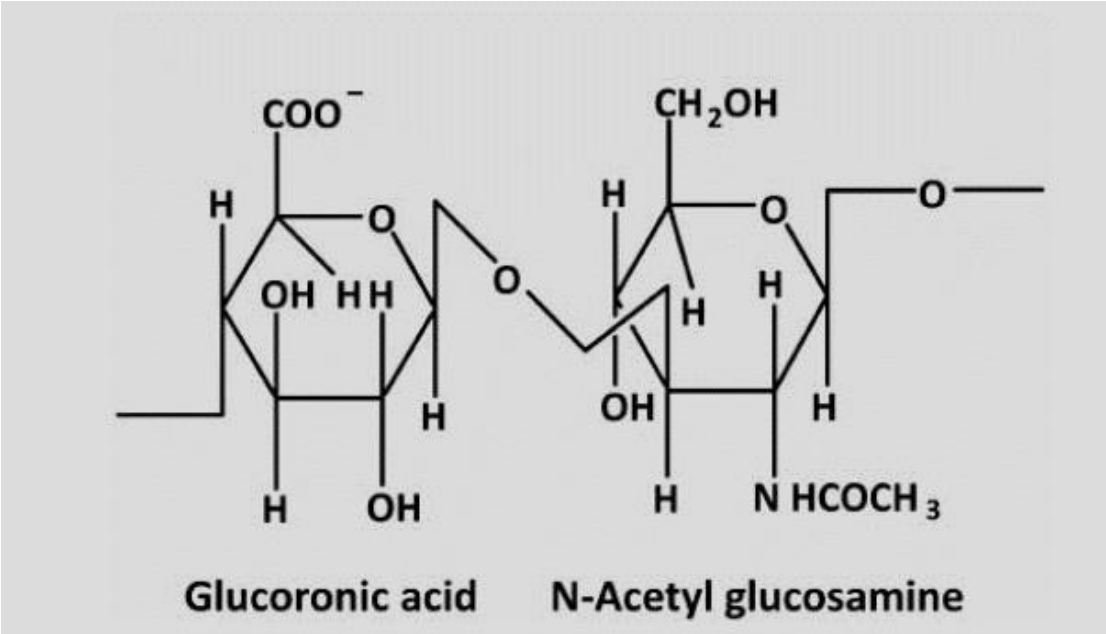

Figure 2.4: Molecular structure of hyaluronic acid, a linear polysaccharide made up of N-acetyl glucosamine and D-glucuronic acid [48].

2.2.2.3. Elastin

Elastin is an essential protein that comprises elastic fibres found in dynamic connective tissues that are subjected to repetitive deformation. They provide tissues with extensibility and resilience with minimised energy loss [42]. Elastin forms 13% of the valves and is the most concentrated in the ventricularis. It is vital for the functionality of valves and dominates at low strains [35].

Elastin is extremely hydrophobic in nature as it is rich in nonpolar amino acids. Tropoelastin, the precursor of elastin is composed of over 75% nonpolar amino acids, including glycine, alanine, and leucine. Glycine forms more than 30% of elastin, akin to collagen, however, it has a lower proportion of proline and hydroxyproline [49]. The remaining polar amino acids include lysine, aspartate, glutamate and arginine [50].

Polymerisation of tropoelastin into an elastic fibre takes place extracellularly. Once processed intracellularly, it is released into the ECM and undergoes a process called coacervation. This is an entropically driven process that results in aggregation of tropoelastin molecules prior to cross-linking. Tropoelastin aligns onto a microfibrillar scaffold composed of microfibrils including fibrillin and fibulin which in turn form elastic fibres where elastin comprises 90% of the entire fibre. After coacervation, the aligned fibres are cross-linked.

Cross-linking of elastin involves multiple steps where the hydrophilic domains containing lysine residues are a major component. The tetra-functional cross-links, desmosine and isodesmosine are the dominant type of cross-links formed in elastin. Other types include bi-functional and tri-functional cross-links known as dehydrolysinonorleucine and dehydromerodesmosine, respectively [51]. Fig.2.5

shows the formation of a desmosine cross-link, three lysine residues are oxidised by LOX into allysine residues (R2, R3 and R4) which further react with a lysine residue (R1). These cross-links can form within the tropoelastin molecules as well as between multiple molecules. Elastin contains over fifteen cross-links per elastin unit, whereas collagen contains one-to-two [52]. Hence, it is a highly insoluble three-dimensional network. There have been many speculations on the structure of elastin. Fig.2.6 summarises the four main models proposed to date. These include the random coil [53], liquid drop [54], oiled-coil [55] and fibrillar models [56], [57]. Although the structures differ in these models, the consensus is that elastin's elasticity is driven by entropy where the increase in order (decrease in entropy) acts as a spontaneous driving force to return elastin to its original configuration.

Elastin is the most extensible biosolid with a strain-to-failure of 100-220% and a Young's modulus of 300-600 kPa [58]. Individual elastin fibres have a Young's modulus of 1.2 MPa and extend up to 200% [59], [60]. It is a very durable protein with a half-life of over 70 years, hence its expression in adult cells is low, and only activated in the case of injury or disease [61], [62]. In valves, endogenous expression of tropoelastin is significantly decreased with age, it is 12% in adolescence and 4% in adults [63]. *In vitro* elastogenesis (synthesis of elastin) is a major bottleneck in cardiovascular TE [64], [65].

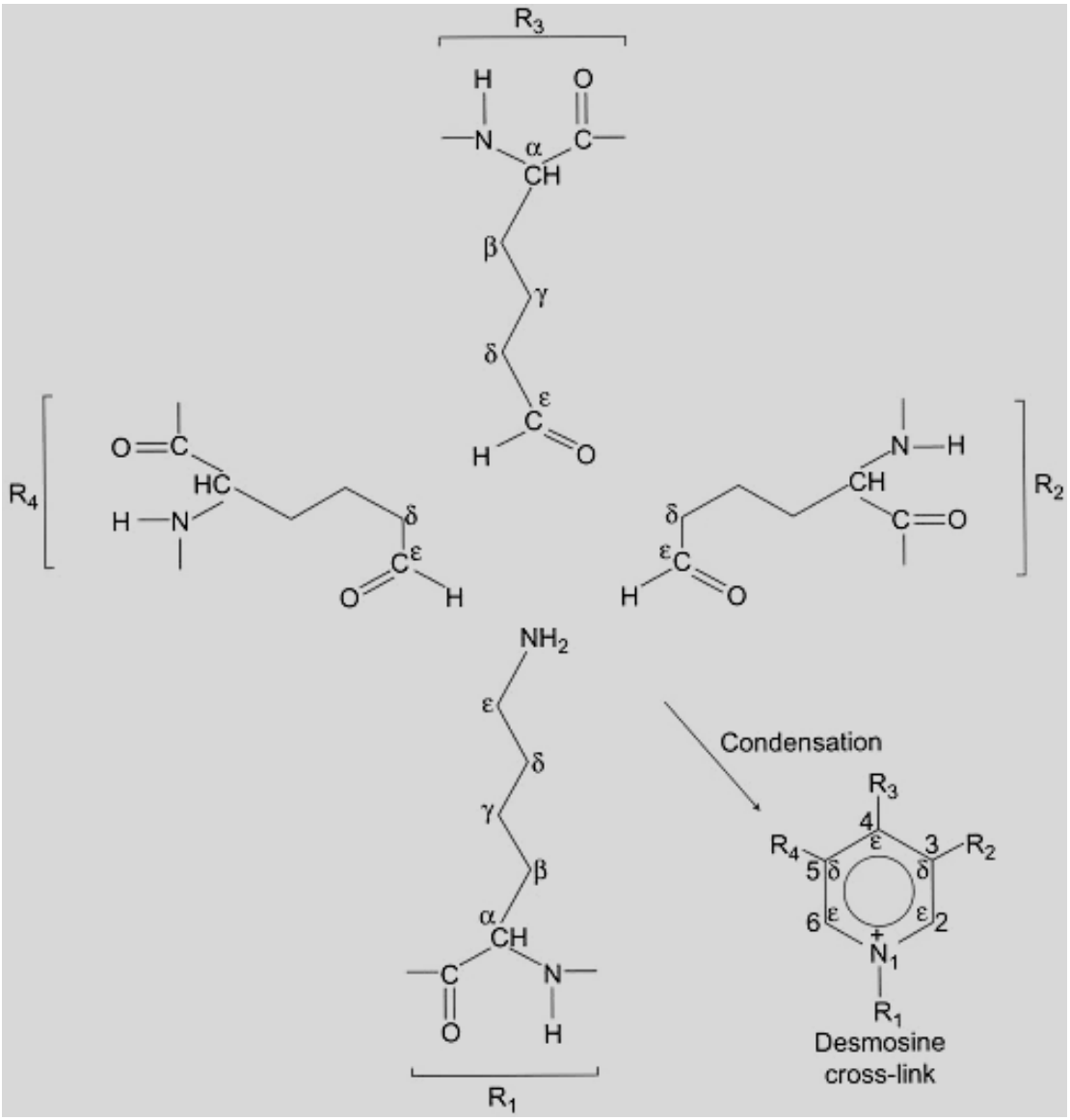

Figure 2.5: Elastin cross-link formation. Involves the reaction of three oxidised lysine residues (R2, R3 and R4) which spontaneously bind to another lysine residue (R1) to form a desmosine cross-link [66].

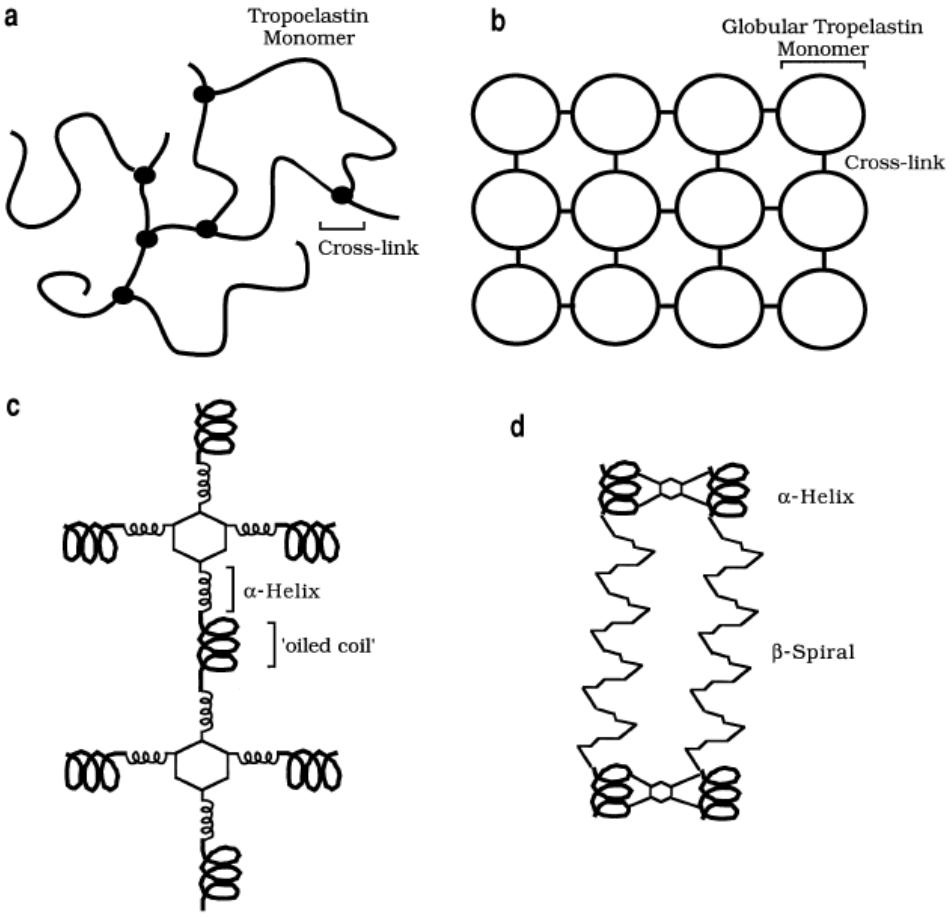

Figure 2.6: The structures of elastin proposed to date. (a) Random coil model contains randomly orientated tropoelastin molecules cross-linked at random points. (b) Liquid drop model is composed of globules of tropoelastin that are cross-linked to each other. (c) Oiled-coil model contains hydrophobic regions termed "oiled coils" which are cross-linked by α-helices. (d) Fibrillar model contains loose helices (β-spirals) that are linked by cross-linking regions composed of α-helices [67].

2.2.2.4. Valvular Cells

The outer surface of the layers, which are in direct contact with the blood are coated in a sheath of cells called the valvular endothelial cells (VECs). VECs experience shear stresses on both sides of the cusps. During systole, the ventricular side is exposed to higher shear stress due to higher velocity and laminar blood flow. Valvular cells are mechanoreceptive and therefore sense changes in stress in their vicinity and respond to them via specific biological signalling to valvular interstitial cells (VICs) [68]. VICs

are a heterogenous population of cells that are present in all three layers and involved in maintaining valvular homeostasis. VICs repair and remodel by adapting to physiological loads [69]. There are five types of VICs, which all originate from mesenchymal cells, but differ in phenotype, these include: embryonic progenitor endothelial cells (eVICs), quiescent VICs (qVICs), activated VICs (aVICs), progenitor VICs (pVICs) and osteoblastic VICs (oVICs). After valvulogenesis, VICs are continuously remodelling the ECM and the micro-damage that occurs during the cardiac cycle by responding to humoral and mechanical cues to maintain its durability and mechanical integrity [70].

VICs exhibit plasticity and switch phenotypes as shown in Fig.2.7, their plasticity is controlled by biochemical and biomechanical cues. The phenotype of VICs is dependent on multiple factors that are not fully understood but have been related to age, species, location in the valve and state of disease. VICs exhibit myofibroblast-like phenotype (aVICs) in foetal and post-natal valves where they are highly active and responsible for the remodelling of valves, in this state they stain positive for alpha-smooth muscle actin (α-SMA). In adult valves, VICs have a predominantly quiescent fibroblast-like phenotype (qVICs) and stain positive for vimentin [71].

VICs exhibit properties of both muscle (contractile) and non-muscle cells (ECM secreting). Their contractility has been related to the expression of sacromeric proteins specific to structural skeletal muscles, including troponin isoforms and α- and β-myosin heavy chain [72], [73] as well as α-SMA. α-SMA is a marker for myofibroblasts and smooth muscle cells which compose 57% of VICs [74] and is expressed by aVICs when they are remodelling the ECM. Quiescent fibroblasts are converted to active myofibroblasts during repair and remodelling of valves, however,

prolonged activation of myofibroblasts is associated with calcification and fibrosis as it promotes osteogenic differentiation of qVICs to oVICs. It is important that they revert to a quiescent state after tissue remodelling to prevent disease.

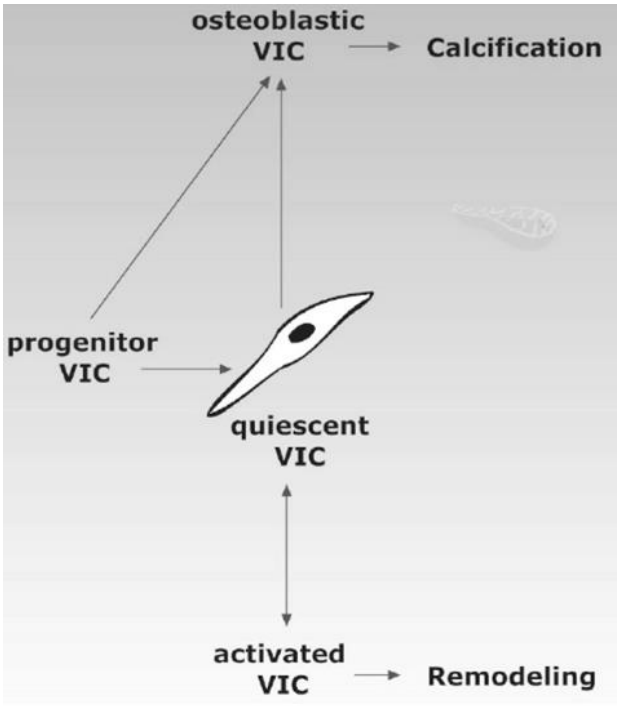

Figure 2.7: Plasticity of valvular interstitial cells (VICs), after differentiation to progenitor VICs, they can further differentiate into active, quiescent and osteoblastic phenotypes depending on chemical and mechanical stimuli [75].

2.2.3. Mechanical Properties

The heart valves operate in a highly dynamic environment where they withstand high transvalvular pressure and repetitive stress without plastic deformation [76], [77]. Valves behave as a bonded unit [78] that open and close approximately $3x10^9$ times during a lifetime [69]. Fig.2.8 shows the configuration of the cusps during systole and diastole. During systole, the valves open by bending backwards (flexural force) to allow the blood to flow. When the blood passes the cusps, they experience shear

stresses and in diastole the cusps shut close, they stretch (tensile force) to seal the aorta and prevent retrograde [79]. Flexure is the dominant mode of deformation in valves, where the valves are exposed to tension (ventricularis) and compression (fibrosa) simultaneously. Valves exhibit flexural anisotropy and are naturally curved towards the ventricularis due to the difference in stiffness of the layers (Fig.2.9).

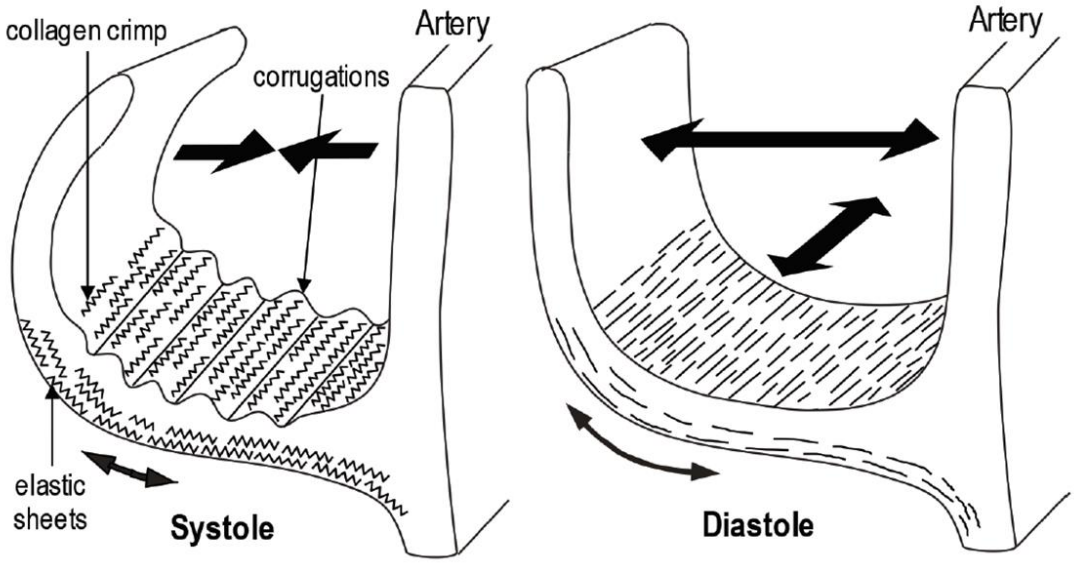

Figure 2.8: Structure of leaflet during systole (open) and diastole (closed) [80].

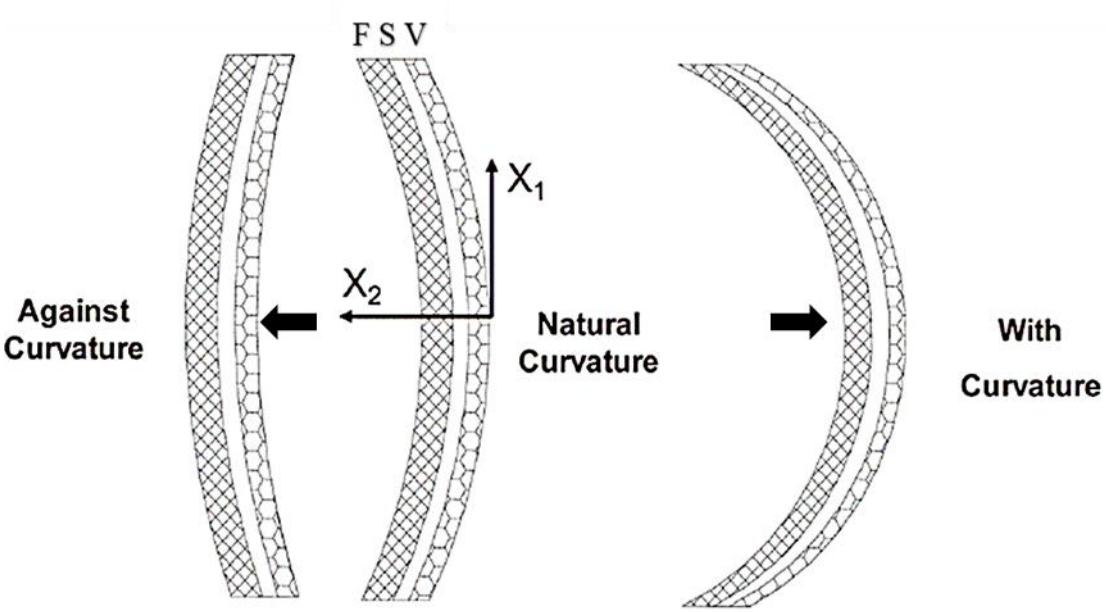

Figure 2.9: Curvature of heart valves with and against curvature where F is fibrosa, S is spongiosa and V is the ventricularis [79].

Tensile testing is the most commonly used mechanical test used to characterise the bulk mechanical properties of valves. Under tension, the valves exhibit a non-linear or bilinear mechanical response. The stress-strain curve for a valve is composed of three main regions as shown in Fig.2.10. These are: (a) the linear elastic region which occurs at low strains when the collagen fibres are slack and the load is taken up by the elastic fibres, (b) the transition phase which is non-linear and the start of the transfer of force from the elastic fibres to the uncrimped collagen fibres and (c) the collagen phase which is dominated by the straightened collagen fibres that carry the load before the valve ruptures where the collagen and elastic fibres fail [80].

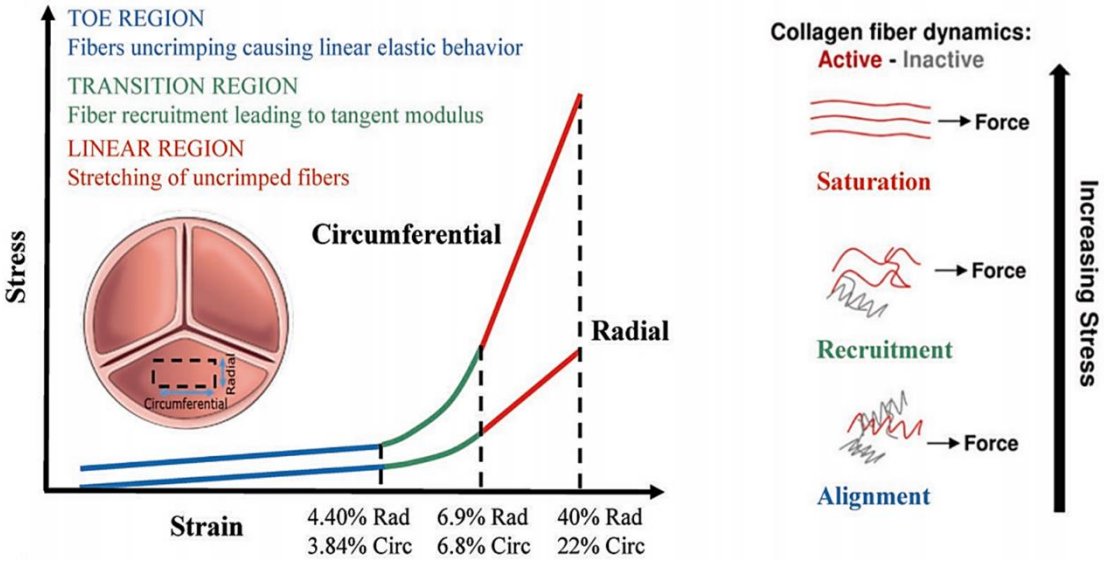

Figure 2.10: Non-linear stress-strain response of a heart valve showing three regions; the elastic, transition and collagen phase [81].

Valves exhibit anisotropic mechanical properties; they are stiffer and less extensible in the circumferential direction compared to the radial direction [34]. There are disparities in the literature regarding the mechanical properties of valves, this is likely due to differences in the samples and testing methodology used. Data available on the mechanical properties of valves has been recently reviewed [82], [83]. Balguid *et al* reported the Young's modulus of human valves to be 15MPa vs 2MPa in the circumferential vs radial direction, whereas the strain to failure was 22% vs 30% in the circumferential direction compared to radial, respectively [84]. The ventricularis has a significant role in allowing extensibility and recoil of the valves, it can elongate up to 63% in the radial direction compared to 22% in the circumferential direction. This is significantly more than the fibrosa which extends up to 28% in the radial direction compared to 20% in the circumferential [85]. Determining the moduli for each layer has been challenging, especially for the spongiosa as it is thin and, in the centre, making it harder to isolate. However, Hinderer *et al* [86], have been able to

characterise each layer using atomic force microscopy, the Young's modulus was reported to be 13.8kPa, 6.1kPa and 12.3kPa for the fibrosa, spongiosa and ventricularis, respectively.

Although the mechanical properties of native valves are important for a tissue engineered valve, they are not necessarily design goals as scaffolds would undergo *in vitro* mechanical conditioning to improve the mechanical properties prior to implantation.

2.2.4. Valvular Heart Disease and Current Treatment Options

Valvular heart disease (VHD) affects people of all ages, in the USA, 2.5% of the population have some form of VHD [87]. The most common cause is calcific aortic valve disease (CAVD) which is dominant in people above 65 years of age [88]. CAVD is characterised as the redifferentiation of qVICs to oVICs which deposit calcium in the valves and express collagen excessively resulting in stenotic valves [89], [90]. In developing countries, VHD is more likely to be caused by rheumatic heart disease and globally it affects over 15 million people [91], [92]. 20% of all cardiac surgery performed worldwide accounts for treatment of VHD [93] accounting for over 370,000 valve replacements annually and predicted to rise to 800,000 by 2050 [94].

Current forms of treatment include valve repair or replacement. The repair of defects is limited, and replacements are more common. Valves are replaced with prosthetic implants, of which there are two major types, mechanical and biological. Mechanical implants are made from synthetic materials whereas biological implants are tissues from human cadavers or of xenogeneic (from a different species) origin. The

advantages and disadvantages of mechanical and biological valves has been summarised in Table 2.1.

There have been significant advances in the development of artificial valves since their introduction in 1952 as a ball-and-cage valve by Hufnagel [95]. Multiple variations followed to overcome the poor haemodynamics and thrombosis caused by the design and the materials chosen, in fact it has been reported that eighty versions exist [96], of these, the main types have been summarised in Fig.2.11. After the ball-and-cage design, tilting disc valves and bileaflet valves were introduced that offered better haemodynamics. However, limitations such as the thrombogenicity of the materials and the need for resizing operations in children are yet to be overcome.

Biological valves are less thrombogenic and offer better haemodynamics. There are three main types: autografts (same living being), allografts or homograft (same species) and xenografts. Autografts are limited to children with congenital valve disease and involves a procedure developed by Donald Ross in 1962 where the patients diseased aortic valve is replaced with their healthy pulmonary valve, and the pulmonary valve is replaced with an implant [97]. Allografts are donated human cadavers, the first was implanted in 1956 by Murray, Heimbecker ad Bigelow, these are less common due to limited supply [98]. Xenografts, on the other hand, are obtained from animal sources. Currently, bovine pericardium and porcine valves are widely used. These were introduced in 1968 with complications associated with immunogenicity. Through investigations, protocols were developed to shield antigenic components of the tissues by washing or electrolysis. Tissue valves are treated with glutaraldehyde to reduce antigenicity and cross-link free amino acids to increase its durability by increasing their resistance to enzymatic degradation [99]. Additionally,

technology such as transcatheter aortic valve replacement (TAVR) developed in the early 2000s provide a micro-invasive delivery technique, as opposed to the invasive cardiopulmonary bypass (open-heart) surgery. The main advantage of autografts is that the cells embedded in the valves do not need to be removed as required in allografts and xenografts. The naturally cellularised valves used in the Ross Procedure offer the advantage that they can remodel the valves in the same way as native valves, this is because the presence of autologous cells enables remodelling and consequently long-term functionality of the valves as suggested by El Hamamsy *et al* [7]

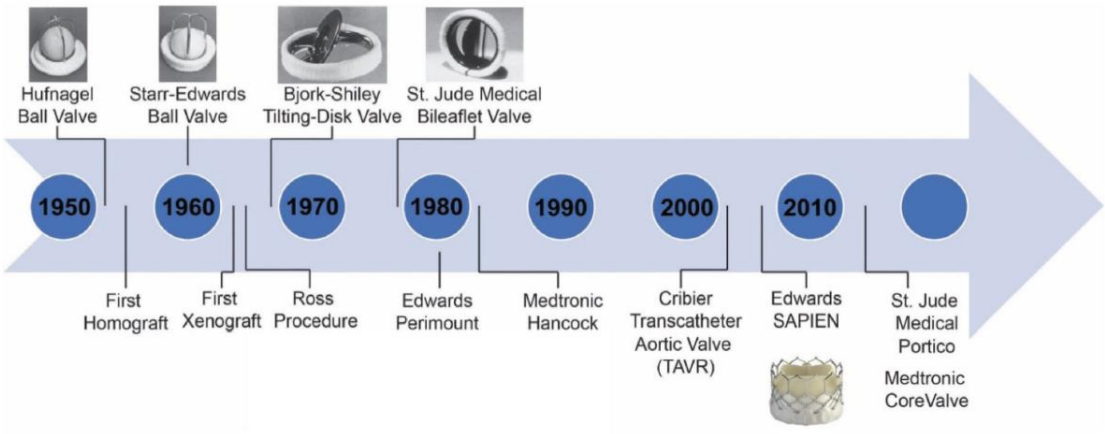

Figure 2.11: Timeline of introduction of mechanical and biological valve replacements over the last 70 years [100].

Table 2.1: Comparison of the advantages and disadvantages of mechanical and biological heart valve prostheses.

Prosthesis	Advantages	Disadvantages
Mechanical	☐ Readily available ☐ Durable (>20 yrs) [101]	☐ Requires anticoagulation therapy to prevent thrombosis ☐ Poor haemodynamics ☐ Requires multiple operations to adjust size in children

Biological	☐ Good haemodynamics ☐ Can be implanted using minimally invasive techniques - reduces recovery time significantly	☐ Limited supply ☐ Less durable (12-15 yrs) ☐ Calcifies rapidly in children ☐ Age-dependent structural valve deterioration ☐ Cells cannot remodel tissue

A major drawback of xenografts is that they are susceptible to age-dependent structural valve deterioration (SVD) due to their immunogenicity. Fixing xenografts has been shown to reduce immunogenicity, however, it is not eliminated as glutaraldehyde only targets the antigens of proteins and not those of carbohydrates. Specifically, galactose-α-1,3-galactose (α-Gal) antigens cause hyperacute rejection as they are not expressed in humans [102]. The rejection results in the upregulation of xenoreactive antibodies that target α-Gal and recruit macrophages to the site of implantation, these cells respond by releasing matrix degrading factors that in turn stiffens the matrix and gives rise to the production of calcification promoting factors [103]. Moreover, glutaraldehyde is inefficient at cross-linking the elastic fibres in valves due to the limited amine groups (<1% [104]) available in elastin, therefore they are susceptible to enzymatic attack [105] and subsequent calcification due to the loss of elastin [106].

Mechanical failure of bioprosthetic valves have been associated with the degradation of elastin and poor homeostasis of elastic fibres which leads to fibrosis due to increased stiffness [107]. The effect of loss of elastin was studied by Lee *et al* [6], they compared a valve digested with elastase to a non-treated valve and found that removal of elastin reduced the extensibility from 43% to 18% strain in the radial direction, and increased stiffness and elongation in the relaxed state (i.e. resilience had decreased). The incorporation of exogenous elastin on bioprosthetic valves has been suggested as a possible method to overcome the loss of elastin. Lei *et al* [108], treated xenografts with

tropoelastin and found an increase in insoluble elastic fibre formation and improved mechanical properties, although, the strain-to-failure was significantly lower than that of native valves (12%). Additionally, fixing xenografts alters the viscoelastic properties of valves significantly (Fig.2.12) where the fixed valve is a whole magnitude stiffer than the untreated sample [109]. This change in mechanical properties promotes pathological remodelling and calcification.

The motivation for TE of heart valves comes from the potentially life-threatening drawbacks and limited durability of currently available prosthetic valves. TE valves would be particularly beneficial for infants born with congenital heart disease, as current treatment options are non-viable.

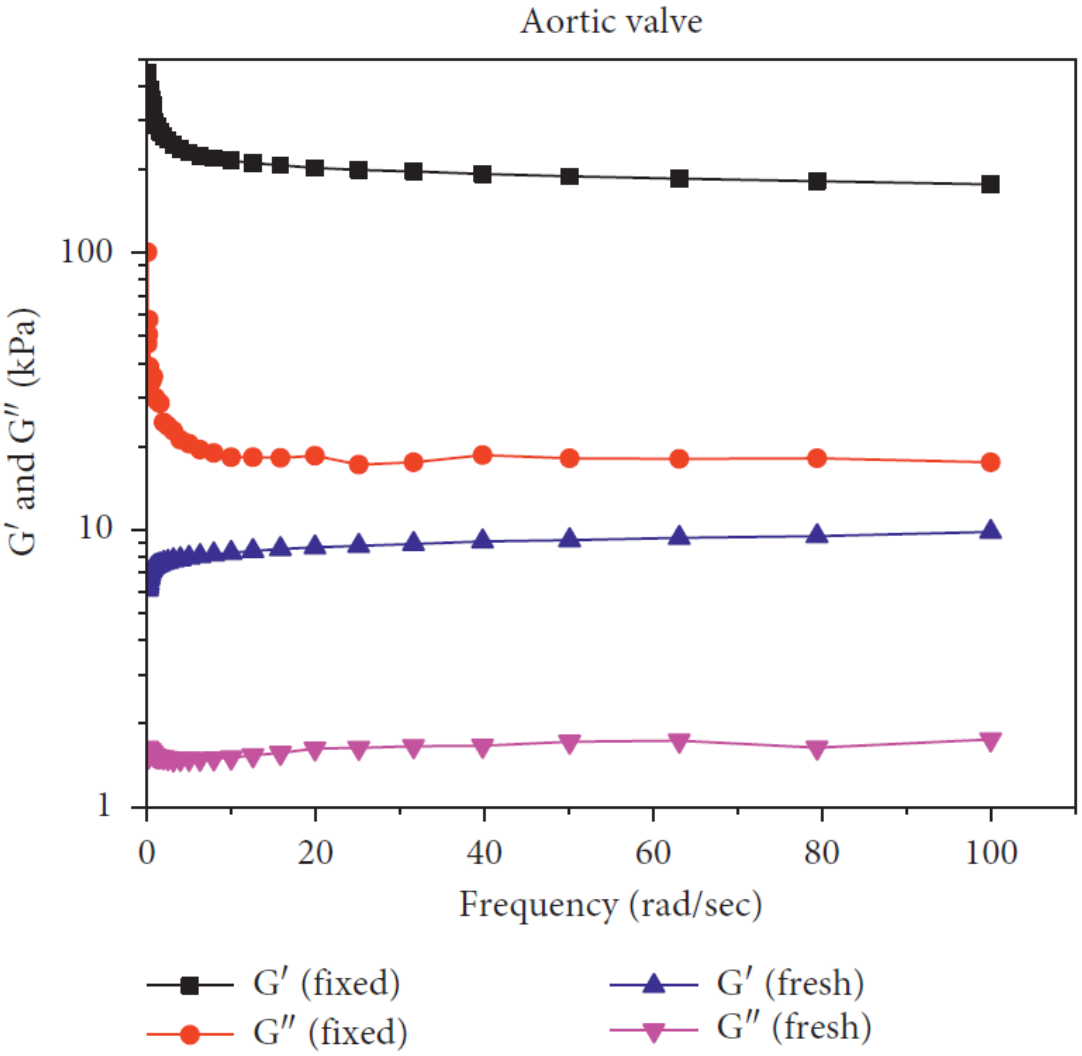

Figure 2.12: Frequency sweep obtained by oscillatory shear test comparing a fixed (formaldehyde treatment) and a fresh xenograft, 100% strain, from 0-100 rad/sec [109].

2.3. Strategies for Heart Valve Tissue Engineering

TE is a promising field that offers the potential to regenerate connective tissues and model diseases. It involves combining three essential elements: cells, scaffolds, and biological signals. The scaffold in tissue engineering is essentially an artificial ECM that supports seeded cells and guides tissue generation. To fabricate a functional valve substitute, it is essential to mimic the ECM as closely as possible and achieve similar

characteristics [110]. The ECM should stimulate cells to grow, differentiate and eventually deposit new ECM that matches the native valves. The choice of material of the scaffold holds great significance, it must have biological ligands that promote cell differentiation and growth as well as have mechanical integrity to withstand the pressure experienced by valves.

2.3.1. *In vitro* tissue engineering

In vitro TE involves producing a functional construct prior to implantation. Fig.2.13 summarises the process involved. In *in vitro* methods, cells (either donated or the patient's) are isolated and expanded before being cultured on a scaffold. Biochemical and mechanical stimuli are provided to stimulate the cells to deposit ECM as they would endogenously. The bioreactor mimics the dynamic environment experienced by the valves. Once mechanically conditioned, the scaffold should theoretically be functional and therefore is implanted into the patient.

Before an *in vitro* tissue engineered valve can be translated, there are several limitations that need to be overcome. The cell source is a major challenge; a viable patient specific source of cells is yet to be identified, standardisation of culturing protocols and a need for feeder free protocols where xenogeneic components must be replaced with xeno-free alternatives. Techniques would need to be automated and must comply with the International Organisation for Standardisation. There has been progress in blood vessels, for example, Humacyte® [111] in the USA are the first to be producing TE blood vessels for clinical application using donated human cells and an 8-week culture process.

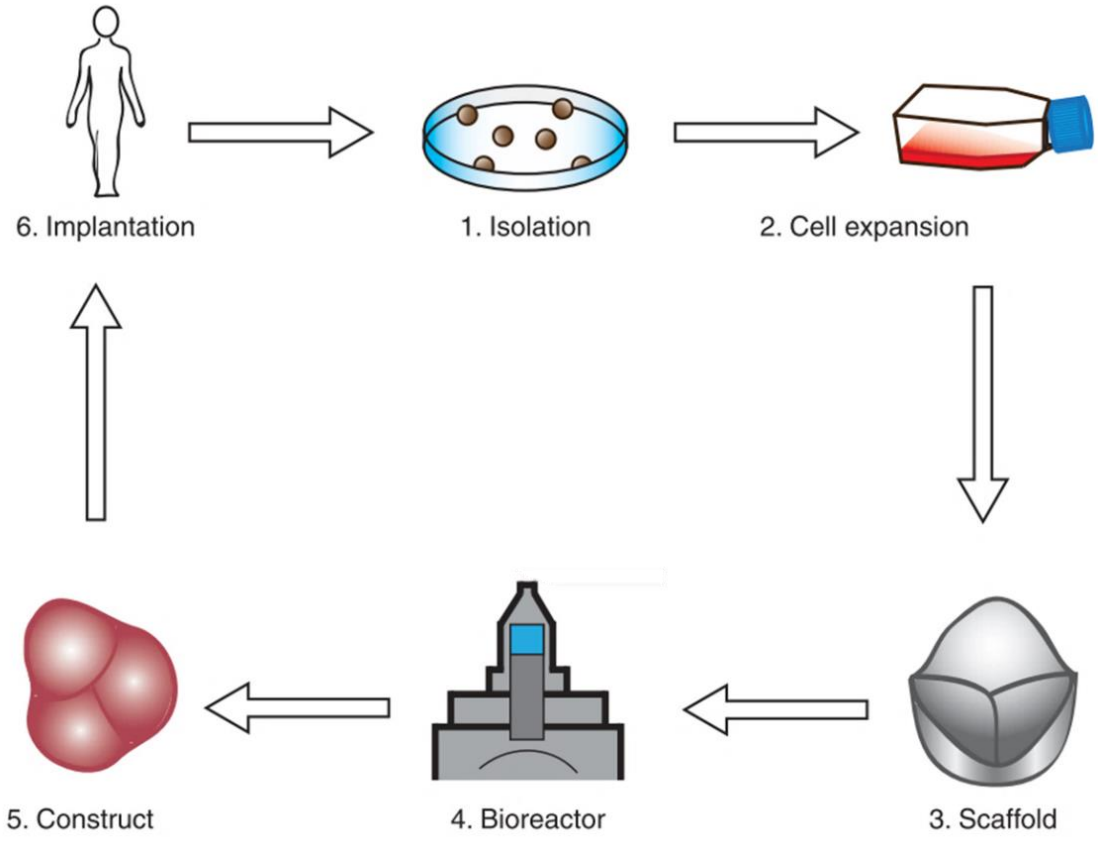

Figure 2.13: Process for in vitro tissue engineering where cells are isolated either from the patient or a donor (1), expanded (2) and cultured on a scaffold (3) before being mechanically conditioned (4) and then implanted in vivo (6) [112].

2.3.2. *In vivo* and *in situ* tissue engineering

In vivo and *in situ* TE have become increasingly popular due to their potential of developing an off-the-shelf valve, potentially overcoming several technical and regulatory challenges that *in vitro* methods pose [113]. In *in vivo* TE, the scaffold is subcutaneously implanted in a cavity where it can be encapsulated by fibrous tissue before it is removed and implanted in the heart [36], [114]. Whereas in *in situ* TE, the scaffold is placed directly in the heart. These methods take advantage of the body's innate immune response to foreign materials and uses the body as a bioreactor to induce endogenous regeneration, as it would if it were healing a wound. A functional

scaffold (with or without growth factors) is implanted at the site of disease or injury, this attracts cells to the site and a cascade of inflammatory events direct a specific host response that eventually results in de-novo tissue formation and scaffold degradation. This method relies on two factors, first, the scaffold's bioactivity to recruit suitable. host stem cells or progenitor cells and second, the intrinsic regenerative capacity of the recruited cells. Relying on the host's regenerative capacity limits the potential of this strategy as it varies with age and could lead to disrupted tissue formation [115], [116]. Additionally, in adults there is insufficient circulation of progenitor cells and reduced migratory and prolific function, this approach would be better suited to treating congenital disease as children have higher levels of circulating progenitor cells [117]. The major advantages of this approach are that the need for autogenic cells and mechanical conditioning are eliminated. However, as seen with *in vitro* methods, there are several challenges that must be overcome for ISTE to be efficacious. It is essential to understand the mechanisms underlying inflammatory responses and the effect of the scaffold's properties such as the surface chemistry and microarchitecture on cell response [118]. A recent proof-of-concept study used an ovine model to study the regenerative capacity of elastomeric scaffolds. The main finding was that although the scaffold promoted ECM deposition, the scaffold had not degraded after 12 months. Further experiments are required to validate these findings and assess the quality of the ECM formed as immature fibres would be unlikely to maintain functionality of the valve long-term [119].

2.3.3. Cell Sources

An ideal source of cells for HVTE would be one that exhibits phenotypic plasticity. As VICs are a diverse population of cells, multiple cell types have been investigated for HVTE applications as reviewed by Jana *et al* [120]. The behaviour of VICs on scaffolds has been studied extensively, however its application in TE is impractical due to the scale required. Cells that exhibit similar phenotypes to VICs have also been investigated, these include fibroblasts [121], myofibroblasts [122], [123], smooth muscle cells [124]–[126] and endothelial cells [127]. Studies have shown that although they are easier to isolate and express similar characteristics to VICs, the sacrifice of intact tissue is undesirable, and their proliferative capacity is limited.

The most popular stem cell type has been mesenchymal stem cells (MSCs) which can be isolated from bone marrow [128], adipose tissue [129] and umbilical cord derived [130] stem cells. MSCs are multipotent cells and can differentiate into multiple lineages such as smooth muscle cells and chondrocytes. Although promising results have been reported, there are concerns regarding the stability of MSCs and their tendency to lead to fibrotic tissue as osteoblast-like VICs are commonly expressed [131].

Pluripotent stem cells (PSCs) have the ability to self-renew as well as differentiate into all types of cells found in the body. There are two types of PSCs, embryonic and induced. Induced pluripotent stem cells (iPSCs) are morphologically and functionally similar to human embryonic stem cells. iPSCs are the patient's somatic cells that are reprogrammed using specific factors [132]. The discovery of iPSCs overcame major ethical concerns associated with the use of embryonic stem cells. Since their discovery, iPSCs have been researched extensively as potential therapeutics and for disease

modelling. iPSCs are differentiated prior to implantation as undifferentiated cells could lead to the formation of teratomas as well as rejection by the hosts immune system.

There are multiple pathways that can be activated from all three germ layers (ectoderm, mesoderm and endoderm) depending on the factors provided [133]. For heart valves, the mesoderm is the most important as it gives rise to components of the circulatory system. Fig.2.14 shows the possible cell types that can be obtained by inducing cells to differentiate into the mesoderm lineage, these include endothelial cells, MSCs, haematopoietic cells or cardiomyocytes. To date, a protocol for iPSC-derived VICs has not been reported, this is mostly likely due to its heterogenicity.

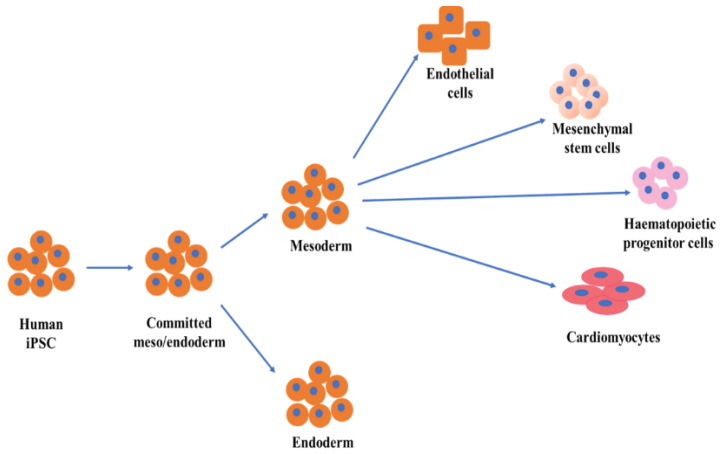

Figure 2.14: Differentiation of iPSCs after reprogramming into two of the three embryonic lineages. Once committed to the mesoderm lineage, the addition of biochemical factors can lead to differentiation into four possible cell types: endothelial cells, mesenchymal stem cells, haematopoietic cells, or cardiomyocytes. Adapted from [133].

iPSCs differentiated to MSCs have been studied for applications in HVTE [134], [135]. The expression of α-SMA as well as the presence of collagen type I and GAGs was reported. However, further studies to understand how iPSC-MSCs mature and

whether they lead to calcification as observed in BM-MSC are yet to be conducted. A recent study reported the differentiation of human iPSC to pre-valvular endocardial cells (HPVCs) that displayed embryonic phenotype and underwent EMT as observed in valvulogenesis [136]. HPVCs are yet to be investigated in 3D constructs for TE applications.

This thesis will study the potential application of iPSC-derived cardiomyocytes (iPSC-CMs) for HVTE as they are heterogenous population of cells with similarities to the population of VICs as will be discussed in chapter 6.

2.3.4. Requirements for Heart Valves

The primary requirements for scaffolds are: (1) biocompatibility, (2) a porous interconnected network, (3) adequate mechanical strength and (4) biodegradability.

Biomaterials come into direct contact with proteins that adsorb to the surface by specific integrins after implantation. Therefore, it is essential to use biocompatible materials that do not elicit an immune response, but instead promote neo-tissue formation.

Porosity of at least 90% [137] is essential for thorough cellularisation and the exchange of nutrients and waste products. The pore size required to promote cellular adhesion and proliferation is between 50-150 μm [138]. A balance needs to be struck with the pore size, as the larger the pores are the lower the specific surface area. Although larger pores are preferred for exchange of media, a lower specific surface area reduces the number of surface ligands for cells to bind to [139], [140].

Mechanical properties of the scaffold are responsible for activating intracellular pathways and regulating VIC phenotype [141]. A functional valve replacement must

withstand the haemodynamic forces and bear the load during each cardiac cycle without experiencing fatigue. For tissue engineering applications, a softer matrix is preferred [142] as it simulates the modulus of healthy heart valves (~6-14 kPa [86]), matrices with higher moduli have shown to promote calcification due to the increased stiffness (27 kPa) [143].

A balance between endogenous neo-tissue formation (synthesis of new ECM) and host-mediated degradation is essential for a functional valve. The scaffold must degrade at a similar rate to the replacement of the scaffold and the degradation products must be non-cytotoxic. These processes are controlled by phagocytic cells (macrophages/monocyte lineages) which interact with the material upon implantation and mediate the host response.

2.4. Scaffolds for Heart Valve Tissue Engineering

2.4.1. Fabrication Techniques

The technique used to fabricate scaffolds is significant as it controls the properties of the scaffolds and scalability of the process. The most popular techniques used for HVTE are electrospinning and freeze-casting.

Electrospinning involves the ejection of a charged polymer solution through the nozzle of a syringe and its collection as dry polymer fibres [144], [145]. Fig.2.15a shows the setup of a typical device and the variables that control the properties of the fibre. Fig.2.15b shows a scanning electron microscopy image of an electrospun scaffold. Electrospinning offers scaffolds with nanoscale control; however, dense scaffolds (low

porosity and small pores) form due to the high concentration of polymer required to produce coherent fibres, this in turn restricts mass transport and cellular infiltration. Additionally, electrospun fibres have poor reproducibility due to their dependence on environmental conditions as well as potential cytotoxicity due to the use of high concentrations (above 250 ppm) of organic solvents such as 1,1,1,3,3,3,-hexafluro-2-propanol (HFP) [146].

Freeze-casting involves the freezing of a polymer suspension and removal of the solvent by sublimation to yield a porous scaffold as shown in Fig.2.16 [147]. The phase diagram in Fig.2.17a shows the steps involved in lyophilisation. The solvent changes from liquid to solid by cooling at ambient pressure. At this point, ice crystals nucleate, and the polymer chains move away from the point of nucleation resulting in growth of the crystals. The size of the crystals is defined by the difference between the temperature of the polymer and the freezing temperature [148]. The ice is removed by sublimation when the temperature and pressure are below the triple point [149], resulting in a porous structure (Fig.2.17b) which is the negative of the ice. The architecture of lyophilised scaffolds is dependent on conditions that control the nucleation and growth of crystals, these include the freezing rate and concentration of the polymer suspension. The main advantages of freeze-casting are that highly porous interconnected networks can be fabricated relatively simply in a controlled and reproducible manner.

The applicability of fabrication techniques is dependent on the biomaterials available and their processability. In this work, processability refers to the ability to manipulate a material into multiple structures and sizes to form a product.

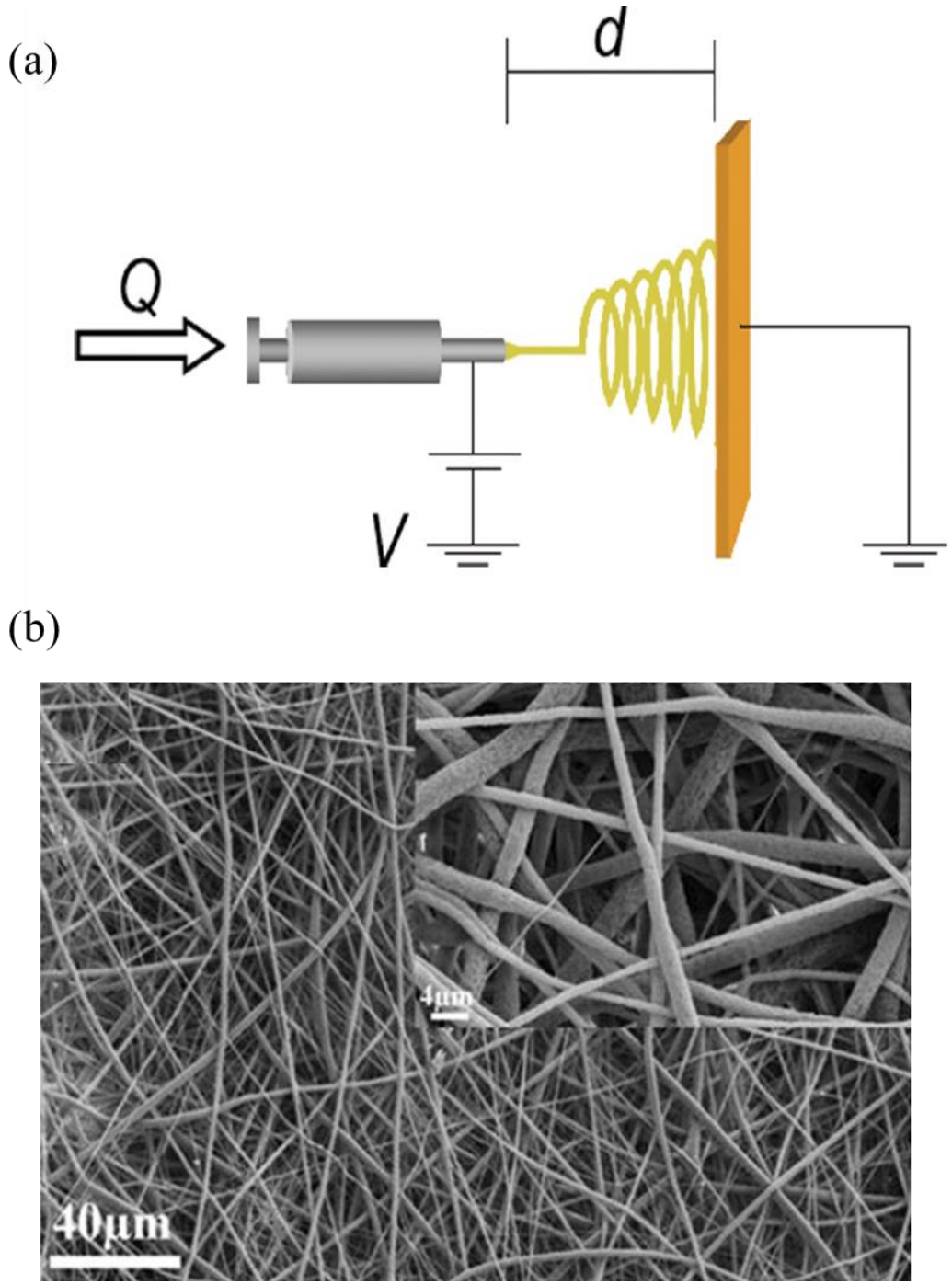

Figure 2.15: Setup of an electrospinning device (a). Includes a syringe pump that contains the polymer solution that is released at a specific flow rate (Q) and operates at a specific voltage (V) to release fibres which are collected on a mat placed at a distance (d) away from the tip of the syringe [145]**. An electrospun composite scaffold (b) composed of polycaprolactone (PCL) and poly L-lactic acid (PLLA) which have a diameter of 1.9-2.3 µm [150].**

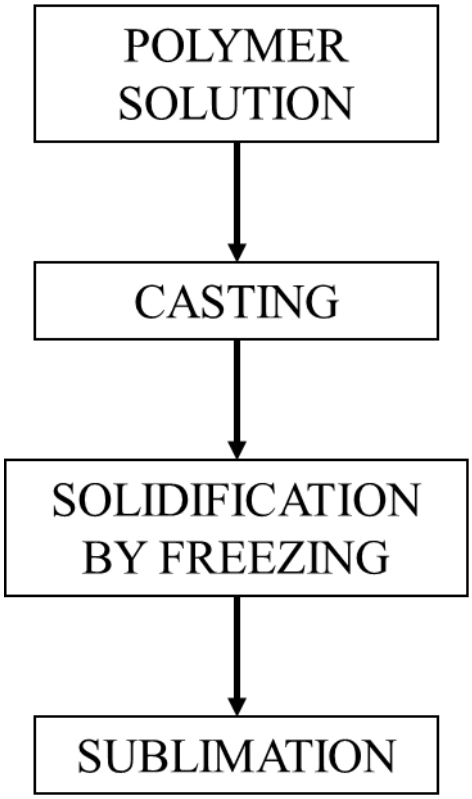

Figure 2.16: Steps to produce a freeze-casted sample. Involves preparation of the solution, casting in a mould and solidification by freezing then removal of the water-based solvent (in frozen form) by sublimation leaving a porous structure.

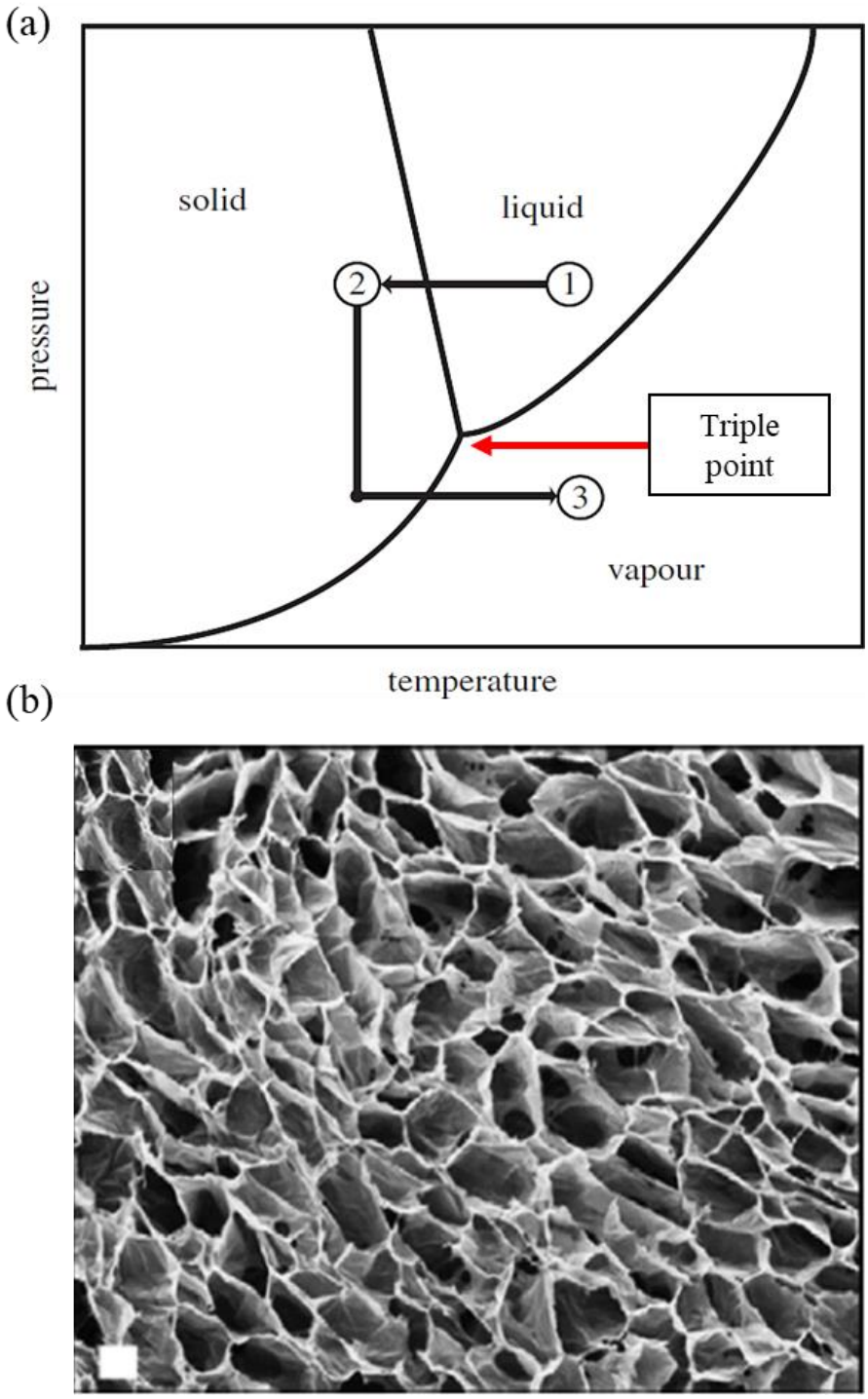

Figure 2.17: (a) Phase diagram showing the changes in the solvent from liquid (1) to solid (2) after freezing and gas by sublimation (3) after heating at low pressure below the triple point [149]. (b) Freeze-casted collagen scaffold, 1% wt/v (scale bar: 100 µm) [151].

2.4.2. Materials for Scaffolds

2.4.2.1. Decellularised Tissues

Decellularised valves are xenogeneic (or allogenic) tissues that are treated to remove cellular debris, retaining the ECM which theoretically exhibits structural and mechanical characteristics akin to the non-treated valve. The preserved valve is either repopulated with autologous cells *in vitro* or implanted *in situ* without cells [152], [153]. The repopulation of tissues has been challenging due to the high density of the structures [154].

There are mixed results regarding the effect of decellularisation on the mechanical properties of valves as the type of reagent affects the properties of the valve differently. Grabow *et al* [155], reported an increase in stiffness after decellularisation due to the loss of ground substance and crimp in the elastic network responsible for the pre-load. Whereas, Liao *et al* [156], compared three different types of decellularisation agents with native valves and reported a decrease in stiffness for all treatment types due to the loss of the collagen network.

2.4.2.2. Synthetic Polymers

Synthetic polymers commonly used HVTE include: poly (glycolic acid) (PGA), poly (lactic acid) (PLA), poly (caprolactone) (PCL), poly (hydroxyalkanoate) (PHA), poly (glycerol sebacate) (PGS) and poly(ethylene glycol) (PEG) [157]–[160]. These materials offer superior mechanical properties and tuneability of degradation characteristics. However, they do not exhibit a bilinear stress-strain response as observed in native valves (2.2.3). Therefore, while they can be tailored to match the bulk mechanical properties, they do not perform similarly and lose more energy (low

resilience and high hysteresis) resulting in eventual failure as it cannot withstand the increased pressure gradients [161]. Additionally, synthetic materials exhibit poor bioactivity, and often are encapsulated upon implantation due to inflammation [162]. Methods to improve the bioactivity include modification by functionalisation, for example, the addition of arginine-glycine-aspartic acid (RGD) peptides [125] to promote cell-matrix interactions. Degradation of synthetic materials can also cause inflammation as the by-products are acidic and decrease the pH of the body [163].

2.4.2.3. Collagen-Based Scaffolds

Type I collagen is a natural choice due to its abundance in valves and weak immunogenicity [164]. It has been studied extensively as a biomaterial for TE and is the "gold standard" [165]. Natural sources of collagen are obtained from animal derived sources, including the skin and Achilles tendon [166]. After isolation and purification, collagen can be reconstituted to obtain a processable slurry [167]. Collagen offers superior bioactivity compared to synthetic variants. It has intrinsic biochemical cues (RGD peptide sequences) that interact with integrins to guide tissue regeneration [168].

The bioactivity of 1%wt/v collagen scaffolds has been demonstrated for human VICs which maintained their phenotype and promoted proliferation as well as upregulation of collagen and elastin genes [129], [169], [170]. The synthesis of GAGs has also been reported by myofibroblasts isolated from porcine hearts [171], [172]. Although the intrinsic bioactivity maintains cellular function, a limitation of these scaffolds is their poor mechanical properties. Mechanical conditioning of collagen gels has been studied by Shi *et al* [173], [174], who reported increased stiffness after 8 weeks of conditioning with smooth muscle cells. While the Young's modulus was improved by conditioning,

the strain-to-failure reported was 9.3% [173] which is significantly lower than that required for functional valves. Similarly, Chen *et al* [175] reported a strain-to-failure of 15-19% for various compositions. The strain-to-failure of collagen is intrinsically low as it is inextensible (2.2.2.1). Biomechanical conditioning [176] and coating [177] of collagen scaffolds to increase the expression of elastin have yielded suboptimal results suggesting that elastin also plays a biochemical role. Contraction of collagen scaffolds after cell seeded is a common phenomenon [173]–[175]. It has been speculated that this occurs as collagen is synthesised excessively and elastin production is low [178]. Although, collagen provides high stiffness, it is insufficient as an independent material to emulate the mechanical characteristics of native valves entirely and requires the addition of a material that can provide the extensibility of elastin and promote elastogenesis.

2.4.2.4. Hyaluronic Acid-Based Scaffolds and Composites

HA is prevalent in the spongiosa layer and relatively simple to process due to its solubility in water-based solvents. It requires cross-linking via the carboxyl or hydroxyl groups to produce insoluble hydrogels [179]. Hydrogels fabricated after methacrylation have been reported to support porcine VIC encapsulation and affect their phenotype in a modulus dependent manner [180]. Puperi *et al* [181], produced similar hydrogels which were functionalised with the RGD peptide and tailored to match the compressive moduli of the spongiosa (5 kPa). They found the hydrogels promoted the synthesis of HA synthesising enzymes; however, elastin was not expressed. This is in contrast to the hydrogels investigated by Masters *et al* [182], who reported a two-fold increase in elastin by hydrogels composed of low MW HA. Additionally, Ramamurthi *et al* [183], reported the expression of elastin was not

significantly different to polystyrene controls for hydrogels cross-linked with divinyl sulfone. The contrast in the results are due to the size of the HA used and the extent of cross-linking, lower MW HA promotes elastin synthesis, however, it has poor structural integrity and therefore is unsuitable for designing constructs. HA has been used widely to improve the expression of elastin, factors such as copper nanoparticles [184], transforming growth factor beta-1 (TGF- β1) [185], [186] and LOX [187] have been incorporated as potential candidates to improve elastogenesis. Modification of HA to improve the mechanical properties using chemical reagents and high concentrations of solute results in denser structures that ultimately limit cellular infiltration [183], [188].

Studies have incorporated collagen and GAGs to produce composites that take advantage of collagen's bioactivity and the tuneability of GAGs. Brigham *et al* [189], fabricated semi-interpenetrating networks using type I collagen and HA and found that the addition of collagen increased the compressive modulus at all concentrations of HA. Also, the collagen only samples exhibited superior fibroblast adhesion compared to HA only samples due to increased swelling. Similarly, Suri *et al* [190], fabricated micropatterned collagen and HA gels that were photo-crosslinked to improve the storage modulus. They found the modulus increased by two-fold without affecting the cell viability for the first 7 days. However, they did report a decrease in swelling capacity after cross-linking. For the spongiosa layer, high retention of water is essential as it acts as a buffer between the external layers. Nazir *et al* [191], [192] reported a sequential method to produce interlaced scaffolds that do not affect the swelling characteristics significantly and reported larger pores (66-126 μm) compared to those of the micropatterned scaffolds (2-10 μm). Although, collagen and HA-based scaffolds

offer multiple advantages, they are still insufficient at emulating the entire valve as there is a need for extensibility.

2.4.2.5. Elastin-Based Scaffolds and Composites

The incorporation of elastin is essential for proper functionality of valves and the promotion of elastogenesis. Polymeric elastin has historically been limited as a biomaterial due to its insolubility [193]. The isolation and purification of elastin from natural sources relies on its chemical inertness as the surrounding ECM molecules are solubilised [194]. Elastin can be extracted and purified from tissues rich in elastin such as the aorta and the neck ligament of bovine or equine as insoluble fibres [195]. The most common treatments involve either autoclaving it successively, treating with hot alkali or non-elastolytic enzymes [196]. Purified elastin is insoluble in all reagents except those that hydrolyse amide bonds [197], its insolubility has made it challenging to study its structure as most analytical biochemistry techniques require soluble molecules.

Methods which hydrolyse amide bonds include partial hydrolysis which is commonly used to study ECM molecules. Amide bonds are selectively cleaved using organic acids to hydrolyse the polymer into shorter peptides and amino acids [198]. Partial hydrolysis of elastin by ethanedioc (or oxalic) acid was first reported by Partridge et al [199], [200], who completely solubilised the protein to yield two fragmented forms of elastin, widely referred to as α- and β-elastin. Other methods of solubilising elastin include boiling it in urea [201], potassium hydroxide [202] or treating with elastase [9], [203]. Ethanedioc acid produces the highest yield of soluble elastin, hence it is commonly used and commercially available as a material for research purposes.

Synthetic forms of soluble elastin include elastin-like polypeptides (ELPs) and recombinant tropoelastin produced by bacterial systems [204], [205].

To the best of the author's knowledge, elastin only scaffolds have not been fabricated for HVTE applications. The mechanical and structural properties of elastin-only scaffolds for vascular, skin and cartilage tissue engineering applications have been summarised in Table 2.2.

α-elastin is commonly used as a biomaterial, it requires the reconstitution of the fragmented fibres by coacervation. Porous α-elastin scaffolds fabricated by gas foaming have heterogenous pores that range from 4-80 μm [206]–[208]. The structures fabricated using this technique are highly dense due to the concentration of protein required for coherency (100mg/ml). This in turn affects cellular adhesion and the infiltration capacity as well as proliferation [206], [207], [209]. Hydrogels formed by α-elastin are challenging to characterise in tension due to their poor integrity. Coacervated gels have a Young's modulus of 11kPa and a strain-to-failure of 27.5% [208] compared to electrospun scaffolds that are significantly stiffer (184MPa) but less extensible (1%) [210].

Table 2.2: Mechanical and structural properties of elastin-only based scaffolds. NR- not reported.

Biomaterial, Cross-linker	Fabrication Technique, Concentration	Mechanical Properties	Pore size, Porosity	Cell line, Application	Ref
α-elastin, ethylene glycol diglycidyl ether (EGDE)	Film casting produced by coacervation, 200 mg/ml	Young's modulus: 0.004-0.12 MPa, Strain to failure: NR	NR	Smooth muscle cells, Vascular tissue engineering	[209]
α-elastin, glutaraldehyde	Hydrogels produced by gas foaming (high pressure CO_2 system), 100 mg/ml	Young's modulus: 0.011 MPa Strain to failure: 27.5%	Pore size: 35 µm (top surface) and 20 µm (cross-section) Porosity: NR	Fibroblasts, Skin tissue engineering	[208]
α-elastin, hexamethylene diisocyanate (HDMI) [206] or glutaraldehyde [207]	Hydrogels produced by gas foaming (high pressure CO_2 system), 100 mg/ml	Compressive modulus: 0.004-0.0019 MPa Energy loss: 1.4-20.4%	Pore sizes between 3.9- 79.8 µm Porosity: NR	Fibroblasts, Skin tissue engineering	[206], [207]
α-elastin, glutaraldehyde	Electrospun membranes, random and aligned, 20% wt/v	Young's modulus: 0.33 MPa Reported no hysteresis up to 50% strain	721 nm- 2.12 µm Porosity: NR	Mouse embryo fibroblast 3T3 cells, Skin tissue engineering	[210]
α-elastin, HDMI	Electrospun scaffolds, 20% wt/v	Young's modulus: 184 MPa (dry) Strain to failure:	Fibre diameter: 0.5-3 µm Porosity: NR	Embryonic palatal mesenchymal cells,	[211]

		1% (dry)		Multiple biomedical applications	
ELPs, tris-succinimidyl aminotriacetate	Coacervated hydrogels, 125 mg/ml	Shear modulus: 0.006 MPa (1.6 Hz) Phase angle: ~ 12° (1.6 Hz)	NR	NR, Multiple biomedical applications	[212]
ELPs, transglutaminase	Enzyme mediated gel formation, 100 mg/ml	Shear modulus: 0.00026 MPa Phase angle: ~10°	NR	Chondrocytes (encapsulated), Cartilage tissue engineering	[213]
Thiolated ELPs, photo-crosslinked	Hydrogels, 10% wt/v	Young's modulus: 0.0013 MPa Strain to failure: 419% Compressive modulus: 0.003 MPa Energy loss: 35.1 %	4.7 µm Porosity: NR	Mesenchymal stem cells and human umbilical vein endothelial cells, Vascular tissue engineering	[214]
ELPs, photo-crosslinked	Dense spin coated films, 5% wt/v	Young's modulus: 250 MPa Strain to failure: 2.5%	N/A	Adipose derived stem cells, Multiple biomedical applications	[215]
Recombinant tropoelastin, HDMI	Electrospun fibres, 20% wt/v	Young's modulus: 289 MPa (dry)	Fibre diameter: 1.5-7 µm	Embryonic palatal mesenchymal cells,	[211]

		Strain to failure: 15% (dry)	Porosity: NR	Multiple biomedical applications	
Recombinant tropoelastin, HDMI	Electrospun fibres, 20% wt/v	Young's modulus: 0.11-0.27 MPa Ultimate Strain: 1.5-2.6%	Fibre diameter: 1-2.5 µm Porosity: NR	Vascular smooth muscle cells, Vascular tissue engineering	[216]
Recombinant tropoelastin, bis(sulfosuccinimidyl) suberate	Sponges produced by coacervation followed by freeze-drying, 100 mg/ml	Young's modulus: 0.22-0.28 MPa Strain to failure: 200-370%	20-250 µm Porosity: NR	*In vitro*- Epithelial cells *In vivo* study in guinea pigs up to 13 weeks, Skin tissue engineering	[217]
Recombinant tropoelastin, lysyl oxidase (from yeast *Pichia pastoris*)	Hydrogels, 100 mg/ml	Young's modulus: 0.008-0.012 MPa Strain to failure: 280%	NR	NR, Skin tissue engineering	[218]
Recombinant tropoelastin, glutaraldehyde	Electrospun fibres with open weaved structure, 20% wt/v	Young's modulus: 0.27 MPa Strain to failure: NR	Pore Size: 2-4 µm Porosity- 10-30%	Fibroblasts, Skin tissue engineering	[219], [220]
Recombinant tropoelastin, disuccinimidyl suberate	Electrospun scaffolds, 15% wt/v	Young's modulus: 0.15 MPa	NR	Endothelial cells,	[221]

	Strain to failure: 77%	Vascular tissue engineering

ELPs are derived from the pentapeptide poly(VPGXG), where X can be any amino acid except proline [222]. The advantage of ELPs is that they can be modified by the insertion of different amino acids in the sequence, usually lysine is chosen to facilitate cross-linking [10]. Chemically cross-linked ELPs have low moduli which can be improved by culturing *in vitro* [212], [213]. Photo-cross-linking is a popular method that uses ultraviolet light. Zhang *et al* [214], fabricated highly elastic gels with a strain-to-failure of 419% and a Young's modulus was 1.3 kPa. As ELPs are short sequences, they require functionalisation to improve the cell-ECM interaction and adhesion of cells significantly [215].

Electrospinning is commonly employed for tropoelastin-based scaffolds. Electrospun tropoelastin scaffolds have pores typically between 1-7μm [211], [216], [219], [220]. In the hydrated state the Young's moduli of fibres are between 110-280 kPa [216], [219], [220] which is three orders of magnitude higher in the dry state [211]. Due to the low porosity of scaffolds fabricated from electrospun fibres, cells are generally prone to remain on the surface. Porous sponges can be fabricated with larger pores (20-250μm) as shown by Mithieux *et al* [217]. Their scaffolds performed similarly to native elastic fibres mechanically with a Young's modulus of 220-280kPa and a strain-to-failure of 200-370%. However, a mild immune response and fibrous encapsulation was found when implanted *in vivo* in comparison to collagen controls. This is likely due to the change in chemistry of the scaffolds post-cross-linking. The same research group produced tropoelastin hydrogels that were cross-linked with LOX [218], however, the hydrogels were almost thirty-fold less stiff than the chemically cross-linked sponges. A possible reason for this is that LOX is not the only component

involved in cross-linking of tropoelastin, there are multiple molecules that facilitate the process.

Elastin-only scaffolds are fabricated to study the properties of elastin and its applicability in TE. However, naturally, elastin is not present in any connective tissue independently, it is always present as a composite with other ECM molecules. Hence, elastin-based composite scaffolds were also reviewed, specifically focusing on collagen (summarised in Table 2.3). To the best of the author's knowledge, to date there have only been two studies that reported the application of elastin-based composites for HVTE applications [175], [223]. Of which, one did not study the structural or mechanical properties of the gels, but found the gels promoted endothelial to mesenchymal transition [223]. The remaining studies have focused on applications in vascular, skin, hernia and cartilage tissue engineering as shown in Table 2.3.

As observed with α-elastin-only scaffolds, the addition of a second material does not significantly improve the porosity of scaffolds produced by gas foaming and hydrogels lack interconnectivity [208], [224]. For tropoelastin and α-elastin-based hydrogels, the substitution of α-elastin for tropoelastin improved the mechanical properties of scaffolds, tropoelastin-only hydrogels were superior with a strain-to-failure of 82% [208]. When comparing only soluble forms of elastin, tropoelastin has the most appropriate mechanical properties for soft tissues. However, in terms of bioactivity and biocompatibility, it has been shown to repeatedly provoke a foreign body response as was observed for electrospun collagen and tropoelastin scaffolds implanted in mice [225].

Cross-linking of soluble elastin's is crucial to obtain insoluble matrices with structural integrity; however, it is at the expense of biocompatibility. The most commonly studied are glutaraldehyde [207], [208], [210], [219], [220], [224]–[226], hexamethylene diisocyanate (HDMI) [206], [211], [216] and bis(sulfosuccinimidyl) suberate [217], [227]. 1-ethyl-3-(3-dimethyl aminopropyl)carbodiimide (EDC) is a zero-length cross-linker commonly used for collagen-based scaffolds. It is superior to other chemical cross-linkers as residual cross-linker can be removed simply by washing due to its solubility in water [228].

Collagen and elastin-based composites are commonly fabricated using freeze-casting as blending of compositions is relatively simple and scaffolds with higher porosity (>99%) and pore sizes (85-180μm) [175], [229] can be produced. A recurring challenge with collagen-elastin composites is that the addition and/or substitution of elastin does not improve the extensibility of scaffolds as one would expect. Multiple compositions of collagen and elastin-based scaffolds containing ELPs [230], [231], α-elastin [232]–[234] and insoluble elastin [175], [229], [233], [234] have been fabricated and have reported no significant difference compared to collagen controls as shown in Fig.2.18. This is likely due to the intrinsic properties of commercially available elastin (bovine) as scaffolds composed of collagen and insoluble elastin from equine sources reported relatively high strain-to-failure (35-150%) compared to collagen controls [235]–[237]. These studies used an in-house method to isolate elastin which was composed of relatively long fibres compared to commercially available elastin. However, coherency and interconnectivity in these scaffolds is poor due to the limitations of the processability of insoluble elastin (Fig.2.19).

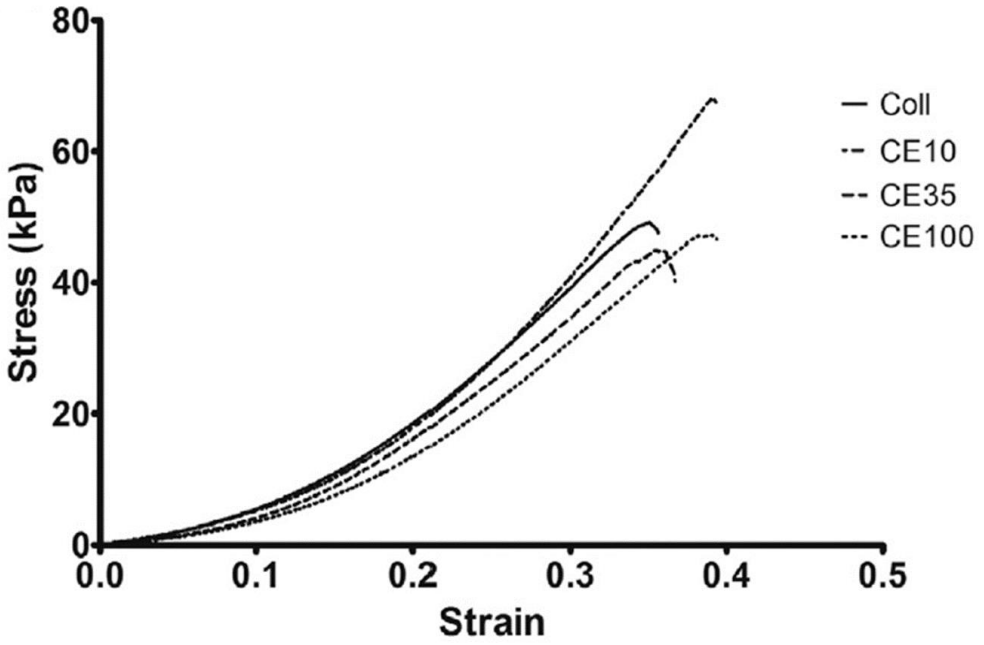

Figure 2.18: Stress-strain curves for collagen (Coll) and collagen-elastin (CE) composites with different concentrations of insoluble elastin [229].

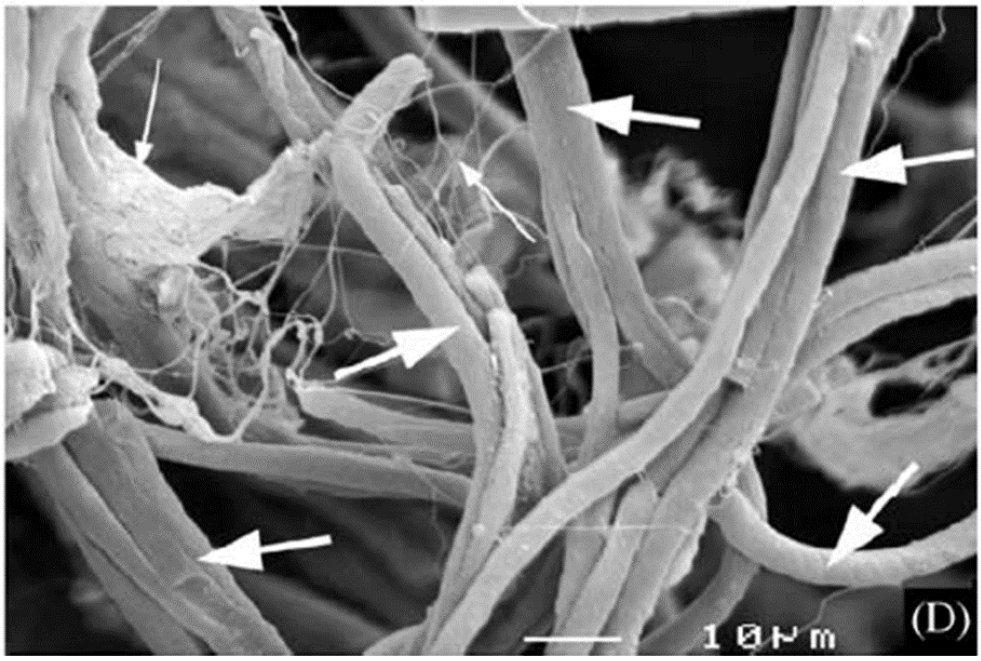

Figure 2.19: Scanning electron microscopy image of a collagen and elastin composite, arrows show insoluble elastin fibres (equine source) [235].

Table 2.3: Mechanical and structural properties of elastin-based composite scaffolds. NR- not reported; N/A- not applicable.

Biomaterial, Cross-linker	Fabrication Technique, Concentration	Mechanical Properties	Pore size, Porosity	Cell line, Application	Ref
Tropoelastin and α-elastin, glutaraldehyde	Hydrogels produced by gas foaming (high pressure CO_2 system), 100 mg/ml	Young's modulus: 0.011-0.047 MPa Strain to failure: 27.5-81.9%	Pore size: 35 µm (top surface) and 20 µm (cross-section) Porosity: NR	Fibroblasts, Skin tissue engineering	[208]
α-elastin and Poly (ε-caprolactone) composites, glutaraldehyde	Scaffolds produced by gas foaming and salt leaching, 50 mg/ml α-elastin	Compressive modulus: 1.3 MPa Energy Loss: 48.1%	Pore Size: 540 µm Porosity: 23-91%	Chondrocytes, Cartilage tissue engineering	[238]
Type I soluble collagen and recombinant ELPs, transglutaminase	Gels, 3:1 ratio of collagen to ELP	Storage modulus: 0.00001-0.0002 MPa (1 Hz) Loss modulus: NR (1 Hz)	Pore size: ~50-100 µm Porosity: NR	Fibroblasts, HUVECs, and smooth muscle cells, Multiple biomedical applications	[230]
Type I soluble collagen (rat tendon) and ELPs, uncross-linked	Gels, 2.5 mg/ml collagen and 100 mg/ml ELPs	Young's modulus: 1.6 MPa Strain to failure: 38.5%	NR	*In vivo* study in rats	[231]

				Vascular tissue engineering	
Type I soluble collagen (ovine) and recombinant tropoelastin, glutaraldehyde	Electrospun scaffolds, 20% wt/v	Young's modulus: 0.14-0.84 MPa Strain to failure: NR	Fibre diameter: 2.5-7.5 µm Porosity: 54-64%	*In vitro*- Fibroblasts *In vivo* study in mice up to 6 weeks Skin tissue engineering	[225]
Type I collagen and α-elastin blends, 1,4-butanediol diglycidyl ether	Scaffolds produced by freeze-casting, 20 mg/ml collagen and 10wt%	Young's modulus: 0.54 MPa Strain to failure: 33%	Pore size: 35 µm Porosity: 79%	Bone marrow-mesenchymal stem cells Hernia tissue engineering	[232]
Type I collagen (soluble) and α-elastin, EDC/NHS	Electrospun fibres, 1-5% wt/v	NR	Fibre diameters: 220-600 nm	Smooth muscle cells Vascular tissue engineering	[239]
Type I collagen and insoluble or α-elastin, 1-ethyl-3-(3-dimethyl aminopropyl)carbodiimide	Dense films by air-drying, 1% wt/v	**Collagen/Insoluble Elastin** Young's modulus: 2-31 MPa	N/A	HT1080 cells derived from fibrosarcoma compared to	[233]

(EDC) and N-hydroxysuccinimide (NHS)		Strain to failure: 10-21% **Collagen/Soluble Elastin** Young's modulus: 50-150 MPa Strain to failure: 8-10%		Rugli cells derived from glioma Multiple tissue engineering applications	
Type I soluble collagen and insoluble or α-elastin, uncross-linked	Electrochemically aligned fibres, 200 mg/ml (60:40)	**Collagen/Insoluble Elastin** Young's modulus: 3 MPa Yield Strain: 13-15% **Collagen/Soluble Elastin** Young's modulus: 2 MPa Yield Strain: 13-15%	NR	Smooth muscle cells Vascular tissue engineering	[234]
Type I soluble collagen and α-elastin, uncross-linked	Gels encapsulated with cells, 3mg/ml collagen and 0.6 mg/ml elastin	NR	NR	VICs and VECs (porcine) Valvular tissue engineering	[223]

Type I and III collagen and insoluble elastin, glutaraldehyde	Electrospun fibres, 40-40-20% wt/v	NR	Fibre size: 0.5 µm	Human umbilical vein endothelial cells, aortic smooth muscle cells and dermal fibroblasts Vascular tissue engineering	[226]
Type I collagen and insoluble elastin. dehydrothermally cross-linked	Scaffolds produced by freeze-casting, 0.5% wt/v collagen and 10, 35 or 100wt% elastin	Young's modulus: 0.36-0.41 MPa Strain to failure: 37-43%	Pore size: 85-96 µm Porosity: >98.8%	Smooth muscle cells Vascular tissue engineering	[229]
Type I collagen and insoluble elastin (equine), EDC/NHS	Scaffolds produced by freeze-casting, 1% wt/v	Young's modulus: 0.42-1.01 MPa Strain to failure: 125-150%	Pore size: 20-100 µm Porosity: NR	Human myoblasts and fibroblasts Multiple tissue engineering applications	[235]
Type I collagen and insoluble elastin (equine), EDC/NHS and poly(propylene	Porous films produced by freeze-casting, 1% wt/v	Young's modulus: 8 MPa Strain to failure:	Pore size: 100-160µm Porosity:	Smooth muscle cells	[236]

glycol)-bis-(2-aminopropyl ether)		35-60%	81%	Vascular tissue engineering	
Type I collagen and insoluble elastin (equine), EDC/NHS	Scaffolds produced by freeze-casting, 2% wt/v	Young's modulus: 0.04 MPa Strain to failure: 100%	Pore size: 131 µm Porosity: 90%	Smooth muscle cells Vascular tissue engineering	[237]
Type I collagen and insoluble elastin, uncross-linked	Scaffolds by freeze-casting, 1% wt/v	Young's modulus: 0.04-0.23 MPa (dry) Strain to failure: 14% (dry)	Pore size: 180 µm Porosity: 99%	Cardiosphere-derived cells (rats) Valvular tissue engineering	[175], [240]

A commercially available source of natural elastin that can provide both the mechanical and biological cues without compromising biocompatibility is required. This thesis will study the process of solubilising elastin from insoluble elastin to obtain a processable source of elastin and study its properties. As mentioned previously, a monolithic scaffold is insufficient for emulating native valves. Each layer of the valve plays a specific role in the function and durability of valves and therefore scaffolds that can mimic each layer and function with synchrony are required.

2.4.3. Tri-layer Scaffolds

Over the last decade there has been more appreciation for the complexity and sophisticated architecture of valves, and the acceptance that isotropic structures and monolithic scaffolds are incapable of simulating the complex environment. However, there is very little literature on artificially designed tri-layer scaffolds for HVTE applications. This is in part due to the limitations of the materials and fabrication techniques available.

Tedder *et al* [241], designed tri-layer scaffolds using decellularised pericardium as the two outer layers and a pulmonary artery for the middle layer which were fused together using a bio-adhesive. Although the scaffolds were bioactive, the high density of the constructs limited cells to the surface. Additionally, they were significantly stiffer than native valve controls and exhibited high energy loss. As seen with bioprosthetic valves, decellularised tissues also calcify, this was specifically observed in regions which contained the glutaraldehyde-based adhesive. Similarly, Tseng *et al* [242], designed laminated hydrogels using two stiffer outer layers and an inner softer layer from poly(ethylene glycol) diacrylate (PEGDA) which were encapsulated with VICs and

photo cross-linked. They demonstrated that this technique can be used to fabricate hydrogels with strong interfaces and did not observe delamination in tension.

PCL based electrospun scaffolds are particularly popular due to their "elastic" properties. Jana *et al* [243], fabricated electrospun scaffolds composed of three differently aligned layers, these were: circumferential, random and radial to mimic the fibrosa, spongiosa and ventricularis, respectively. The scaffolds exhibited high compliance (yield strain of 60%), however, the mechanical properties were not sufficient to withstand the pressures in valves. Moreover, the stress-strain response was not bilinear as observed in native valves. The same group studied similar tri-layered PCL constructs *in vivo* and found that collagen and elastin synthesis was lower than control samples and the samples become encapsulated after two months [244].

Natural materials are more appropriate for HVTE due to the direct contact with blood. Duan *et al* [245] fabricated tuneable HA and gelatin based tri-layers using 3D printing. Their technique enables the homogenous distribution of cells and biomaterial during fabrication but is limited by availability of printable biomaterials and their viscosity. The hydrogels were able to support VICs *in vitro*, however, further work on the mechanical properties is required. Collagen-based tri-layer scaffolds fabricated by freeze-casting are able to mimic the flexural anisotropy observed in valves as shown by Chen *et al* [246] suggesting they are an appropriate model for future work.

2.5. Aim of This Work

The goal of this thesis is to identify a source of elastin that can be used to design scaffolds to mimic the composition of the ventricularis layer of native valves. Elastin will fulfil both mechanical and biochemical roles that will contribute to the scaffold's

longevity. As discussed above, elastin is limited as a biomaterial due to its insolubility and it is essential to identify a natural source of elastin that is processable.

The aims of this thesis were to:

- Investigate the process of solubilising elastin by partial hydrolysis and identify a potential source of elastin that has improved polymer-solvent interactions and can be used to fabricate scaffolds.
- Fabricate elastin-only, collagen-elastin, coll-HA and tri-layer scaffolds using freeze casting and evaluate their pore characteristics.
- Evaluate the swelling and degradation characteristics of the elastin-based scaffolds and understand the effect of elastin substitution on the scaffolds.
- Evaluate the mechanical properties of elastin-based scaffolds and if the substitution of elastin has any significant effect on the tensile and compressive properties, with particular attention on the effect of the composition on the strain-to-failure and extensibility of scaffolds.
- Evaluate the cellular response of scaffolds by determining the effect of the composition on cell viability, adhesion, and gene expression.

3

Isolation & Characterisation of Fibrillar Elastin Gel

3.1. Introduction

There are two forms of natural elastin that are currently available as a biomaterial as discussed in Section 2.4.2.5. Polymeric elastin is limited as a biomaterial due to its highly cross-linked nature and consequent insolubility and α-elastin, which can be produced by solubilising polymeric elastin has very poor structural integrity. This thesis studies the isolation of a novel form of elastin which was discovered by the author during initial experiments in January 2017.

Partial hydrolysis involves refluxing insoluble elastin (IE) with ethanedioic acid up to six times until it is completely solubilised into α-elastin, as reported by Partridge *et al* [247] (Fig.3.1.) Each reflux yields an insoluble residue that is refluxed again and a soluble product of hydrolysis which is separated. During preliminary experiments which aimed to reproduce α-elastin, a viscous substance was observed after three successive refluxes which formed a gel upon purification. This chapter reports the method used to isolate the gel (termed Fibrillar Elastin Gel, FEG) and characterises its properties.

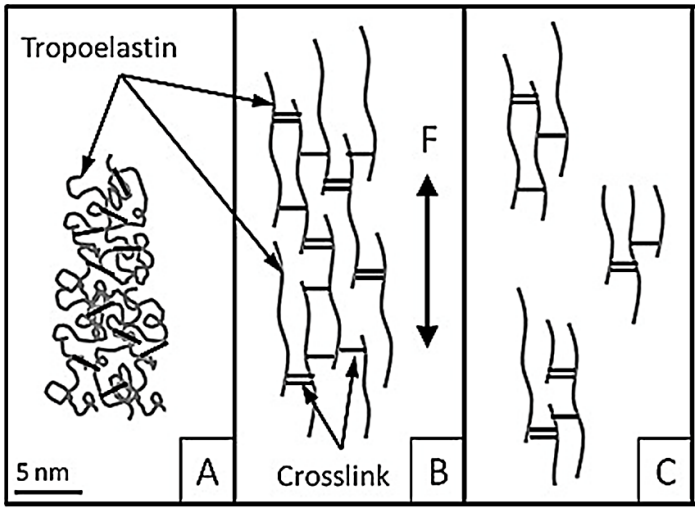

Figure 3.1: Hydrolysis of polymeric elastin by partial hydrolysis where the polymer (B) is randomly cleaved as shown in (C) into smaller fragments [248].

3.2. Materials & Methods

3.2.1. Isolation & Purification of Fibrillar Elastin Gel

FEG was isolated and purified using the method summarised in Fig.3.2 which is a modified version of Partridge *et al's* protocol that completely solubilised elastin [247]. 1:10 w/v of IE powder (bovine neck ligament, Sigma Aldrich Ltd, U.K.) was gently mixed with 0.25 M of ethanedioic acid (purified grade, Sigma Aldrich, U.K.) by gently folding the powder into the acid, avoiding the formation of air bubbles. The mixture was transferred to a 100 ml round bottomed flask (Borosilicate Glass Round Bottom Flask, Socket: 14/23, Sigma Aldrich, U.K.) which was attached to an air condenser (Quickfit™ Borosilicate Glass Liebig Condenser, C1/11/SC, Thermo Fisher Scientific, U.K.). The condenser was attached to the tap of the sink with PVC Reinforced Hose (Department of Materials Stores) secured with hose clips (11-16 mm). The mixture was heated to 100±2°C using a water bath placed on a hot stirring plate (Stuart US152 Hot Stirrer, RS Components, U.K.) at a speed of 300 rpm for 70 mins as shown in Fig.3.3. The water bath was covered with aluminium foil to maintain the temperature and monitored throughout the experiment using a regular Mercury thermometer (-10°C to +110°C, 176mm, Department of Materials Stores). The mixture was quenched rapidly after 70 mins using an ice bath (0 °C) for at least 5 mins. The mixture was then transferred to a 50 ml centrifuge tube (Polypropylene, Corning® CentriStar™ Cap, Sigma Aldrich, U.K.) and centrifuged (Heraeus Megafuge 1.0 Centrifuge, Thermo Fisher Scientific, U.K.) at 5000 rpm for 5 mins. The supernatant from each hydrolysis was removed and stored at 4°C until required for dialysis. The pellet obtained after centrifugation was mixed with fresh ethanedioic acid and subjected to two further hydrolyses, obtaining an insoluble pellet after each hydrolysis.

After three sequential hydrolyses, the pellet was purified by washing in excess (1:4 v/v) deionised-water (Grade 2 water and European Pharmacopoeia Grade 2 water, Scientific Laboratory Supplies, U.K.) for 1 hour, followed by four times for 20 mins each and finally on the centrifuge three times for 5 mins each. The washing converted the pellet into a gel-like substance, which is referred to as FEG. The FEG was stored by one of these two methods: (1) As a gel at 4°C (Zanussi, DF 50/16, U.K.) until required for further experiments or (2) as a dry sponge at 4°C. The gel was dried into a sponge by transferring the gel into Polystyrene anti-static weighing dishes (Sigma Aldrich, U.K.), freezing overnight (at -20 °C), and freeze-drying (Christ I-5, Martin Christ, Germany) for 24 hrs under vacuum of 0.05 mbar, which was achieved with an Edwards RV2 Two Stage High Vacuum Pump 240V E2M2 (Edwards, U.K.). The cooling rate was not controlled. The supernatants from each hydrolysis were dialysed against deionised-water using a 1 kDa dialysis membrane (Pur-A-Lyzer™ Mega Dialysis Kit, Sigma Aldrich, U.K.) for four days, the water was replaced every day. The final dialysed solution was frozen overnight (at -20 °C) and freeze-dried for 24 hrs. The freeze-drying process resulted in a powder which was stored at 4°C until required for further experiments. Another method of washing that was tested was using 0.1 M sodium chloride (NaCl) for 1 hr and then washing in deionised-water four times for 20 mins each. This method resulted in precipitation of the gel (separation from the solution) and therefore was only used for microstructural studies.

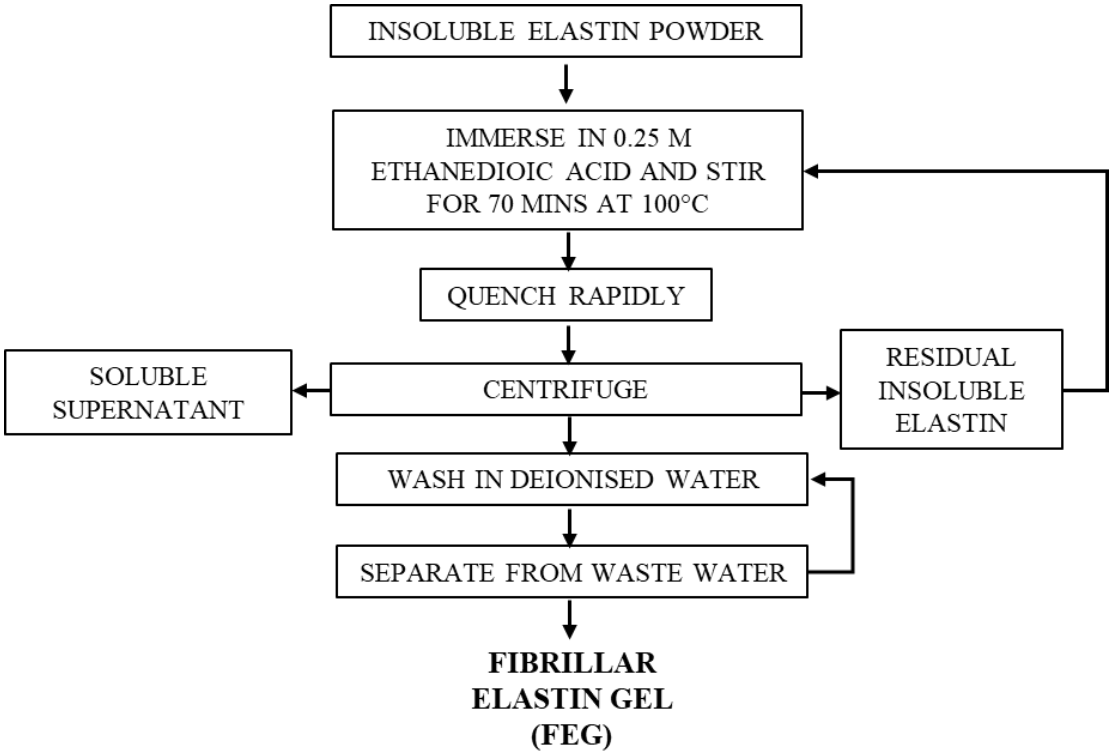

Figure 3.2: Summary of procedure to isolate and purify Fibrillar Elastin Gel.

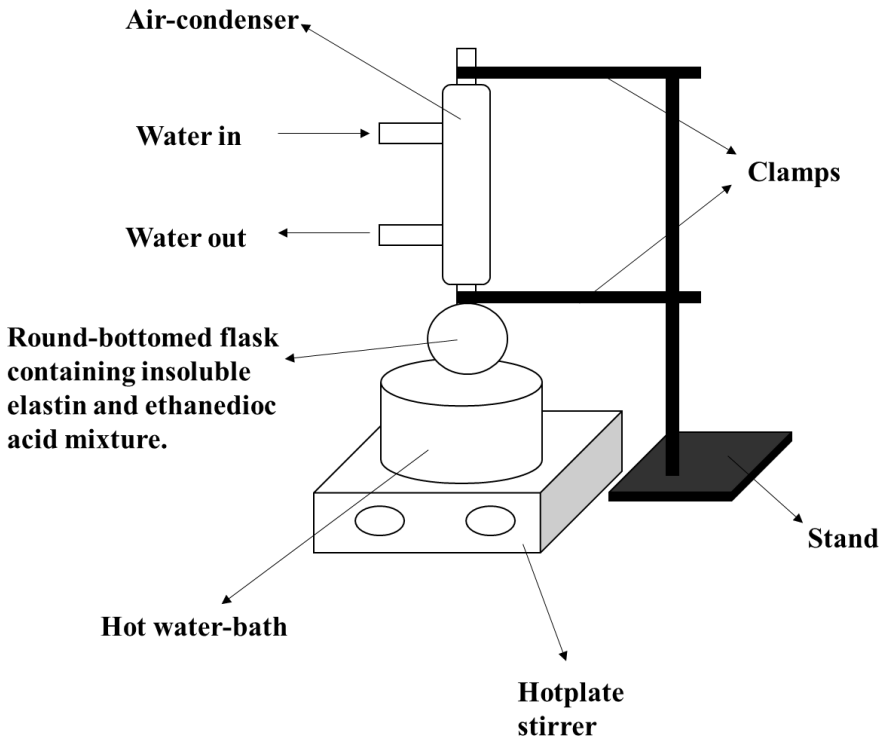

Figure 3.3: Apparatus set-up for hydrolysis of insoluble elastin into Fibrillar Elastin Gel.

3.2.2. Laser Scanning Confocal Microscopy (LSCM)

500 µL of the FEG was pipetted on to a rectangular glass microscope slide (76mm x 26mm, 1.2 to 1.5mm thickness). The sample was flattened using a coverslip and stored at 4°C. Samples were excited by multiple wavelengths (458, 488 and 559nm) and the emission was collected following excitation at 488nm. Fluorescence images were obtained using the Olympus Fluoview FV1000 Confocal Microscope at the Dunn School of Pathology, University of Oxford. All images were taken using the 60 X objective lens by Dr. Alan Wainman.

3.2.3. Scanning Electron Microscopy (SEM)

SEM was used to study the microstructure of dry FEG and the insoluble and soluble counterparts. It has a large depth of field and samples are relatively easy to prepare. Two methods of drying were used, either air-drying or freeze-drying. To prepare air-dried samples, ~100 µL of the gel was pipetted onto aluminium pin stubs (12.5 mm x 6 mm, Agar Scientific, U.K.) covered with adhesive carbon tabs (12 mm, Agar Scientific, U.K.) and left to air-dry under a flow-cabinet overnight. Freeze-dried samples were placed on stubs using tweezers.

The microstructure of the IE residue from the first two hydrolyses was also studied. After the first hydrolysis, the mixture was centrifuged, the residue was removed using a spatula and washed in deionised-water three times for 30 mins each to remove the acid. The sample was then pipetted onto stubs lined with carbon tabs. The same method was used for the residue from the second hydrolysis. The microstructure of the soluble supernatants from each hydrolysis was also studied using SEM. After dialysis and

freeze-drying (3.2.1.) the samples were placed on carbon lined stubs using a spatula. The microstructure of the IE powder (as received from the manufacturer) was also studied, samples were prepared as mentioned above.

As the gel was a homogenous solution which coalesced into a dense structure upon drying. The precipitated material obtained after washing the gel in 0.1 M NaCl was used to study the microstructure. The washed precipitate was sonicated (QH Kerry, Kerry Ultrasonics Limited, U.K.) for 10 mins in deionised-water before being pipetted onto carbon coated stubs and left under the flow-cabinet to air-dry overnight.

All samples on stubs were painted with three strokes of Acheson Silver DAG 1415M (Agar Scientific, U.K.), from the edge of the sample to the tip of the stub. The samples were sputter coated with gold for 1 min using the Bio-Rad, Polaron Division E5400 SEM Coating System (Quorum Technologies Ltd, U.K.). Coating was performed in vacuum under an inert atmosphere of argon with a pressure of 0.08 mbar, a voltage of 0.6 kV and a current of 2.0 mA. Once coated, samples were imaged using the Zeiss EVO® MA10 SEM (Zeiss, U.K.) at the David Cockayne Centre for Electron Microscopy, University of Oxford. The chamber was maintained under a vacuum of $1x10^{-5}$-$1x10^{-6}$ mbar, images were generated using the secondary electron mode at a working distance of 7-12 mm. An accelerating voltage of 10 kV was achieved using a tungsten source, and a probe current between 26-100 pA. Prior to imaging, the gun was aligned, and the aperture and astigmatism were corrected manually.

Post imaging analysis was conducted using ImageJ® (National Institutes of Health, U.S.A.). The diameters of 100 or more particles were measured to obtain an average and the standard deviation. The composition of IE was determined by adjusting the

threshold of an image and determining the area, eliminating a component, and re-measuring the area. The change in area was used to determine the percentage volume fraction that was either globular or fibrillar, this was repeated for nine images to obtain the average and standard deviation.

3.2.4. Fourier Transform Infrared Spectroscopy (FT-IR)

FT-IR is a commonly used analytical technique that can provide useful information about the functional groups present in a material. FT-IR is particularly useful as it is suitable for insoluble materials and can reveal important details regarding the protein conformation. Other analytical biochemical techniques either require crystalline (X-ray crystallography) or soluble samples (nuclear magnetic resonance and circular dichroism) [43]. These techniques were not utilised for FEG as they would require complete solubilisation which essentially forms α-elastin.

FT-IR involves transmitting infrared light (IR) through a sample as a function of wavelength. The energy absorbed at each wavelength is characteristic of molecular vibrations that are associated with the material's functional groups. The absorbance (A) of IR by a sample can be determined using the Beer-Lambert Law:

$$A = -\log\left(\frac{I}{I_0}\right) = \varepsilon bc \qquad \text{(Equation 3.1)}$$

where I and I_0 are the intensities of the transmitted (sample) and incident (background) radiation, respectively. Absorbance is related to the concentration (c) of the molecules in a sample where b is the path length and ε is the molar absorptivity [249].

The effect of hydrolysis at the molecular level was studied using FT-IR by comparing IE to its insoluble and soluble counterparts. FT-IR was performed using the Varian Excalibur FTS 3500 Spectrometer at the Oxford Materials Characterisation Services,

University of Oxford using a standard protocol. The FT-IR had a diamond Attenuated Total Reflectance (ATR) accessory which allowed samples to be tested directly. IE powder (as received), freeze-dried FEG and freeze-dried soluble elastin's 1, 2 and 3 (SE1, SE2 and SE3) were studied in the dry state. Samples were tested at a wavenumber range of 400-4000cm^{-1}, with a resolution of 4cm^{-1} and 64 scans. Spectra were enhanced by performing second derivative using the Savitzky–Golay algorithm in Origin® 2017 (OriginLab Corporation, USA) software. Amide I and Amide III bands were deconvoluted using the peak deconvolution application on Origin® 2020 and fitted with Gaussian curves. The composition of the secondary structure was determined by comparing the ratios of each component to the area of the respective band [250].

3.2.5. Amino Acid Analysis (AAA)

The effect of hydrolysis on the amino acid composition of IE was compared to FEG. Samples with a concentration of 1% wt/v were prepared, IE was used as received and compared to freeze-dried FEG. 6 M Hydrochloric acid (HCl, Sigma Aldrich, U.K.) was placed in a round bottomed flask and the samples were weighed and added. Samples were purged with nitrogen (Oxygen Free, Industrial Grade, BOC, U.K.) by inserting two needles through a rubber septa cap (Sigma Aldrich, U.K.), one purging nitrogen into the sample and the other removing air from the sample. The samples were hydrolysed in a vacuum oven (Gallenkamp Vacuum Oven) under nitrogen at 110°C for 21 hrs. Hydrolysis resulted in a dark yellow-brown solution. The HCl was removed using a rotary evaporator (Büchi® R-200 Rotary Evaporator, Sigma Aldrich, U.K.) under nitrogen to prevent oxidation of the sample. The sample was rotated at a medium speed (~200 rpm) at a temperature of 40°C using a thermostat-controlled water-bath

and condensation was prevented by circulating cold tap water through the condenser. A cold trap was attached between the vacuum pump (Single Stage Vacuum Pump, TW-1A, ultimate vacuum of 10 Pa) and the rotary evaporator and maintained at a temperature of 0°C using an ice-bath. The acid evaporated within 30-40 mins leaving a sticky residue. The residue was dissolved in deionised-water to give a final concentration of 1%wt/v and transferred to glass vials. Three samples of each type were prepared from different batches. Once prepared samples were stored at -80°C (Sanyo, Ultra Low Freezer) until required for AAA.

LC-MS experiments were conducted at the Department of Chemistry by Dr. Elisabete Pires. Samples were derivatised and C18 reversed-phase analysis of derivatised samples was performed using the Thermo Ultimate 3000 UHPLC system coupled directly to a Q-Exactive HF Hybrid Quadrupole-Orbitrap mass spectrometer, the settings used have been summarised in Table 3.1. The raw data was processed using Progenesis QI for small molecules (Waters, Elstree, UK).

Table 3.1: Summary of settings for Thermo Ultimate 3000 UHPLC system

Setting	Condition
Injection	5 µL partial loop with pre- and post-injection program
Column	Waters AccQ-Tag column (2.1x100mm)
Flow Rate	0.5mL/min
Run time	9.5 mins
Mobile Phases (A&B)	AccQ-Tag reagents prepared as recommended by Waters (Waters PLC, Elstree, UK).
Gradient Elution programme	0mins, 0.1%B; 0.54min, 9.1%B; 5.74min, 21.2%B; 7.74mins, 59.6%B; 8.04min, 90%B; 8.05min, 90%B; 8.64min, 0%B; 9.5min, 0.1%B
Column Temperature	40°C throughout experiment
Settings for mass spectrometry	Positive ion mode separately using a scan-range from m/z 70-1050 and resolution set to 70,000

3.2.6. Rheology

The rheological properties of the FEG in the hydrated state was studied to understand the behaviour of the gel prior to any manipulation. Rheology was conducted using a Physica MCR 301 Rheometer installed with RheoCompass® software (Anton Paar, U.K.). All rheology experiments were conducted at the Laboratory for In-situ Microscopy and Analysis, Department of Engineering, University of Oxford. A 25 mm stainless steel parallel plate geometry (79044, Anton Paar, U.K.) with a gap set at 1 mm and a normal force of 0.5 N was used. The sample was placed in between the plate and the stage using a spatula and the edges were trimmed to remove excess sample. Dynamic frequency sweeps for FEG were performed from 0.1 to 10 Hz at 20°C with a constant strain of 5%. The temperature was controlled using a Peltier temperature control (Deben, U.K.). Amplitude sweeps were conducted prior to the frequency sweeps to ensure operation within the linear viscoelastic region.

Viscoelastic properties of interest included: the storage modulus (G'), loss modulus (G"), complex viscosity (η*), and loss factor (tanδ). A small oscillatory strain (γ) was applied to the samples (Equation 3.2) and the resultant stress (σ) was measured (Equation 3.3) as a function of time (t) where ω is frequency of deformation [251]. G' and G'' are determined from the complex modulus, G*, and the phase angle, δ, (Equation 3.4). The tanδ is the ratio of the G'' and G' (Equation 3.5) and η* was determined using Equation 3.6 where η'=G''/ ω and η''=G'/ ω.

$$\gamma(t) = \gamma_0 (\cos \omega t) \qquad \text{(Equation 3.2)}$$

$$\sigma(t) = G^* \sigma_0 \cos(\omega t + \delta) \qquad \text{(Equation 3.3)}$$

$$G' = G^* \cos \delta \text{ and } G'' = G^* \sin \delta \qquad \text{(Equation 3.4)}$$

$$\tan\delta = \frac{G''}{G'} \quad \text{(Equation 3.5)}$$

$$|\eta^*| = \sqrt{(\eta')^2 + (\eta'')^2} \quad \text{(Equation 3.6)}$$

3.2.7. Swelling of FEG as a Function of pH

Swelling tests at different pH were conducted to understand the effect of rehydrating freeze-dried FEG. pH solutions from pH 1-12 were prepared using 1M HCl (Sigma Aldrich, U.K.) and 1M sodium hydroxide (NaOH) (Thermo Fisher Scientific, U.K.) as the starting solutions. The pH was adjusting using stock solutions of 1-5M HCl or 1-5M NaOH and measured using a pH meter (Mettler Toledo™, Thermo Fisher Scientific, U.K., accuracy of ± 0.01), which was calibrated with standard buffer solutions. Buffers were not used to prepare swelling media as they may affect the degree of swelling.

The dry mass of 5-10 mg of the FEG was measured using an analytical balance (Mettler Toledo™, AB204, U.K.). The sample was placed in the pH solution and left at room temperature overnight without agitation. The samples were removed and drained on a metallic mesh for 1min before the wet mass was recorded and the pH was re-measured. Three samples for each pH were tested. The extent of swelling was determined using Equation 3.7.

$$\text{Swelling Ratio } (Q_m) = \frac{\text{mass}_{wet} - \text{mass}_{dry}}{\text{mass}_{dry}} \quad \text{(Equation 3.7)}$$

The degree of ionisation of carboxyl and amino groups were determined to understand the effect of pH on the swelling of FEG. The total charge, N_T, of a protein is dependent on the charge of ionisable amino acid residues at different pH. N_T can be determined

using Equations 3.8-3.9 where *i* is the degree of ionisation, *N* is the number of amino acid residues and the subscript *p* and *n* are positively and negatively charged residues, respectively [252], [253]. The degree of ionisation for elastin was determined using the ionisable functional groups identified by AAA (3.3.3) and listed in Table 3.2.

$$N_T = \sum_{p}^{positive} i_p N_p + \sum_{n}^{negative} i_n N_n \qquad \text{(Equation 3.8)}$$

$$\text{where } i_p = \frac{1}{10^{pH-pKa}+1} \text{ and } i_n = \frac{-1}{10^{pKa-pH}+1} \qquad \text{(Equation 3.9)}$$

Table 3.2: Parameters used to determine the theoretical net charge of elastin.

Amino Acid	Functional Group	Number of Residues*	pKa$^{\phi}$
Lysine, α-NH_2	-NH_2	6	10.28
Aspartic acid, α-COOH	-COOH	3	2.98
Glutamic acid	-COOH	9	3.08
Serine	-OH	6	9.15
Threonine	-OH	8	9.12
Tyrosine	-OH	7	10.07

Values were determined from the amino acid sequence using the number of residues per molecule for bovine elastin[195] and pKa valuesϕ[253].*

3.3. Results

3.3.1. Isolation & Purification of Fibrillar Elastin Gel

Parameters which were controlled during the hydrolysis process include the concentration of ethanedioc acid, the temperature of the water bath, the time taken per hydrolysis and the number of hydrolyses required. Preliminary tests involved studying different concentrations of acid as well as the time taken per hydrolysis as shown in Table 3.3. The results of interest were the yield of FEG obtained and the water uptake ratio of the gel as higher solvent absorption suggested improved interaction with solvents, in this case, deionised water. It was found that at least 0.25M acid was required to hydrolyse elastin, and above 0.4M, the gel hydrolysed excessively, reducing the yield as well as the integrity of the material in the swollen state. Hydrolysis in 0.25M ethanedioc acid for 70 mins, repeated three times was chosen as the best combination of conditions to isolate FEG.

Table 3.3: Parameters tested to hydrolyse insoluble elastin into Fibrillar Elastin Gel

Ethanedioc Acid Concentration (M)	Total Number of Hydrolyses	Reaction Time (mins)	Yield (%)	Water Uptake Ratio (%)
0.25	Three	60	24	640
0.25	Three	70	24	3490
0.40	Two	60	20	5690
0.50	Two	60	4	3530

An obvious change observed during the hydrolyses was the change in colour of the supernatant as well as the remaining elastin residue after each hydrolysis as shown in Fig.3.4. As each hydrolysis passed, the intensity of the yellow coloured supernatant

and remaining residue increased. It was found that this was an indication of partial hydrolysis, as when the residue was not brighter yellow, it did not swell as much in deionised water. The change in colour is associated with the level of hydrolysis and successful cleavage of desmosine bonds. It was also found that when the residue had solubilised too much, as seen when using 0.5M acid, the insoluble residue was darker brown in colour, indicating the process had approached complete hydrolysis.

The final gel was obtained after thoroughly washing the insoluble residue from the third hydrolysis. After washing in deionised water, the paste-like substance changed into a gelatinous substance with a final concentration of 3%wt/v. The gel obtained after purification is shown in Fig.3.5a in the hydrated state and Fig.3.5b in the freeze-dried state as a sponge-like material.

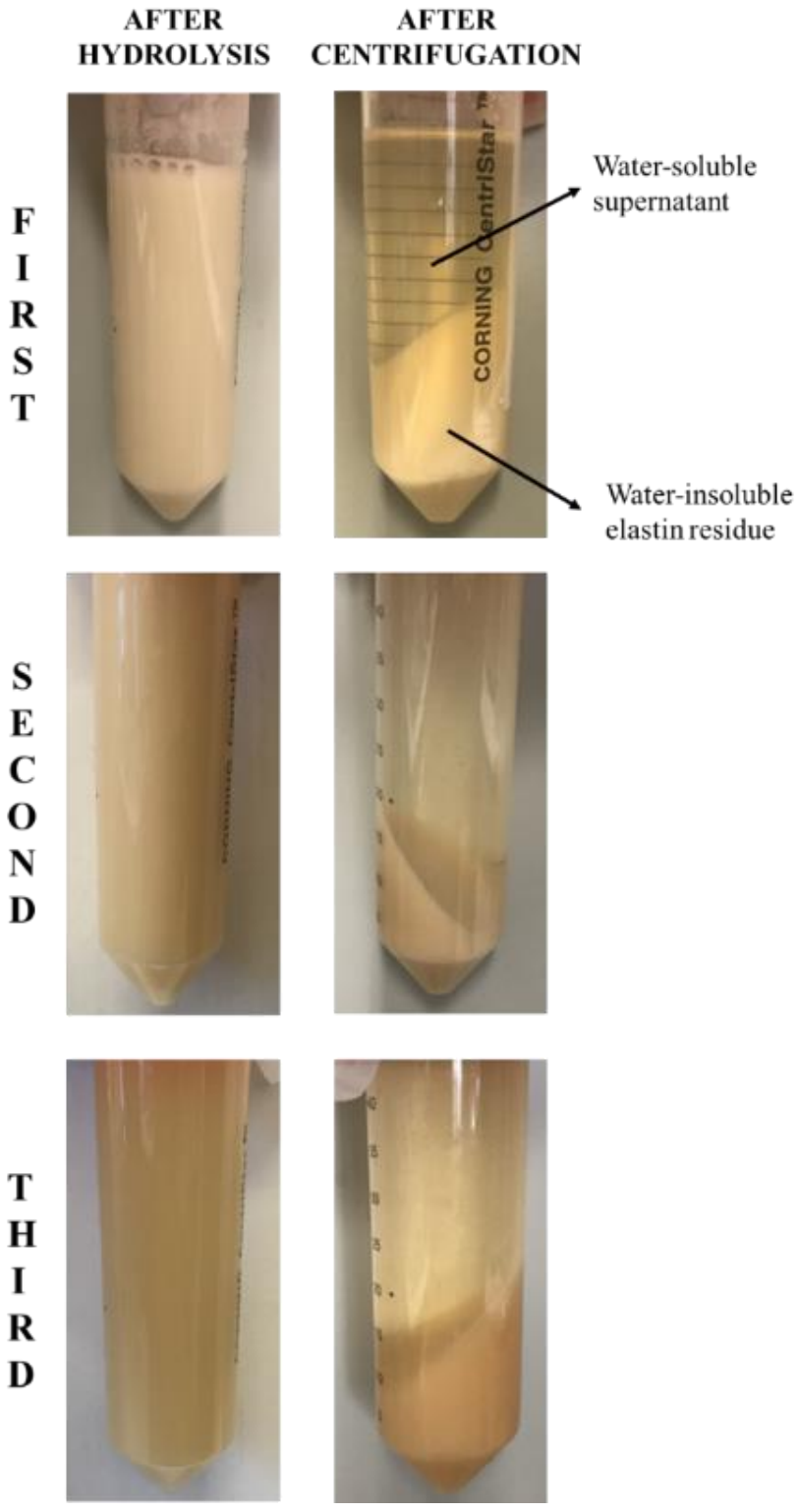

Figure 3.4: Elastin and ethanedioc acid mixture after hydrolysis (left) and after centrifugation (right), repeated three times for 70 mins each. After centrifugation, a yellow supernatant (top) and an insoluble residue (bottom) are observed. Not to scale.

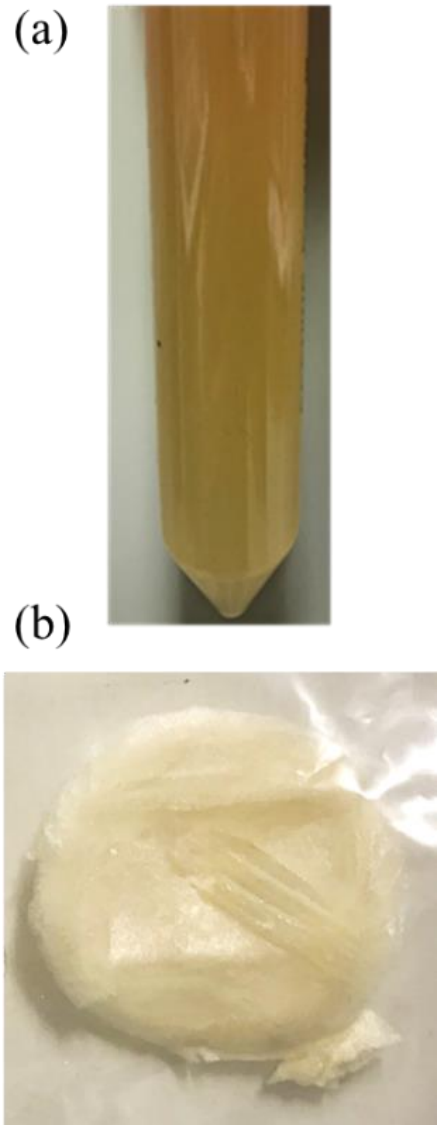

Figure 3.5: Fibrillar Elastin Gel (3%wt/v) after purification in the hydrated state in a centrifuge tube (a) and in the freeze-dried state (b) as a sponge-like material. Both types of FEG were stored at 4°C. Not to scale.

3.3.2. Microstructure of FEG

Scanning electron microscopy (SEM) was used to understand the effect of the isolation process on the microstructure of all forms of elastin obtained before and after each hydrolysis (up to the third hydrolysis). The IE powder (as received from the manufacturer) is presented in Fig.3.6. SEM revealed it was composed of two main components, 37% globular and 63% fibrillar form of elastin. The fibrillar component was present as loose fibres (58%) as well as bundles of fibres (42%). The diameters of the particles are presented in Table 3.4, and the particle size distribution for the globular particles and the loose rods in Fig.3.7. There was a significant difference between the size of the globules and the fibres as well as the bundles of fibres. The bundles of fibres were the largest component of the IE powder, however, there was no significant difference between the diameter of the loose fibres and the fibres comprising the bundles, suggesting that the loose fibres may have been originally present in bundles and separated during the milling (post-extraction) process.

Table 3.4: Average diameter of particles present in insoluble elastin powder.

Particle Type	Average Diameter (µm)
Globules	23.0 ± 8.0
Loose Fibres	6.7 ± 1.7
Fibres present in bundles	5.1 ± 1.9
Bundles of fibres	58.0 ± 21.0

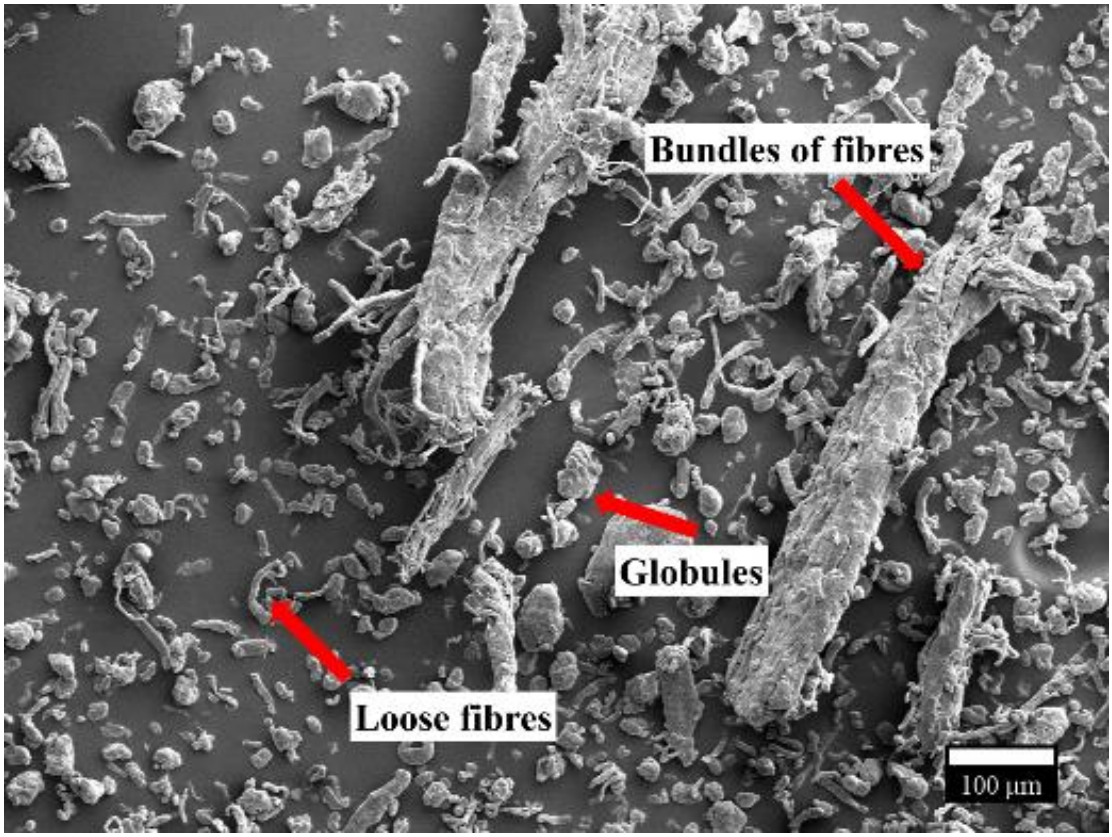

Figure 3.6: SEM image of insoluble elastin powder (as received from the manufacturer). The fibrillar component was present as either loose fibres (58%) or bundles of fibres (42%), marked by the red arrows.

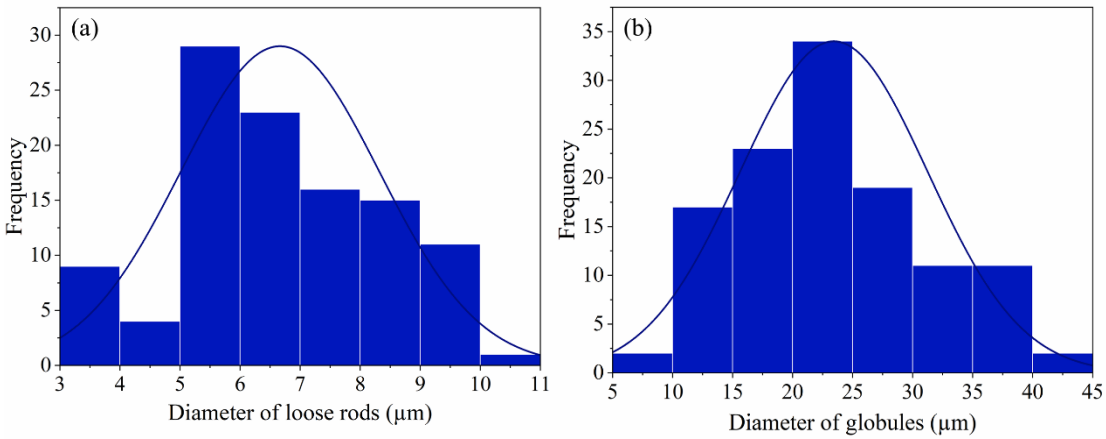

Figure 3.7: Diameters of particles present in insoluble elastin powder (as received from the manufacturer), showing (a) loose rods which had an average diameter of 6.7 ± 1.7 µm and (b) globules which had an average diameter of 23.0 ± 8.0 µm. n>100. Graphs have been fitted with a normal distribution.

The insoluble and soluble elastin products formed after each hydrolysis were also studied and have been presented in Fig.3.8. The images obtained for the soluble elastin from all supernatants appeared flake-like and were indistinguishable, indicating that the elastin had structurally changed (they were no longer globular or fibrillar) after solubilisation and coalesced into thin flakes due to their fragmented nature. The insoluble residues, on the other hand, appeared different after each hydrolysis. The insoluble residue from the first hydrolysis was similar to the IE powder (raw material) as it had a mixture of bundles of fibres and globules as well as loose rods, suggesting the first hydrolysis does not result in significant changes to the structure of the elastin. The residue from the second hydrolysis appeared to have fewer globules and the bundles appeared looser than those observed in both the first residue and the raw material, implying that the fibres had started dissociating by the second hydrolysis. By the final hydrolysis, the residue obtained (which is the material in question) contained no visible bundles of fibres, and the fibres merged into a uniform sheet of elastin. Fig.3.9 shows a magnified image of the air-dried residue which was composed of independent fibres that were randomly orientated. From these results, it was apparent that the limited hydrolysis method applied in this study resulted in the dissociation of the fibres present in bundles of fibres of elastin. SEM was used to further understand the microstructure of the fibres obtained in the third hydrolysis. Attempts were made to dilute the gel using deionised-water to form concentrations with 10%, 20% and 50% FEG, however, there was no major improvement in the images obtained as the fibres appeared to coalesce when dried. Freeze-dried FEG (Fig.3.10) was found to coalesce into a porous foam-like structure. The gel was also studied in the hydrated state using

LSCM (Fig.3.11), a heterogenous mixture of loose fibres with no particular orientation was observed where fibres in larger bundles had split longitudinally.

The final method used to study the microstructure of the fibres obtained in the third hydrolysis was precipitation. Precipitation is commonly used to purify proteins and was applicable to the FEG as it was challenging to separate the fibres from the deionised-water it was dispersed in. The precipitated fibres appeared to twist into multiple bundles of fibres orientated parallel to the long axis of the fibres as shown in Fig.3.13a. The fibres comprising the gel had diameters typically between 2.5-8.5μm (Fig.3.12) with an average diameter of 5.0±1.3μm and a rod-like microstructure as shown in Fig.3.13b. There was no statistically significant difference between the fibres observed in the precipitated bundles and the fibres observed in the bundles found in IE. These results suggest that the fibres were of the same origin and therefore the fibres isolated as the FEG had retained the mature fibrous nature of IE fibres after sequential hydrolysis. The average diameter of the bundles of fibres formed from the gel after precipitation was 60±14μm, which was also not significantly different compared to the bundles observed in IE. Additionally, these results suggest that NaCl initiated the self-assembly of the randomly orientated dissociated fibres into aligned fibres that formed bundles. Therefore, the results imply that the gel exhibits coacervation, a phase separation process that self-aggregates monomeric elastin before fibrillogenesis takes place. To confirm this, the gel was also heated at 37°C in phosphate buffered saline (physiological conditions) and a phase transition was observed where the homogenous FEG suspension completely separated from the solution to form aggregated elastin.

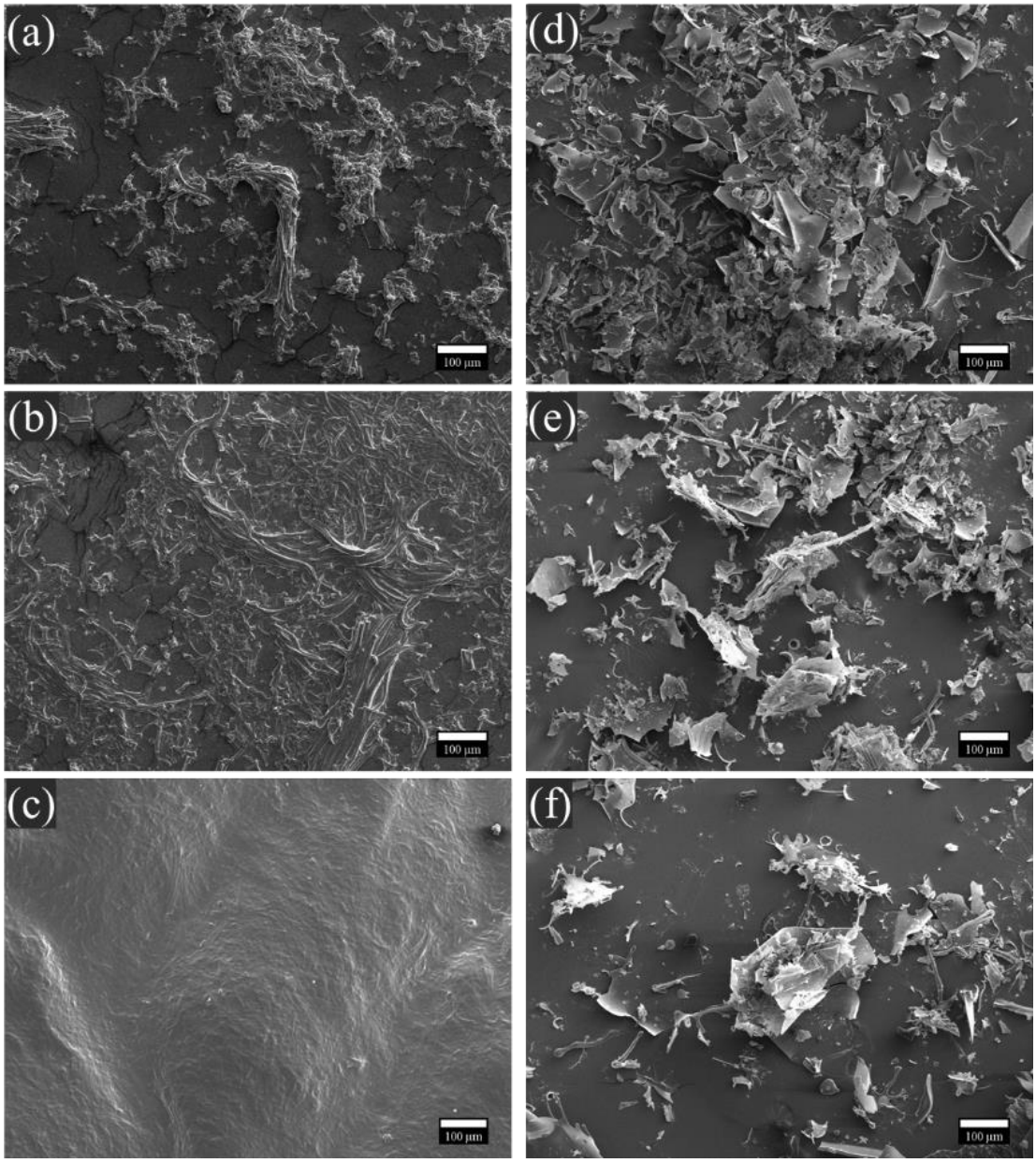

Figure 3.8: SEM images of the air-dried IE residues from hydrolyses 1 (a), 2 (b) and 3 (c) and the freeze-dried soluble supernatant from hydrolyses 1 (d), 2 (e) and 3 (f) after dialysis against deionised water.

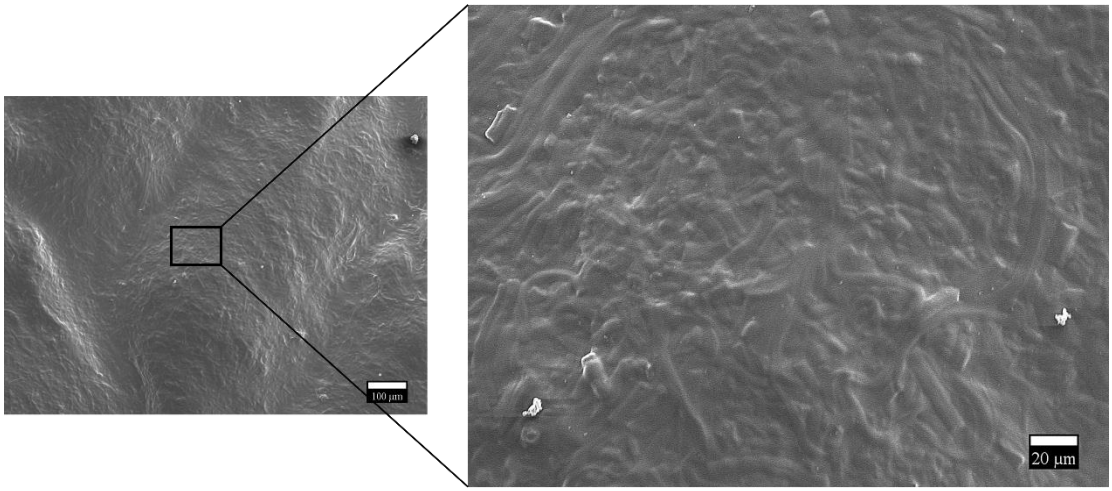

Figure 3.9: SEM image of the insoluble elastin residue obtained from the third hydrolysis, called fibrillar elastin gel, at a magnification of 100 x (left) and 400 x (right). Samples were air-dried at room temperature.

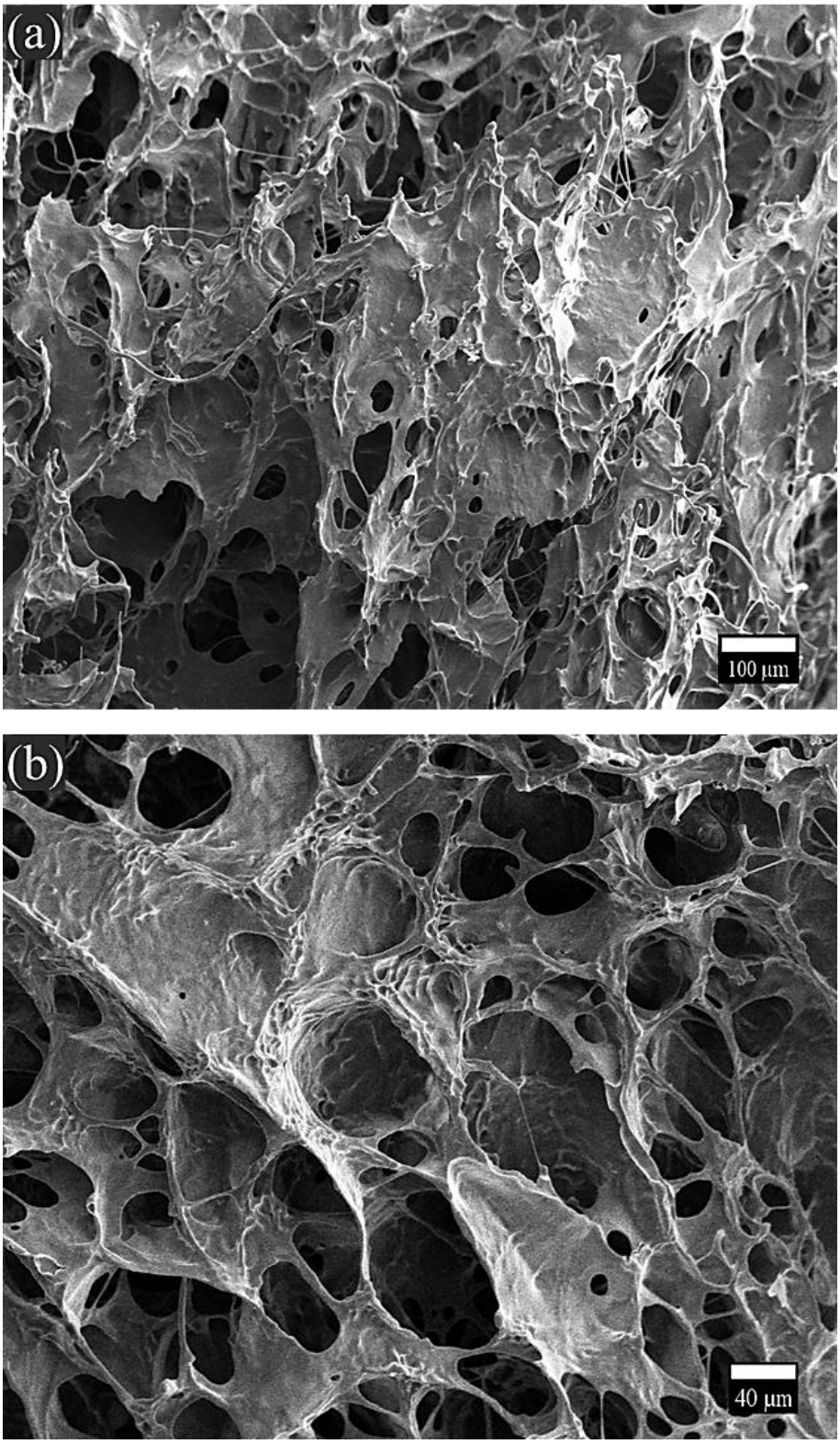

Figure 3.10: SEM images of freeze-dried fibrillar elastin gel at a magnification of 100 x (a) and 200 x (b) . Samples were prepared by freezing the gel at -20°C and freeze-drying under a vacuum of 0.05 mbar.

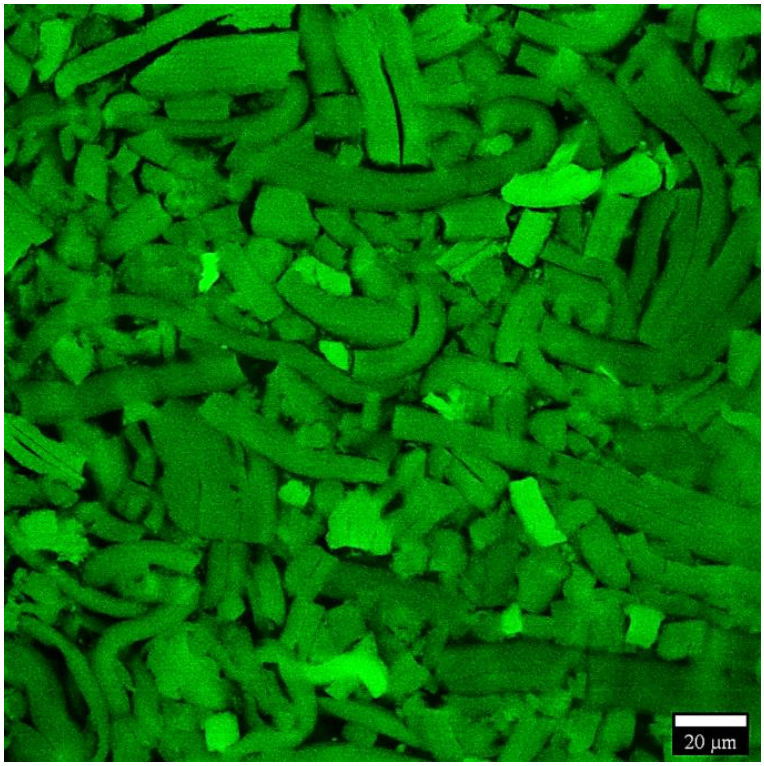

Figure 3.11: Laser scanning confocal microscopy image of fibrillar elastin gel in the hydrated state, taken at a magnification of 60 x using the 488 nm argon laser with no specific staining.

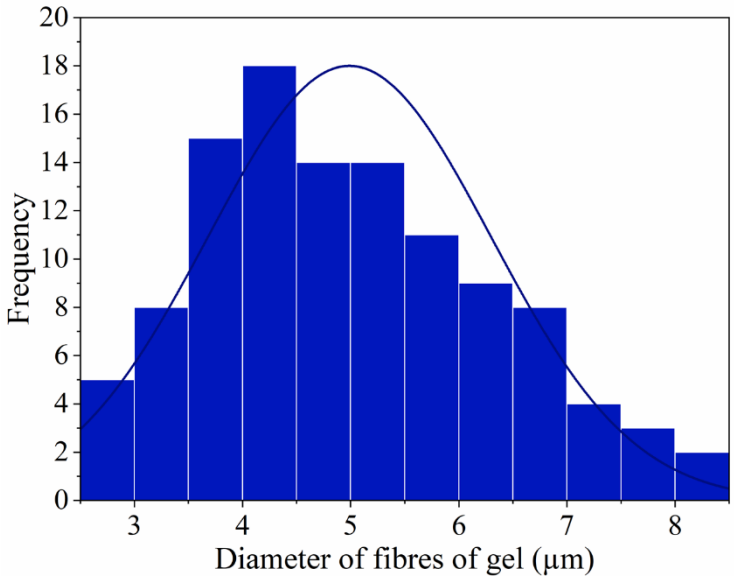

Figure 3.12: Distribution of diameters of fibres present in precipitated fibrillar elastin gel which had an average diameter of 5.0 ± 1.3 µm. Precipitation was carried out in sodium chloride. Graphs have been fitted with a normal distribution.

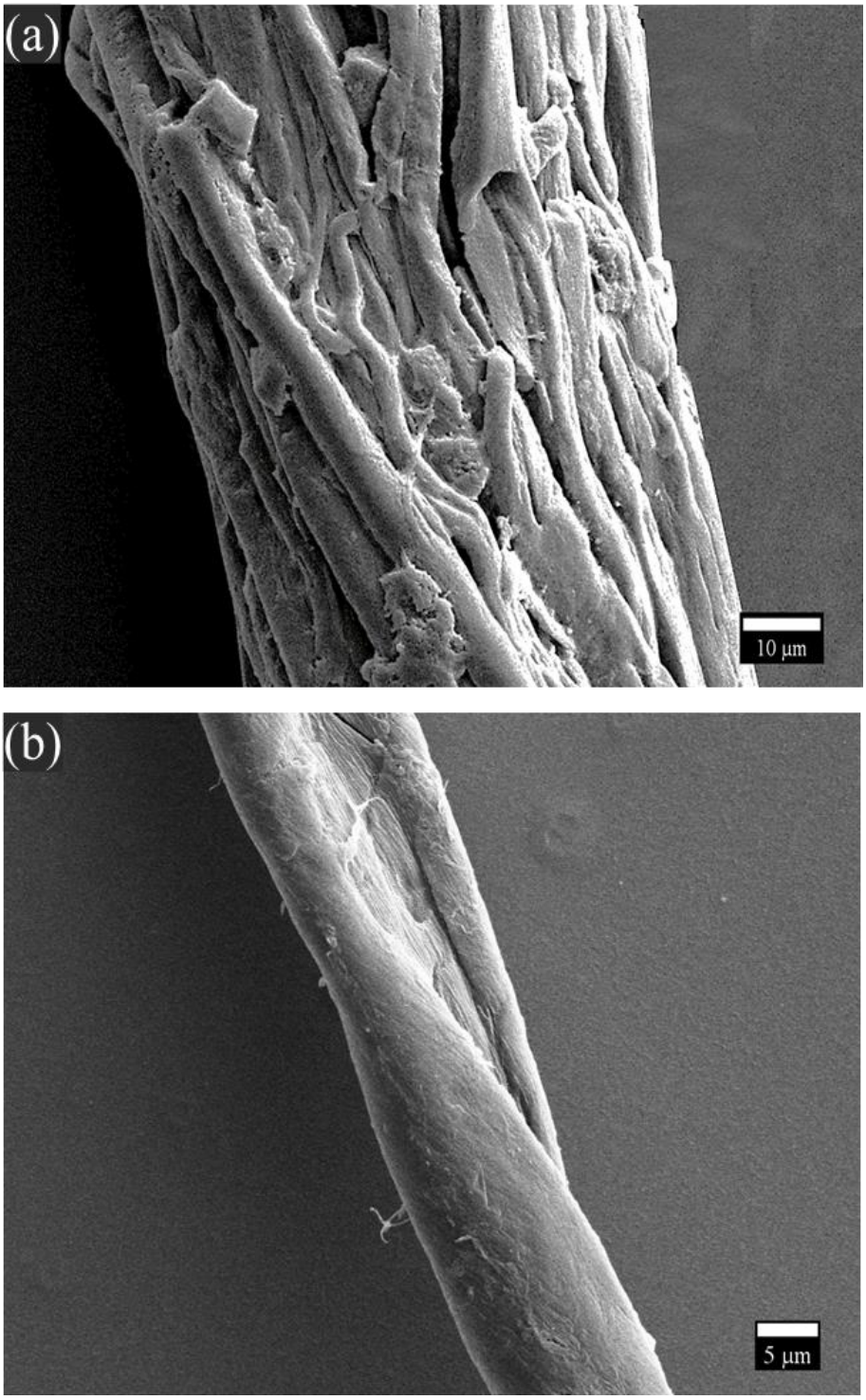

Figure 3.13: A bundle of elastin fibres (a) and (b) an individual elastin fibre obtained by precipitation of fibrillar elastin gel in sodium chloride.

3.3.3. Infrared Spectroscopy of FEG

As this form of hydrolysis selectively cleaves amide bonds, the effect of hydrolysis on the secondary structure of all forms of elastin was studied using FT-IR. The infrared spectra for the IE powder, the soluble elastin peptides (SE1, SE2 and SE3) from each hydrolysis and FEG have been presented in Fig.3.14. The band assignments for each sample can be found in Table 3.5, all characteristic bands of elastin were detected, including Amide I, II, III and A. The Amide III peak of FEG shifted significantly by more than $5cm^{-1}$ compared to the other samples. The peak areas of the Amide I and A bands were compared. Fig.3.15 shows a significant increase in intensity of the Amide I band of the hydrolysed samples (SE1-3) with an incremental increase between the three compared to IE and FEG. With each hydrolysis the Amide I content increases in the soluble samples, which implies there is a decrease in amide bonds (80% C=O stretching [254]) due to hydrolysis.

Table 3.5: Band assignments for FT-IR spectra [255].

Sample	Absorption Band (cm^{-1})					
	Amide A	**Amide I**	**Amide II**	**CH_2 bending**	**Amide III**	**C-O stretching**
IE	3286	1633	1528	1336	1238	1163
FEG	3288	1635	1530	1336	1230	1165
SE1	3293	1635	1535	1335	1238	1161
SE2	3291	1634	1523	1336	1235	1163
SE3	3288	1634	1521	1336	1240	1165

Insoluble elastin powder (IE, as received from the manufacturer), fibrillar elastin gel (FEG), soluble elastin's produced after hydrolysis 1 (SE1), hydrolysis 2 (SE2) and hydrolysis 3 (SE3), which were dialysed and freeze-dried.

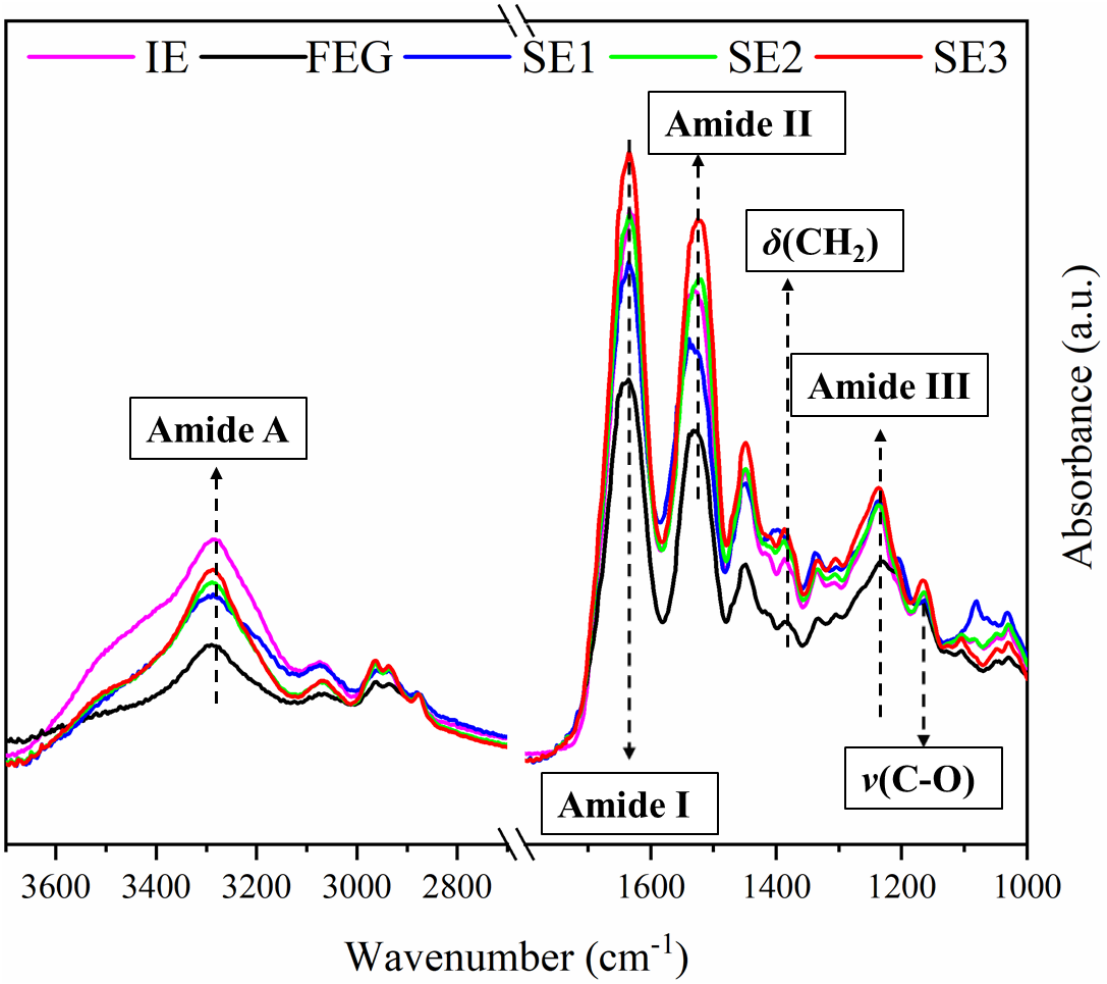

Figure 3.14: FT-IR spectra with major peak assignments (a) for insoluble elastin powder (IE, as received from the manufacturer), fibrillar elastin gel (FEG), soluble elastin's produced after hydrolysis 1 (SE1), hydrolysis 2 (SE2) and hydrolysis 3 (SE3), which were dialysed and freeze-dried. The data has been normalised at 2872 cm^{-1}.

The Amide I band is the most sensitive to changes in secondary structure of the backbone of proteins. The resolution of the Amide I band was enhanced by determining the second derivative of all samples to reveal overlapping peaks (shown in Table 3.6). The Amide I band was deconvoluted into four main components, β-structures at 1631cm^{-1}, unordered-structures (random coils) at 1645cm^{-1}, α-helices at 1652cm^{-1} and β-turns at 1668cm^{-1} which were present for all forms of elastin. The deconvoluted Amide I peak is shown in Fig.3.16 for IE and FEG, and the estimations

of the composition of the secondary structure for all samples are shown in Table 3.8. The results suggested that IE and FEG have different secondary structures as there was a 1.6-fold decrease in the α-helix component of IE compared to FEG from 23±2% to 14±2%, respectively (Table 3.8). SE3 also had the highest content of α-helices compared to the other soluble elastin's, suggesting that the hydrolysis led to a loss of α-helices. There was no obvious change in the content of unordered-structures. The β-structure component was complex for the FEG and soluble samples, with an additional peak at 1618cm^{-1}. There was no significant difference in the β-sheet content for IE and FEG, however, SE1 and SE2 showed a significant increase, possibly due to loss of the globular elastin and loose fibres.

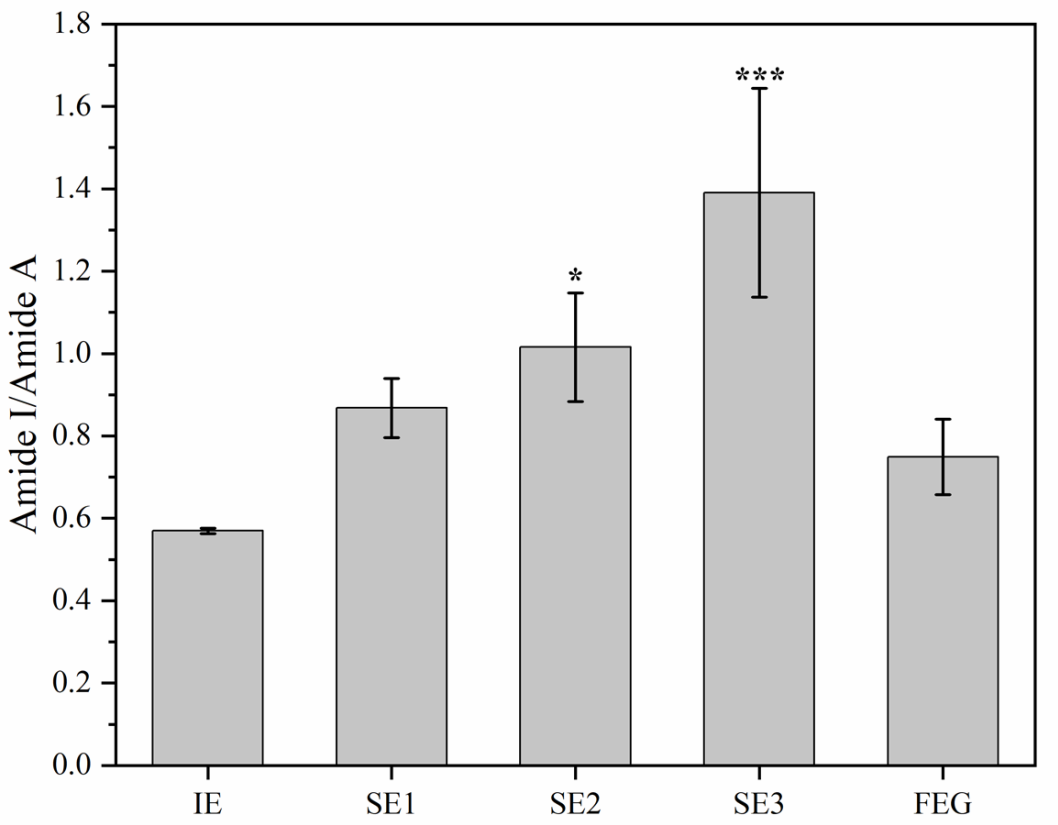

Figure 3.15: Peak area ratios of Amide I to Amide A determined by integrating peaks of Fig.3.14 for insoluble elastin powder (IE), fibrillar elastin gel (FEG), soluble elastin's produced after hydrolysis 1 (SE1), hydrolysis 2 (SE2) and hydrolysis 3 (SE3). Statistical analysis involved one-way ANOVA as mentioned in 4.2.9, where *p<0.05, ***p<0.0005 when compared to IE, n≥3.

Although, the Amide I band is used to determine the secondary structure, the narrow range limits its potential, hence, the Amide III peak was also deconvoluted (Table 3.7). The second derivative revealed that there was no major difference for the α-helix, β-turns and unordered-structures. As observed with the Amide I peak, β-structures had more than one component at 1205 and 1229-36cm^{-1} and there was a significant difference of -5cm^{-1} or more in the β-sheet structure for FEG samples. The decomposition of the peak into its substructures (Fig.3.17 and Table 3.9) revealed a significant increase in the composition of the peak at 1205cm^{-1} which increased 3-fold in FEG compared to the other sample types.

Table 3.6: Secondary structure assignments for the deconvoluted components of the Amide I peak [255], [256]**.**

Sample	Second Derivative of Amide I			
	α- helix	**β-sheet**	**Unordered structure**	**β-turns**
IE	1652	1634	1645	1669
FEG	1652	1618 1634	1645	1669
SE1	1651	1617 1634	1645	1668
SE2	1652	1619 1635	1645	1668
SE3	1652	1619 1635	1645	1668

Table 3.7: Secondary structure assignments for the deconvoluted components of the Amide III peak [257], [258]***.**

Sample	Second Derivative of Amide III			
	α- helix	**β-sheet**	**Unordered structure**	**β-turns**
IE	1305 1336	1279	1260	1205* 1236
FEG	1305 1335	1277	1265	1205* 1229
SE1	1305 1337	1283	1263	1203* 1235
SE2	1305 1337	1281	1263	1205* 1234
SE3	1305 1335	1278	1263	1209* 1235

Table 3.8: Estimated composition of secondary structure derived from the peak areas of the deconvoluted Amide I peak.

Sample	Secondary Structure Decomposition (%) of Amide I			
	α- helix	**β-sheet**	**Unordered structure**	**β-turns**
IE	23	30	40	7
FEG	14	7 25	47	7
SE1	18	8 33	32	9
SE2	16	8 37	32	7
SE3	25	6 25	36	8

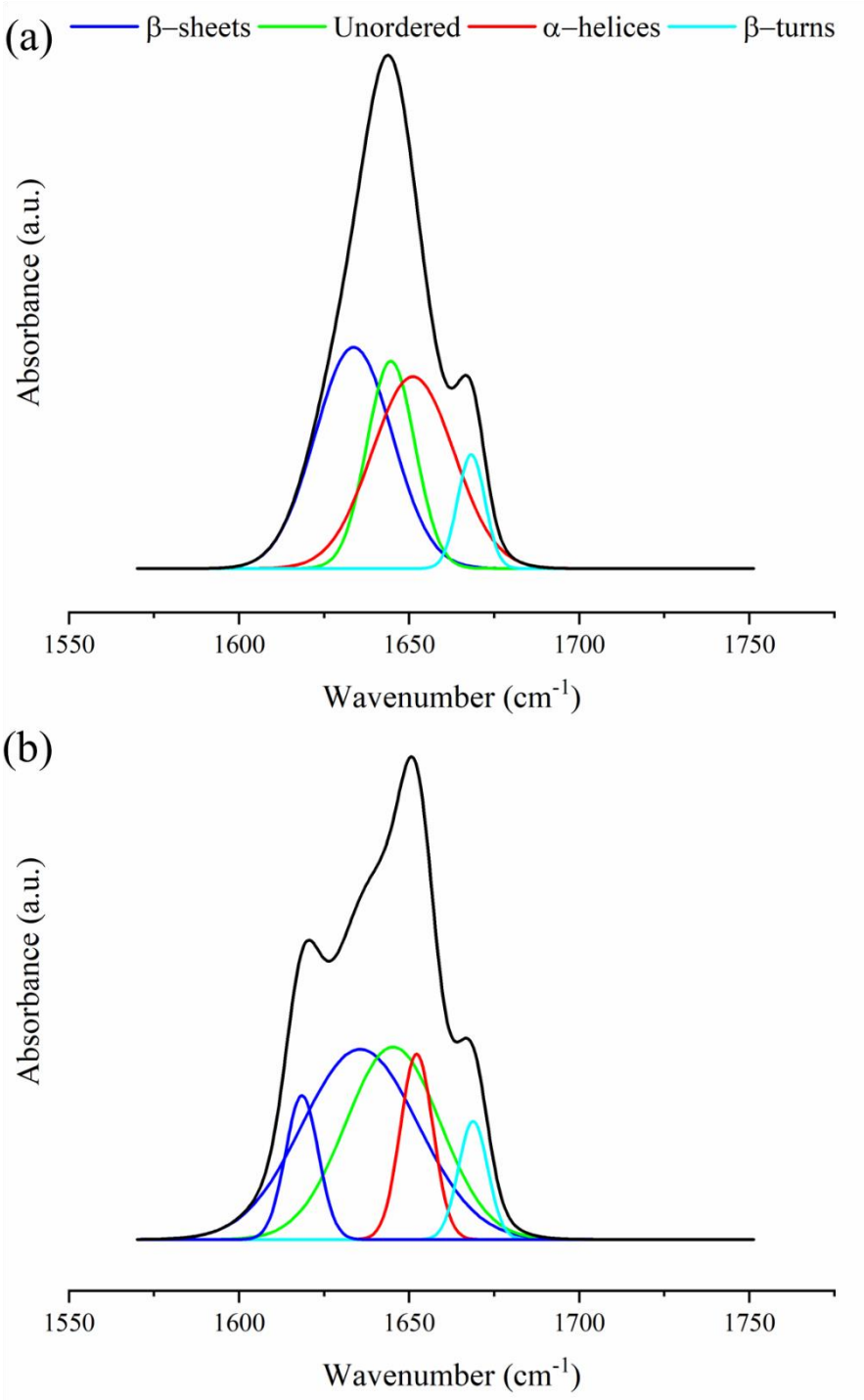

Figure 3.16: Deconvoluted Amide I peak for (a) insoluble elastin powder (IE, as received from the manufacturer) and (b) fibrillar elastin gel (FEG). The second derivative was used to identify components of the secondary structure.

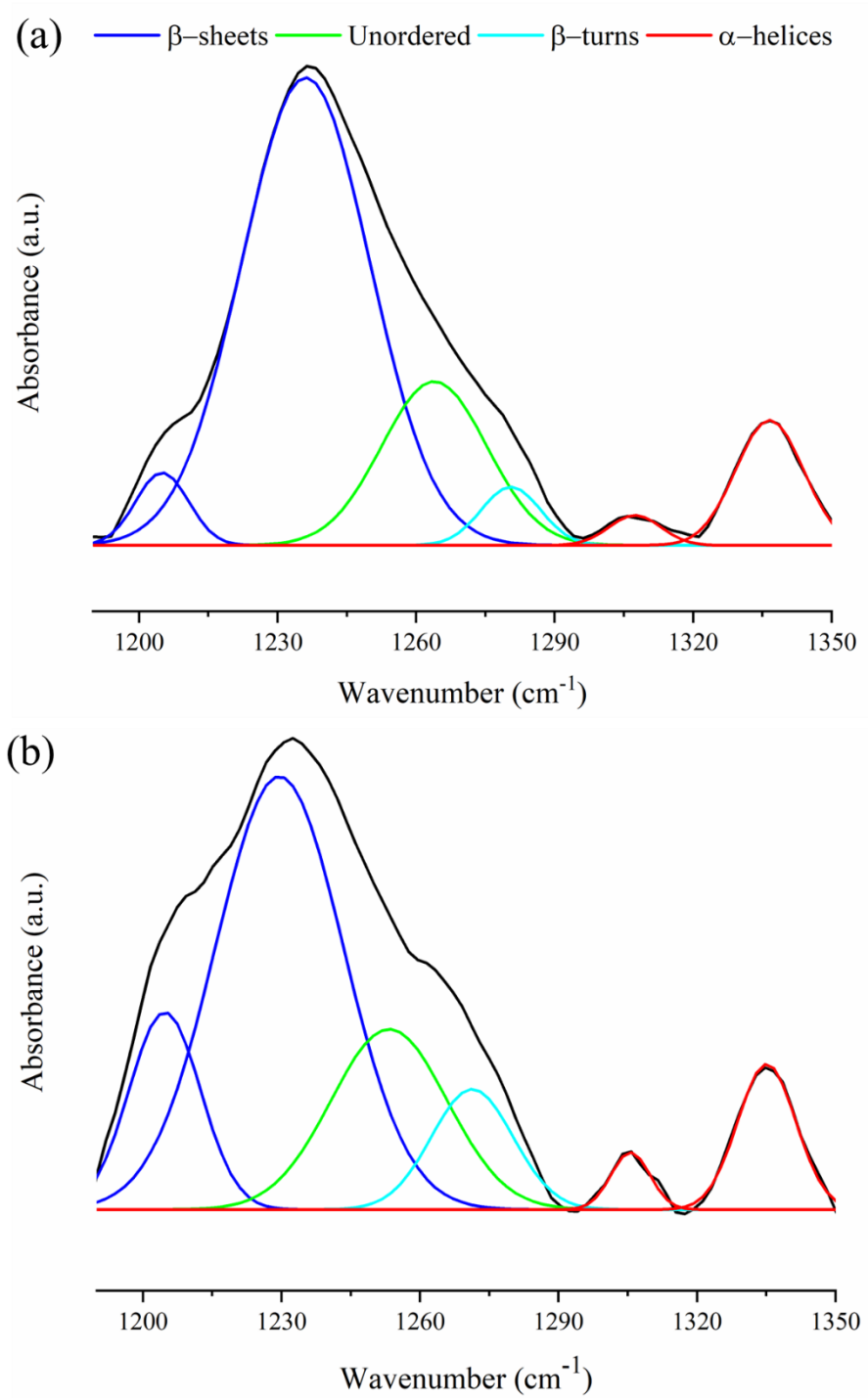

Figure 3.17: Deconvoluted Amide III peak for (a) insoluble elastin powder (IE, as received from the manufacturer) and (b) fibrillar elastin gel (FEG). The second derivative was used to identify components of the secondary structure.

Table 3.9: Estimated composition of secondary structure derived from the peak areas of the deconvoluted Amide III peak.

Sample	Secondary Structure Decomposition (%) of Amide III			
	α- helix	**β-sheet**	**Unordered structure**	**β-turns**
IE	11	4 63	18	4
FEG	10	13 50	18	9
SE1	11	7 59	21	2
SE2	10	4 65	19	2
SE3	12	2 65	14	7

The amino acid composition of IE and the gel was compared using liquid chromatography–mass spectrometry (LC-MS) (Table 3.10). The gel had a higher abundance of the non-polar amino acid residues: glycine, proline, valine, leucine, alanine, isoleucine, phenylalanine, and tyrosine. Whereas, the polar residues: aspartic acid, lysine, glutamic acid, serine, and threonine had a lower abundance. These results suggest the hydrolysis method cleaved amide bonds resulting in solubilisation of the polar residues involved in forming cross-linking domains and the remaining insoluble component is composed of mostly hydrophobic residues.

Table 3.10: Abundance of amino acid residues in Fibrillar Elastin Gel relative to insoluble elastin powder.

Amino Acid	Relative Abundance
Aspartic acid	0.3
Lysine	0.5
Glutamic acid	0.7
Serine	0.7
Threonine	0.9
Glycine	1.0
Proline	1.1
Valine	1.1
Leucine	1.2
Alanine	1.3
Isoleucine	1.3
Phenylalanine	1.3
Tyrosine	1.4

3.3.4. Rheology of FEG

The viscoelastic properties of FEG were studied using rheology. It is commonly used to study protein-based gels. Fig.3.18 shows the storage modulus, loss modulus and loss factor as a function of frequency as well as the complex viscosity and complex modulus. The storage modulus is constantly 7-fold higher than the loss modulus at all frequencies resulting in an almost constant loss factor of 0.15, indicating that the gel behaves elastically with low energy loss. Although the complex modulus increases with frequency, the complex viscosity decreases by an order of a magnitude from 710Pa.s at 0.1Hz to 88Pa.s at 1Hz. As the frequency increases, the viscosity continues

to decrease steadily, which suggests that the FEG exhibits shear thinning behaviour and therefore is a pseudoplastic fluid. Table 3.11 presents the results for FEG at a frequency of 1Hz. The Young's modulus, E, was predicted using the following relationship: $E=3G'(1+\nu)$, where ν =0.2 for compressible gels [259].

Table 3.11: Viscoelastic properties of fibrillar elastin gel (FEG) at 1 Hz.

Viscoelastic Properties of FEG	
Storage Modulus, G' (Pa)	504 ± 20
Loss Modulus, G'' (Pa)	70 ± 3
Loss Factor, tanδ	0.1 ± 0.003
Complex Modulus, E* (Pa)	510 ± 20
Complex Viscosity, η* (Pa.s)	88 ± 3
Young's Modulus, E, (Pa)ϕ	1210 ± 47

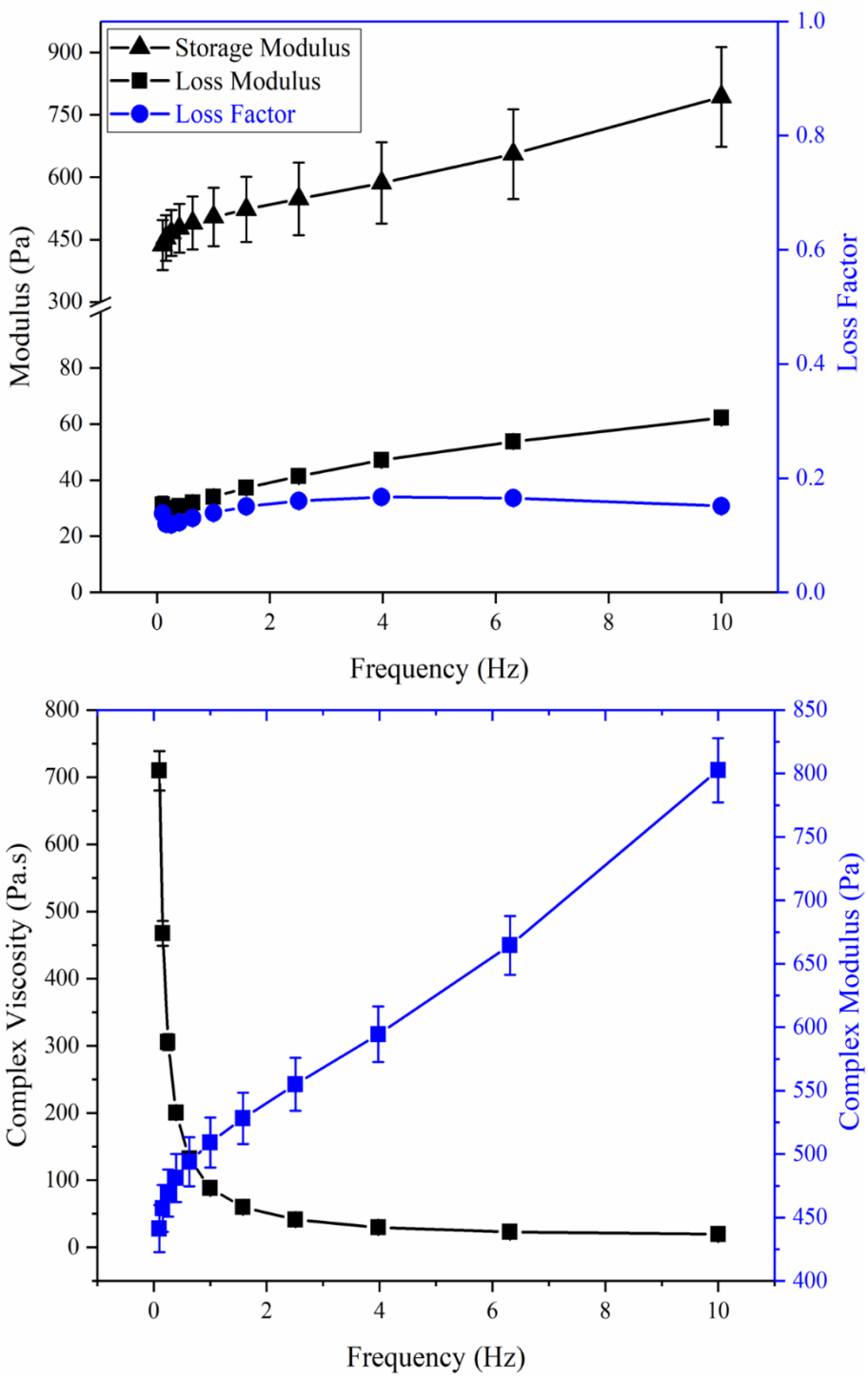

Figure 3.18: Viscoelastic properties of fibrillar elastin gel including the storage and loss modulus and the corresponding loss factor (top), the complex viscosity and complex modulus (bottom). Properties were measured using rheometry at a frequency between 0.1-10 Hz, at room temperature and a constant strain of 5%, n=3.

3.3.5. Swelling Characteristics of FEG

Swelling studies were performed to understand if it was possible to rehydrate the freeze-dried FEG to form a gel-like material again. Swelling was prioritised as the characteristic of interest as interaction of FEG with solvents will determine its utility as a potential material for further applications.

The solvent absorption after 24 hrs of swelling is shown in Fig.3.19 and Table 3.12. The extent of swelling was dependent on the total charge of FEG. In acidic solutions, FEG absorbed the most solvent, up to 2300-2600% between pH's 2-3 with no significant difference between them. In this range, FEG was positively charged (+37) and exhibited high water uptake (except at a pH of 1) whereas when 4<pH<8 the charge was relatively constant around +13 where it buffered with no significant difference and showed poor water uptake (3-fold lower than pH of 2-3). Above pH of 10, FEG was negatively charged (-35) and exhibited a significant increase in solvent absorption, where the samples swelled by 2.5-fold in comparison to pH's 4-9.

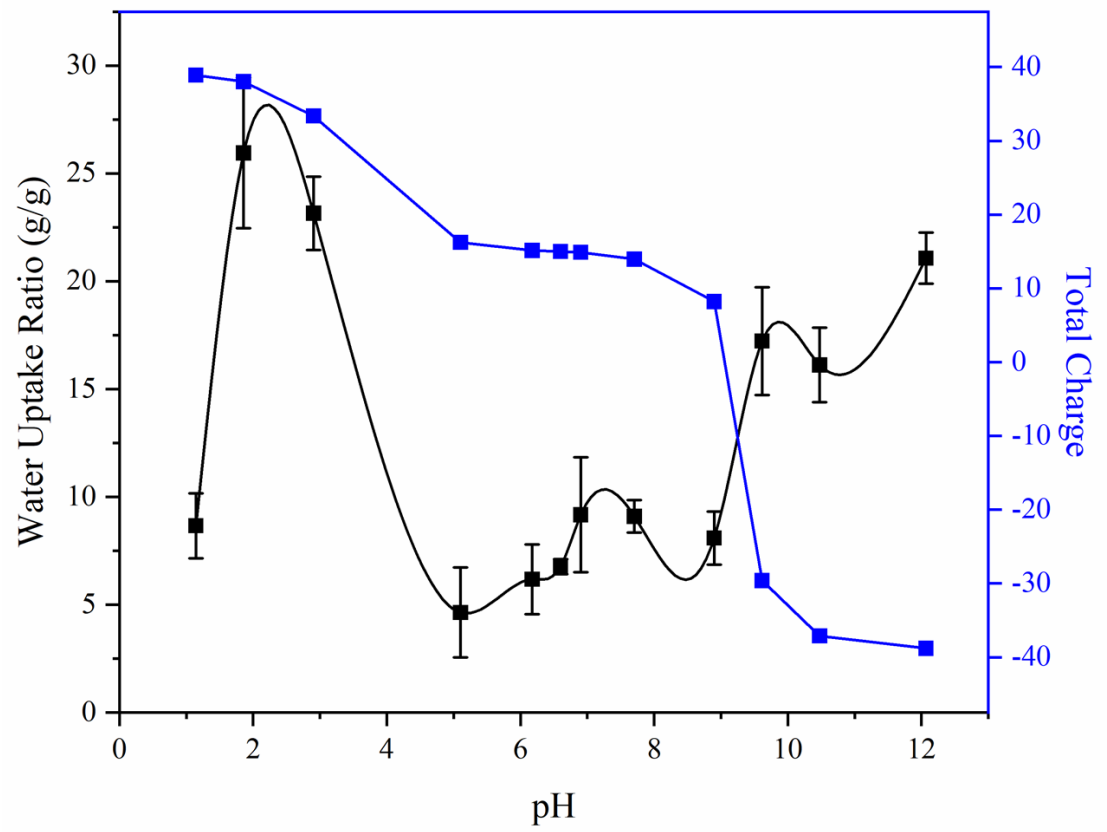

Figure 3.19: Dependence of equilibrium swelling ratio of freeze-dried fibrilar elastin gel on the pH of swelling media with theoretical net and total charge of bovine elastin overlaid as determined by Equation 3.8 and 3.10, respectively, n=3.

Table 3.12: Solvent absorption of freeze-dried fibrillar elastin gel

Initial pH	Final pH	Water Uptake Ratio (g/g)
1	1.1 ± 0.02	8.7 ± 1.5
2	1.9 ± 0.20	26.0 ± 3.5
3	2.9 ± 0.15	23.2 ± 1.7
4	5.1 ± 0.25	4.6 ± 2.1
5	6.2 ± 0.01	6.2 ± 1.6
6	6.6 ± 0.19	6.8 ± 0.3
7	6.9 ± 0.02	9.2 ± 2.7
8	7.7 ± 0.05	9.1 ± 0.8
9	8.9 ± 0.05	8.1 ± 1.2
10	9.6 ± 0.02	17.2 ± 2.5
11	10.5 ± 0.24	16.1 ± 1.7
12	12.1 ± 0.03	21.1 ± 1.2

3.4. Discussion

3.4.1. Microstructure of FEG

The average diameter of the fibres observed in FEG was 5.0 ± 1.3 µm which agrees with those reported for elastin fibres from nuchae ligament [60], [260]. Therefore, the limited hydrolysis method conducted in this study retains the structural integrity of polymeric elastin fibres. If further hydrolysis were to be conducted on the insoluble gel, the fibres obtained would have been hydrolysed further into filaments (4-5 nm) as observed with α-elastin [261]–[263] and reported to be present in elastin fibres [264], [265].

α-elastin was prepared for preliminary experiments by the author where it was found that the integrity of the fibres was poor, and scaffolds composed of α-elastin collapsed after freeze-drying (Fig.3.20), which was also true for cross-linked samples. Although α-elastin has structural order, coacervating it does not form the large bundles of fibres found in this study as it is completely fragmented into nano-filaments, instead smaller bundles are observed [262], [265]. Complete hydrolysis results in the irreversible loss of the structural hierarchy of elastin which cannot be recovered by coacervation.

The microstructural results imply that the limited hydrolysis process solubilised the globular and majority of the loose fibres present in the IE powder during the first three hydrolyses. Therefore, to obtain the gel, which is a dispersion of dissociated fibres, the remaining bundles of fibres unfolded. The source of elastin used in this study is heterogenous. Partial hydrolysis of elastin has previously been conducted with elastin that was excluded by size using a fine-mesh to obtain purified samples containing

mostly loose fibres [200]. The exclusion of the bundles of fibres from these samples may explain why such a gel has not been reported to date by this method.

Elastin exhibits autofluorescence intrinsically, this has been reported to be due to three possible reasons: (1) desmosine cross-links [266], (2) tri-amino pyridinium derivatives [267] or (3) exogenous nitrogen-heterocyclic compounds [268]. This suggests that the fibres are polymeric in nature and that they retain inter-fibril cross-links.

The structure of elastin can be deciphered from its degradation products by comparing it to the original sample. The propensity of FEG to self-assemble into bundles of fibres suggests that the bundles are responsible for providing the extensibility conferred by elastin. Therefore, the following structural model is being proposed for elastin in Fig.3.21 where the elastic fibres are composed of bundle of fibres. These bundles form fibrillar domains and are stabilised into a 3D network by cross-linking to globular domains. The fibrillar domains are arranged with a hydrophobic core and hydrophilic exterior which cross-link with other bundles as shown in Fig.3.21a. The limited hydrolysis performed in this study results in liberation of individual fibres from bundles of fibres to form a gel (Fig.3.21b). It should be noted that FEG is formed of fibres that contain inter-fibril cross-linking and are insoluble in solution. The FEG exhibits the ability to self-assemble into bundles of fibres when exposed to physiological conditions (Fig.3.21c). The ability to self-assemble into bundles again by coacervation is unique to FEG. It is hydrophobically driven and the formation of tightly bound bundles indicates hydrophobic interactions between fibres facilitates cross-linking. For the structure proposed in Fig.3.21 to be able to provide extensibility and recoil, it is essential that water forms a part of the structure as without water elastin is extremely brittle [269]. Therefore, it is being proposed that water is present in

interstitial spaces within fibres as well as bulk water that acts as a solvent between bundles of fibres.

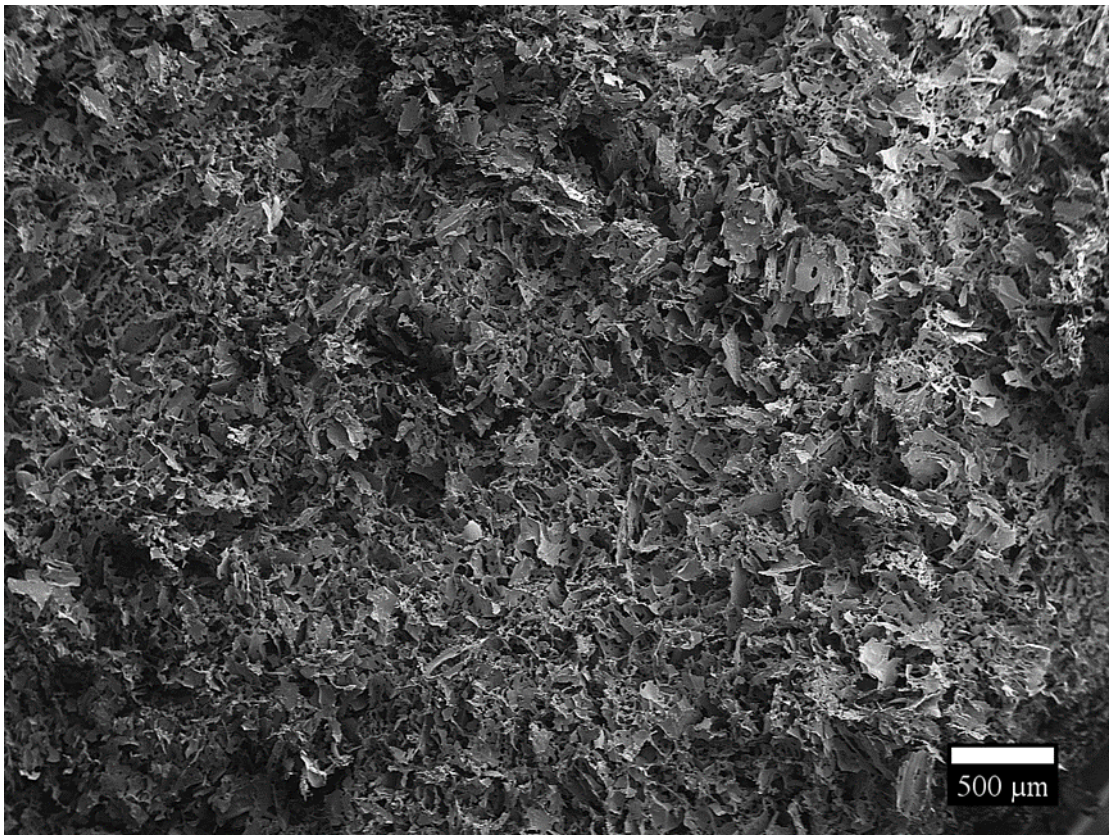

Figure 3.20: Representative SEM image of α-elastin, prepared by hydrolysing insoluble elastin completely using 0.25 M ethanedioc acid for 60 mins, five times repeatedly. The supernatants of each hydrolysis were collected and dialysed to obtain a purified solution. The solution was freeze-dried to reveal a fragmented structure.

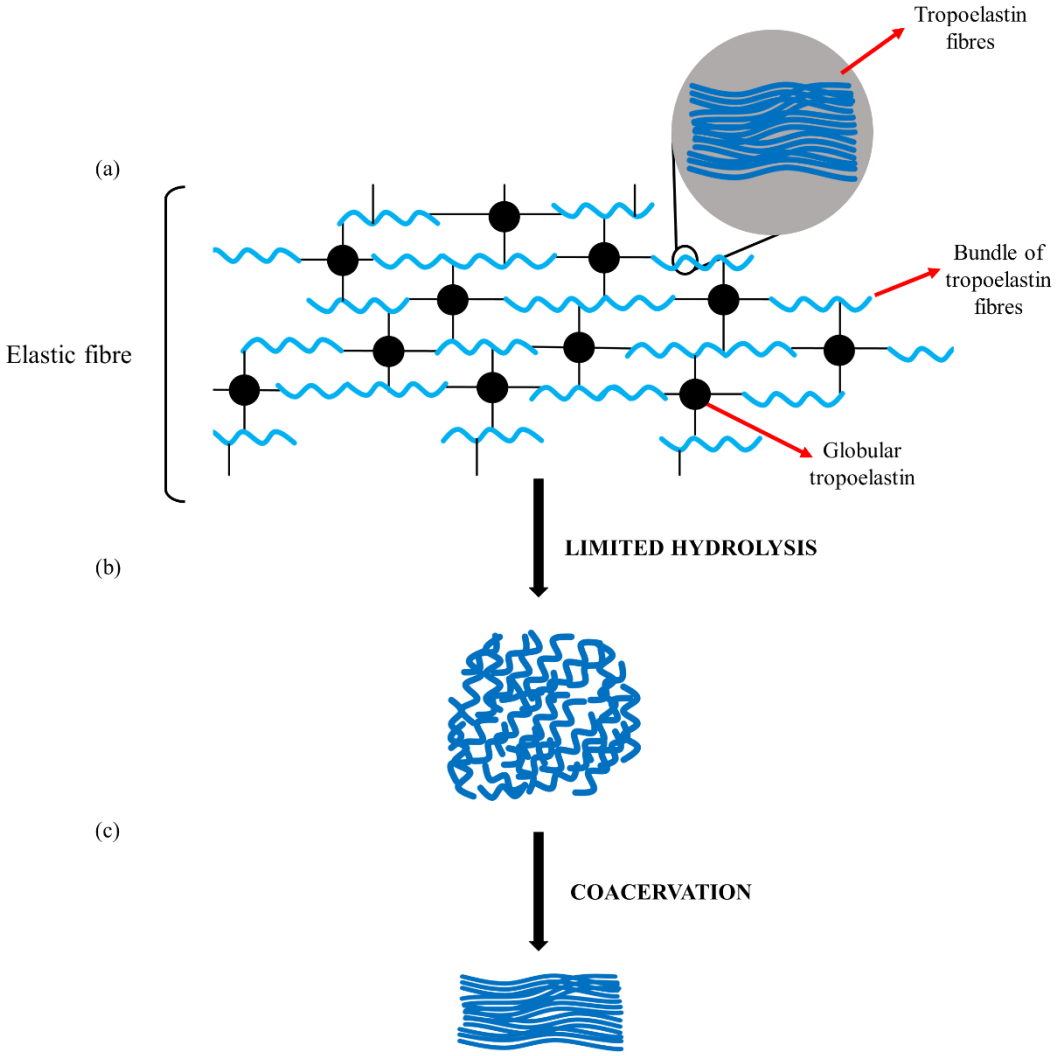

Figure 3.21: Proposed model for the structure of elastic fibres, composed of twisted bundles of fibres of tropoelastin (fibrillar domains) cross-linked by globular domains to form a 3D network (a). Limited hydrolysis of bundles of elastin fibres results in liberated fibres that aggregate into a gel (b) and self-assembly of fibres into bundles after coacervating the gel in physiological conditions (c).

3.4.2. Infrared Functionalisation of FEG

There was no significant shift in the infrared spectra to imply that IE denatured by hydrolysis which is consistent with the findings of previous studies for α-elastin [255], [270], [271]. The Amide I band for FEG showed a decrease in α-helices compared to IE, suggesting that the secondary structure of FEG is different to IE and that the hydrolysis process led to the loss of α-helices. α-helices account for cross-linking domains whereas the β- and unordered-structures form the hydrophobic domains responsible for the high extensibility of elastin [272]. Although the results suggest FEG has a predominantly β-sheet structure, this is due to the loss of α-helices rather than an increase in β-structures as the β-sheet content is not significantly different. The loss of α-helices can be explained by its lower stability and resistance to degradation compared to β-structures which has been shown experimentally [273]. Debelle *et al* deconvoluted the Amide I band and reported: 10% α-helices, 45% unordered-structures and 45% of β-structures (sheets and turns) for both IE (bovine) and soluble elastin (kappa) with no significant difference between the two forms [274]. Their results differ to those reported in this thesis as a significant decrease in the α-helix component was found after hydrolysis, this could imply that the method used by Debelle to isolate IE may have hydrolysed it and therefore a difference could not be observed as it is in close agreement with the structures observed in FEG (14% α-helices, 39% unordered-structures and 47% of β-structures).

The intramolecular β-structure observed at 1633-5cm^{-1} is representative of β-sheets which forms due to interactions within fibres [275]. For all forms of the elastin, except IE, an additional shoulder at 1618cm^{-1} was detected, this corresponds to intermolecular β-structures and is the result of interactions between fibres [256], [276]. Intermolecular

β-structures have not been reported for natural elastin (both insoluble and soluble forms), however, they have been identified as β-spirals (helical repeat of β-turns) in synthetic elastin-like-polypeptides (ELPs) at 1615cm^{-1} [277]. The study also suggested that traditional peak assignments for proteins were not applicable to ELPs due to their unique β-spiral structure and reported that a band at 1656cm^{-1} was associated with β-spirals as opposed to α-helices as commonly practised [278]. However, the presence of α-helices in elastin has been confirmed by techniques such as circular dichroism [271] as well as FT-IR [255]. Additionally, the band at 1618cm^{-1} was not observed in IE, therefore, it can be assumed that the additional peak is associated with intermolecular β-structures.

The Amide I band between 1613-21cm^{-1} has been associated with weak aggregation of β-structures [256], [279], [280]. It was also detected in the soluble elastin peptides produced after each hydrolysis (SE1-3) and showed higher intensity for samples hydrolysed for longer (SE3>SE2>SE1). The aggregation of proteins can be induced by heat as it promotes the unfolding of proteins [279], [281]. A mechanism for the formation of FEG by aggregation will be proposed in Section 3.4.5.

The Amide I band is most commonly used to study the secondary structure of proteins; however, it is more susceptible to environmental conditions [282]. The Amide III band (C-N stretching and N-H bending [283]) offers higher sensitivity and resolution, however, it has been studied less in comparison to the Amide I band. Both FEG and IE samples revealed two peaks for β-sheets after deconvolution. The bands at 1205cm^{-1} and 1229cm^{-1} can be correlated to the Amide I band at 1635cm^{-1} and therefore are representative of β-sheets [258]. Therefore, a possible explanation for the higher intensity at 1205cm^{-1} is that it is representative of intermolecular β-sheets in Amide III

as the band at 1618cm^{-1} was in Amide I. The shift of the Amide III band for FEG implies that its conformation is different to IE and that it has a higher concentration of intermolecular β-sheets due to interaction between fibres.

There was a decrease in all major absorption bands for FEG which implies that it has fewer polar residues compared to IE. The Amide A band (N-H bending [254]) was 1.8-fold larger for IE compared to FEG, suggesting that there was a decrease in N-H bonds due to the hydrolysis, this coincides with the increase in the Amide I band observed in SE1-3 (Fig.3.15). The AAA results agree with the findings of FT-IR as they suggest the hydrolysis cleaved amide bonds resulting in solubilisation of the polar residues, and the remaining insoluble component is composed of mostly hydrophobic residues. The limitation of the AAA is that the quantities of cross-linking residues could not be determined using this technique as the desmosine and isodesmosine residues were too large to run through the column.

The FT-IR and AAA results suggest that FEG has a predominantly β-sheet structure (39%) due to a loss of α-helices and therefore consists of fewer polar residues which form the cross-linking domains in elastin. The α-helices were hydrolysed and decreased from 23% to 14% in FEG leaving the hydrophobic, non-polar residues as proposed in Fig.3.22. The gel forms due to higher interaction between (intermolecular) and within (intramolecular) fibres (Fig.3.23).

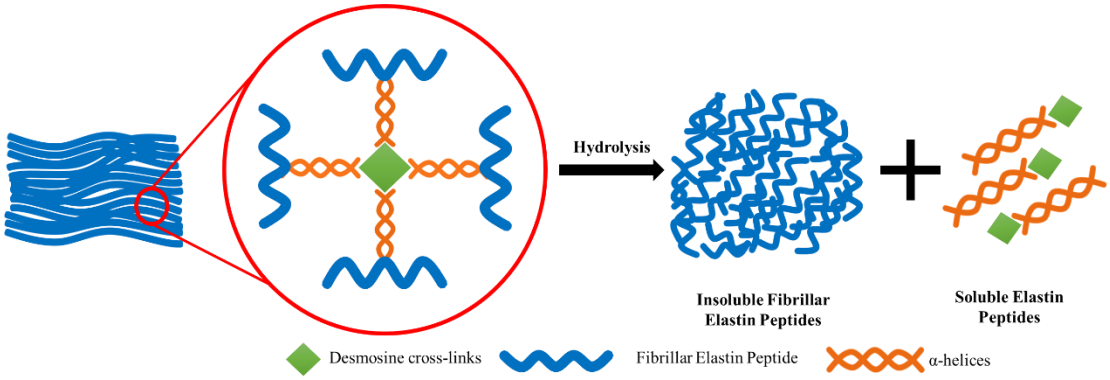

Figure 3.22: Limited hydrolysis of insoluble elastin results in the cleavage of amide bonds that form desmosine cross-links between bundles of elastin fibres. Upon cleavage, the bundles, which are predominantly β-structures, dissociate and aggregate by intermolecular interactions. The soluble supernatant is composed of the hydrophilic cross-linking domains which are rich in α-helices.

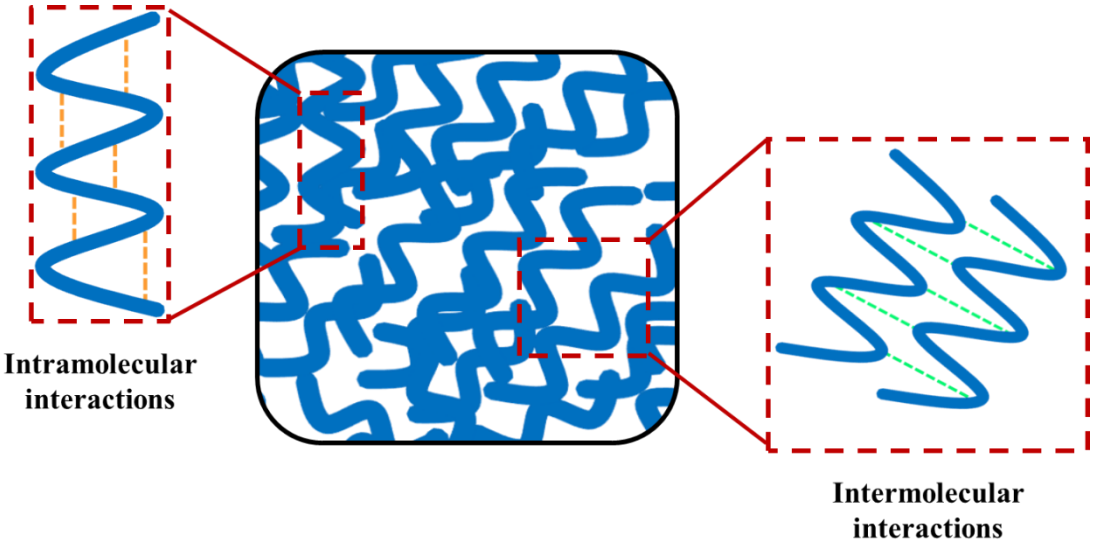

Figure 3.23: Intermolecular interactions between fibrillar elastin gel fibres which corresponds to the new shoulder at 1618cm^{-1} (Figure 3.16) and the intramolecular interactions within fibres which is assigned to the peak at 1634cm^{-1}.

3.4.3. Rheology of FEG

The purpose of conducting rheology was to confirm if the material isolated was a gel or a viscous liquid. It was found that FEG behaves as a gel as there was no crossover between G' and G'' and G'>G'' at all frequencies [284]. This suggests the rod-like fibres comprising FEG are interacting by some form of cohesive force, which in turn is preventing the fibres from moving freely, resulting in the formation of a 3D network. However, as the storage and loss modulus are dependent on frequency, the interaction type between the fibres is non-covalent and therefore intermolecular in nature, implying it is a "weak gel" [285]. The infrared and AAA results suggest that the intermolecular interaction may be hydrophobic in nature as the gel is composed of fibres which have an increased abundance of hydrophobic residues. This also agrees with the microstructural findings, as coacervation is a dominated by hydrophobic domains [286], [287].

The gradient of the log*(F)* vs log*(G')* was 0.06, indicating that the gel behaved similar to elastic solid as also implied by the low loss factor. The gel-like behaviour of FEG in comparison to α-elastin can be explained by its aspect (length to diameter) ratio. The elastic response observed is likely due to the aggregation of fibres. Aggregation occurs when the concentration of fibres is above a critical concentration where continuous contact can be achieved, and a 3D network can form. The number of contact points between fibres controls the probability of aggregation [288]. The contact between fibres is dependent on the concentration of fibres, the aspect ratio and electrostatic interactions which in turn have an effect on the viscosity of the system and subsequent viscoelastic properties [289]. Kerekes and Schell have defined a crowding factor, N_C, for fibre dispersions [290]. N_C can be determined using Equation

3.11, where ϕ, is the volume fraction of fibres; D, is the fibre diameter and L, is the fibre length.

$$Nc = \frac{2}{3}\phi\left(\frac{L}{D}\right)^2 \qquad \text{(Equation 3.11)}$$

N_C has been correlated to the rheological behaviour exhibited by fibre dispersions, where N_C<16 for fluid-like systems (dilute); N_C~30 for "weak" gels (semi-concentrated) and N_C>60 for strong gels (concentrated) [291].

As FEG exhibited a weak gel-like response (N_C~30), the length of the fibres comprising FEG can be determined using Equation 3.11. Assuming a density of 1g/cm^3 and using the diameter of FEG determined by SEM, L was estimated to be ~194μm. The aspect ratio of α-elastin solution can also be determined as preliminary rheological data confirmed its viscous liquid behaviour as it contains fewer cross-links (Fig.3.24). The length of α-elastin fibres was therefore estimated to be <110nm. These results imply the gel-like behaviour exhibited by FEG is associated with its higher aspect ratio (~39) which is due to its polymeric nature as shown by SEM (3.3.2.). The poor structural integrity of α-elastin can be explained by its 1.7-fold lower aspect ratio. Similarly, electrospun scaffolds composed of highly concentrated α-elastin (20%wt/v) fibres have an aspect ratio that is 3.5-fold lower than that of FEG [211], [216]. The aspect ratio is important when designing scaffolds as a smaller ratio limits the structural integrity and subsequent mechanical properties.

The complex shear modulus at 1.6 Hz (frequency of a resting heart [292]) was found to be 510Pa for FEG, this is significantly higher than that reported for uncross-linked coacervated ELPs (80Pa [293]) and comparable to ELPs cross-linked with tissue

transglutaminase (260Pa [213]) as shown in Table 3.13. Although, the concentrations of the ELPs were 13-fold and 4-fold higher, respectively, than FEG, and therefore are not directly comparable as the modulus is concentration dependent. A very important parameter for elastin is its high resilience (90% [42]) which it owes to its low energy loss when deformed. From Table 3.13 it can be seen that soluble forms of elastin have significantly lower resilience compared to FEG. This is significant as when designing scaffolds to emulate dynamic tissues such as heart valves, it is important to be able to incorporate materials that exhibit similar mechanical characteristics.

Table 3.13: Comparison of loss factor and associated resilience of elastin-based materials taken at 1.6Hz.

Material	Storage Modulus (Pa)	Loss Factor (no units)	Resilience (%)	Ref
Fibrillar Elastin Gel, 3%wt/v	510	0.1	53	This study
α-elastin, 5%wt/v	0.04	0.5	4	This study
ELPs, 324mg/ml	80	11.4	$7.8x10^{-30}$	[293]
ELPs, 100mg/ml (cross-linked)	260	0.2	28	[213]

Resilience (R) was determined using the relationship: $R=e^{-2\pi\delta}$ [41].

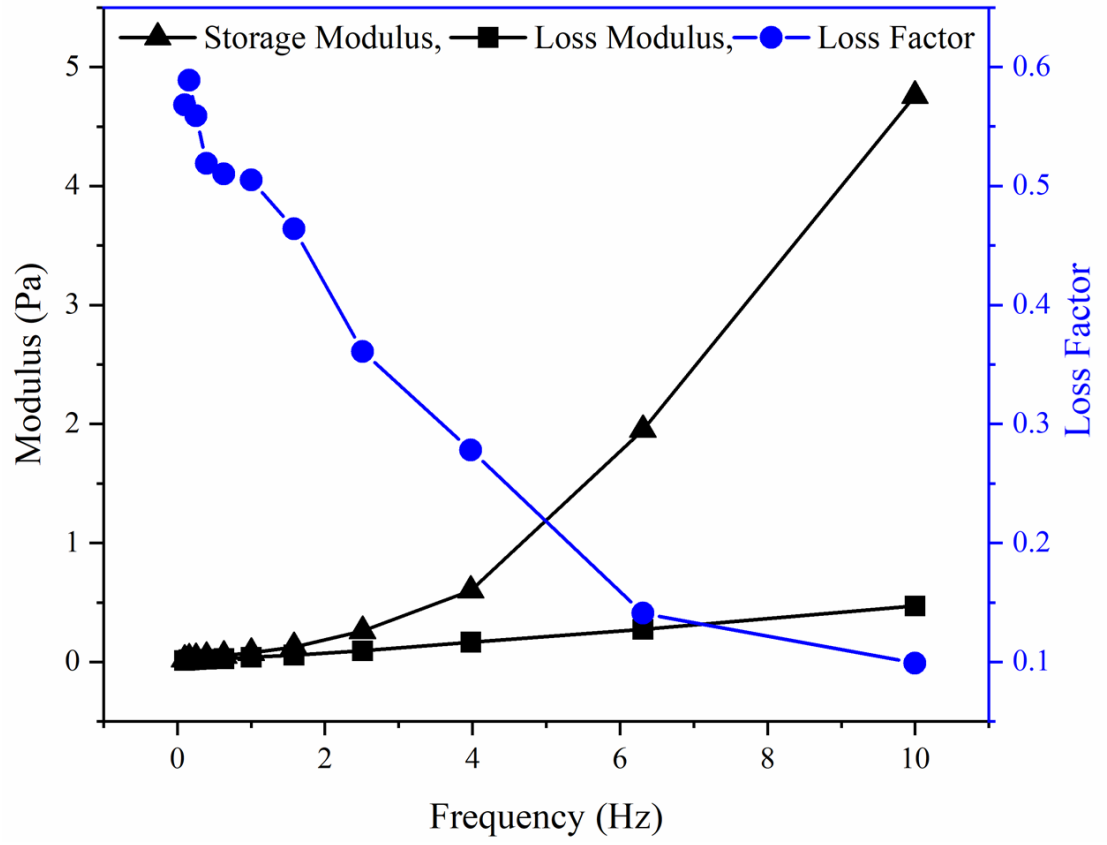

Figure 3.24: Viscoelastic properties of α-elastin solution (5%wt/v) including the storage and loss modulus and the corresponding loss factor. Properties were measured using rheometry at a frequency between 0.1-10 Hz, at room temperature and a constant strain of 1%, n=1.

The shear thinning properties of FEG occur due to the aligning of fibres with the direction of flow to reduce their effective surface area and therefore resistance to flow. This behaviour has been observed in ELP-based gels even at high concentrations [293]–[295]. The sharp decrease at low frequency (0-2Hz) and the absence of a low shear plateau is unusual. A similar trend was observed by Cirulis *et al*, [296] who associated this behaviour with the formation of flocs that appear as a "string of beads". Therefore, it can be suggested that the decrease in viscosity occurs due to aggregation of fibres in the direction of flow. The aggregation arises from the change in intermolecular interactions due to the excluded volume effect where the excluded

volume interaction dominates at equilibrium when the gel is in the swollen-state (electrostatic repulsion) and inter-fibrillar interactions (hydrophobic attraction) dominate as FEG changes to an aggregated-state with increase in frequency [294]. This phase transition will be discussed further in Section 3.4.4.

3.4.4. pH-Sensitivity of FEG

The precipitation of FEG observed when neutralised by salt (3.3.1) implied that intermolecular interactions play a role in the formation of FEG. Additionally, after dehydration (air-drying and freeze-drying), the rehydration of FEG using deionised-water or buffers did not yield a gel. Therefore, the effect of pH on the swelling characteristics of FEG was studied to understand the polymer-solvent interactions as the pH of a solvent affects the distribution of a protein's net charge.

A U-shaped, non-monotonic curve was observed for swelling as a function of pH (3.3.5) which suggests that FEG contains a similar concentration of positive and negative charges and is balanced at the minimum of the curve where the isoelectric point (pI) is reached. However, the highest water uptake was observed at pH of 2 which suggests FEG contains more basic groups as also implied by the AAA results. The pH dependent swelling observed due to change in charge suggests FEG is a weak polyampholyte (has a low charge density). Polyampholytic gels have no net charge near the pI, become cationic below the pI (pH<4 for FEG) and anionic above the pI (pH>10 for FEG), as the charge of the protein is positive or negative, respectively, as shown in Fig.3.25. The change in charge occurs due to protonation (below pI) or deprotonation (above pI) of the functional groups listed in Table 3.2. When pH>pI, the increase in negative charges due to ionisation of residues increases the hydrophilic

nature of FEG, this in turn gives rise to an osmotic pressure and the gel swells due to high electrostatic repulsion. Similarly, when pH<pI, the increase in the number of positive charges results in electrostatic repulsion and consequent increase in the degree of swelling.

The decrease in swelling at pH of 1 occurs as maximum ionisation is reached at pH of 2-3 and therefore no further swelling occurs below this range. The collapsing of FEG at pH of 1 can be explained by the shielding of the positively charged residues (NH_3^+) by excess Cl^- ions. The increase in ionic strength ($\geq 10^{-1}$M) of the swelling media causes the salt screening effect which reduces the electrostatic repulsion force and therefore swelling capacity of the gel [297], [298]. A plateau region is observed about the pI (4<pH<8), which is ~5.6 and in close agreement with that reported for α-elastin [247], [299]. The plateau region occurs as the pH inside FEG remains around ~pI whilst the pH of the solution changes as the total charge is stable at +13 (Fig.3.19), this is due to the higher concentration of fixed charges (oppositely ionised carboxyl and amino groups) in FEG compared to the concentration of mobile H^+ ions in the swelling media [300], [301].

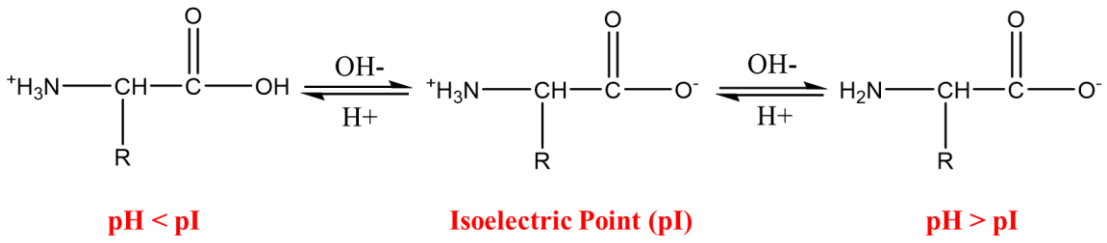

Figure 3.25: Polyampholytic behaviour of FEG where R is the functional group. Net charge of amino acids at the isoelectric point (pI) is zero, net charge is positive when pH<pI and negative when pH>pI.

The osmotic pressure difference between the gel and the solution is the driving force for swelling and develops due to the Donnan membrane effect as there is a lower chemical potential inside FEG compared to the swelling media [302]. The difference in the swelling phenomenon of FEG as a function of pH can be explained by the thermodynamics of swelling. The degree of swelling is dependent on three competing factors which affect the free energy of the system: (1) polymer-solvent interactions, (2) deformation of the gel upon exposure to the solvent and (3) the ionic contribution from the change in charge of the polymer [303], [304].

The total osmotic swelling pressure of a gel is controlled by the mixing, elastic and ionic contributions [305]. For amphoteric gels, the ionic contribution is assumed to dominate as it is ionisable by mobile ions present in the swelling media [304]. The ionic contribution is dependent on the difference between the concentration of mobile ions present in the gel and the solvent [305]. The increased water-uptake at low and high pH is associated with an increase in the ionisation of residues due to the increase in concentration of mobile ions in the solvent. This also increases the interaction between FEG (the polymer) and the solvent due to increased electrostatic repulsion between polar residues. Around the pI ($4<pH<7$), the osmotic pressure was the lowest due to electrostatic and hydrophobic attraction as shown in Fig.3.26. FEG collapses due to neutralisation of charges near the pI as it has a higher concentration of fixed charges compared to the solvent, this in turn results in a low osmotic pressure as mobile ions cannot exchange and therefore swelling is hydrophobically driven where the structure collapses due to aggregation of fibres [306].

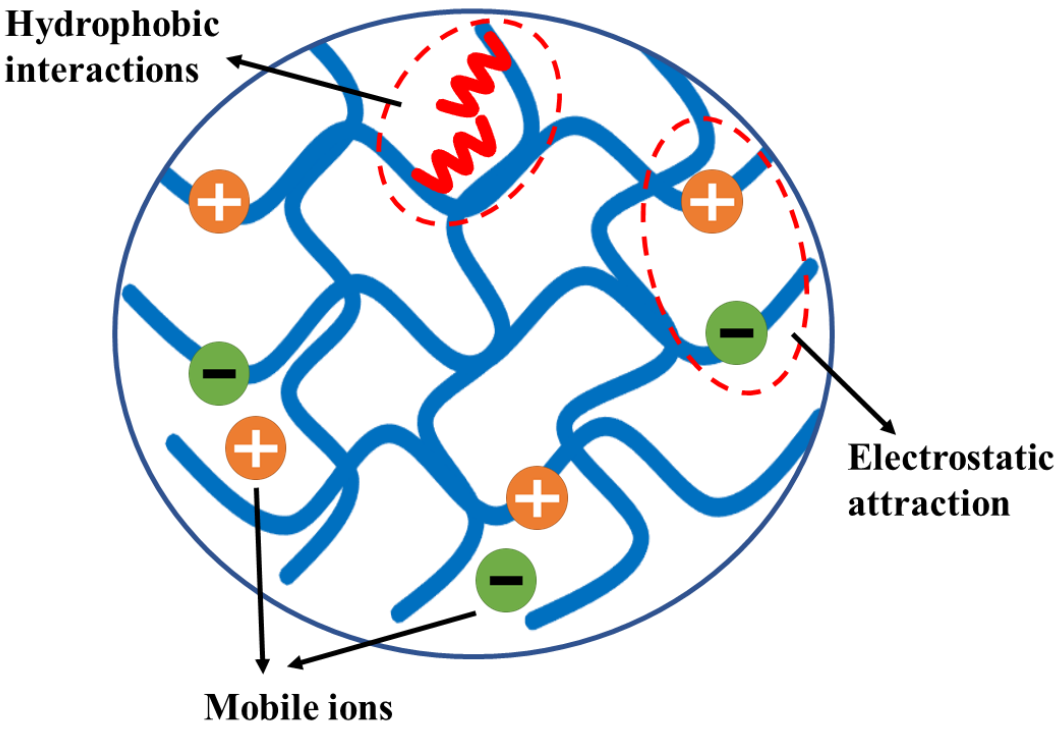

Figure 3.26: Simplified representation of intermolecular interactions existing in fibrillar elastin gel when pH~pI. Electrostatic attraction between ionised functional groups of polar amino acid residues and hydrophobic interaction between non-polar amino acid residues co-exist.

The swelling response can be explained by the change in intermolecular forces with pH due to the change in interaction free energy (ΔF). Fig.3.27 illustrates the ΔF as a function of pH. It can be seen that electrostatic interactions (hydrophobic attraction) are favourable when the net charge density is low (near the pI) whereas repulsion between positively charged residues (low pH) and negatively charged residues (high pH) results in high free energy making it thermodynamically unfavourable to interact and therefore leads to electrostatic repulsion.

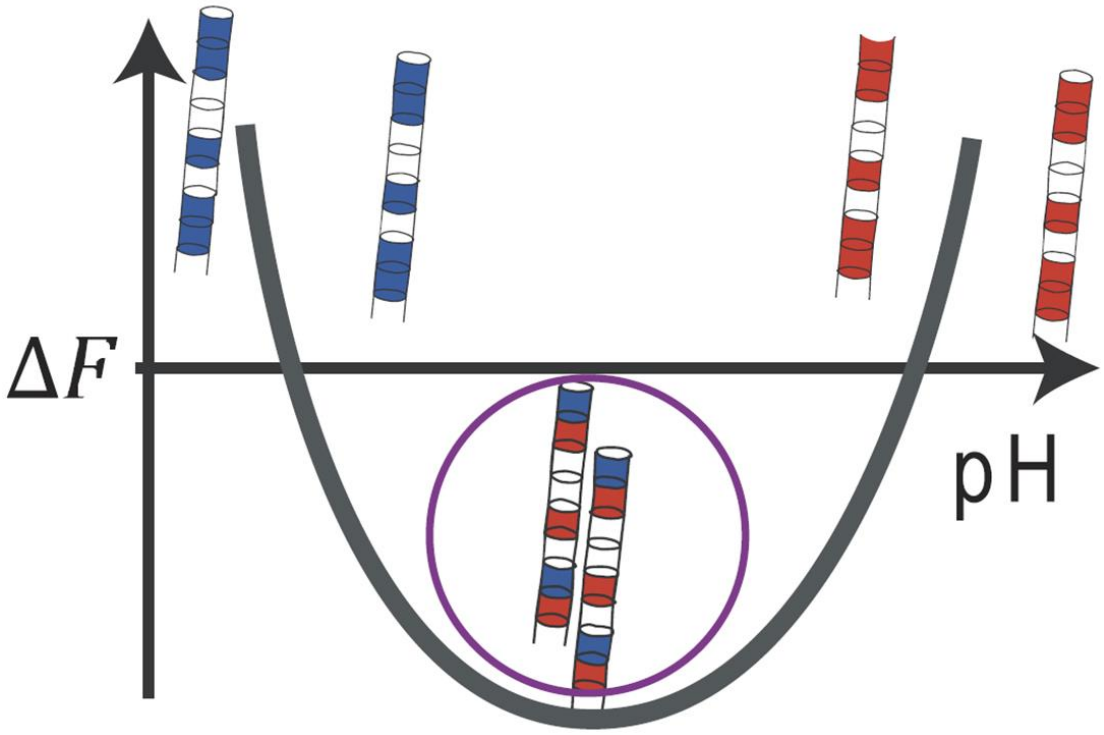

Figure 3.27: Interaction free energy as a function of pH for collagen fibres. Diagram shows an increase in interaction energy being associated with an increase repulsion, at low pH this is due to charging of amine groups (blue) and at high pH it is due to charging of carboxyl groups (red). Near the isoelectric point, charges are balanced and therefore the free energy is low enough to allow fibre aggregation by interaction between charged groups [307].

The change in intermolecular interactions results in different volumetric phases at different pH due to the chemical composition of elastin. A collapsed phase was observed when pH~pI (4<pH<7) and a highly swollen phase at low (<4) and high (>10) pH. In the collapsed state, gels are expected to be denser and stiffer whereas they are softer in the swollen state [308]. Electrostatic and hydrophobic attraction form physical cross-links when pH~pI (Fig.3.26). The increase in cross-linking density is associated with a higher osmotic shear moduli, G, which can be predicted from the equilibrium swelling data using the relationship: $G=Q_m^n$ where *n* is a constant that is dependent on the thermodynamic quality of the solvent, it is -2.3 or -3.0 for a good or

theta solvent, respectively [309]–[311]. Fig.3.28 presents the predicted results with the change in volume fraction as a function of pH. A bell-shaped curve with a maximum at the pI of FEG was observed for both types of solvents. Volume fraction has been experimentally shown to be low for good solvents and high for poor solvents [303]. This agrees with the findings of this thesis as when at low and high pH where the highest swelling occurred due to electrostatic repulsion, the gel was most hydrophilic, and the interaction between FEG and the solvent was strongest (Fig.3.29). Whereas when pH~pI, the water-uptake was lowest due to stronger protein-protein interactions and therefore reduced interaction between FEG and the solvent resulting in phase separation and contraction (Fig.3.29) [312]. A collapsed globular structure forms at the pI due to rearrangement of FEG to an aggregated state as the electrostatic attraction increases and FEG becomes more hydrophobic and contracts to reduce the effective surface area by associating with neighbouring fibres [313]. Expansion occurs when FEG transitions to a relaxed rubbery state and extends due to repulsion between molecules [314]–[316].

Although, the gel was soft and challenging to handle at 2<pH<3, complete solubilisation did not occur. Dissolution is prevented by the elastic-refractive forces of polymer chains which resist the mixing contribution. It was found that blending of FEG in the acidic swelling media was required to overcome these forces and form a homogenous gel-like dispersion. This section shows how FEG can be re-solubilised to give a similar water uptake ratio to that of the original gel (2320-2600% vs 3490%) when swollen at 2<pH<3. The re-solubilisation of FEG after drying is important as the gel-like suspension can be used as a structural material to design constructs that exhibit desirable properties of elastin.

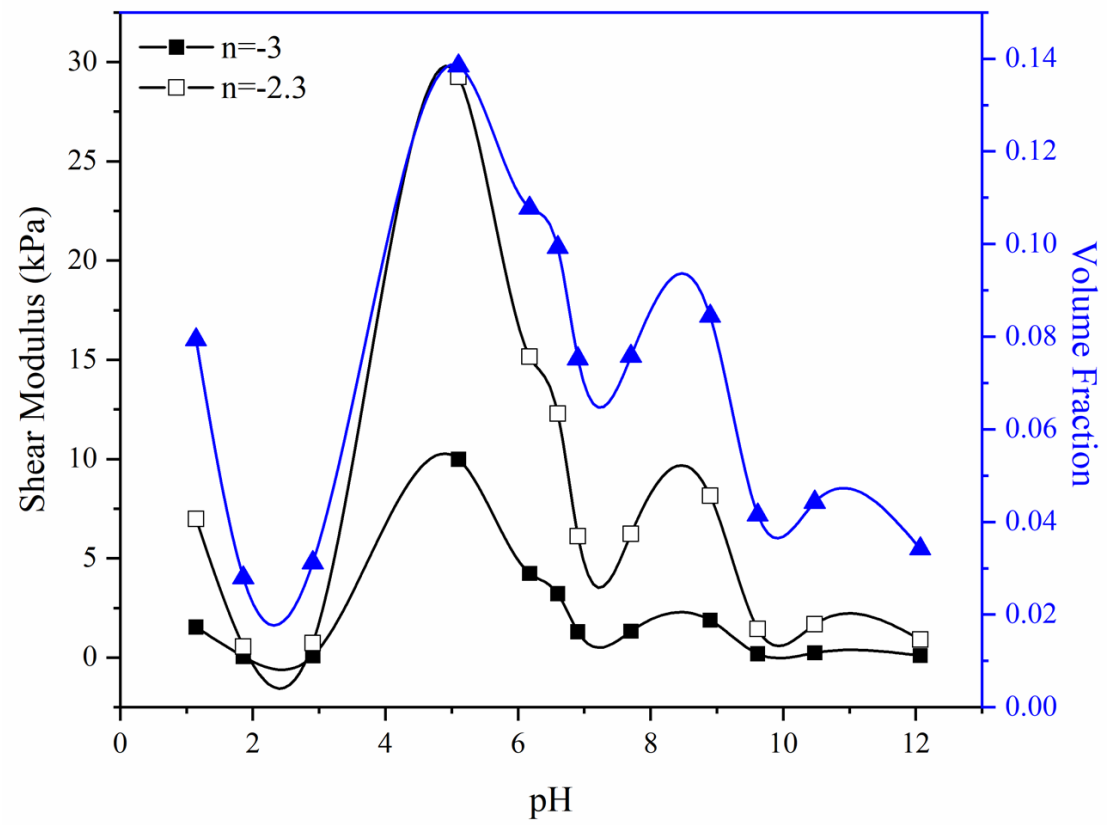

Figure 3.28: Predicted shear moduli (G) and volume fraction (V) of freeze-dried fibrillar elastin gel as a function of the pH of swelling media. G was determined using the relationship $G=Qm^n$, where Qm is the equilibrium swelling ratio (determined by Equation 3.7) and n is a constant dependent on the quality of the solvent. V was obtained using the relationship V=1/Qv where Qv is the volumetric swelling and was determined using the relationship 1+(Qm)(ρpol/ρsol) where ρpol was the density of elastin, taken as 1.33 g/cm^3 [260] and the density of the solvent, ρsol which was assumed to be 1 g/cm3 (water-based solvent) [317].

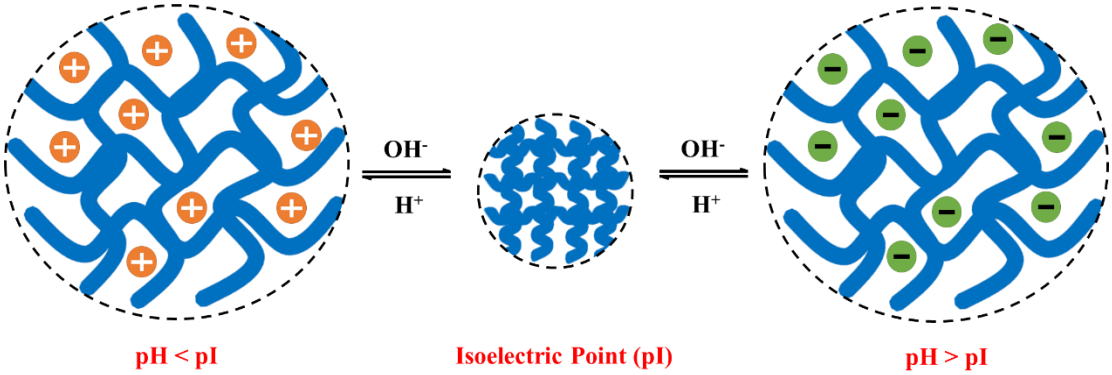

Figure 3.29: Shift in volumetric phases at different pH. Expansion of the gel occurs due to swelling in acidic (pH<4) and basic (pH>9) solutions where electrostatic repulsion dominates due to increase in positive (pH<pI) or negative charges (pH>pI), respectively. Whereas contraction occurs at a plateau region where pH~pI (4<pH<9) and electrostatic and hydrophobic attraction are dominant.

3.4.5. Mechanism of Gelation

The limited hydrolysis applied in this thesis forms an aggregated form of elastin which is intermediate to insoluble (protein) and soluble (polypeptide) forms of elastin (Fig.3.30). Rheology confirmed the isolation of a gel which is composed of polymeric fibres (SEM and LSCM) that have a predominantly β-sheet structure due to the loss of α-helices (FT-IR).

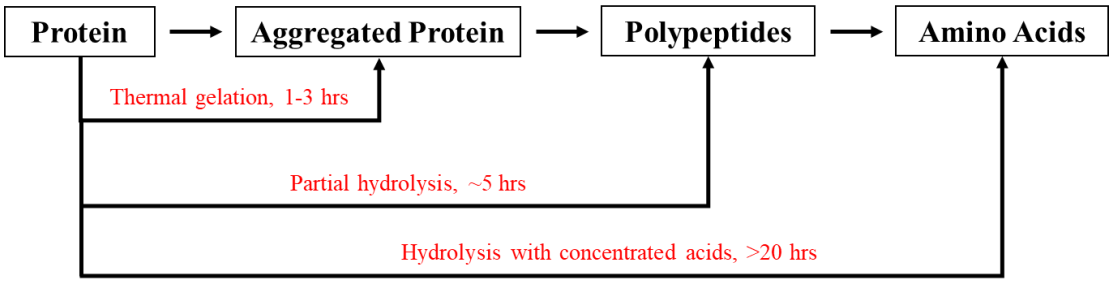

Figure 3.30: The hydrolysis of proteins into an aggregated protein, polypeptides, or amino acids. Denaturation with short reaction time forms an aggregated protein, repeated refluxing in weak organic acids forms polypeptides and complete hydrolysis in strong acids after prolonged periods results in complete degradation into amino acids.

Processing conditions involved in the gelation of FEG include a high temperature (100°C) and a low pH (~0.5<pI). The results discussed in 3.4.1-3.4.5 suggest that upon heating, the bundles of fibres unfold (dissociate) and aggregate (re-arrange) to form a gel. The loss of α-helices promotes the formation of intermolecular β-sheets between the remaining hydrophobic residues due to their exposure upon the hydrolysis of cross-links, as these residues would otherwise be buried as hydrophobic cores. FEG is isolated in the collapsed state as a dense pellet (Fig.3.4), this is due to the high ionic strength of residual oxalate ions ($C_2O_4^{-2}$) which have a charge screening effect as observed for FEG at pH of 1 (3.4.4). In this state, FEG is highly hydrophobic and aggregates due to strong protein-protein interactions. The gel-like form of FEG (Fig.3.5a) is obtained after purification by repeatedly washing with water (avoiding contact with salts). FEG swells as excess ions are removed and the ionic strength is reduced (diluted), this gives rise to electrostatic repulsion and consequently improved solubility (protein-solvent interaction) due to a total positive charge at low pH (2-3) (Fig.3.20). The proposed mechanism for gelation of FEG has been summarised in Fig.3.31.

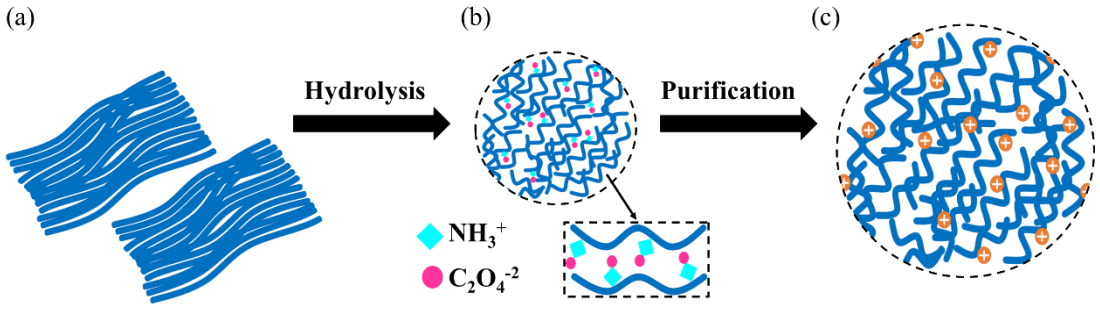

Figure 3.31: Mechanism for limited hydrolysis of insoluble elastin. Process involves (a) the unfolding of bundles of fibres by the application of a high temperature (100°C) and low pH (<pI). (b) The formation of a collapsed gel due to high ionic strength and charge screening of FEG molecules, where protein-protein interactions dominate, and aggregation occurs due to its hydrophobicity. (c) The purification of the collapsed gel results in dilution of the ionic strength and formation of a swollen cationic gel due to an increase in electrostatic repulsion between positively charged FEG molecules.

This phenomenon has been observed in globular proteins such as β-lactoglobulin which have been shown to produce fine-stranded gels after loss of part of their secondary structure [280], [318]–[320]. The appearance of an intermolecular β-sheet structure has also been observed by FT-IR for such proteins due to aggregation after heat-induced unfolding [279]–[281]. The unfolding of elastin is temperature dependent as it must be high enough to dissociate the bundles of fibres. Once unfolded, gelation is dependent on the rate of aggregation of fibres (determined by the strength of electrostatic and hydrophobic interactions) and the critical concentration required for fibres to form intermolecular interactions, in this case 3%wt/v was sufficient [321].

There are multiple factors (temperature, pH, ionic strength, protein concentration, and salt concentration) [319], [322] which affect the aggregation of a protein and can be used to determine the rate of hydrolysis and aggregation, however, this was not the aim of this thesis and therefore was not studied further. To the best of the author's knowledge, this is the first elastin gel to be isolated by limited hydrolysis. The isolation

of an elastin gel by elastase has been reported [323], however, it has not been characterised as a material or explored as a biomaterial to date, possibly due to the expensive enzymatic degradation process involved.

3.5. Summary

This chapter presented a method to isolate a novel form of elastin (FEG) by limited hydrolysis and its characterisation as a material. The main findings include:

- The microstructure of FEG showed rod-like fibres that are akin to polymeric elastin as they have a diameter between 4-6μm and therefore exhibit better structural integrity than soluble forms. These fibres displayed self-assembly which is a characteristic of monomeric elastin. These findings suggested that FEG is an intermediate material with properties that coincide with both polymeric and monomeric elastin.
- FT-IR revealed hydrolysis led to a loss of α-helices and the appearance of a new shoulder at 1618cm^{-1} which is characteristic of intermolecular β-sheets. These structures are associated with globular proteins that exhibit aggregation upon thermal gelation due to improved interaction between fibres.
- Rheological characterisation confirmed that FEG is a gel by the absence of any cross-over between G' and G''. It was also found that the mechanical properties of FEG are suitable for application as a biomaterial due to its low loss factor (0.1) which mimics the properties of natural elastin more closely than synthetic variants.
- FEG is polyampholytic and has a pI of 5.6. It was found to have good polymer-solvent interactions (high water-uptake) in the ionised state at pH's of 2.7 and

12.1 where electrostatic repulsion dominates. The improved solubility of FEG in these conditions can be employed to fabricate constructs as will be discussed in the following chapter.

4

Fabrication & Physicochemical Properties of Scaffolds

4.1. Introduction

This chapter studied the fabrication of fibrillar elastin gel (FEG)-based scaffolds by freeze-casting. Freeze-casting is a conventional fabrication technique that is extensively employed to obtain highly porous interconnected networks. The effect of processing parameters such as the concentration, freezing temperature and composition on the microstructure of scaffolds will be studied. The swelling and degradation characteristics of FEG will also be studied to understand its behaviour in hydrated environments. In particular, the effect of temperature, cross-linking and the presence of salt will be assessed to explain the behaviour of FEG in the wet-state.

4.2. Materials & Methods

4.2.1. Fabrication of Scaffolds

4.2.1.1. Fibrillar Elastin Gel (FEG)-Based Scaffolds

FEG was isolated from insoluble elastin powder as described in section 3.2.1. The gel (3% wt/v) obtained after purification was directly cast in polytetrafluoroethylene (PTFE) moulds using a syringe, frozen at -20°C or -80°C and freeze-dried to obtain FEG based scaffolds. Compositions of 0.5% and 1.0%wt/v were prepared by diluting the gel using acidified deionised water at pH of 2.7 using ethanoic acid. The mixture was stirred magnetically for 10 mins to homogenise the solution and then degassed using a vacuum pump at 10 Pa to remove air-bubbles. The solutions were then cast in PTFE moulds as described above to obtain freeze-dried scaffolds.

4.2.1.2. Collagen-Based Scaffolds

1% wt/v collagen suspension was prepared by adding collagen type I powder from bovine Achilles tendon (Sigma Aldrich, UK) to acidified deionised water. Deionised water was adjusted to pH of 3.2 by adding a few drops of ethanoic acid (Thermo Fisher Scientific, U.K.). The collagen-acid mixture was stirred magnetically for 15 mins before being placed in an ice bath and blended using a handheld blender (Breville, 1HB086, UK). The suspension was centrifuged (Thermo, IEC CL10, UK) at room temperature for 5 mins at 3000 rpm to remove entrapped air bubbles. The suspension was casted directly into moulds using a syringe, frozen at -20°C and freeze-dried as above to yield 100% collagen (100C) scaffolds.

Composite suspensions containing coll and FEG were prepared with concentrations as listed in Table 4.1. FEG isolated in section 3.2.1. was freeze-dried for these scaffolds and rehydrated as follows. Collagen type I and freeze-dried FEG were added to acidic deionised water adjusted to pH of 2.7 by adding ethanoic acid as above. The dry collagen and FEG was added to the acidic water and stirred for 15 mins on a stirring plate.

Table 4.1: Compositions of collagen-FEG composites with a total density of 1%wt/v

Composition	Abbreviation	Collagen (mg/ml)	FEG (mg/ml)
100% collagen-0% FEG	100C	10.0	0.0
75% collagen- 25% FEG	75C-25E	7.5	2.5
50% collagen- 50% FEG	50C-50E	5.0	5.0
25% collagen - 75% FEG	25C-75E	2.5	7.5

4.2.1.3. Collagen- Hyaluronic Acid Based Scaffolds

Collagen-hyaluronic acid (coll-HA) based scaffolds were prepared as described by Nazir et al [191]. A 0.4 %wt/v solution was prepared by adding sodium hyaluronate (22 kDa, Thermo Fisher Scientific, UK) to deionised water whilst stirring on a plate at room temperature. The HA was allowed to mix completely for 20 mins before adding 0.4 M adipic acid dihydrazide (ADH, Sigma Aldrich, UK). Once completely dissolved in the solution, the pH was adjusted to 4.80 using 0.1 M HCl. 20 mM 1-(3-Dimethylaminopropyl)-3-ethylcarbodiimide hydrochloride (EDC, Fluorochem, UK) was added to the solution. At this point freeze-dried collagen scaffolds prepared as described in section 4.2.1.2 were added to the HA-cross-linker solution too. The scaffolds were left in the solution for 24 hrs. The solution was neutralised with 0.1 M NaOH after 24 hrs and the scaffolds were washed in deionised water. Scaffolds were removed and placed in fresh deionised water every 30 mins, five times in total. After washing, the scaffolds were placed in PTFE moulds with deionised water to maintain the shape. The moulds were then placed in the freezer overnight at – 20°C and freeze-dried again the following day for 24 hrs. Pure HA samples were prepared as follows. The HA-cross-linker solution was neutralised with NaOH as above and transferred to a dialysis tube with a molecular weight cut off of 14, 000 g/mol (Sigma Aldrich, UK). The mixture was dialysed against 150 mM NaCl for 24rs and then deionised water for a further 24 hrs. After dialysis the mixture was poured into PTFE moulds, frozen overnight and freeze-dried as above.

4.2.1.4. Tri-layer Scaffolds

Tri-layer scaffolds were composed of one layer of 100C, one layer of coll-HA composite and one layer of coll-FEG composite. The steps involved in assembly of

tri-layers is illustrated in Fig.4.1. To construct the tri-layer, suspensions of 100Cand 50C-50E suspensions were prepared as described in section 4.2.1.2 and stored at 4°C until required. COL-HA composites were prepared as described in section 4.2.1.3, except the collagen scaffolds used were one third of the size of the original scaffolds to account for only the middle layer. After 24 hrs of cross-linking and washing, COL-HA scaffolds were not frozen and freeze-dried, instead they were removed from the water and dried on a metallic mesh for 5 mins. To assemble the tri-layers, first 1 ml of 100C solution was added to the mould using a syringe and spread out using a spatula to coat the mould evenly, the COL-HA scaffolds was placed on top of the 100C layer, and finally the 50C-50E was added as the final layer and spread out evenly. The scaffolds were then placed in the freezer at -20°C overnight and freeze-dried the following day for 24 hrs.

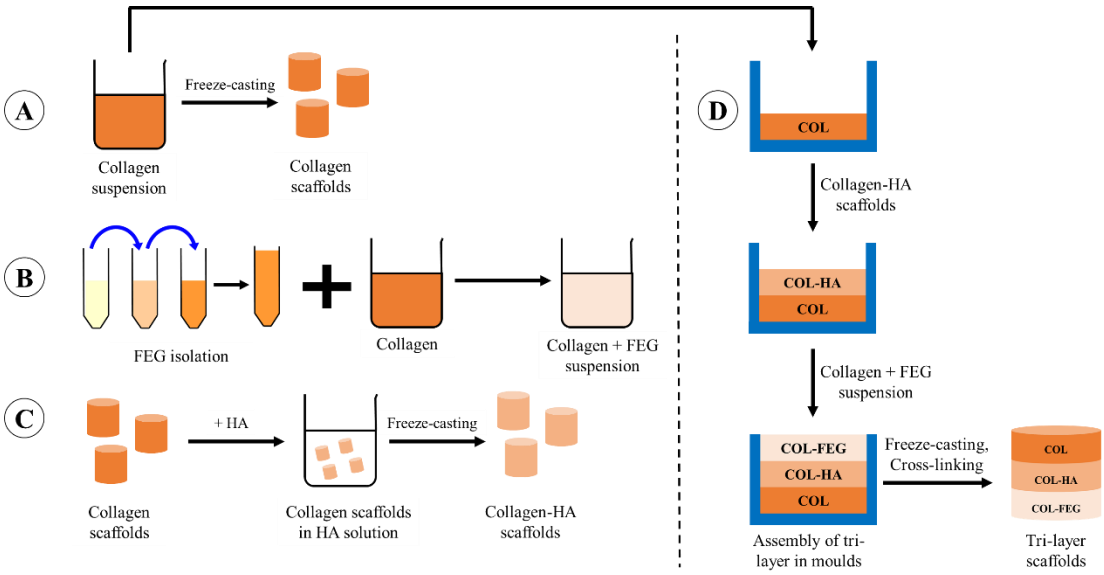

Figure 4.1: Multi-step process involved in the assembly of the tri-layer scaffolds proposed in this study. Collagen (COL) forms the base of all three layers and therefore is prepared first as described in 4.2.1.2. Half the suspension is stored in the fridge whilst the other half is used to fabricate COL only scaffolds by freeze-casting at -20°C (A). Fibrillar Elastin Gel (FEG) was then isolated as described in 3.2.1. and used to prepare a COL-FEG suspension as described in 4.2.1.2. (B). The suspension is stored in the fridge whilst COL-HA scaffolds are prepared. The freeze-dried COL scaffolds are added to hyaluronic acid (HA) solution as described in 4.2.1.3. without the addition of a freeze-drying step (C). Once preparation of all three components is complete, they are assembled in a mould as follows: A layer of COL suspension is added to the mould using a syringe, the COL-HA scaffold is placed above the suspension and the COL-FEG suspension is added above. The composite is frozen and freeze-dried as described in 4.3.1.4. and cross-linked as described in 4.2.1.5. to give a composite tri-layer (D).

4.2.1.5. Cross-linking

All scaffolds except coll-HA based composites were cross-linked as follows. 75% ethanol solution was prepared using ethanol (Sigma Aldrich, UK) and deionised water. 60mM EDC and 30mM N-Hydroxysuccinimide (NHS, Sigma Aldrich, UK) were added to the solution and the pH was adjusted to 4.80 using 0.1M HCl. Freeze-dried scaffolds (FEG based scaffolds from section 4.2.1.1, collagen-based scaffolds from section 4.2.1.2 and tri-layer scaffolds from section 4.2.1.4) were washed in 100% ethanol for 10 mins to remove residual acid. The scaffolds were transferred to the

cross-linking solution and left to stir for 2 hrs at room temperature. After 2 hrs, the samples were washed in deionised water, replacing the water every 30 mins, five times in total. The samples were placed in their moulds with deionised water, frozen overnight at -20°C and freeze-dried for 24hrs.

Scaffolds of multiple shapes and sizes were produced throughout this thesis as listed in Table 4.2.

Table 4.2: Scaffold dimensions for each experiment conducted.

Experiment		Sample Size
Physicochemical	SEM, LSCM, FT-IR	12 mm x 10 mm, sliced transversely to 1 mm in thickness
	Swelling, Degradation	7 mm diameter x 16 mm thickness
Mechanical	Compression	12 mm x 10 mm
	Tensile	10mm x 4mm x 2mm (FEG-only) 20 mm x 6 mm x 3mm
	Rheology	100 mm x 15 mm, reduced to 25 mm discs using a punch
	Self- Deflection	40 mm x 8 mm x 4 mm
Biological	Cell attachment, cell viability, qPCR, DNA quantification and imaging	12 mm x 10 mm, sliced transversely (4 mm thick) and reduced to 8 mm discs with a punch
	Mechanical test at day 14	20 mm x 6 mm x 3mm

4.2.2. Scanning Electron Microscopy (SEM)

The microstructure of all scaffolds and the morphology of pores was studied using SEM. Cylindrical samples were sliced into transverse sections using a razor blade. They were adhered to aluminium stubs using carbon tab and coated as described in section 3.2.3. Images were analysed on ImageJ to determine the pore size (diameter of pores) distribution, assuming they were elliptical. Distributions were truncated by

limiting the area to 3000- infinity. Surface porosity was determined by analysing the area fraction of voids to pore walls on ImageJ.

Total porosity of scaffolds was determined using the dimensions and mass of the scaffold as follows. The dimensions (diameter and height) of all scaffolds of interest were measured using a digital caliper (Mitutoyo™, CD-6"CSX, Japan), and the mass was measured using a balance (Mettler Toledo™, AB204, UK). The density of each scaffold, $\rho_{scaffold}$, was determined using Equation 4.1. Porosity was determined using Equation 4.2 where the density of the material, $\rho_{material,}$ is either 1.35 g/cm^3 for collagen [324], 1.33 g/cm^3 for elastin [260] or 1.23 g/cm^3 for hyaluronic acid [325].

$$\rho_{scaffold} = \frac{\text{mass (g)}}{\text{volume (cm}^3\text{)}} \quad \text{(Equation 4.1)}$$

$$\text{Porosity} = 1 - \frac{\rho_{scaffold}}{\rho_{material}} \quad \text{(Equation 4.2)}$$

4.2.3. Laser Scanning Confocal Microscopy (LSCM)

LSCM was used to understand the distribution of collagen and FEG fibres in non-seeded composite scaffolds in the hydrated state. Scaffolds were sliced with a razor blade and 8 mm discs were punched to fit a 96 well plate for staining. Blocking buffer (DPBS + 1% Bovine Serum Albumin + 0.05% Triton X-100) was added to the samples to reduce background from the samples and left for 1 hr at room temperature. The samples were incubated with 50 µL diluted (1:500) rabbit anti-collagen I antibody (Abcam, UK, ab34710) for 48 hrs at 4 °C. The samples were washed again with DPBS at least three times, incubated with 50 µL diluted (1:500) goat anti-rabbit, Alexa Fluor 647 (Thermo Fisher Scientific, UK) for 48 hours at 4 °C, samples were left in the dark during this period. All samples were washed in DPBS and stored at 4°C as they were

until required for imaging. Z-stack images were taken using the Olympus Fluoview FV1000 Confocal Microscope as mentioned in section 3.2.2. Collagen was excited at 647nm as it was the only wavelength where the autofluorescence of elastin was not observed. All post-imaging processing was carried out on ImageJ.

4.2.4. Rheology of Suspensions

Collagen-based suspensions prepared in section 4.2.1.2. were tested before freeze-drying and then after as cross-linked scaffolds. The suspensions were tested as described in section 3.2.6 for FEG.

4.2.5. Fourier Transform Infrared Spectroscopy (FTIR)

FT-IR was performed on FEG-based scaffolds, collagen-based scaffolds, and coll-HA composites to understand the effect of cross-linking on functional groups. Samples were tested as described in section 3.2.4. The second derivative was performed on Origin after normalising the spectrum for the C-H group as this bond is not affected by the cross-linking procedure.

4.2.6. Swelling

The water uptake ratio (Q_m) was determined for all FEG based and collagen-based samples by comparing the increase in mass to the original mass of the dry sample as shown in Equation 4.4. Samples had an original mass of 10 mg samples and dimensions as stated in Table 4.2. All samples were tested in PBS for 24 hrs at room temperature. PBS was chosen as a solvent for swelling as it simulates physiological conditions in terms of osmolarity and ion concentrations. The effect of temperature was studied for FEG-based scaffolds only where uncross-linked and cross-linked

samples were studied in PBS and deionised water for 24 hours at temperatures of 4, 20 and 37 °C.

$$Q_m = \frac{mass_{wet} - mass_{dry}}{mass_{dry}} \quad \text{(Equation 4.3)}$$

Theoretical volumetric swelling ratio (Q_v) was also determined using the relationship where ρ_p and ρ_s are the densities of the polymer and solvent, respectively (1g/cm^3 for water):

$$Q_v = 1 + \frac{\rho_p}{\rho_s}(Q_m) \quad \text{(Equation 4.4)}$$

The swelling data was used to determine the polymer-solvent interaction parameter (χ) using the following simplified Flory Huggins theory [326], [327]:

$$\chi = \frac{\ln(1 - v_{2m}) + v_{2m}}{v_{2m}^2} \quad \text{(Equation 4.5)}$$

where v_{2m} is the volume fraction which was obtained by taking the reciprocal of Q_v.

The molecular weight between cross-links (M_c) was determined using the following relationship [328], [329]:

$$M_c = \frac{V_1}{v} \times \left(\frac{1}{2} - \chi\right) \times (Q_V)^{\frac{5}{3}} \quad \text{(Equation 4.6)}$$

where V_1 is the molar volume of the solvent (18 mol/cm^3), v is the specific volume of the dry polymer (0.741cm^3/g for collagen and 0.752cm^3/g for elastin). The effective cross-link density (v_e) was determined using [328], [329]:

$$v_e = \frac{\rho_p}{M_c} \quad \text{(Equation 4.7)}$$

Q_v was determined experimentally for uncross-linked FEG scaffolds and cross-linked collagen-based scaffolds by comparing the increase in volume to the original volume of the dry sample as shown in Equation 4.5. Samples were studied in deionised water for 24 hours at 4, 20 and 37°C.

$$Q_v = \frac{\text{volume}_{wet} - \text{volume}_{original}}{\text{volume}_{original}} \qquad \text{(Equation 4.8)}$$

The volumetric coefficient of expansion was determined for all uncross-linked FEG using Equation 4.6, where ΔV is the change in volume, V_0 is the original volume, α is the volumetric temperature expansion coefficient and ΔT is the change in temperature.

$$\Delta V = V_o \alpha \Delta T \qquad \text{(Equation 4.9)}$$

4.2.7. Degradation

Non-enzymatic and enzymatic degradation was studied for uncross-linked and cross-linked FEG-based scaffolds and cross-linked collagen-based scaffolds. Samples were prepared as discussed in section 4.2.1, the mass of samples were recorded over either a 24-hr period (collagen-based scaffolds) or a 12-day period (uncross-linked and cross-linked FEG based scaffolds). For collagen- based scaffolds, the samples were immersed in PBS with 0.2 mg/ml sodium azide (Sigma Aldrich, UK) overnight and left in a platform shaker (Jeio Tech BS-31, Medline Scientific, U.K.) to agitate mildly at 37 °C. The samples were removed the following day and drained for 1 min on a metallic mesh, the mass was recorded and taken as the original mass at 0 hrs ($mass_0$). The sample was then either placed in PBS with 0.2 mg/ml sodium azide only (control), 0.1 U/ml collagenase from Clostridium histolyticum (Sigma Aldrich, UK) in PBS with 0.2 mg/ml sodium azide or 0.1 U/ml elastase from porcine pancreas (Sigma Aldrich, UK) in PBS with 0.2 mg/ml sodium azide. The samples were removed at intervals (2

hrs, 6 hrs, 12 hrs and 24 hrs), allowed to drain as above and measured for the new mass ($mass_x$) to determine the mass loss using Equation 4.3.

For FEG-based scaffolds, the original samples were all dry and the same samples were used until the end point. The initial mass of dry samples was measured at day 0 ($mass_0$), the sample was incubated in either PBS with 0.2 mg/ml sodium azide only or 0.1 U/ml elastase in PBS with 0.2 mg/ml sodium azide for either 1, 2, 4, 8 or 12 days in a platform shaker at 37°C. Samples were removed at each time point, washed in deionised water, frozen and freeze-dried before measuring the dry mass again ($mass_x$) to assess the mass loss at each time point.

$$\text{Mass Loss } (\%) = \frac{\text{mass}_{(0)} - \text{mass}_{\text{x}}}{\text{mass}_{(0)}} \qquad \text{(Equation 4.10)}$$

4.2.8. Statistical Analysis

Results have been expressed as mean ± standard deviation. The results were compared with one-way analysis of variance (ANOVA) with a Tukey's HSD post-hoc test using SPSS version 26.0, IBM, Armonk, NY, IBM Corp. For values of $p<0.05$, the difference was considered statistically significant.

4.3. Results

4.3.1. Fabrication and Cross-linking of Scaffolds

Fabrication of FEG based scaffolds using the technique mentioned above was chosen to avoid freeze-drying twice. However, re-hydrating freeze-dried FEG at a pH of 2.7 could have also been used (Section 3.4.4.) to fabricate FEG-based scaffolds. Although concentrations of 0.5% and 1.0%wt/v were studied in this work, it is not recommended for future work as the solutions had a very low viscosity and collapsed upon freeze-

drying. Therefore, the concentration recommended for FEG only scaffolds would be 3%wt/v and above as they result in the stiffest scaffolds which do not collapse after freeze-drying as shown in Fig.4.2a.

Two preliminary methods were attempted to fabricate collagen and FEG based composite scaffolds that would appear "interlaced", where the FEG would form a secondary network running through the collagen scaffold. However, it was found that the extreme hydrophobicity of FEG when it came into contact with other materials prevented those ideas from being realised. First, adding 100C scaffolds to FEG in the hydrated state to allow interpenetration was attempted. Secondly, 100C scaffolds were added to FEG in the hydrated state with cross-linking agents. In both cases, it was found that the FEG precipitated due to proximity to its isoelectric point (pI) and resulted in scaffolds with FEG simply deposited on the surface of the collagen as shown in Fig.4.3. Therefore, the option of mixing dehydrated collagen with dehydrated FEG to create suspensions in acidic solutions was chosen as it made it possible to accommodate for the isoelectric points of both collagen and FEG and produce homogenous suspensions that did not result in precipitation or phase separation of the FEG.

Two preliminary methods were attempted for tri-layers. Initially, all the layers were constructed individually and "glued" together using collagen suspension as shown in Figs.4.4a and b (technique 1). However, it was found that this method resulted in scaffolds that were very distorted and densified (pores collapsed). The second attempt involved a similar approach to the methodology selected, however, instead of assembling immediately, the suspensions loaded individually in the mould and given time to freeze prior to adding each layer. This method was not selected as it was found

to result in incongruity at the interface (Figs.4.4c and d, technique 2) which would be the cause of delamination. Instead, the final method which involved assembling the tri-layer immediately without freezing the layers individually was chosen, it resulted in congruent scaffolds and no obvious mismatch at the interface was observed at the micro-level (Figs.4.4e and f, technique 3).

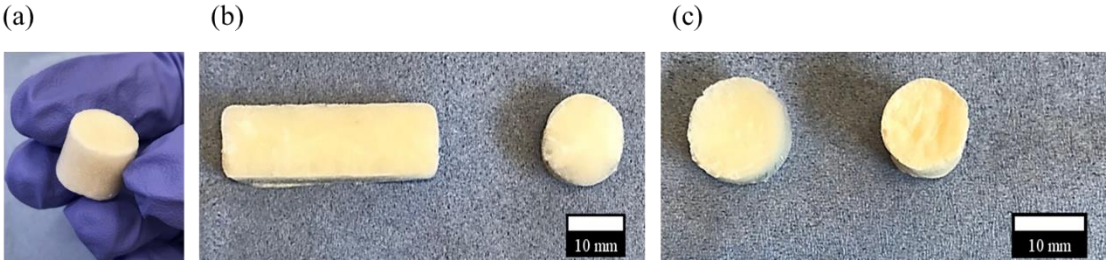

Figure 4.2: Photographs of (a) cylindrical uncross-linked FEG scaffold, (b) uncross-linked FEG scaffolds of different dimensions and (c) compares the size of a uncross-linked (left) and cross-linked (right) FEG scaffold. All scaffolds had a final density of 3% wt/v.

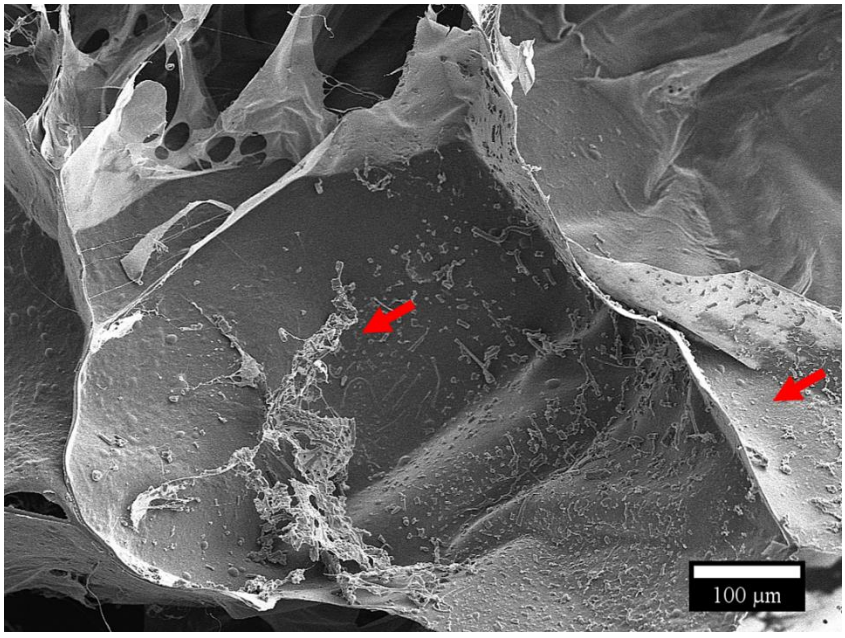

Figure 4.3: SEM image of the collagen and FEG composite fabricated by adding a collagen scaffold directly to FEG in its hydrated state. Image shows deposition of FEG (shown by red arrows) on the surface of the collagen struts with no interaction between the materials.

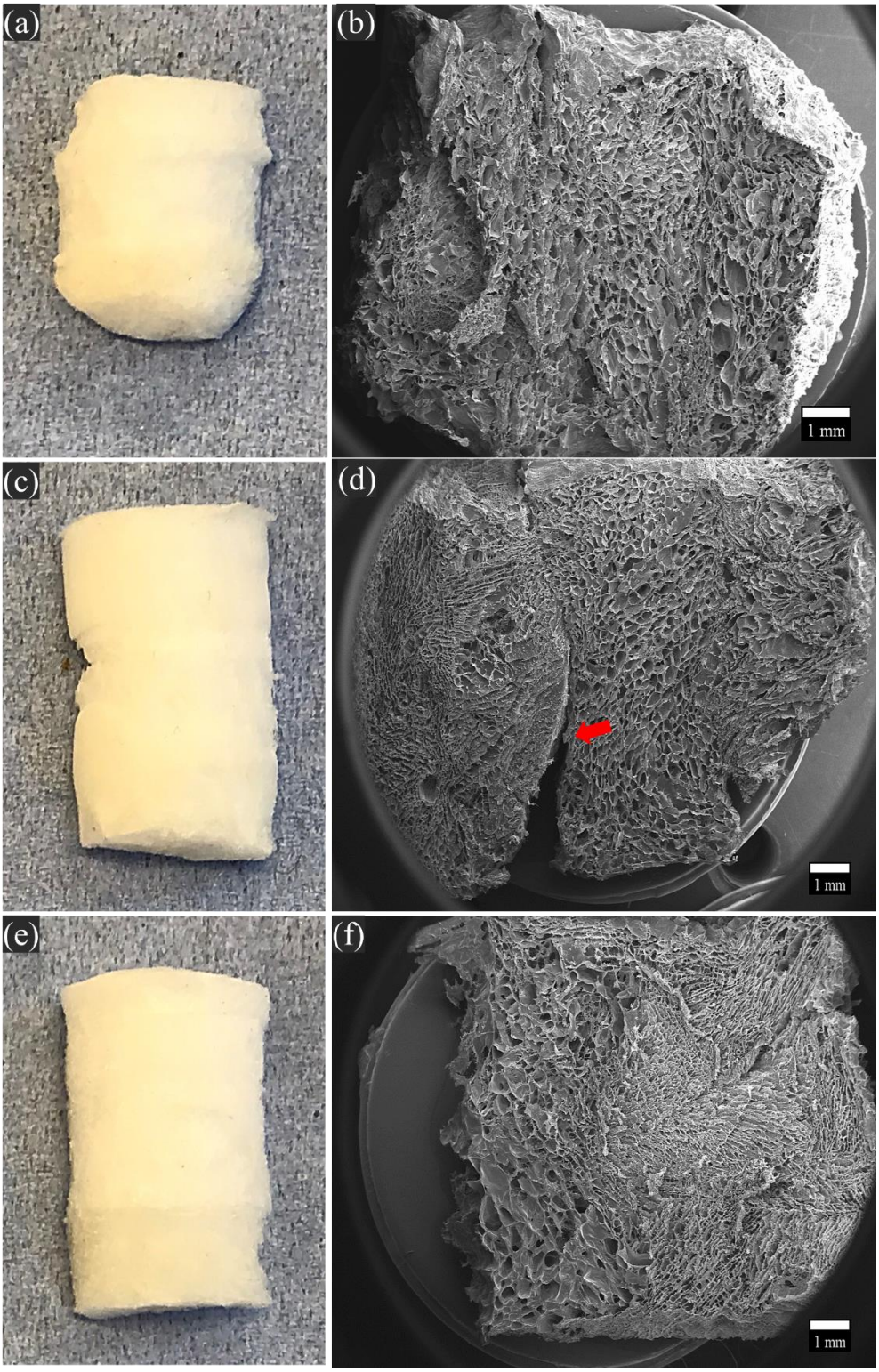

Figure 4.4: Photographs and SEM images of tri-layers produced using technique 1 (a) and (b), technique 2 (c) and (d) and technique 3 (e) and (f). Information of techniques can be found in the text. Photographs show tri-layers with 100% collagen, coll-HA and 50% collagen-50% FEG from top to bottom and SEM images show 100% collagen, coll-HA and 50% collagen-50% FEG from right to left.

4.3.2. Rheology of Suspensions

Frequency sweeps were performed on 100C and COL-FEG based suspensions prior to fabricating scaffolds to study the properties of the suspensions. Fig.4.5 shows the results for the storage and loss modulus for each composition, where the substitution of COL for FEG significantly reduces the moduli. Although they both behave as gels, 25% replacement of collagen resulted in a significant decrease (7-fold) in the storage modulus. For 50C-50E samples, there was overlap of the storage and loss modulus at all frequencies and a cross-over point at 5 Hz (relaxation frequency) where the storage and loss modulus are equivalent. The loss factor was constant at all frequencies for 100C (Table 4.3), however, as more collagen was replaced with FEG, the loss factor increased as G'' exceeded G'.

Complex viscosity for all the suspensions was also measured at different frequencies (Fig.4.6), it was found that the viscosity decreased as the frequency increased for all compositions and therefore all samples exhibited shear thinning behaviour. However, the extent of decrease in the viscosity with the replacement of collagen was significant. The complex viscosity decreased by more than 30-fold when 50% or more collagen was substituted for FEG.

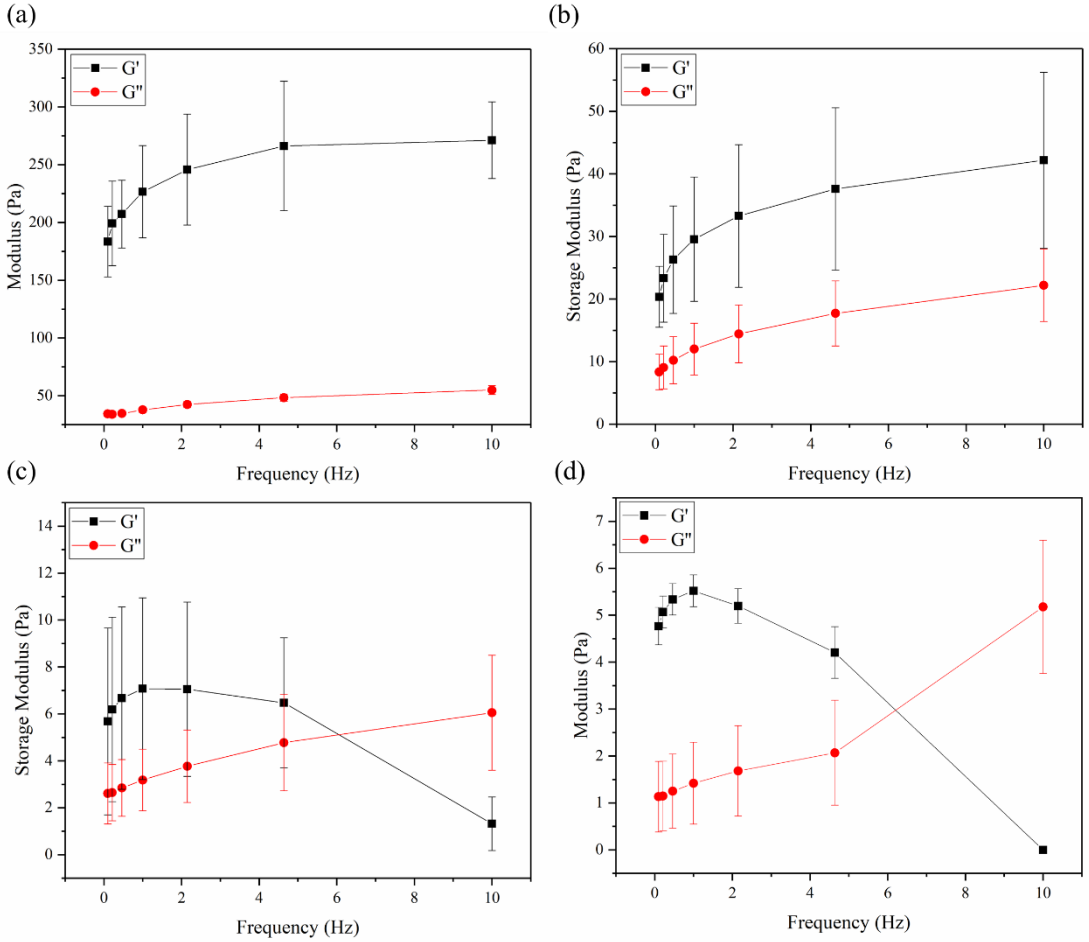

Figure 4.5: Frequency sweep results for suspensions showing the storage (G') and loss (G'') modulus for (a) 100% collagen, (b) 75% collagen-25% FEG, (c) 50% collagen- 50% FEG and (d) 25% collagen-75% FEG suspensions. Frequency: 0.1-10 Hz, strain amplitude of 5% and temperature of 20 °C.

Table 4.3: Viscoelastic properties for compositions measured at 1 Hz.

Composition	Storage Modulus (Pa)	Loss Modulus (Pa)	Loss Factor	Complex Viscosity (Pa.s)	Complex Modulus (Pa)
100% COL	226.6 ± 40.0	37.8 ± 2.2	0.2 ± 0.03	36.6 ± 6.3	229.8 ±39.4
75% COL-25% FEG	29.6 ± 9.9	12.0 ± 4.1	0.4 ± 0.05	5.1 ± 1.7	31.9 ± 10.7
50% COL-50% FEG	7.1 ± 3.9	3.2 ± 1.3	0.5 ± 0.1	1.2 ± 0.6	7.8 ±4.0
25% COL-75% FEG	5.5 ± 0.3	1.4 ± 0.9	0.4 ± 0.07	0.7 ± 0.4	4.3 ± 2.7

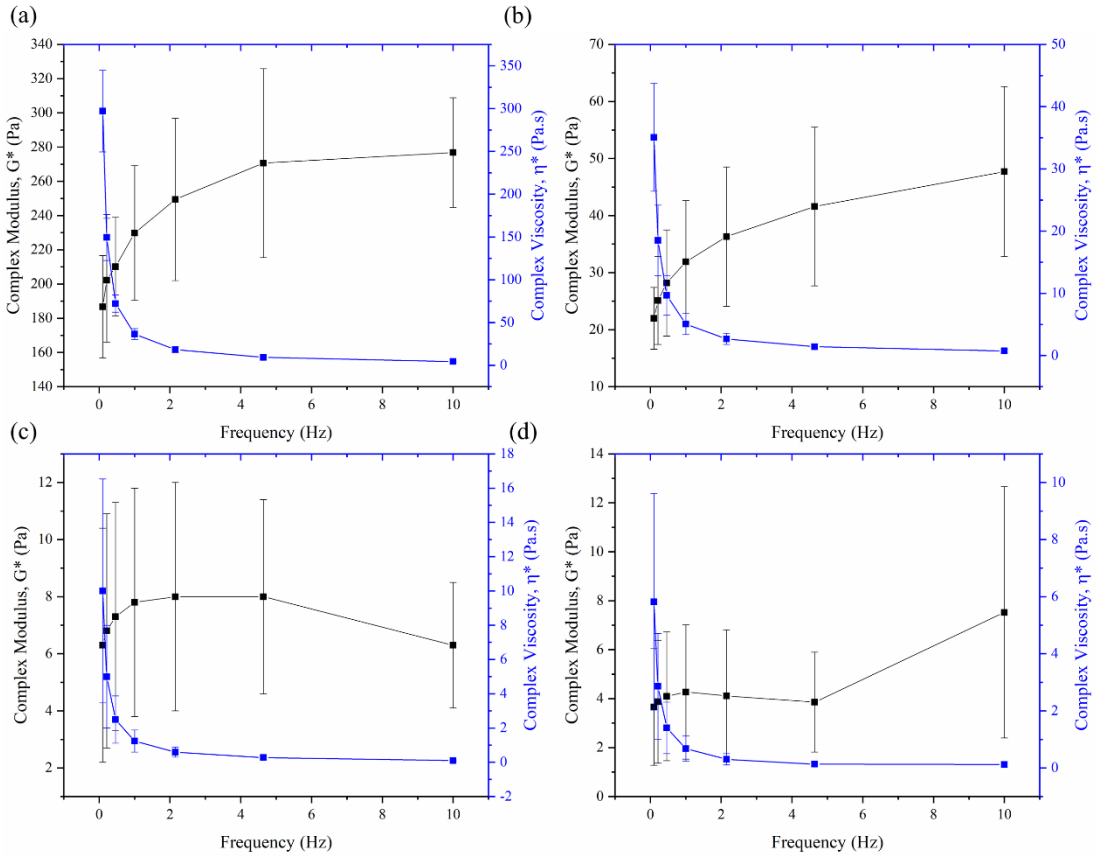

Figure 4.6: Frequency sweep results for suspensions showing the complex modulus (G*) and complex viscosity (η*) for (a) 100% collagen, (b) 75% collagen-25% FEG, (c) 50% collagen- 50% FEG and (d) 25% collagen-75% FEG suspensions. Frequency: 0.1-10 Hz, strain amplitude of 5% and temperature of 20 °C.

4.3.3. Microstructure of Scaffolds

The scaffold morphology varied significantly between the scaffold types, and therefore, the pores were treated as ellipses when processing the images instead of assuming the pores were spherical as two measurements would be taken for each pore, one of the major axis and one of the minor axis.

The first group of scaffolds studied were uncross-linked FEG-based scaffolds which were fabricated at concentrations of 0.5, 1.0 and 3.0%wt/v at either -20 or -80°C. Fig.4.7 presents the SEM images taken for these scaffold types. It was found that at

lower concentrations of FEG, the pores appeared more elongated and less well-defined, whereas at higher concentrations they were equiaxial and uniform. Secondary pores which are perforations observed in the struts (pore walls) of the scaffold were observed for all FEG-based samples, however, scaffolds with lower concentrations of FEG had discontinuous pore walls. It was found that scaffolds with lower concentrations of FEG were challenging to handle during sample preparation for SEM challenging compared to 3.0%wt/v.

The pore size distribution is presented in Fig.4.8, and the average pore sizes with aspect ratios in Table 4.4. There was no significant difference between the average pore sizes of samples frozen at -20°C, however, at -80°C it was found that the higher the concentration of FEG the smaller the average pore size. Scaffolds composed of 1.0%wt/v FEG had significantly smaller pores than 0.5%wt/v and scaffolds with a concentration of 3.0%wt/v had significantly smaller pores than samples composed of 0.5 and 1.0%wt/v. The pore wall thickness and surface porosity of scaffolds are presented in Table 4.5.

3.0%wt/v scaffolds were studied in the uncross-linked and cross-linked state as they did not collapse post-freeze-drying. The microstructure of scaffolds after cross-linking are shown in Fig.4.9. It was found that the cross-linking procedure resulted in very large pores (Fig.4.9b), however, these pores were uncommon and did not occur throughout the scaffold, and therefore were not taken into consideration when measuring the average pore size. As shown in Fig.4.9c and d, scaffolds that were cross-linked resulted in shrinkage of pores from 63±9μm to 46±6μm which was significantly lower and coincided with a volumetric contraction of 54.6±6.6%. 3.0%wt/v FEG scaffolds had coherent pores and a porosity of 94.0±1.01%.

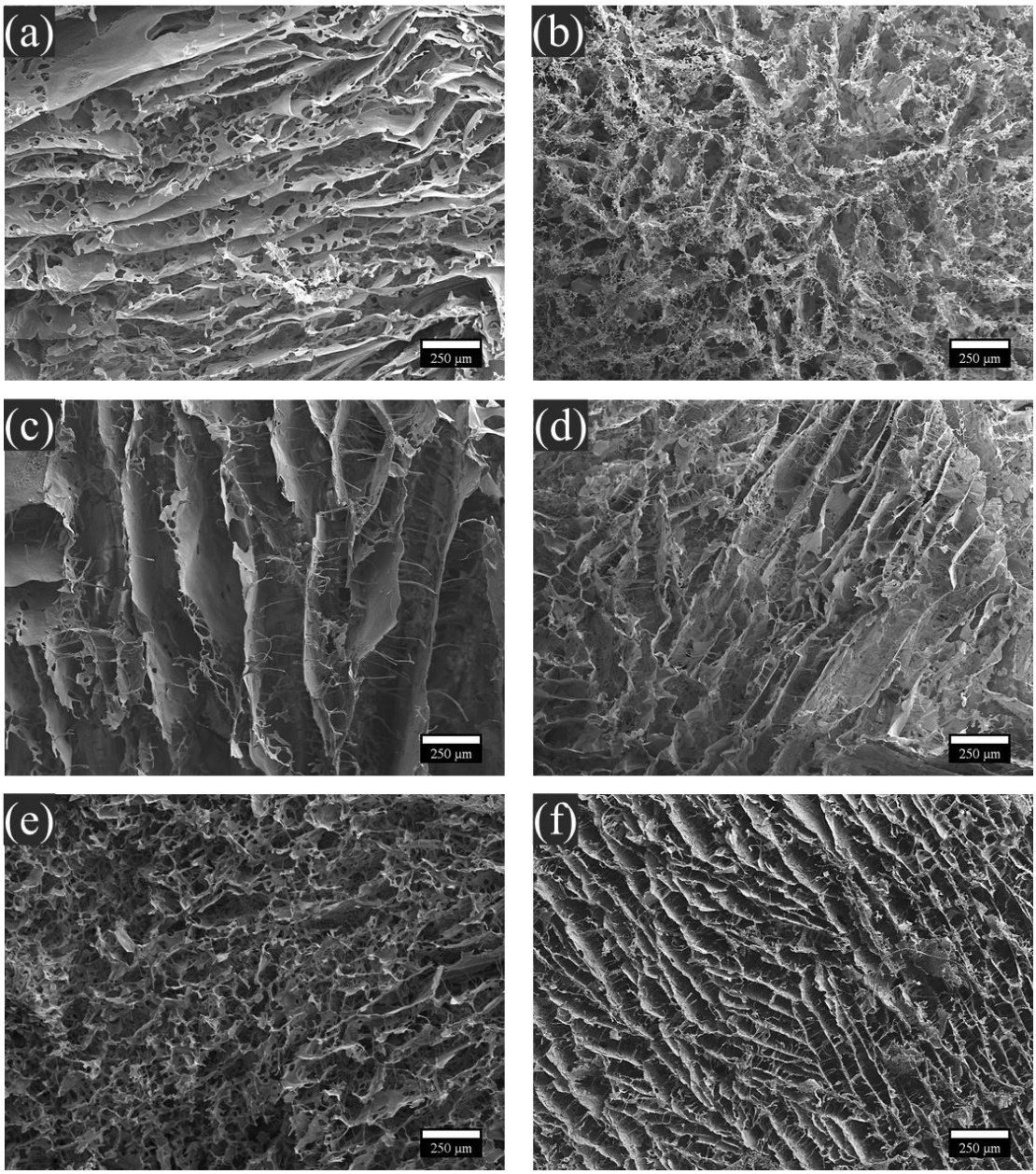

Figure 4.7: FEG-based scaffolds (uncross-linked) with concentrations of: 0.5% wt/v frozen at -20°C (a) or -80°C (b), 1.0% wt/v frozen at -20°C (c) or -80°C (d) and 3.0% wt/v frozen at -20°C (e) or -80°C (f).

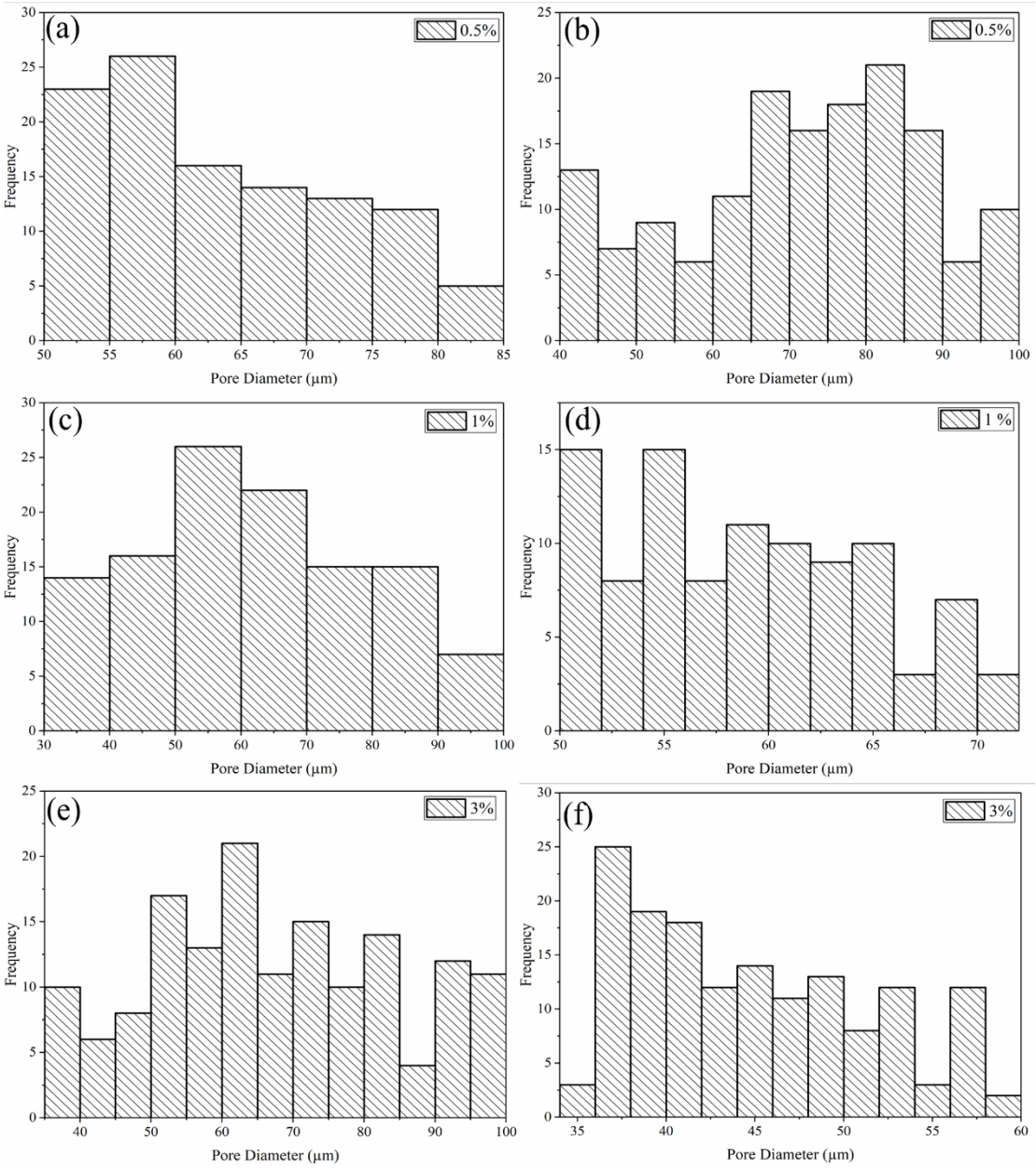

Figure 4.8: Pore size distribution of FEG-based scaffolds (uncross-linked) with concentrations of: 0.5% wt/v frozen at -20°C (a) or -80°C (b), 1% wt/v frozen at -20°C (c) or -80°C (d) and 3% wt/v frozen at -20°C (e) or -80°C (f). Area was truncated between 3000-infinity, n>100.

Table 4.4: Average pore size and aspect ratio of FEG-based scaffolds

Concentration of FEG (%wt/v)	Average Pore Size (µm)		Aspect Ratio	
	-20 °C	-80 °C	-20 °C	-80 °C
0.5	63 ± 9	71 ± 15	2.6 ± 0.1	2.4 ± 0.1
1.0	62 ± 17	59 ± 6***	2.5 ± 0.1	2.5 ± 0.2
3.0	68 ± 17	44 ± 7***	2.8 ± 0.1	1.6 ± 0.2

*where ***p<0.0005 and n>100 for different concentrations of FEG.*

Table 4.5: Pore wall thickness and surface porosity of FEG-based scaffolds

Concentration of FEG (%wt/v)	Wall Thickness (µm)		Surface Porosity (%)	
	-20 °C	-80 °C	-20 °C	-80 °C
0.5	21 ± 3	18 ± 2	84.8 ± 4.8	79.2± 3.0
1.0	16 ± 4	9 ± 2	89.3 ± 0.4	77.7 ± 1.7
3.0	16 ± 4	6 ± 1	77.4 ± 0.7	76.8 ± 1.0

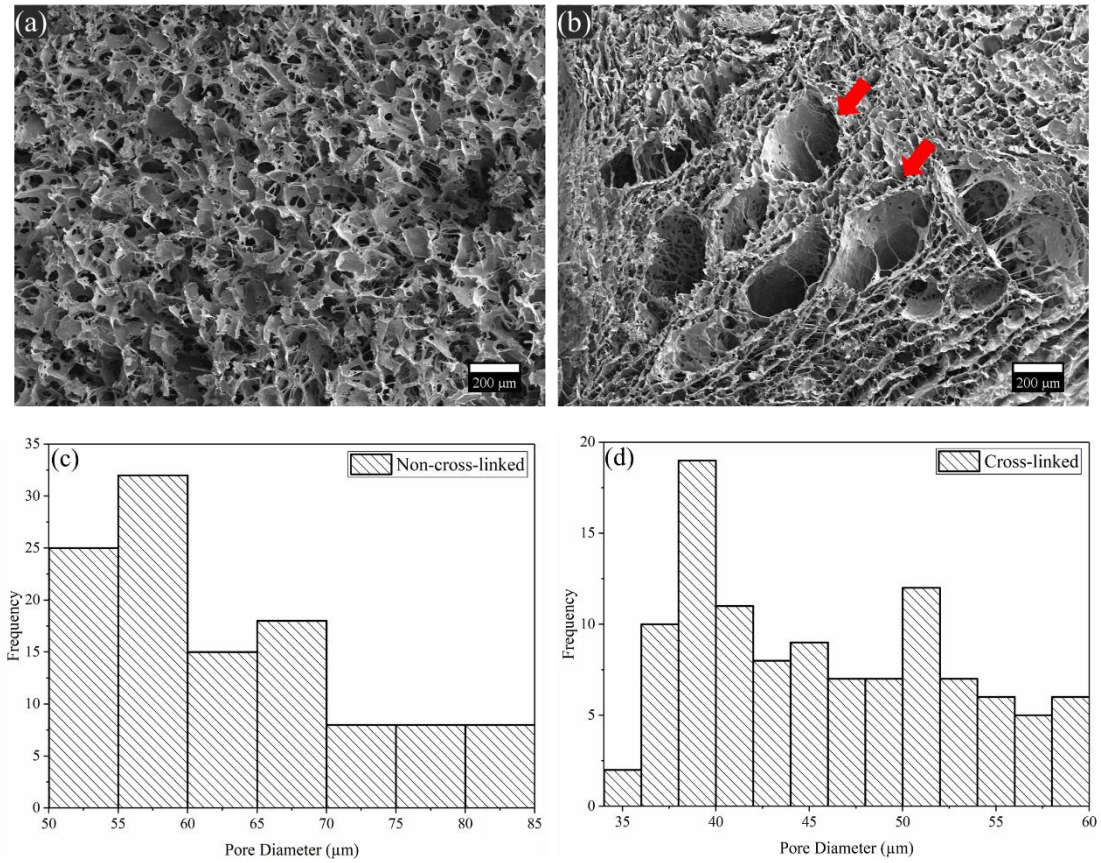

Figure 4.9: 3.0%wt/v FEG scaffold (a) uncross-linked and (b) cross-linked with the pore size distribution for (c) uncross-linked and (d) cross-linked scaffolds where n>100. Area was truncated between 3000-infinity.

In addition to studying the microstructure of FEG-based scaffolds, the effect of the substitution of collagen for FEG on the pore characteristics was of interest. Fig.4.10 and 4.12 show the SEM images and pore size distribution of scaffolds composed of 100C, 75C-25E, 50C-50E and 25C-75E that were uncross-linked (left) or cross-linked (right). Table 4.6-7 show the results for the average pore size, wall thickness and aspect ratio. It was found that the replacement of collagen resulted in pores transforming form very homogenous, circular pores in 100C scaffolds to more elongated and plate-like pores as the concentration of FEG increased. This difference was observed in the size of the pores, it was found that with the substitution of FEG, the diameter of the pores increased significantly up to 50% replacement of collagen, however, for 25C-75E

samples, the pores were significantly smaller with an average pore size of 60±14μm compared to 110±32μm, 171±56μm and 174±41μm for 100C, 75C-25E and 50C-50E samples, respectively. FEG was not deposited on the surface of the collagen struts even at higher magnifications, instead the scaffolds appeared homogenous and the pores were coherent for all compositions as shown in Fig.4.11. This was confirmed with LSCM (Fig.4.13) which showed that both collagen and FEG coexist and the FEG is integrated into the collagen struts as short rods in the uncross-linked state.

The cross-linking procedure changed the microstructure of scaffolds containing FEG as the pores appeared more circular for all cross-linked samples, whereas there was no significant difference in the microstructure or pore size of 100C scaffolds after cross-linking. It was found for composites, cross-linking reduced the pore size of the scaffolds significantly to 130±17μm and 143±25μm for 75C-25E and 50C-50E, respectively. As seen with the uncross-linked variants, 25C-75E appeared to have the smallest pores amongst the scaffold types studied, however, there was no significant difference in the pore size after cross-linking. LSCM was also studied on cross-linked composite scaffolds, however, it was found that collagen could not be stained for after cross-linking, therefore only the elastin component was shown in Fig.4.13. It was found that the cross-linking procedure connected the rods seen in uncross-linked scaffolds resulting in a more integrated scaffold, this is especially apparent in 50C-50E and 25C-75E samples. This could explain why the pore sizes appear smaller in cross-linked samples as well as the change in volume after cross-linking which will be presented in section 4.3.5. The struts appear to have a rougher surface in 25C-75E, this is also seen in the SEM images where the surface appears rougher as the concentration of FEG increases, compared to 100C which appears relatively smooth. As well as

forming coherent scaffolds, the composites were highly porous with a porosity over 98% (Table 4.8) for all scaffolds and no significant difference between 100C and the composites was observed.

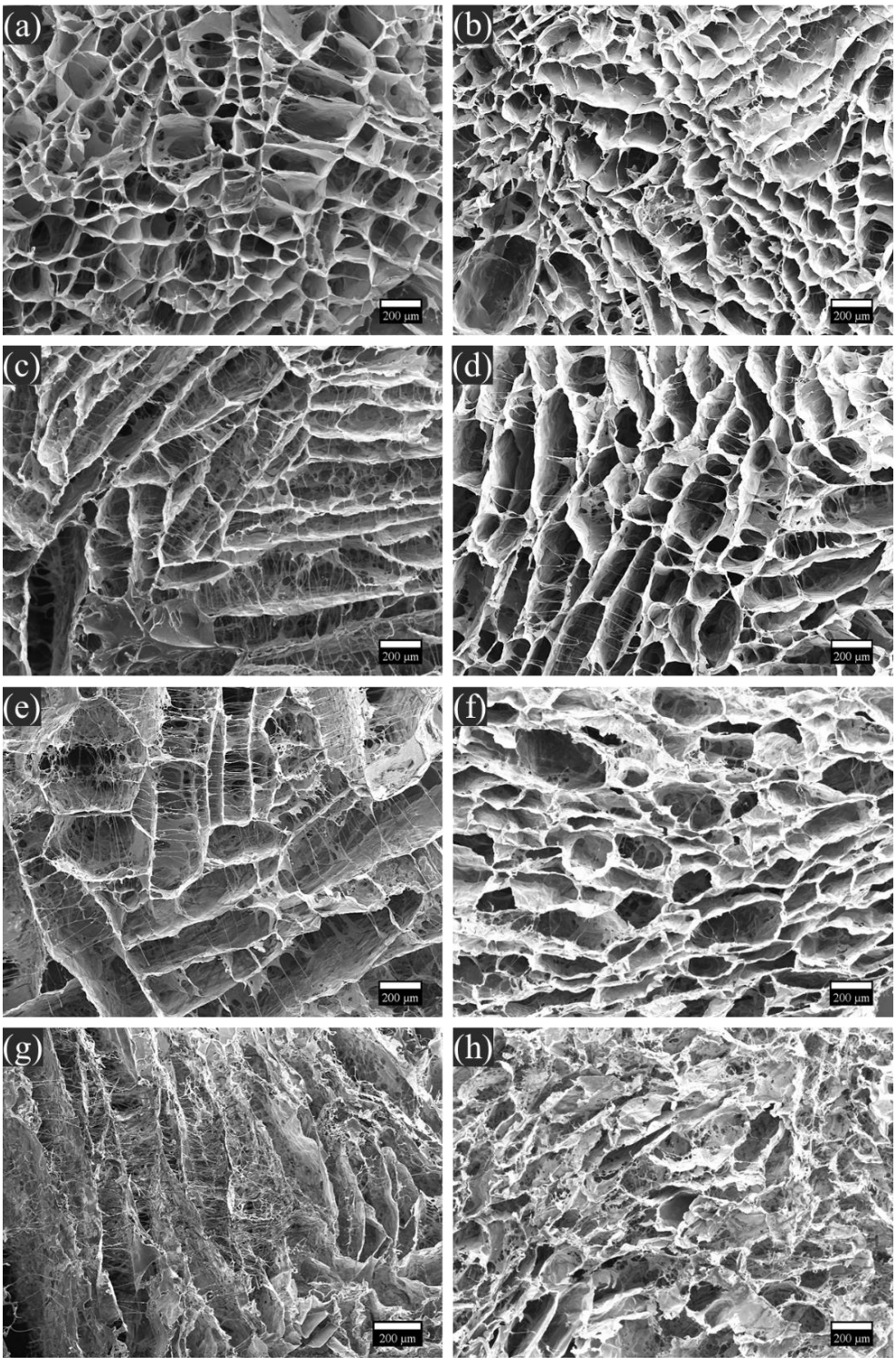

Figure 4.10: SEM images of collagen-FEG based scaffolds with compositions of 100% collagen (a) uncross-linked and (b) cross-linked, 75% collagen-25% FEG (c) uncross-linked and (d) cross-linked, 50% collagen- 50% FEG (e) uncross-linked and (f) cross-linked and 25% collagen-75% FEG (g) uncross-linked and (h) cross-linked.

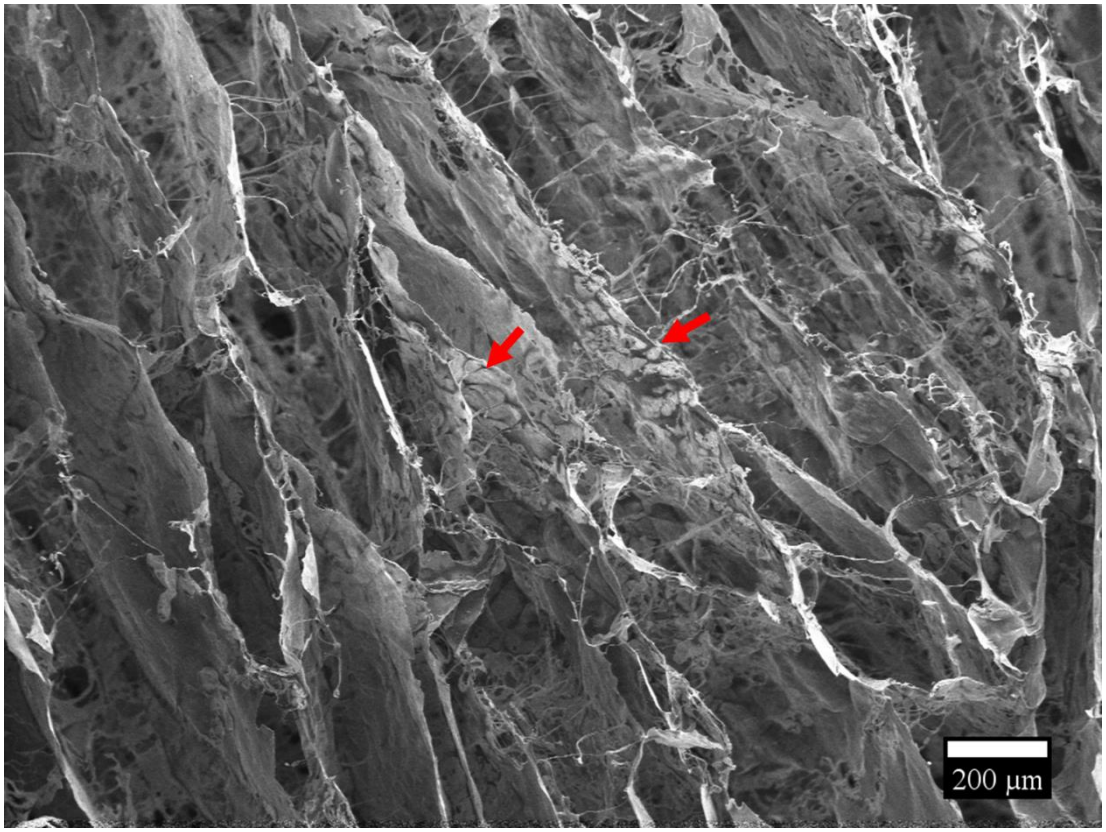

Figure 4.11: Scanning electron microscope image of cross-linked 25% collagen-75% FEG scaffold with red arrows showing embedded FEG fibres as darker rods.

Table 4.6: Average pore size for scaffolds composed of FEG only and collagen-FEG composite scaffolds.

Sample	Average Pore Size (µm)	
	Uncross-linked	Cross-linked
100% FEG	63 ± 9	46 ± 6***
100% COL	110 ± 32	118 ± 19
75% COL-25% FEG	171 ± 56***	130 ± 17***
50% COL-50% FEG	174 ± 41***	143 ± 25***
25% COL-75% FEG	60 ± 14***	52 ± 8***

*where ***p<0.0005 in comparison to scaffolds containing no FEG (100% collagen), and n>100.*

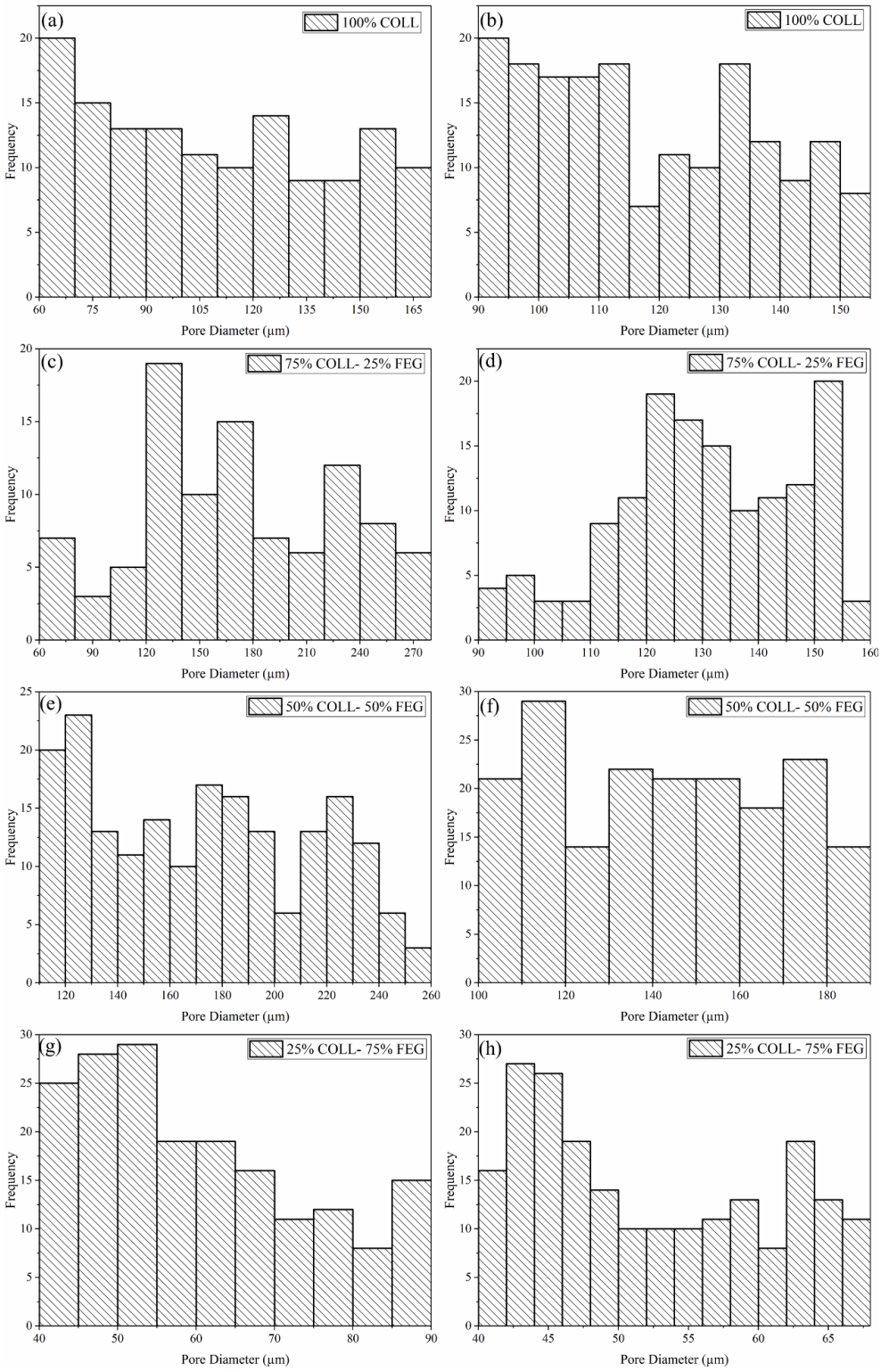

Figure 4.12: Pore size distribution of collagen-FEG based scaffolds with compositions of 100% collagen (a) uncross-linked and (b) cross-linked, 75% collagen-25% FEG (c) uncross-linked and (d) cross-linked, 50% collagen- 50% FEG (e) uncross-linked and (f) cross-linked and 25% collagen-75% FEG (g) uncross-linked and (h) cross-linked. Area was truncated between 3000-infinity, where n>100.

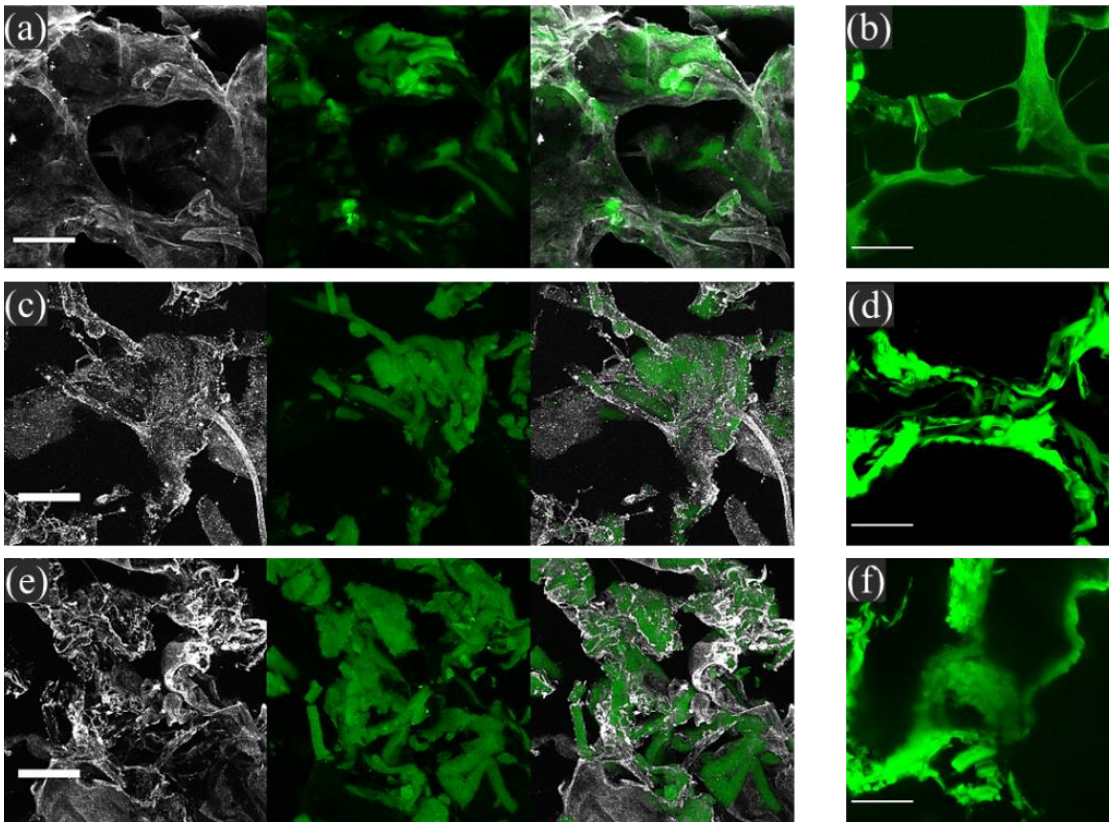

Figure 4.13: Laser scanning confocal microscopy images of 75% collagen-25% FEG (a) uncross-linked and (b) cross-linked, 50% collagen-50% FEG (c) uncross-linked and (d) cross-linked and 25% collagen-75% FEG (e) uncross-linked and (f) cross-linked. Collagen shown in grey and elastin in green. Scale bar is 50 µm.

Table 4.7: Pore wall thickness and aspect ratio of collagen-FEG composite scaffolds

Sample	Wall Thickness (µm)		Aspect Ratio	
	Uncross-linked	Cross-linked	Uncross-linked	Cross-linked
100% FEG	16 ± 4	22 ± 4	2.8 ± 0.1	2.4 ± 0.1
100% COL	28 ± 4	25 ± 4	2.5 ± 0.2	2.4 ± 0.1
75% COL-25% FEG	19 ± 5	26 ± 5	2.7 ± 0.3	2.6 ± 0.3
50% COL-50% FEG	21 ± 5	28 ± 6	2.4 ± 0.1	2.6 ± 0.3
25% COL-75% FEG	34 ± 5	35 ± 3	2.6 ± 0.3	2.8 ± 0.2

Table 4.8: Porosity and Surface Porosity of collagen-FEG composite scaffolds

Sample	Total Porosity (%)	Surface Porosity (%)
100% FEG	94.0 ± 1.01	78.0 ± 0.4
100% COL	98.8 ± 0.11	67.5 ± 0.7
75% COL-25% FEG	98.9 ± 0.07	64.4 ± 1.0
50% COL-50% FEG	98.4 ± 0.30	64.7 ± 1.7
25% COL-75% FEG	98.0 ± 0.18	71.1 ± 1.1

The microstructure of coll-HA based scaffolds was also studied as it would form the middle layer of the tri-layer scaffolds. The cross-linking of HA was shown to change the microstructure of flake-like particles to plate-like struts (Fig.4.14a and b). When incorporated with collagen, the HA formed a light network of HA which surrounded the collagen struts (Fig.4.14c), these scaffolds had an average pore size of 82±13μm and surface porosity of 62.9±2.2%. Coll-HA composite scaffolds were combined with 100C and 50C-50E suspensions to form tri-layer scaffolds as shown in Fig.4.10. It was found that the tri-layer resembled 100C and coll-HA scaffold closely, however, the 50C-50E appeared elongated and plate-like. SEM revealed that the layers integrated well and the interface between layers was undistinguishable. Tri-layer scaffolds had average pore sizes of: 124±14μm, 90±18μm and 102±27μm for the 100C, coll-HA, and 50C-50E layer, respectively. The surface porosity tri-layers was 64.4±2.5%.

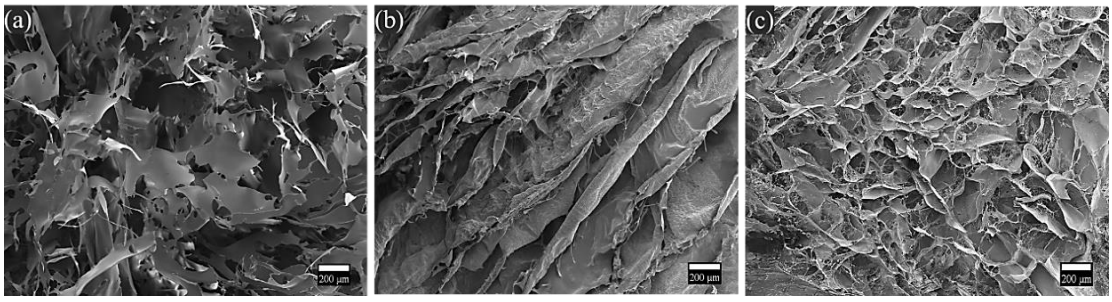

Figure 4.14: SEM images of (a) uncross-linked hyaluronic acid (side view), (b) hyaluronic acid cross-linked with ADH and EDC (side view) and (c) collagen-hyaluronic acid scaffolds (cross-section).

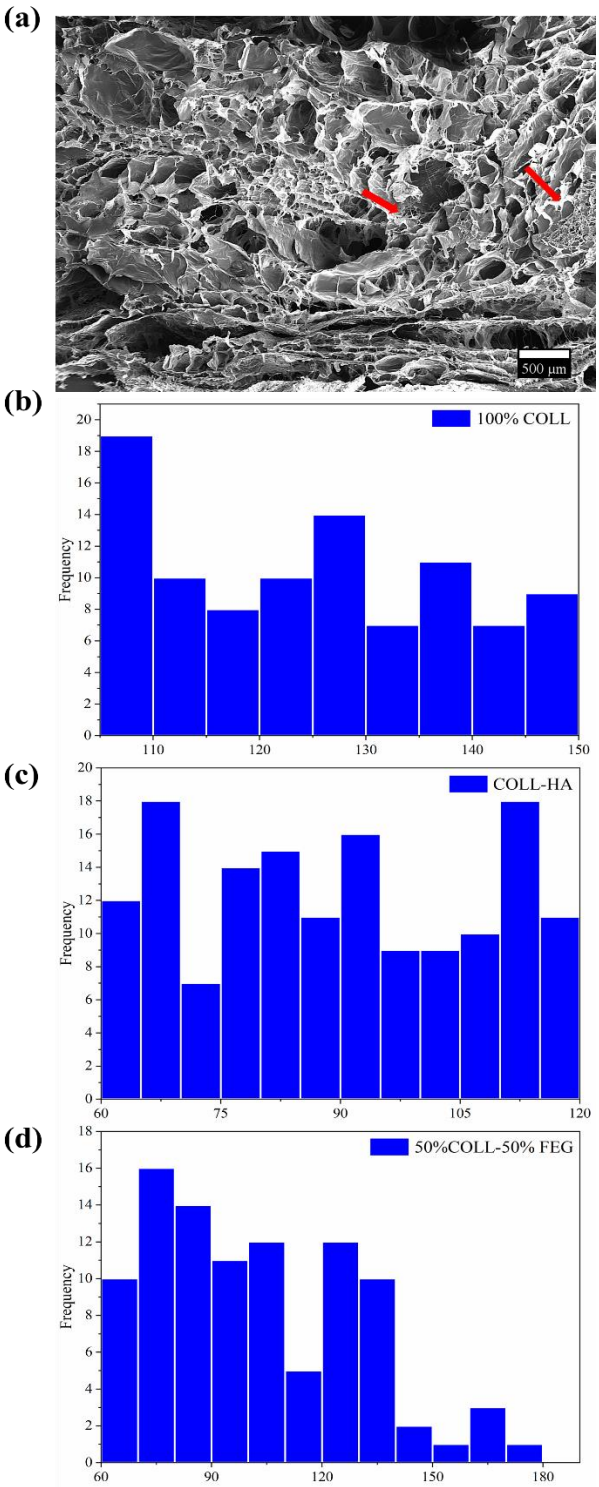

Figure 4.15: SEM image of cross-section of a cross-linked tri-layer scaffold (a) and the pore size distribution for each layer: (b) 100% collagen (top third), (c) coll-HA (middle third) and (d) 50% collagen-50% FEG (bottom third). Red arrows show fine mesh-like structure of interlacing HA. Area was truncated between 3000-infinity.

4.3.4. Infrared Spectroscopy of Scaffolds

To confirm successful cross-linking and its effect on the chemistry of scaffolds, FEG-based, collagen-based and HA and coll-HA scaffolds were studied using FT-IR by comparing the raw materials (as received) to the processed forms: uncross-linked which is freeze-dried once and cross-linked which is freeze-dried twice.

The FT-IR spectra for FEG-based scaffolds is shown in Fig.4.16 with the second derivative. It was found to show all characteristic peaks for elastin as discussed in section 3.4.2. There were no significant shifts in any of the bands as shown in Table 4.9, except for Amide II which showed a shift after cross-linking of -13cm^{-1}. The second derivative of the Amide I peak (results in Table 4.10) revealed that the β-sheets were composed of three main components which showed no significant shifts after cross-linking. The peaks corresponding to the intra- and intermolecular β-sheets appeared to have a higher peak intensity after cross-linking. The ratio of Amide I to Amide A was found to be 0.8±0.1 and 1.3±0.1 for uncross-linked and cross-linked scaffolds, respectively.

The FT-IR spectra for collagen as received and scaffolds that were uncross-linked or cross-linked are presented in Fig.4.17. Characteristic peaks for collagen were all observed and an increase in the broadness of the Amide A, I, II and III was observed. There were no significant differences in the band assignment of all three types of samples, except Amide II which was significantly higher in the uncross-linked and cross-linked collagen samples. The second derivative revealed a significant shift in the peak corresponding to β-sheets as it shifted by 5cm^{-1}. The fabrication process did not affect collagen's triple-helical structure as the Amide III (1245cm^{-1}) to 1456cm^{-1} ratio remained at ~1 for all samples [330].

FT-IR was used to confirm the cross-linking of HA as well as the presence of HA in coll-HA composites. Fig.4.18 compares HA as received to a uncross-linked HA scaffold. It was found that all the characteristic peaks of HA were present (Table 4.11). The band at 3328cm^{-1} corresponded to OH stretching and was found to shift significantly in uncross-linked scaffolds by -20cm^{-1}. The band at 1608cm^{-1} corresponds to stretching of the C=O group in glucuronic acid of HA. The stretching of COO- and COH was present at 1402cm^{-1} and 1035cm^{-1} with no significant differences in both sample types. The cross-linking of HA with ADH and EDC is confirmed by the appearance of the twin peak between 2900-3330cm^{-1}, the band at 3311 cm^{-1} corresponds to the stretching of the N-H group as well O-H stretching band which shifted significantly by -18cm^{-1} after cross-linking. The cross-linking is confirmed by the significant shift of 27cm^{-1} in the amide carbonyl as well as the appearance of the N-H bending peak at 1538cm^{-1} which corresponds to Amide II. Fig.4.19 compares the cross-linked HA to coll-HA scaffolds as well as 100C scaffolds to confirm the difference in their chemistry. There was no significant difference in the peaks of coll-HA compared to cross-linked HA except for the broader peaks which accounts for the presence of collagen as well as the significant shift in the COO- stretching band which shifted by 10cm^{-1} as it corresponds to the both the acid group of HA and amino acid side chains of collagen. As uncross-linked collagen scaffolds were used to prepare coll-HA, these scaffolds were compared to coll-HA to confirm the change in conformation after HA incorporation. The spectra for both samples appeared very similar with the twin peak between 2900-3330 cm^{-1} being the most obvious way of differentiating the two samples. The peaks for coll-HA appeared

broader at all major bands implying that the cross-linking and incorporation of HA to collagen's backbone was successful.

Table 4.9: Band assignments for FT-IR spectra of FEG-based and collagen-based materials [255]**.**

Composition	Absorption Band (cm^{-1})					
	Amide A	**Amide I**	**Amide II**	**CH_2 bending**	**Amide III**	**C-O stretching**
FEG uncross-linked	3291	1634	1531	1335	1228	1165
FEG cross-linked	3291	1638	1518	1339	1227	1163
COL as received	3294	1631	1533	1342	1237	1163
COL uncross-linked	3294	1634	1548	1338	1237	1163
COL cross-linked	3294	1631	1546	1340	1237	1163

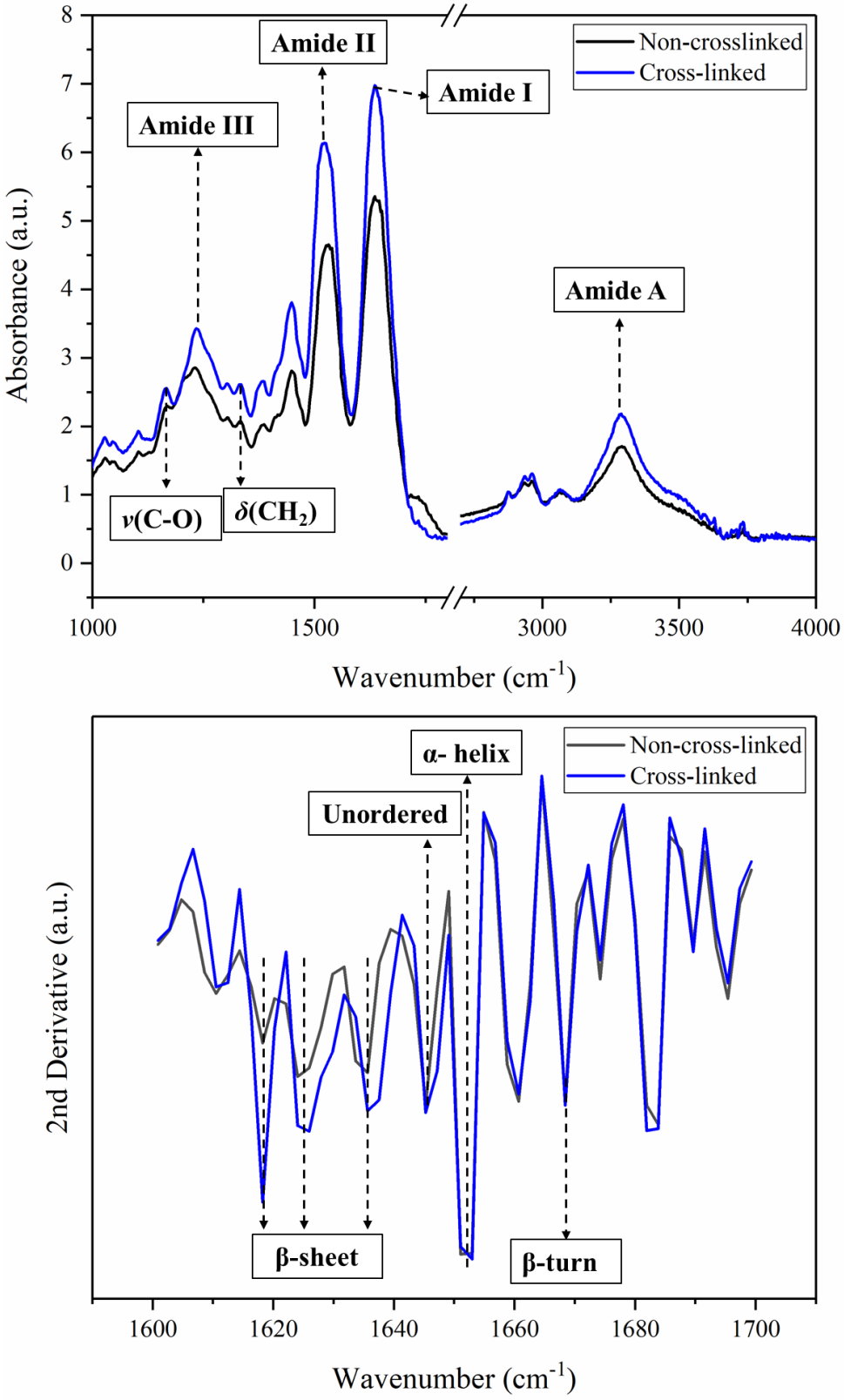

Figure 4.16: FT-IR spectrum (top) of uncross-linked and cross-linked FEG scaffolds between 1000-4000 cm^{-1} and the second derivative (bottom) of the FEG-based scaffolds between 1600-1700cm^{-1}. Data has been normalised at 2872 cm^{-1}.

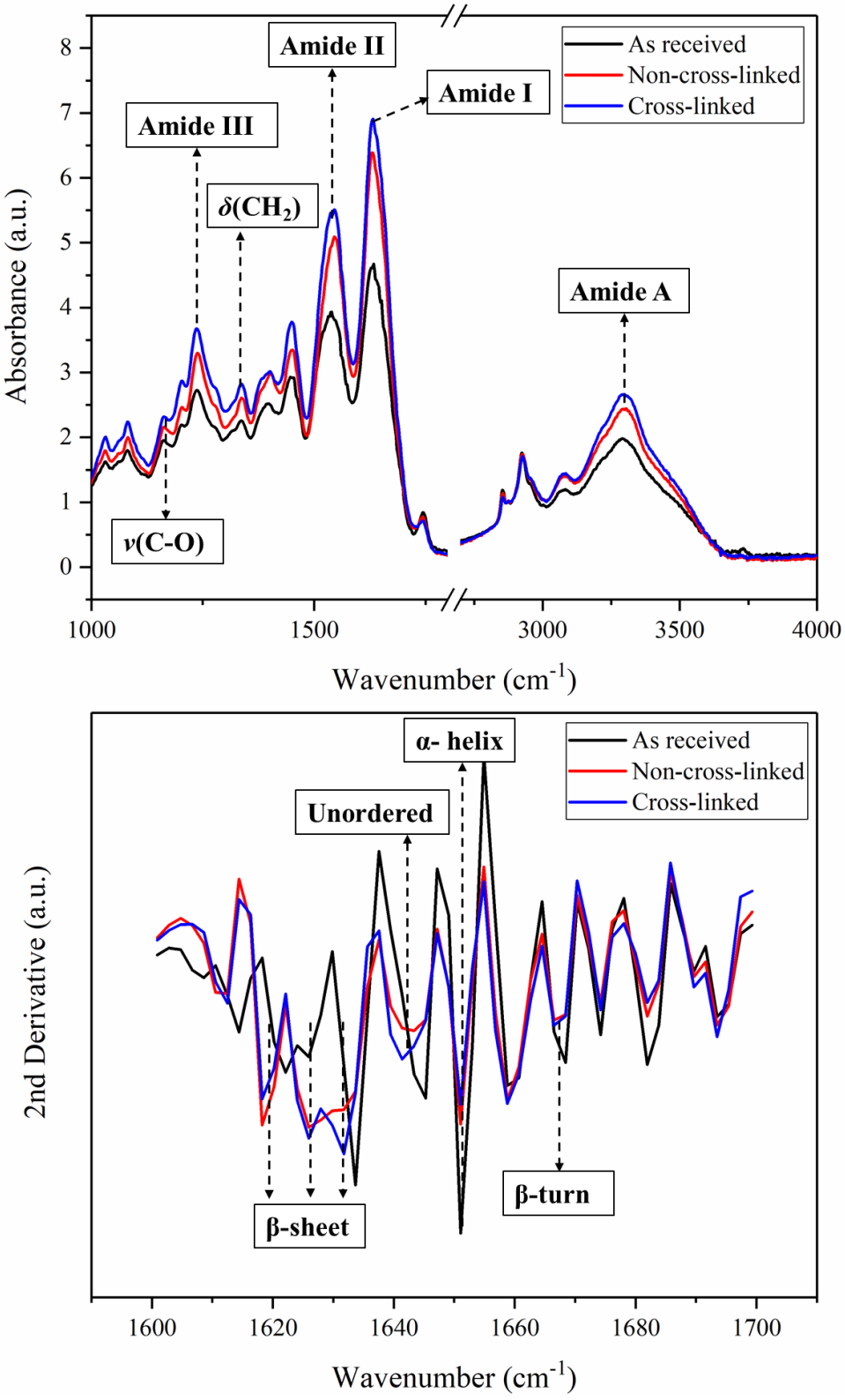

Figure 4.17: FT-IR spectrum (top) of as-received collagen powder, uncross-linked and cross-linked collagen scaffolds between 1000-4000 cm^{-1} and the second derivative (bottom) of the collagen based materials between 1600-1700 cm^{-1}. Data has been normalised at 2872 cm^{-1}.

Table 4.10: Band assignments for second derivative of FT-IR spectra of FEG-based and collagen-based materials [256]**.**

Composition	Second Derivative of Amide I			
	α- helix	**β-sheet**	**Unordered structure**	**β-turns**
FEG uncross-linked	1651	1618 1624 1635	1643	1668
FEG cross-linked	1651	1618 1625 1637	1642	1668
COL as received	1651	1622-25 1633	1644	1669
COL uncross-linked	1651	1618 1625 1631	1643	1667
COL cross-linked	1651	1618 1625 1631	1641	1666

Table 4.11: Band assignments for FT-IR spectra of hyaluronic acid-based materials [331]**.**

Composition	Absorption Band (cm^{-1})						
	v(N-H)	*v*(O-H)	*v*(C=O)	δ(N-H)	*v*(COO-)	*v*(C-N)	*v*(COH)
HA as received	--	3328	1608	--	1402	--	1035
HA uncross-linked	--	3308	1603	--	1408	--	1030
HA cross-linked	3311	3290	1630	1538	1438	1273	1035
COL-HA	3311	3290	1629	1534	1448	1275	1038

v=stretching vibration, δ=in plane bending vibration

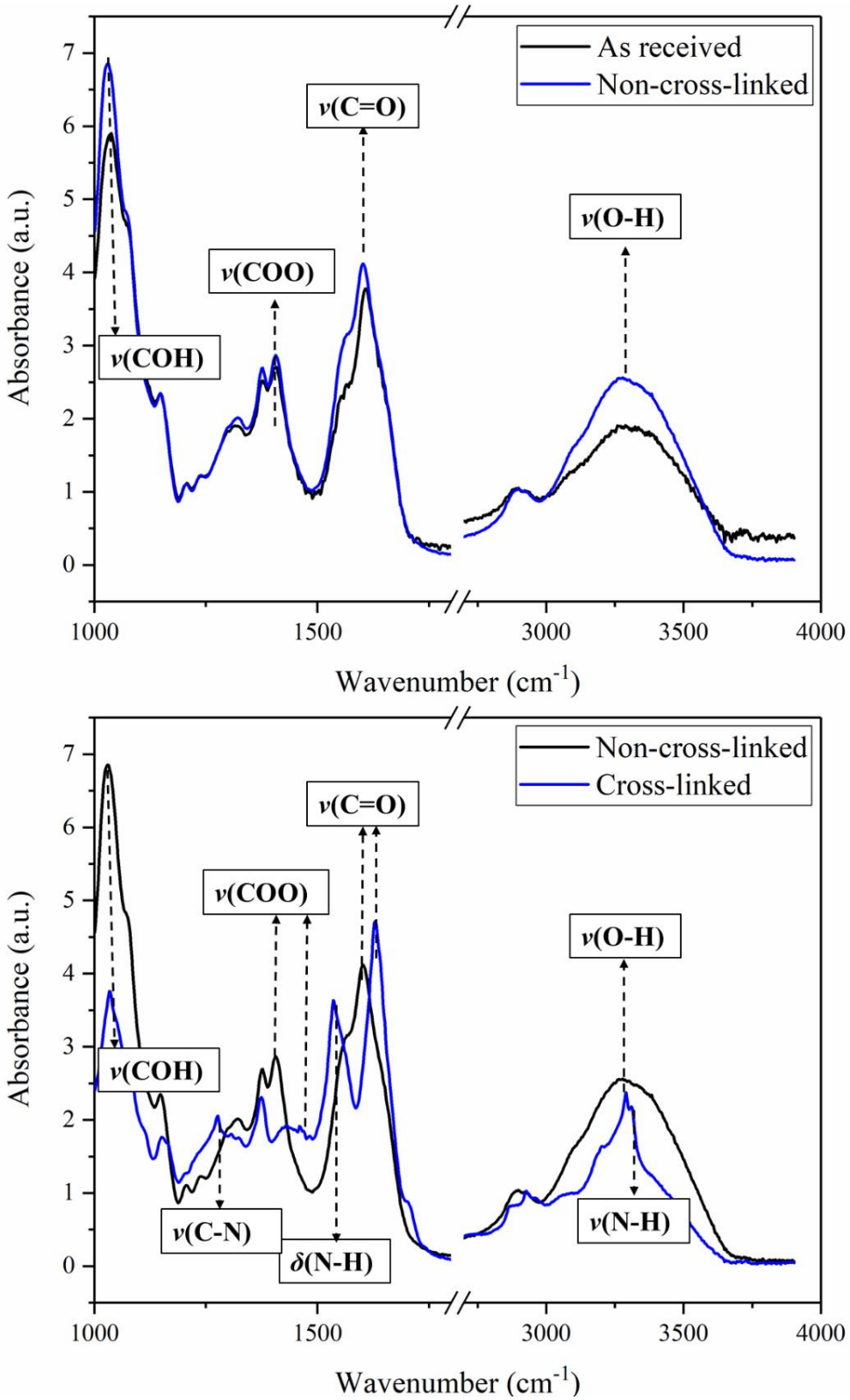

Figure 4.18: FT-IR spectra of as-received hyaluronic acid powder compared to uncross-linked hyaluronic acid scaffolds (top) and uncross-linked hyaluronic acid (ADH and EDC) and cross-linked scaffolds (bottom) between 1000-4000 cm^{-1}. Data has been normalised at 2925 cm^{-1}.

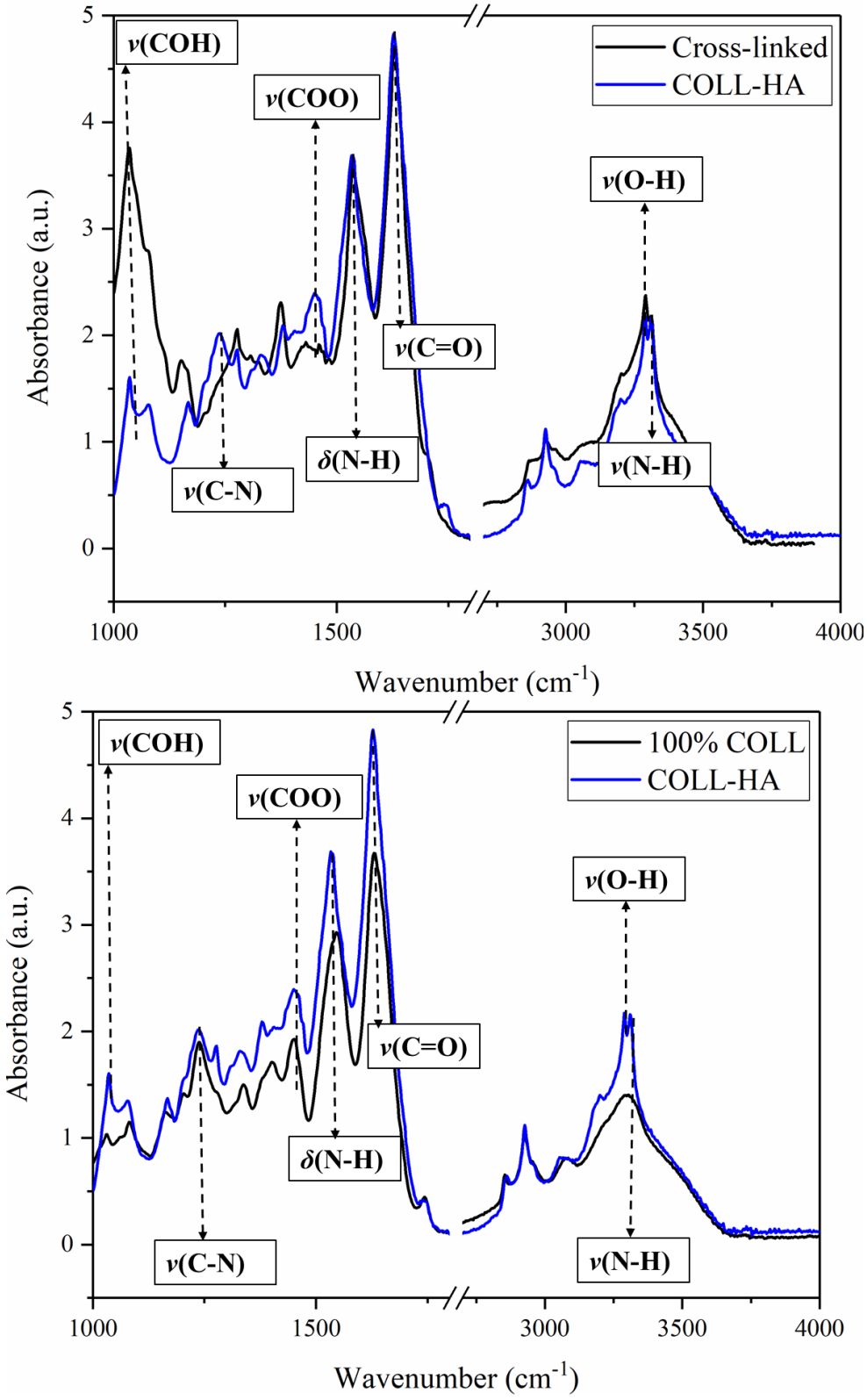

Figure 4.19: FT-IR spectra of cross-linked hyaluronic acid (ADH and EDC) and collagen-hyaluronic acid (coll-HA) scaffolds (top) and 100% collagen (uncross-linked) and coll-HA scaffold between 1000-4000 cm^{-1}. Data has been normalised at 2925 cm^{-1}.

4.3.5. Swelling Characteristics

The swelling response over a 24-hr period for uncross-linked and cross-linked FEG scaffolds in PBS are shown in Fig.4.20. The results show that solvent uptake occurs rapidly initially (within 30 mins of exposure) and then reaches equilibrium after 3 hrs of exposure with no significant difference up to 24 hrs. It was found that uncross-linked samples absorbed PBS at a faster rate of 217±115%/hr compared to 156±100%/hr for cross-linked samples. Both samples exhibited a similar response and reached equilibrium at comparable times, however, there was a significant difference in the final mass of the solvent absorbed, where uncross-linked and cross-linked scaffolds had an uptake of 560±30% and 380±30%, respectively.

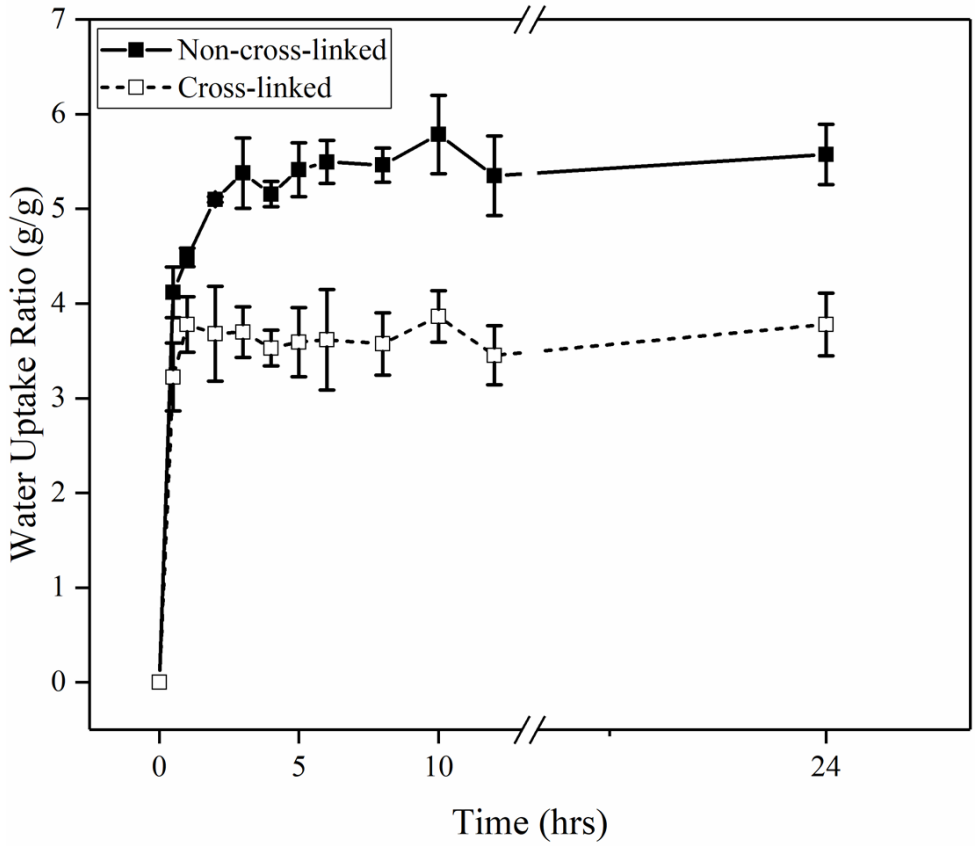

Figure 4.20: Solvent absorption profile over a 24-hr period at 37°C for uncross-linked and cross-linked fibrillar elastin gel-based scaffolds in phosphate buffered saline, n=3.

Solvent absorption after 24-hrs was measured for both uncross-linked and cross-linked scaffolds in deionised water and PBS at temperatures of 4, 20 and 37°C (Fig.4.20). It was found that both the uncross-linked and cross-linked scaffolds absorbed significantly more solvent when the solvent was deionised water, a very strong negative correlation between the mass of solvent absorbed and the temperature of the solvent was found for both sample types. A comparable trend was observed for samples exposed to PBS instead of water. It was found that uncross-linked samples absorbed more solvent irrespective of the type of solvent at all temperatures, whereas for cross-linked samples the mass of solvent absorbed was significantly lower only at 37°C for both solvents as shown in Table 4.12. Cross-linking led to a 5-fold, 4-fold and 3-fold decrease in the mass of water absorbed 4, 20 and 37 °C, respectively and a 3-fold, 2-fold and 1.5-fold decrease in the mass of PBS absorbed at 4, 20 and 37 °C, respectively. The volume fraction, polymer-solvent interaction parameter, molecular weight between cross-links and effective cross-link density have been summarised in Tables 4.13-14. Effective cross-linking of FEG by EDC was suggested by the 2.6-fold increase in cross-linking density.

Table 4.12: Solvent absorption after 24-hrs for uncross-linked and cross-linked FEG scaffolds

Sample	Solvent	Temperature (°C)		
		4	20	37
Uncross-linked	PBS	18.8 ± 1.3***	11.7 ± 0.4***	5.8 ± 0.4***
	Deionised Water	50.7 ± 3.6**	34.9 ± 4.2**	16.4 ± 0.4***
Cross-linked	PBS	6.7 ± 0.8	5.5 ± 0.3	3.9 ± 0.3**
	Deionised Water	10.3 ± 1.5	8.1 ± 0.9	5.3 ± 0.3**

***p<0.005 and ***p<0.0005 for change in temperature, n=3.*

Table 4.13: Volume Fractions (ϕ) and Interaction Parameters (χ) for 3%wt/v FEG-based scaffolds

Solvent	Temperature (°C)	ϕ		χ	
		Uncross-linked	Cross-linked	Uncross-linked	Cross-linked
Deionised Water	4	0.016	0.080	0.505	0.515
	20	0.024	0.101	0.508	0.525
	37	0.050	0.154	0.517	0.555
PBS	4	0.043	0.123	0.528	0.545
	20	0.070	0.147	0.537	0.555
	37	0.146	0.216	0.558	0.586

Table 4.14: Molecular Weight Between Cross-Links (M_c) and Effective Cross-Link Density (v_e) for 3%wt/v FEG-based scaffolds

Temperature (°C)	Mc		v_e	
	Uncross-linked	Cross-linked	Uncross-linked	Cross-linked
4	117.5	46.4	0.011	0.029
20	100.6	40.8	0.013	0.033
37	60.9	31.3	0.022	0.042

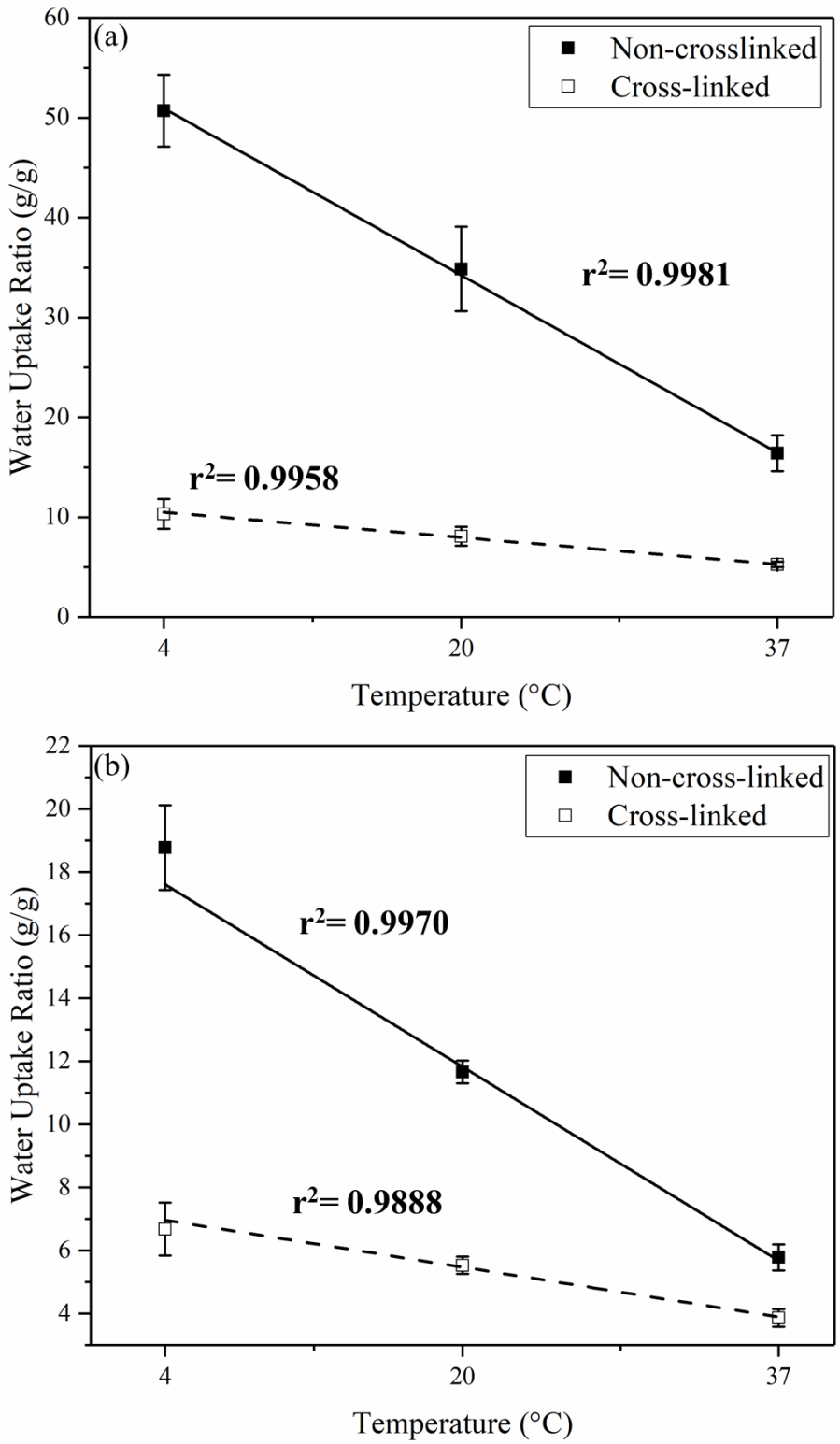

Figure 4.21: Solvent absorption for uncross-linked and cross-linked FEG scaffolds after 24-hrs at temperatures of 4, 20 and 37°C in (a) deionised water and (b) phosphate buffered saline. Shows the coefficient of determination (r^2) and n=3.

The effect of solvent absorption on the volume of uncross-linked FEG scaffolds with respect to temperature was studied using deionised water. Fig.4.22 shows that at lower temperatures, the samples expanded significantly (p<0.005) in comparison to the original volume. Photographs of the samples showing change in colour and size with increasing temperature can be seen in Fig.4.23. The samples contracted above room temperature (20°C), resulting in a reduction in the volume by 6-fold at higher temperatures. A very strong negative linear relationship between volumetric swelling and temperature was found (r^2= 0.9427) and a transition temperature of 30°C. The volumetric coefficient of expansion (α) was calculated to be -0.004 K^{-1} for these samples.

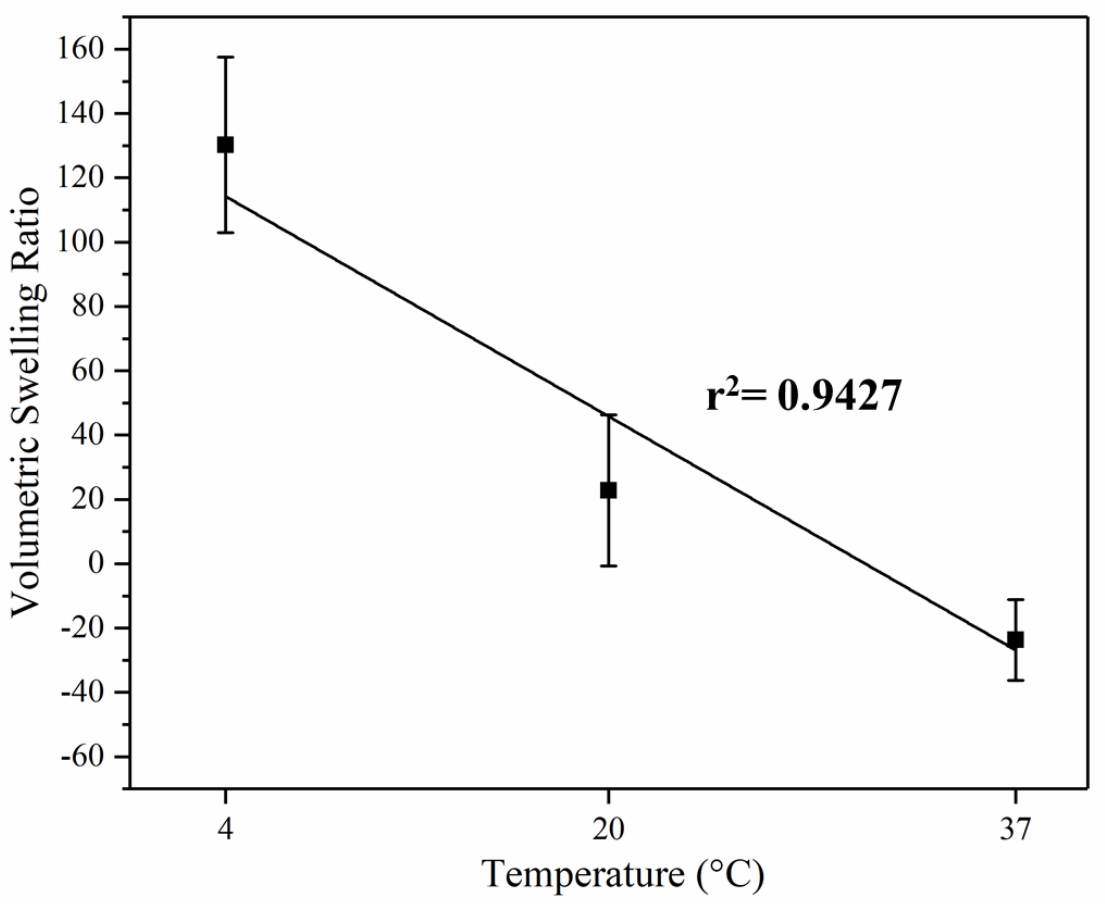

Figure 4.22: Change in volume after 24-hrs of solvent absorption for uncross-linked FEG scaffolds at temperatures of 4, 20 and 37°C in deionised water. Shows the coefficient of determination (r^2), n=3.

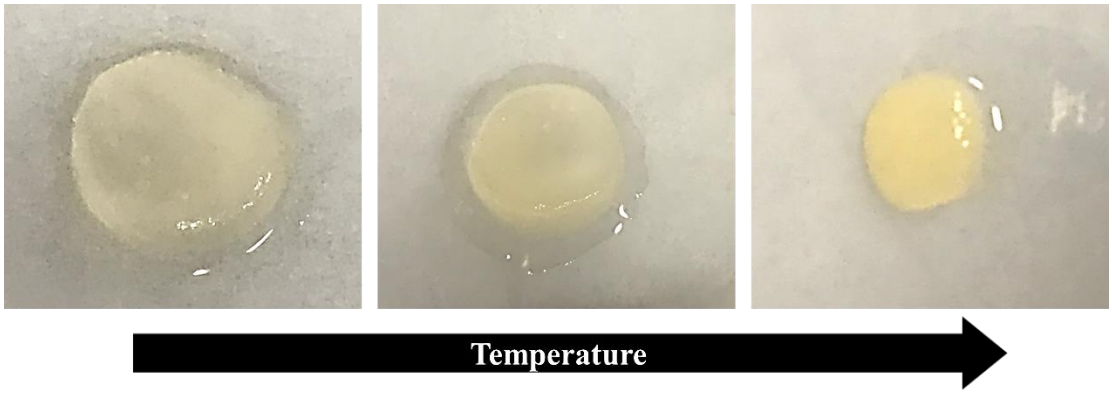

Figure 4.23: Photograph showing the change in volume of uncross-linked fibrillar elastin gel scaffolds swelled in deionised water at temperatures of 4°C (left) to 20°C (middle) and 37°C (right). A change in colour from transparent to opaque was observed with increase in temperature (not to scale).

Solvent absorption for collagen-based scaffolds was also studied in physiological conditions. Fig.4.24 shows the results for the mass of PBS absorbed after 24 hrs of swelling. It was found that the substitution of collagen for FEG resulted in a significantly lower absorption of solvent in a concentration dependent manner where the increase in FEG resulted in a decrease in the water uptake ratio. As collagen was replaced there was a 1.3-fold , 2.5-fold and 3.0-fold decrease in the water uptake ratio in 75C-25E, 50C-50E and 25C-75E, respectively where the solvent absorbed decreased significantly from 3810±210% to 1270±30% (Table 4.15). Collagen scaffolds were tested at different temperatures as a control (Fig.4.25). No significant difference was observed between temperatures in deionised water, however a 1.2-fold decrease in water-uptake was observed in PBS. The polymer-solvent interaction parameter, M_c and v_e have been summarised in Tables 4.16. M_c and v_e were normalised to uncross-linked scaffolds to determine the effect of cross-linking. Cross-linking was effective for 100C and 75C-25E samples, however, at higher concentrations of FEG there was no significant difference after cross-linking.

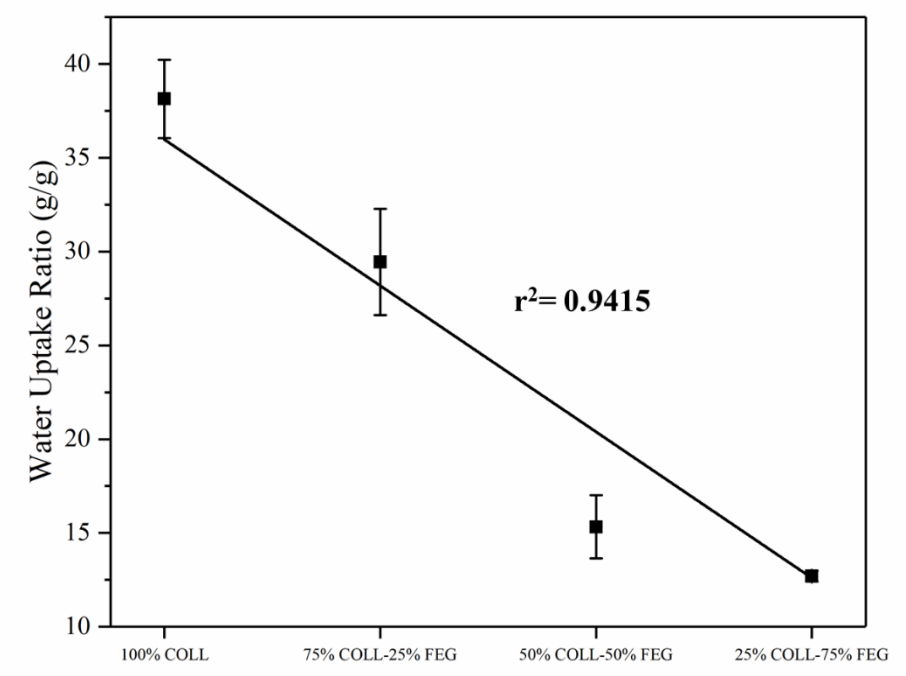

Figure 4.24: Solvent absorption in phosphate buffered saline at 37°C after 24-hrs for 100% collagen, 75% collagen-25% FEG, 50% collagen- 50% FEG and 25% collagen-75% FEG scaffolds. Shows the coefficient of determination (r^2) and n=3.

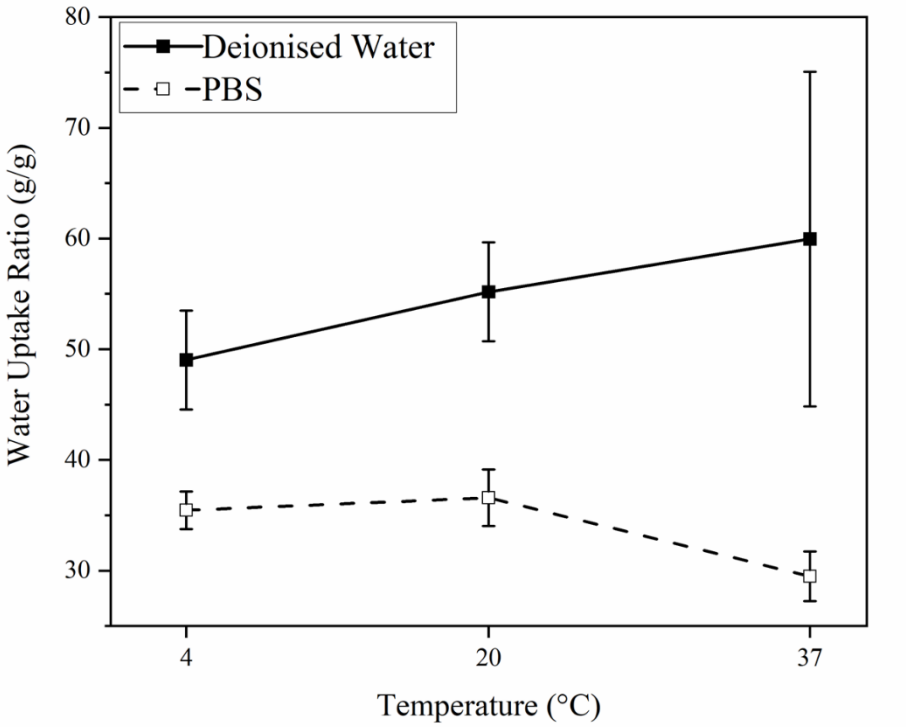

Figure 4.25: Solvent absorption for collagen only scaffolds after 24-hrs at temperatures of 4, 20 and 37°C in deionised water and phosphate buffered saline, n=3.

Table 4.15: Solvent absorption after 24-hrs in phosphate buffered saline at 37°C

Composition	Water Uptake Ratio (g/g)
100% FEG uncross-linked	5.6 ± 0.3**
100% FEG cross-linked	3.8 ± 0.3
100% COL	38.1 ± 2.1
75% COL-25% FEG	29.4 ± 2.3**
50% COL-50% FEG	15.3 ± 1.7***
25% COL-75% FEG	12.7 ± 0.3***
COL-HA	22.7 ± 2.1
TRI-LAYERS	26.0 ± 3.0

Table 4.16: Interaction Parameters (χ), Molecular Weight Between Cross-Links (M_c) and Effective Cross-Link Density (v_e) for 1%wt/v collagen-FEG-based scaffolds

Sample	χ	Normalised Mc	Normalised v_e
100% COL	0.506	0.7	1.5
75% COL-25% FEG	0.509	0.5	1.8
50% COL-50% FEG	0.512	1.1	0.9
25% COL-75% FEG	0.515	1.2	0.9

Samples tested in phosphate buffered saline at 37°C.
Mc and ve have been normalised to data for uncross-linked scaffolds.

The effect of the substitution of collagen for FEG on the volume of scaffolds after cross-linking was also studied. Fig.4.26 shows the effect of the replacement of collagen for FEG on the volume, it was found that above 50% FEG, the scaffolds contracted significantly after cross-linking. Scaffolds containing 100Cand 75C-25E contracted by 14.7±3.5 % and 12.8±4.4% respectively, with no significant difference between these two samples (Table 4.17). However, above 50% replacement resulted in a 2-fold and 3.7-fold decrease in the volume of the scaffolds for 50C-50E and 25C-75E samples, respectively. Samples containing 75%FEG behaved similar to samples

containing 100%FEG as there was no significant difference in the change in volume after cross-linking, although they are not directly comparable due to the difference in density of the scaffolds.

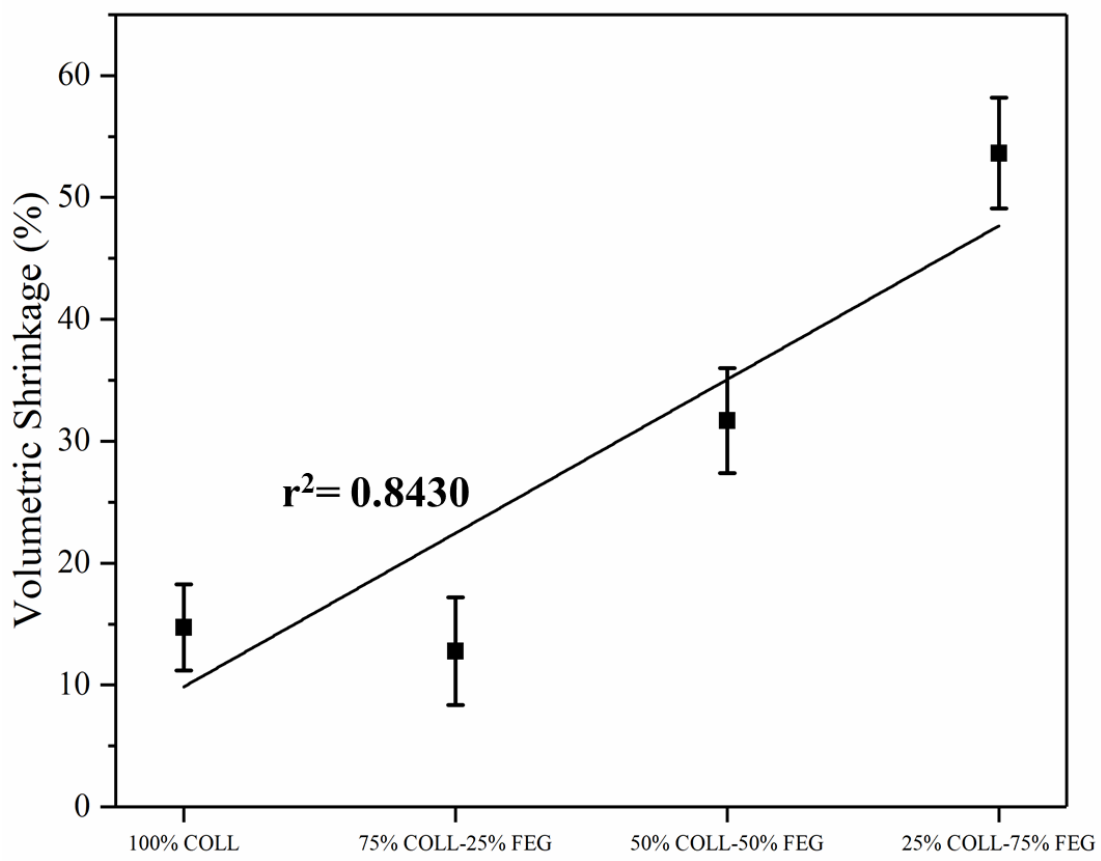

Figure 4.26: Change in volume after cross-linking with EDC/NHS for 100% collagen, 75% collagen-25% FEG, 50% collagen- 50% FEG and 25% collagen-75% FEG scaffolds. Shows the coefficient of determination (r^2) and n=3.

Table 4.17: Change in volume after cross-linking with EDC/NHS

Composition	Volumetric Shrinkage (%)
100% FEG	54.6 ± 6.6
100% COL	14.7 ± 3.5
75% COL-25% FEG	12.8 ± 4.4
50% COL-50% FEG	31.7 ± 4.3**
25% COL-75% FEG	53.6 ± 4.6***

***p<0.005, ***p<0.0005 for scaffolds compared to 100% COL, n=3.*

4.3.6. Degradation Characteristics

Biodegradation results for FEG-based scaffolds are presented in Fig.4.27 where the solvent used was either PBS only or PBS and elastase. It was found that in PBS only, there was no statistically significant difference in the response up to day 4 where uncross-linked scaffolds exceeded cross-linked scaffolds significantly by losing 21.4% of the mass compared to only 2.1% mass loss for cross-linked samples. After day 8, there was no significant difference in the mass loss of the uncross-linked samples. The effect of elastase is more significant as it directly targets elastin cross-links resulting in the degradation of the protein over time. As expected, uncross-linked scaffolds degrade faster than cross-linked scaffolds as the cross-linking increases the resistance to elastase. However, there is no significant difference in the degradation profile after day 4 and the cross-linked scaffolds start to degrade at a similar rate to uncross-linked scaffolds.

The degradation profile of collagen and coll-FEG based scaffolds are presented in Fig.4.28 with the mass remaining after 24-hrs in Table 4.18. There was no significant difference between the samples in PBS only over a 24-hr period where 10-17% of the

mass of the scaffolds was lost. 100C and 75C-25E scaffolds were very stable over the 24-hr period as only 10.3% and 15.4% of the original mass was lost as observed in PBS only. When more than 50% collagen was replaced there was a significant loss of mass after 24-hrs in collagenase which coincided with the concentration of FEG in the scaffolds, that is approximately 50% loss in 50C-50E samples and 75% loss in 25C-75E. In elastase, there was almost no change in the mass of 100C and 75C-25E scaffolds showed no significant difference to the controls in PBS only. Whereas, for the composites with more than 50% FEG the mass loss corresponded very closely with the mass of FEG present in each scaffold type, where there was a loss of 55.5% and 73.1% in 50C-50E and 25C-75E, respectively.

Table 4.18: Mass of scaffolds after 24 hours of degradation in phosphate buffered saline, 0.1 U/ml collagenase and 0.1 U/ml elastase.

Composition	Mass Remaining (%) after 24 hrs		
	PBS	Collagenase	Elastase
100% COL	90.0 ± 7.4	90.7 ± 12.5	99.5 ± 0.9
75% COL-25% FEG	84.2 ± 3.6	84.6 ± 9.3	88.9 ± 2.1
50% COL-50% FEG	86.5 ± 9.3	59.1 ± 6.5*	44.5 ± 9.6***
25% COL-75% FEG	83.3 ± 12.8	28.6 ± 3.6***	26.9 ± 4.1***

*where *p<0.05, ***p<0.0005 0005 for scaffolds compared to 100% COL, n=3.*

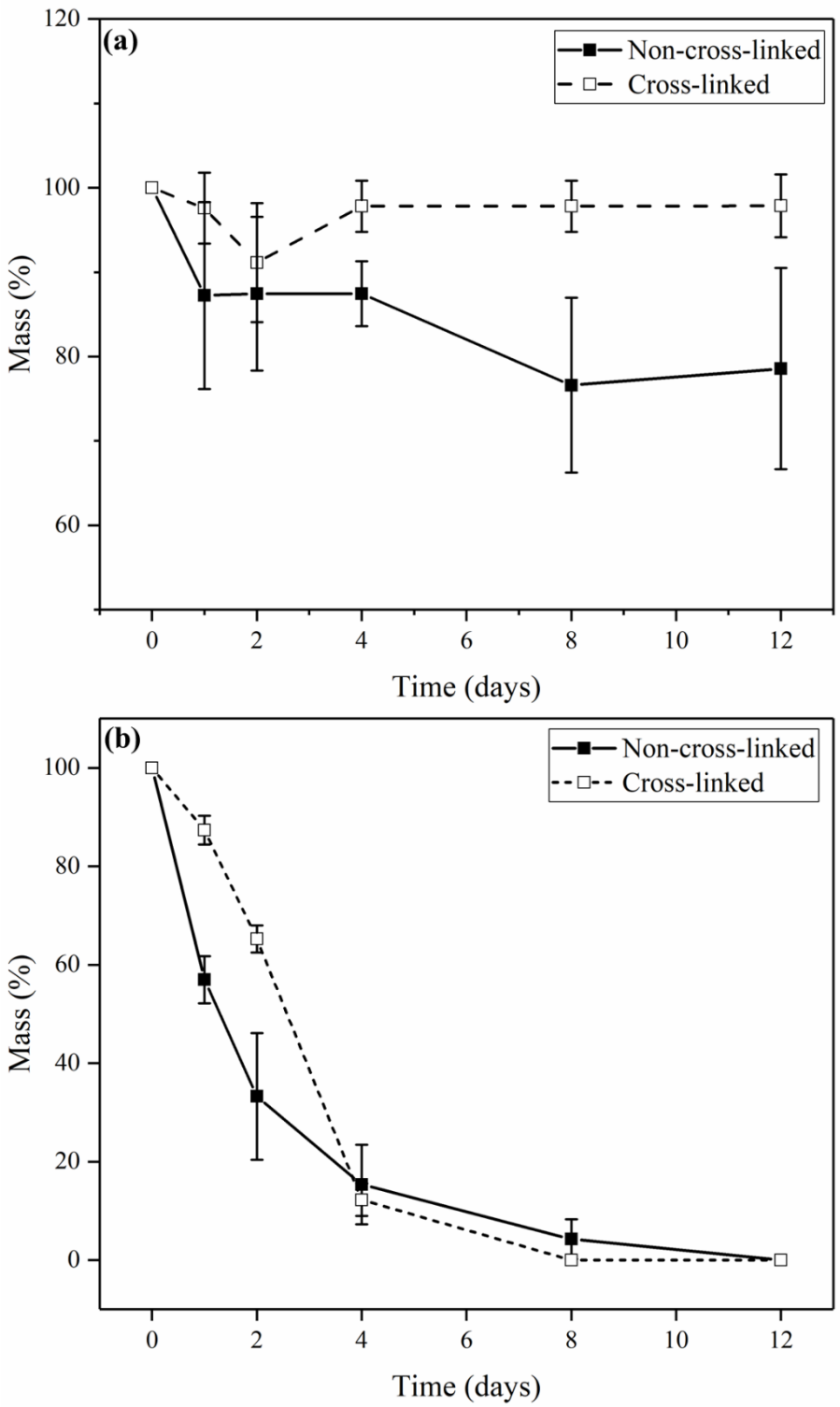

Figure 4.27: Degradation characteristics of uncross-linked and cross-linked FEG-based scaffolds in (a) phosphate buffered saline only and (b) in 0.1 U/ml porcine elastase for a 12 day period, n=3.

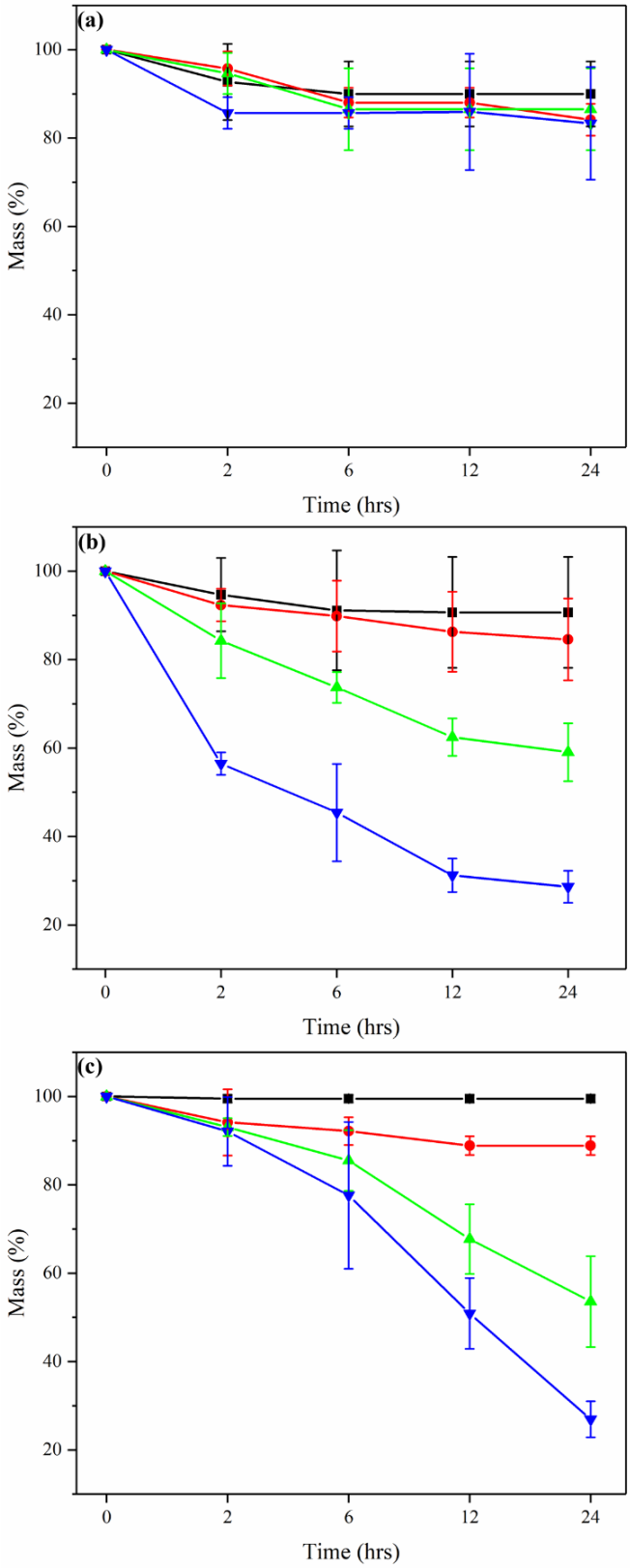

Figure 4.28: Degradation characteristics of ■ 100% collagen, ● 75% collagen-25% FEG, ▲ 50% collagen- 50% FEG and ▼25% collagen-75% FEG scaffolds in (a) phosphate buffered saline, (b) collagenase and (c) elastase over 24 hours, n=3.

4.4. Discussion

4.4.1. Effect of Processing Conditions

4.4.1.1. Formation of Suspensions & Rheological Properties

The polyampholytic behaviour of collagen has been studied extensively [332] and its ionisation at acidic pH is frequently practised to obtain slurries for the fabrication of multiple structures [165], [167], [333]. Collagen and collagen-FEG suspensions were prepared in acidic conditions as collagen is known to denature in alkaline conditions [334]. Swelling of the proteins occurs in ethanoic acid as the pH is below the pI of both collagen (7.2-7.8 [307], [335]) and FEG (~5.6). The ionisation of amino acid residues such as lysine, arginine and hydroxylysine in collagen and those listed in Table 3.12 for FEG give rise to electrostatic repulsion between positively charged groups. The suspension/solution forms due to increased polymer-solvent interactions post-ionisation which increase the water-uptake by the protein/s (discussed in Section 3.4.4. for FEG).

The collagen-based suspensions studied exhibited a shear thinning response as has been reported previously [336]–[338]. The rheology results suggest that the substitution of collagen by FEG changes the properties of the suspension from an elastic solid (100C and 75C-25E) to a viscous liquid (50C-50E and 25C-75E) as the concentration of collagen decreases and FEG increases. 100C and 75C-25E suspensions behave as gels as there is no cross-over between the storage and loss modulus and the storage modulus is more dominant at all frequencies. Above 50% replacement, there is a cross-over between the moduli which implies that there is less cohesion between fibres and an increase in physical interactions. The results imply that

with the substitution of collagen for FEG, the interaction between the proteins changes from being chemical to physical. This can be explained by the aspect ratio of collagen and its effect on the crowding factor (N_c) as discussed in 3.4.3. The aspect ratio of collagen is 200 as its length is 300nm and diameter is 1.5nm [339], therefore, N_c, for a 1%wt/v solution of collagen is ~267 which suggests it behaves as a strong gel and therefore is a concentrated dispersion. As N_c is 5.1-fold lower for FEG, the replacement of collagen would decrease the aspect ratio of the composites and therefore the dispersion changes from a concentrated to a semi-concentrated dispersion. The decrease in aspect ratio results in a decrease in viscosity as fibres have a higher freedom of movement and are less packed. Although FEG was substituted for collagen, the effect of its addition is not as prominent as seen in FEG itself, this can be explained by the lower relative density of the composite suspensions (1%wt/v) compared to the FEG dispersion (3%wt/v).

4.4.1.2. Effect of Freezing-Temperature, Concentration & Composition

Freeze-drying is commonly used to dehydrate tissues for microstructural analysis as well as to form constructs as the ultrastructure of extracellular matrix molecules is preserved. This has been shown experimentally for both structures of elastin [340] and collagen where characteristics such as the D-banding in collagen was not significantly affected post-freeze-drying [240]. Freeze-casting or "ice-templating" is a fabrication technique whereby a porous structure forms from a suspension containing two phases, (1) solid particles which are well dispersed in a (2) liquid media (the solvent). It involves the solidification of the solvent, by freezing, and its removal by sublimation, leaving the negative replica of the ice-crystals [147].

Solidification is controlled by the processing conditions which affect the nucleation and growth of ice-crystals, these include temperature, concentration, viscosity, additives and mould design [341], [342]. The effect of processing parameters such as freezing temperature [236], [343]–[345] and concentration (relative density) of suspensions [240], [346] have been studied extensively for collagen-based scaffolds. Freeze-casting has not been implemented for elastin-based scaffolds due to their poor interactivity with solvents. In this work, the effect of freezing temperature on the pore size of FEG-based scaffolds with three different concentrations was studied. The morphology of the pores is controlled by the velocity of the solidification-front (interface between the suspension and newly formed solid) and the resultant morphology of nucleated ice-crystals. During the solidification process, the particles which in this case are FEG and/or collagen fibres, are rejected by the growing ice-crystals and trapped in inter-crystal spaces as shown in Fig.4.29 for FEG.

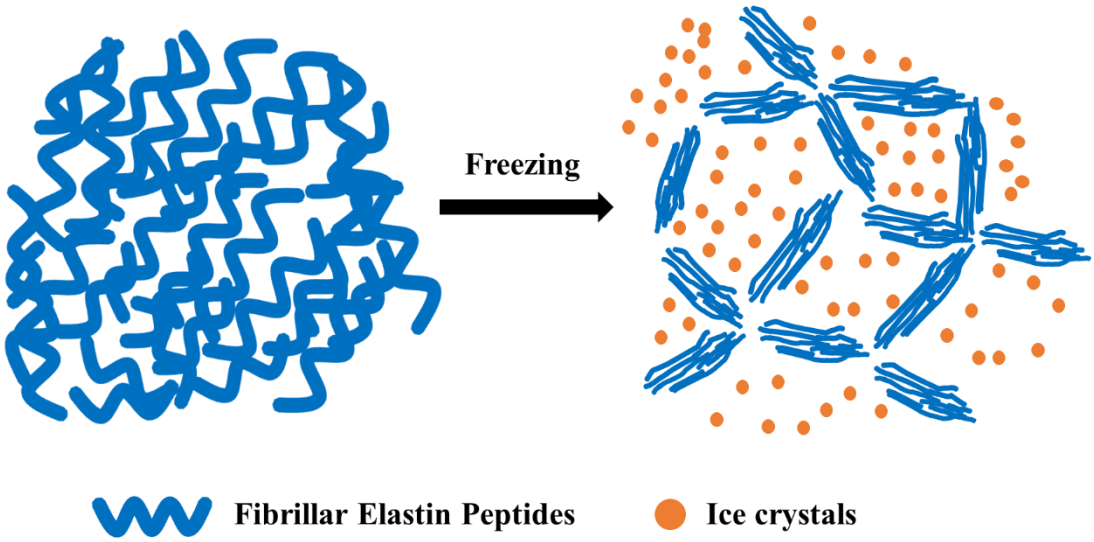

Figure 4.29: Ice crystal growth in fibrillar elastin gel solution where the peptides (blue) concentrate in inter-crystal spaces as they are rejected by the growing ice crystals (orange).

The rejection of particles into inter-crystal spaces is controlled by the interaction between the advancing solidification-front and the particles. For rejection to occur, the interfacial free energy (σ*) between the solidification-front (s) and the particles (p) must be larger than the sum of the interfacial free energies of the solidification-front to the liquid (l) and the particles to the liquid [347], [348]:

$$\Delta\sigma^* = \sigma_{sp}{}^* - \left(\sigma_{sl}{}^* + \sigma_{pl}{}^*\right) > 0 \qquad \text{(Equation 4.11)}$$

The rejection of particles by the solidification-front is dominated by two opposing forces, viscous drag (attractive) and van der Waals forces (repulsive) which reach equilibrium at a critical velocity (V_c). The V_c can be described simply as inversely proportional to the hydrodynamic radius of the particle and controls whether a particle is trapped between growing crystals ($V \geq V_c$) or rejected into the liquid phase ($V < V_c$) [349], [350].

The phase transition from liquid to solid and the resultant ice-crystals is controlled by the freezing temperature and the number of available nucleation sites. Heterogenous nucleation occurs at the open-end of the mould where a smaller degree of undercooling is required to form stable nuclei. The number of critical nuclei (n*) formed is a function of temperature (T) as:

$$n^* = A \exp\left(-\frac{\Delta G^*}{k_b T}\right) \qquad \text{(Equation 4.12)}$$

where the constant, A, is associated with the total number of nuclei of the solid phase; ΔG^*, is the activation energy required to form a stable nucleus and k_b, is the Boltzmann's constant [351]. Ice nucleation is favoured at lower temperatures (higher undercooling) where numerous, smaller pores form that are more uniform, whereas

ice-growth is favoured at higher temperatures (slower undercooling) where fewer, larger pores form as shown in Fig.4.30 [352].

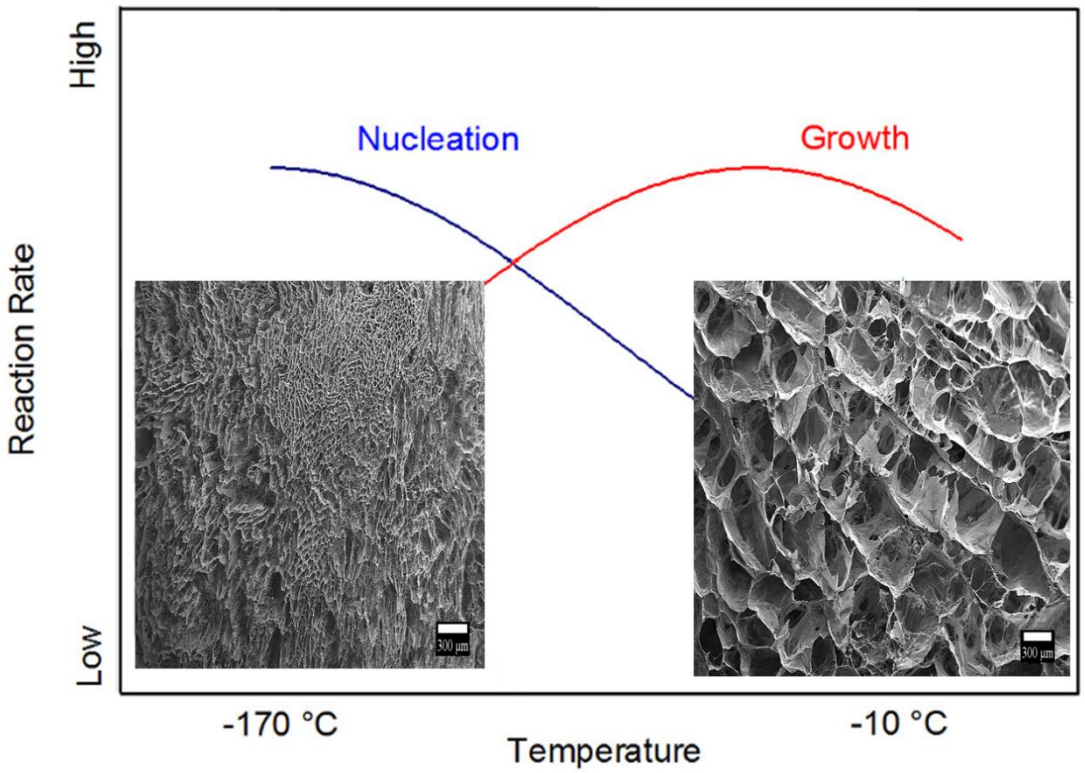

Figure 4.30: Temperature dependent solidification of ice which favours nucleation at low temperatures and growth at higher temperatures. Adapted from reference [353] with collagen scaffold images at -80°C (left) and -4°C (right) with a scale bar at 300µm.

When solidification is initiated, a concentration gradient forms as impurities are rejected from the newly formed ice-front, this reduces the melting point of the liquid and provides sufficient activation energy to the break planar ice-front and form a columnar interface [354]. This phenomenon is known as the Mullins–Sekerka instability and provides the initial activation required to form a columnar structure which eventually leads to different microstructures.

The microstructures reported in Section 4.3.3 showed plate-like (lamellar) structures for FEG-based scaffolds which evolved to equiaxial (isotropic) structures as the concentration of FEG increased from 0.5 to 3.0%wt/v. At concentrations of 3.0%wt/v, significantly smaller pores (1.5-fold) were obtained at the lower freezing temperature (-80°C) as the trend predicts (Equation 4.12), however, this was not observed for the remaining compositions. A possible reason for this variation could be that significant volumetric contraction occurred post-freeze-drying where samples of lower concentrations collapsed. The collapse of scaffolds ≤1.0%wt/v is mostly likely due to poor cohesion between FEG molecules [355].

The pore size, aspect ratio and wall thickness were independent of concentration and freezing temperature for majority of the samples. Dilute suspensions result in lower particle-to-particle interaction and therefore lower viscosity which although not experimentally measured in this study can be suggested to decrease with concentration of FEG molecules as this is commonly observed in biopolymer-based suspensions [337], [355]. At -80°C, a significant difference was observed between the concentrations where the higher the concentration of FEG, the smaller and well-defined the pores were (3.0<1.0<0.5%wt/v). This trend agrees with results observed for collagen-based scaffolds [240], [346] and has been suggested to be due to an increase in mechanical hinderance by the FEG molecules which slows down the growth of ice-crystals and subsequently forms smaller pores. In Section 3.4.3, it was established that FEG is a gel composed of aggregated fibres which exhibit shear thinning properties. Taking the rheological behaviour of FEG into account, it can be suggested that the increase in concentration of FEG is associated with higher aggregation and therefore larger particle size. The larger particles at higher

concentrations result in a lower V_c and therefore promote packing between ice-crystals and the formation of isotropic pores whereas smaller particles result in a higher V_c and rejection into the liquid phase, resulting in a lamellar structure due to poor interfibrillar contact [349], [356].

For collagen-FEG composites, a significant difference in the morphology and pore size was observed. It was found that the substitution of collagen for FEG increased the pore size up to 50% replacement. The effect of the composition on the pore size can be related to the viscosity of the suspensions as it is a critical parameter that can also be used to determine the V_c of the solidification-front [149]. The viscosity of the composites was discussed in 4.4.1.1. where a decrease in viscosity with the substitution of collagen was observed. The decrease in viscosity has an effect on the diffusivity of the particles which can be explained by the Stokes-Einstein relationship [357]:

$$Dc = \frac{k_b T}{6\pi R\eta} \qquad \text{(Equation 4.13)}$$

where D_C, is the diffusion coefficient and R, is the hydrodynamic radius. This suggests that as the concentration of FEG increased, the viscosity decreased, and therefore the diffusivity increased. The decrease in viscosity results in an increase in V_c and therefore the particles are rejected further due to lower mechanical hinderance resulting in larger pores. A significant decrease in pore size was observed for 25C-75E samples which was accompanied by a significant increase in the pore wall thickness compared to the other samples. This could be due to the low viscosity which reduces the cohesion between particles and therefore results in collapse of the scaffold as seen with lower concentrations of FEG-only scaffolds.

Pore sizes for coll-HA scaffolds were in good agreement with those reported by Nazir *et al* [192], and the cross-linking was also effective as concluded by the appearance of twin peaks in FT-IR. Tri-layer scaffolds did not show any significant difference in the pore size compared to the monolayer scaffolds of 100C, coll-HA or 50C-50E. However, the pore morphology of the 50C-50E appeared more lamellar than the monolayer scaffolds, as the 50C-50E layer was closest to the open-end of the mould and therefore experienced a higher degree of undercooling compared to the other layers.

The scaffolds fabricated in this study fall within the optimum pore size required to promote cellular adhesion and proliferation (50-150μm [138]). To the best of the authors knowledge, freeze-casting of elastin-only scaffolds has not been reported to date due to the poor processability of elastin. In this work, FEG-based scaffolds were fabricated successfully and shown to form coherent pores with high porosity (94%) and pore sizes that are more suitable than scaffolds composed of soluble elastin as summarised in Table 4.19. The collagen-based scaffolds had pore sizes between 52-143μm and porosities above 98% which is comparable to those reported for collagen and insoluble elastin-based scaffolds [175], [229], [236], [237] and larger than those reported for collagen and soluble elastin-based scaffolds [225], [230], [232]. The similarity to collagen and insoluble elastin-based scaffolds suggests that FEG is microstructurally similar to polymeric elastin as discussed in 3.4.1. and therefore, can provide better structural integrity compared to soluble variants.

Table 4.19: Average pore size and porosity of elastin-based constructs in comparison to fibrillar elastin gel (FEG)-based scaffolds.

Sample	Average Pore Size (μm)	Porosity (%)	Ref
FEG (3%wt/v)	46–63	94.0	This study
α-elastin (100 mg/ml)	20-35	NR	[208]
α-elastin (100 mg/ml)	4-80	NR	[206], [207]
α-elastin (20%wt/v)	0.5-3.0	NR	[211]
α-elastin (20%wt/v)	0.7- 2.1	NR	[210]

NR=not reported.

4.4.2. Swelling Behaviour of FEG-Based Scaffolds

The extent of the absorption of water and its effect on the volume of the scaffold was studied in Section 4.3.6. FEG-based scaffolds absorbed between 380-560% of water within 3hrs of the experiment which is sufficient for tissue engineering applications ($Q_m \geq 120$-200% [358]). This is significantly higher than insoluble elastin which has been reported to swell by only 46% at 36°C [359]. Uncross-linked FEG scaffolds did not disintegrate, or dissolve as soluble elastin scaffolds tested during preliminary work which implies that FEG molecules are inherently cross-linked. The water absorbed during swelling can be of three forms: primary bound, secondary bound, or bulk (or free) water. When a scaffold is added to the solvent, water diffuses into the network and hydrates the hydrophilic groups by primary bound water, this results in swelling of the scaffold and exposure of hydrophobic groups which also bind to water (secondary bound water). Further water is absorbed (bulk water) until an equilibrium is reached between the elastic-refractive forces of the polymer chains and the mixing contribution of osmotic swelling pressure [360], [361].

The decrease in swelling and the lower swelling rate observed after cross-linking of FEG scaffolds suggests that hydrophilic sites such as lysine were consumed by the cross-linking process. Another possible reason for the difference is the decrease in pore size after cross-linking as larger pores have a lower surface area, and therefore the average diffusion pathlength is reduced resulting in higher diffusion of water into the scaffold as seen with the uncross-linked scaffolds [362]. Additionally, the increase in stiffness post-cross-linking can also be associated with a decrease in water-uptake as the elastic-refractive force of the polymer chains increases and therefore the cross-linked scaffolds cannot extend to the same degree as uncross-linked scaffolds to accommodate for the absorption of water [363]. This is shown by the significant increase (2.5-fold) in the cross-linking density after cross-linking at room temperature.

Both uncross-linked and cross-linked samples showed an increase in cross-linking density with temperature which suggests that the hydrophobic interactions became increasingly stronger. The solubility of FEG was evaluated by determining χ at different temperatures in deionised-water and PBS. The interaction between FEG and the solvent decreased with increase in temperature and was poorer in PBS. FEG had lower and narrower χ between 0.505-0.517 than that reported for elastin at similar temperatures (0.670-0.928) [260]. This suggests that FEG has better polymer-solvent interactions and is less hydrophobic compared to insoluble elastin as the higher the parameter, the weaker the interaction between the polymer and solvent and the stronger the hydrophobic polymer-to-polymer interactions. Taking the swelling results at different pH from Section 3.4.4. it can be said that the acidic solvent (pH of 2-3) and basic solvent (pH of 10-12) have a similar interaction with FEG as water as χ was 0.510 and 0.514, respectively. At the pI, χ was 0.538 which is similar to samples tested

in PBS and had a lower degree of swelling. FEG has better miscibility than elastin, however, it has a high interaction parameter ($0.5<\chi<1.0$) which is borderline between an ideal ($\chi=0.5$) and a poor solvent ($\chi>0.5$) depending on the temperature and solvent [260]. These results suggest that although the miscibility of FEG is higher in comparison to insoluble elastin, it is still insoluble in water and solvents that have a pH close to its pI.

Scaffolds containing FEG exhibited an inverse temperature transition (ITT) at 30°C where the solubility decreased with increasing temperature (4.3.5). This temperature is referred to as the lower critical solution temperature (LCST), it is the critical temperature below which FEG swelled (more miscible) and above which FEG contracted (less miscible). In the swollen state, FEG is extended and has more polymer-solvent interactions whereas it is in a contracted state above the LCST with predominantly polymer-polymer and solvent-solvent interactions, resulting in phase separation. The LCST is an entropically driven phenomenon which is energetically favoured as the increase in temperature increases the entropy of the solvent resulting in a decrease in total free energy [364], [365]. The rearrangement of the solvent occurs due to the "hydrophobic effect" where water becomes less ordered resulting in a higher entropy and the protein aggregates by an increase in intra- and inter-molecular interactions which take place to reduce the interfacial area between the fibres and the solvent [366], [367]. This conformational change of elastin as a function of temperature has been modelled by Urry *et al* [368], [369] using synthetic elastin-like-polypeptides (ELPs). It was found that ELPs collapsed above the LCST and extended below it as shown in Fig.4.33. This phenomenon has also been observed in α-elastin based hydrogels and has been suggested to be responsible for elastin's high

extensibility [370]. ELPs and FEG exhibit a similar negative thermosensitivity due to the abundance of hydrophobic side groups. In elastin, 75% of the amino acid composition contains non-polar, aliphatic functional groups such as glycine, alanine, valine, and leucine [50] which is similar to FEG as the hydrolysis process targeted hydrophilic groups (3.4.3).

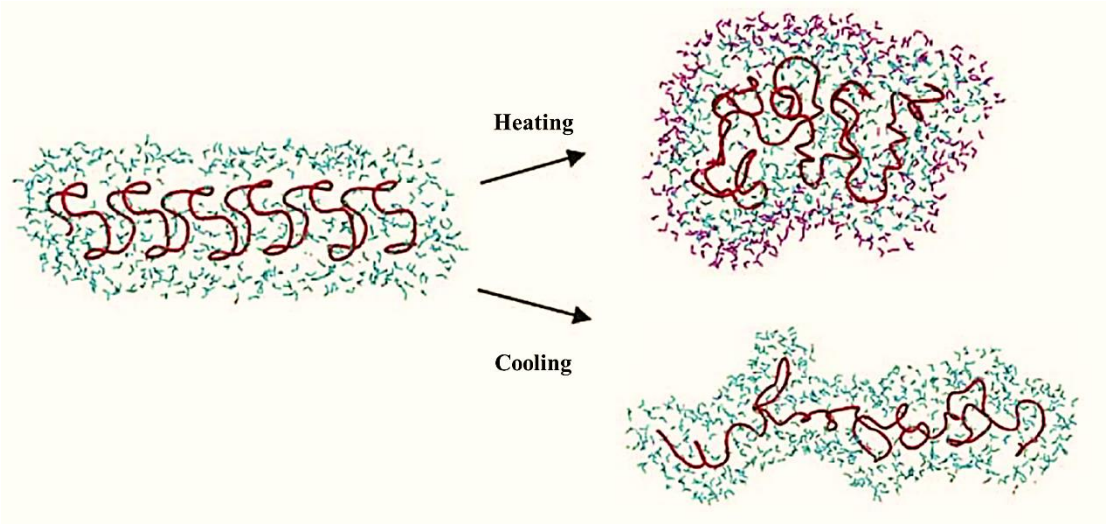

Figure 4.33: Structural change of Elastin-Like-Polypeptides (red polymer chain) with imbibed water (blue). When heated to temperatures above the lower crtical solution temperature (LCST), the structure of the ELP changes to a contracted state where phase separation occurs and there is an increase in hydrophobic protein-protein interactions and solvent expulsion (magenta). When below the LCST, the ELP strucutre is extended in a relaxed state with polymer-solvent interactions and increased miscibility. Adapted from [57].

Samples tested in PBS showed a 2.8-fold decrease in the degree of swelling for all temperatures and an increase in the interaction parameter which implies that the miscibility of FEG is reduced in ionic solvents. The osmotic pressure between the scaffold and the solvent decreases due to the presence of ions. The majority of the water absorbed by FEG is via ionisable groups such as the carboxylate and amine groups. These groups bind to the ions present in PBS (Na^+, K^+ and Cl^-) leading to a charge screening effect which decreases the solubility of FEG [297], [298]. The

decrease in swelling is associated with volumetric contraction as the hydrophobic groups rearrange to reduce the accessible surface area by aggregating as reported for ELPs that were tested with salts that followed the Hofmeister series [371].

Collagen-FEG composites were studied at 37°C and showed a decrease in water-uptake with increase in FEG content as well as a significant volumetric shrinkage post-cross-linking. The results suggest that collagen could not support its structure and contracted due to the dominance of the sensitivity of FEG. The significant shrinkage observed even after the use of ethanol during cross-linking, which has been shown to decrease shrinkage by removing residual acid [236] suggests that it was primarily dominated by the presence of FEG and the proximity of the cross-linking solution (pH of 4.8) to the pI of FEG. To confirm the dominance of FEG in swelling studies, the degree of swelling of collagen-only scaffolds at different temperatures was also studied and showed no significant difference between the scaffolds in deionised-water and therefore no temperature dependence. A difference in water-uptake was observed at 37°C in PBS (1.2-fold) suggesting that collagen experiences contraction, however, this was significantly lower than that observed with FEG-only scaffolds implying that the swelling response observed in composites is dominated by FEG. The contraction observed is most likely due to the hydrophobic groups in collagen of which glycine composes 33%. Collagen only scaffolds exhibited a similar salt screening effect to FEG which has also been reported [372], [373].

The microstructural studies of scaffolds showed that FEG is randomly distributed in the collagen-FEG composites but embedded in the collagen struts physically as shown in Fig.4.34. There was no significant difference in cross-linking density of cross-linked samples compared to uncross-linked samples containing more than 50% FEG. This

could suggest that FEG is physically bound to collagen instead of chemically and also explains why the collagen could not support its structure when FEG collapsed as seen with interpenetrating networks composed of thermosensitive polymers [369]. These results suggest EDC is not sufficient to cross-link smaller concentrations of FEG (0.25-0.75%wt/v) as an increase in cross-linking density was observed with FEG-only scaffolds which had a higher relative density. The reason for this could be the low amine and carboxyl groups in FEG as well as competition between collagen and FEG as they both cross-link via the same route. To confirm this effect further experiments such as a 2,4,6-trinitro-benzenesulfonic acid assay would be required to quantify the concentration of amine groups and the degree of cross-linking. Alternatively, composites which are controlled at the molecular level can be designed by using the "bottom up" approach and taking advantage of both FEG's ability to coacervate and monomeric collagen's ability to undergo fibrillogenesis *in vitro*. This will ensure that the fibres self-assemble at the molecular level and therefore they should theoretically bind by intermolecular interactions.

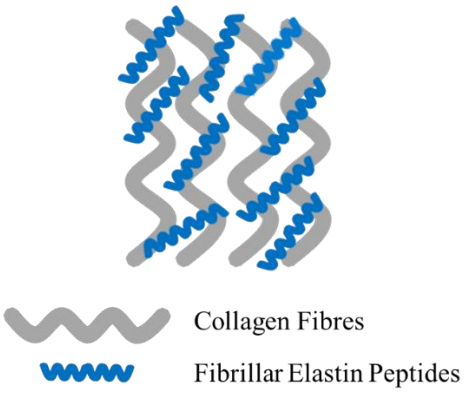

Figure 4.34: Collagen-FEG composite showing the random distribution of FEG fibres deposited on collagen fibres.

4.4.3. Degradation Behaviour of FEG-Based Scaffolds

Biodegradation is important for the replacement of the scaffold by newly synthesised tissue. As FEG is a novel form of elastin, its degradation properties are unknown and therefore were studied in this thesis. It was found that FEG was degradable by elastase and resisted degradation and cross-linking with EDC improved its resistance significantly up to day 4. The results show that in comparison to α-elastin, FEG offers better resistance as it has been shown to degrade within 6-hrs at similar concentrations of elastase [209]. In addition, a similar level of resistance was observed to decellularised elastic tissues which degraded by more than 50% after 4 days [374]. Scaffolds in PBS showed a decrease of 22% over 12 days which implies that some soluble peptides that remained had dissolved during the test, this was absent in cross-linked FEG as the cross-linking process would remove any soluble peptides. These results are promising as they suggest that the degradation characteristics of FEG can be improved by cross-linking and therefore FEG is a tailorable material.

Similarly, collagen-FEG composites showed a 17% decrease in PBS which most likely accounts for some remaining soluble peptides, however, majority of the scaffold was insoluble in PBS. The degradation results show that FEG did not form an independent network in the scaffolds but was physically bound to collagen which is also supported by SEM and LSCM findings (4.3.3). The enzymatic degradation revealed that FEG was susceptible to proteolytic degradation by both elastase which is specific to elastin and collagenase which is not. A possible explanation for this could be that embedded fibres were released when collagen was enzymatically attacked or that FEG is susceptible to degradation by collagenase as this has been seen for ELPs [222], [331].

4.4. Summary

This chapter presented a method to freeze-cast FEG-based suspensions to produce highly porous scaffolds. Scaffold types included monolithic (FEG-only), composites (collagen-FEG), coll-HA and tri-layers. Post fabrication, the physiochemical properties of scaffolds were characterised. The properties of interest were the microstructure of scaffolds, infrared spectroscopy to show the effect of processing and the swelling and degradation characteristics. The main findings include:

- 3%wt/v FEG-only scaffolds were chosen as the best composition for good pore integrity and the least volumetric contraction. This composition was used to fabricate scaffolds and had a porosity of 94% and average pore size between 47-63µm. Cross-linking of the scaffold by EDC/NHS was shown to be effective with the increase in cross-linking density as well as an increase in the Amide I/Amide A ratio as shown by FT-IR. The increase in cross-linking density was found to decrease the water-uptake capacity but improve the resistance to degradation by elastase.
- The effect of temperature and solvent type was studied in detail for FEG-only scaffolds. It was found that FEG had a negative temperature dependence and an ITT at 30°C which affected its molecular conformation and polymer-solvent interaction. At higher temperatures FEG adopted a contracted state with poor water-uptake whereas at lower temperatures it extended and absorbed significantly more solvent.
- Collagen-FEG composites with high porosities (>98%) and average pores sizes between 52-143µm were fabricated. Microstructural analysis revealed physical embedding of FEG fibres in collagen where the latter formed the dominant

structure for all compositions. Additionally, it was found that FEG dominates the swelling characteristics of composites in a concentration dependent manner by showing a decrease in water-uptake with an increase in FEG content.

- A method to fabricate porous, inter-connected tri-layer scaffolds with good inter-layer adhesion and porosity was devised where scaffolds had layer dependent porosity between 90-124μm and mimicked the tri-layer structure of heart valves in terms of composition.

5

Mechanical Properties of Scaffolds

5.1. Introduction

The mechanical properties of a scaffold are important for tissue engineering (TE) applications as they influence the cellular response. This is especially true for valvular interstitial cells (VICs) which are mechanosensitive and have been shown to change phenotype depending on the substrate stiffness [141], [375], [376]. Emulating the non-linear deformation mechanics of heart valves is very important to be able to replace them with a functional alternative. Synthetic polymers that exhibit a plastic deformation regime are employed ubiquitously due to their high mechanical properties and tunability but more often than not lead to fibrous encapsulation and calcification [377]. For *in vitro* TE the mechanical properties of valves are not design goals as it is expected that cells will synthesise new matrix that can match the original if provided with the correct biochemical and biomechanical cues.

This chapter will study the tensile and compressive properties of FEG-based scaffold where particular attention will be given to the mimicking of deformation characteristics of elastin which are a low stiffness and high strain-to-failure. Tri-layer scaffolds will be studied in terms of their tensile and bending properties and compared to monolithic scaffolds to determine the effect of each layer.

5.2. Materials & Methods

5.2.1. Compression & Tensile Testing

Static uniaxial compression and tensile tests were performed using the Dynamic Mechanical Analyser (DMA) 7e (PerkinElmer, UK) which was connected to a 2.5N load cell. Samples were prepared as stated in section 4.2.1 and hydrated in PBS for at least 2 hrs prior to the test and tested at room temperature. Compression was performed unconfined using a standard parallel plate at a rate of 20 mN/min until failure. Tensile samples were mounted with epoxy adhesive to prevent slippage at the grips in the dry state and then hydrated in PBS. Samples were inserted in tensile clamps and secured using screws to prevent slippage, a PBS bath was used to maintain the hydration of the samples. All tensile samples were tested to failure at a rate of 10mN/min with no preload. The dimensions of all samples were measured using a digital caliper prior to testing. Stress-strain curves were plotted to obtain the Young's modulus (E_T), two regions were of interest, low strain (5-10%) and high strain (30-40%).

5.2.2. Rheology of Scaffolds

Collagen-FEG scaffolds were tested using the 25mm stainless steel parallel plate geometry with a constant normal force of 0.5N. Dynamic frequency sweeps for the samples were performed from 0.1 to 10 Hz at 37°C with a constant strain of 5%. During the test, the sample was kept inside a chamber with water-soaked cotton at the edges to minimise water evaporation. The viscoelastic properties of interest include the storage modulus (G'), loss modulus (G''), the loss factor (tanδ) and resilience. The resilience was determined using the following relationship [42]:

$$\text{Resilience } (\%) = e^{(-2\pi\delta)} \times 100 \qquad \text{(Equation 5.1)}$$

5.2.3. Self-Deflection

Self-deflection tests, devised by a previous researcher from the Biomaterials lab were carried out as shown in Fig.5.1 [240], [246]. Collagen-based scaffolds, coll-HA composites and tri-layer samples were prepared as mentioned in Table 4.2 and hydrated with PBS overnight. The dimensions of samples were measured as well as the water uptake ratio as mentioned in Section 4.2.5. Samples were clamped at both ends with a span length of 20 mm and allowed to deflect naturally with the weight of the absorbed PBS. Tri-layer samples were tested both with (WC) and against curvature (AC). A stand was used to fix a camera in one position, images were taken and processed on ImageJ to determine the extent of deflection (D) using Equation 5.2 where h is the distance between the central position of the clamps and the lower surface of the deflected sample as shown in Fig.5.1 and t is the thickness of the scaffold.

$$D = h - \frac{t}{2} \qquad \text{(Equation 5.2)}$$

The bending modulus (E_B) can be determined using Equation 5.3 where Q_m is the water uptake ratio, m_{dry} is the mass of the dry scaffold, g is the gravitational acceleration, l is the span distance and I is the second moment of inertia. Equation 5.3 assumes deflection has a linear relationship with the load.

$$E_B = \frac{5ql^4}{384DI} = \frac{5Q_m m_{dry} g l^3}{384DI} \qquad \text{(Equation 5.3)}$$

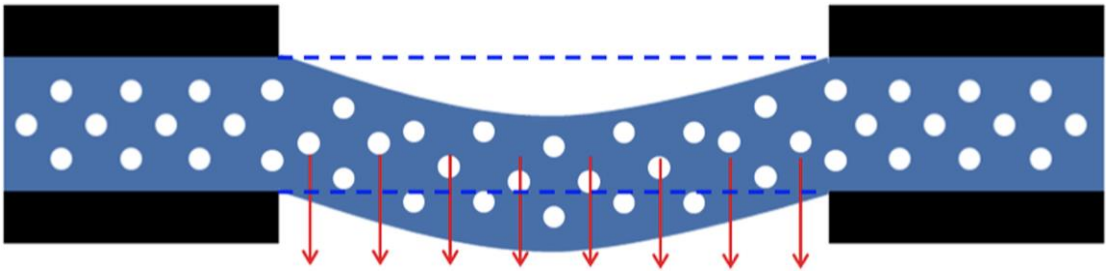

Figure 5.1: Set-up for self-deflection test showing a hydrated scaffold clamped at two ends and deflecting due to gravity [246].

5.3. Results

Representative stress-strain curves obtained for FEG-based scaffolds under compression are shown in Fig.5.2. The compressive modulus (E_C) was measured by taking the gradient of the linear region between 5-10% strain and is presented in Fig.5.3. It can be seen that the cross-linking procedure significantly increased the E_C by 6-fold. Tensile tests were performed on cross-linked FEG scaffolds as non-cross-linked scaffolds were too fragile to be tested under tension. A J-shaped (non-linear) response was observed for all samples which is common for biological materials. E_T was 0.4±0.1kPa at low strain, 15.1±0.9kPa at 40% strain and 21.0±1.2kPa at high strain. The extensibility and strain-to-failure were 47.0±18.2% and 101.0±21.5%, respectively.

E_C for all composites was measured as described earlier for FEG-based scaffolds. Fig.5.4 shows that 100C samples exhibited the highest E_C (3-fold higher), which significantly reduced as collagen was substituted for FEG. The representative curves for all samples under compression are shown in Fig.5.5, it can be seen that all samples exhibit a J-shaped curve. When comparing the composites, it can be seen that with the

replacement of collagen, the samples exhibit more resistance to compression. The results for compression have been summarised in Table 5.1.

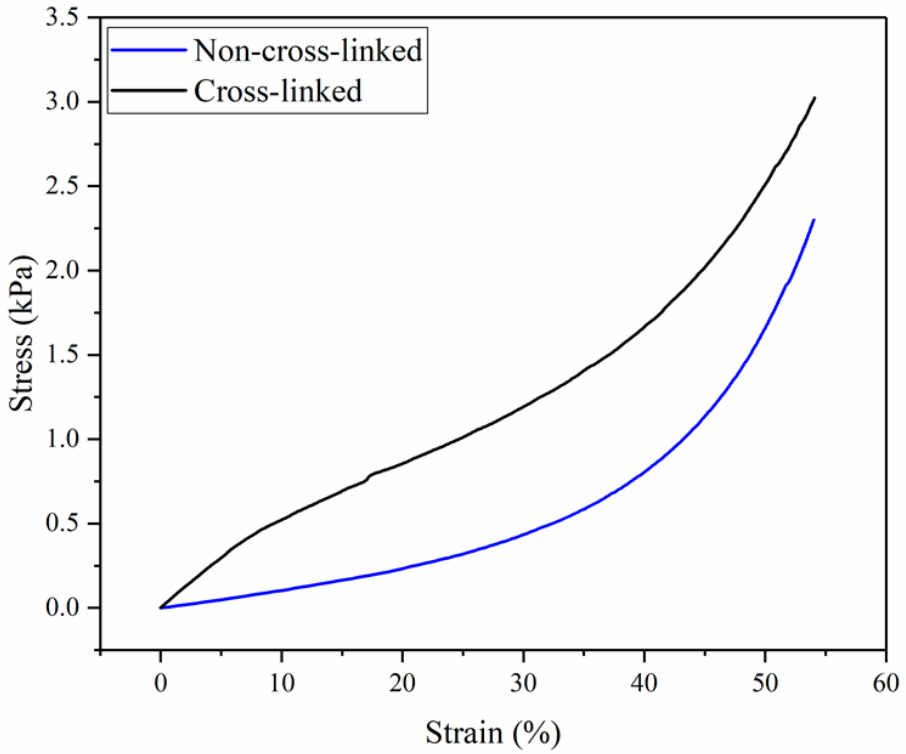

Figure 5.2: Representative stress-strain response of non-cross-linked FEG and cross-linked FEG under compression.

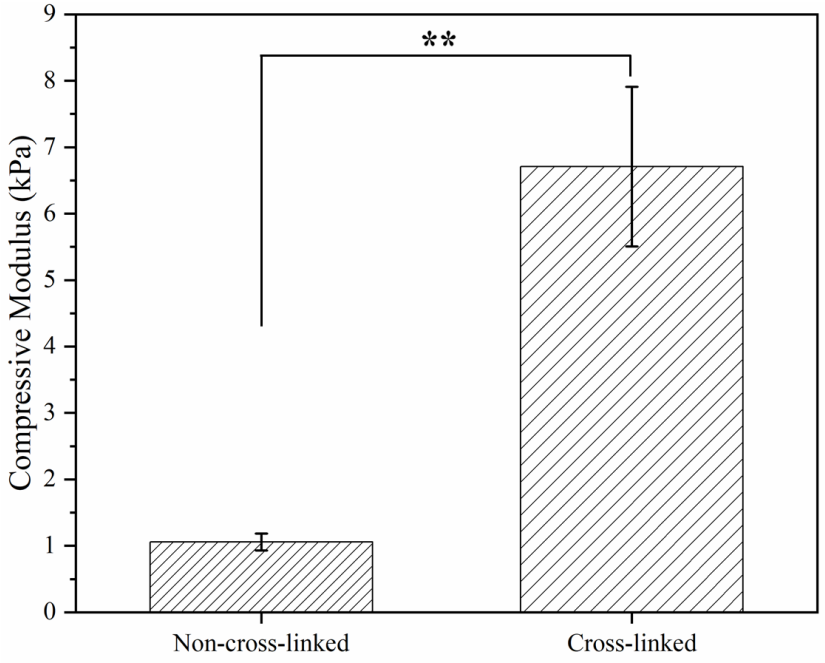

Figure 5.3: Compressive modulus for uncross-linked and cross-linked FEG-based scaffolds, where **p<0.005 and n=3.

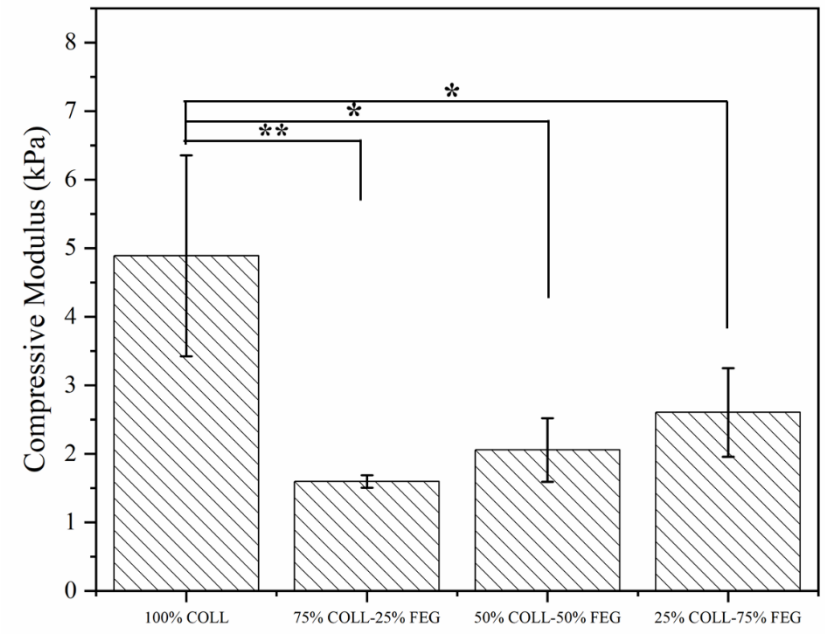

Figure 5.4: Compressive modulus for 100% collagen, 75% collagen-25% FEG, 50% collagen- 50% FEG and 25% collagen-75% FEG scaffolds, where *p<0.05, **p<0.005 and n=3.

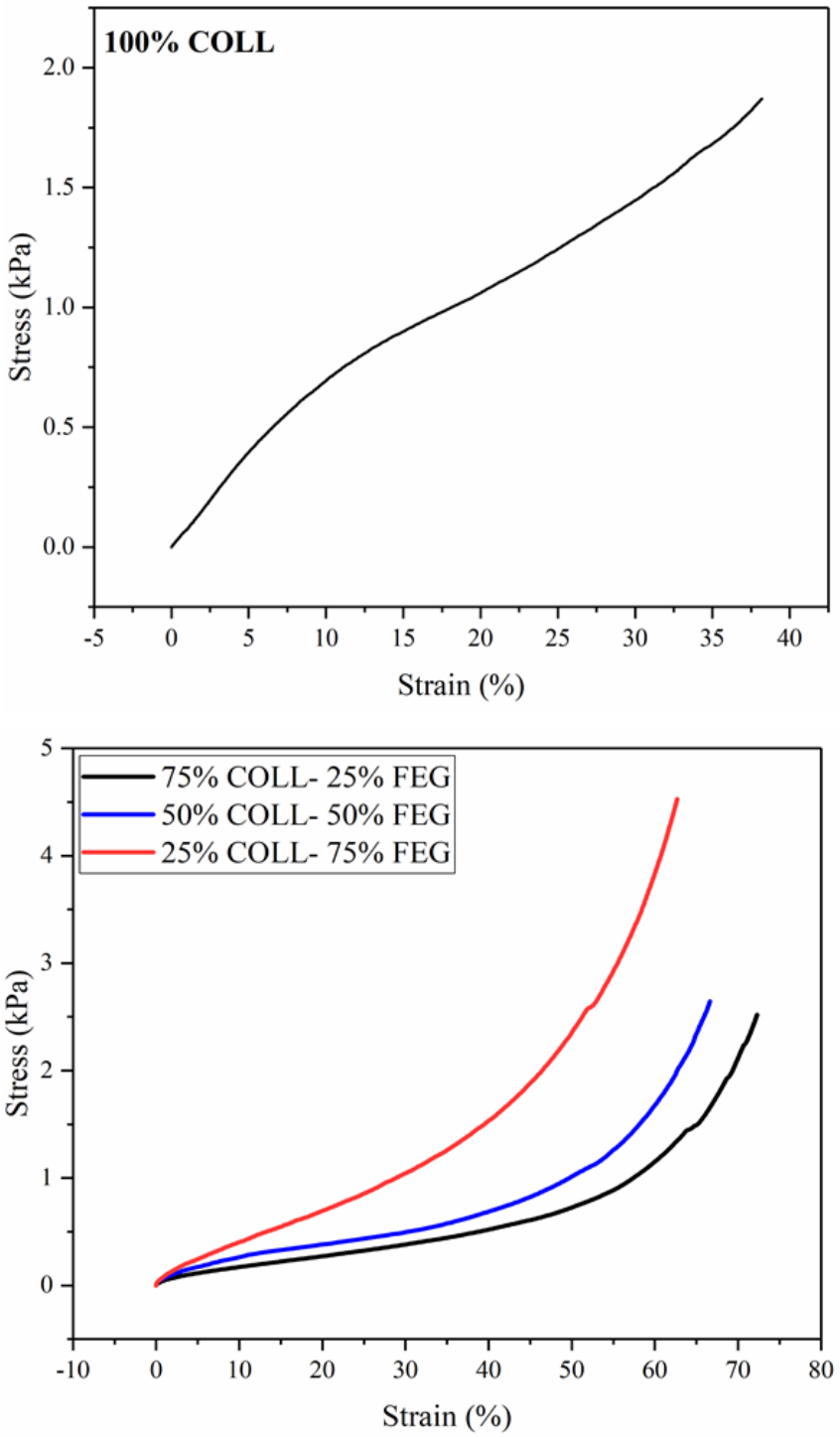

Figure 5.5: Representative stress-strain response of 100% collagen (top) and 75% collagen-25% FEG, 50% collagen- 50% FEG and 25% collagen-75% FEG (bottom) scaffolds under compression.

Table 5.1: Summary of compressive modulus results for FEG-based and collagen-FEG-based scaffolds.

Composition	Compressive Modulus (kPa)
100% FEG NON-CROSS-LINKED	1.1 ± 0.1
100% FEG CROSS-LINKED	6.7 ± 1.2
100% COL	4.9 ± 1.5
75% COL-25% FEG	1.6 ± 0.1
50% COL-50% FEG	2.1 ± 0.5
25% COL-75% FEG	2.6 ± 0.6

Representative stress strain curve of scaffolds under tension are shown in Fig.5.6 for all of the compositions. E_T at low strain was taken as the slope between 5-10% strain, which was challenging as the linear region could not be distinguished as the concentration of FEG increased. Substituting collagen for FEG, resulted in a 3-fold decrease in E_T as 25% collagen was replaced and above 50% replacement, the modulus decreased significantly by more than 25-fold (Fig.5.7). Although the substitution of collagen resulted in a decrease in the modulus, the strain-to-failure significantly increased when more than 50% collagen was replaced with FEG. It was found that the strain-to-failure doubled when 75% collagen was replaced with FEG which was significantly higher than all the compositions (Fig.5.7). The concentration of FEG showed a strong linear correlation with the strain-to-failure, where the coefficient of determination (r^2) was 0.9506. These results suggest that the substitution of collagen for FEG results in more compliant scaffolds. The extensibility of scaffolds is shown in Fig.5.8 where after 25% replacement, a significant difference cannot be seen.

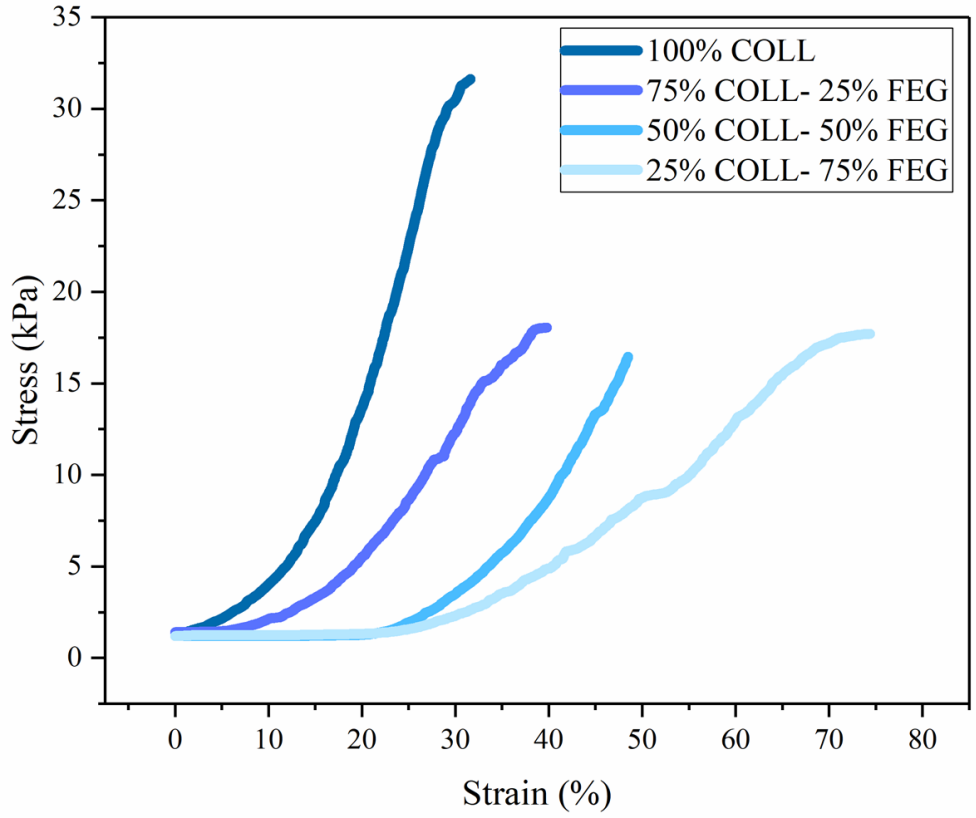

Figure 5.6: Representative stress-strain response of 100% collagen, 75% collagen-25% FEG, 50% collagen- 50% FEG and 25% collagen-75% FEG scaffolds under tension.

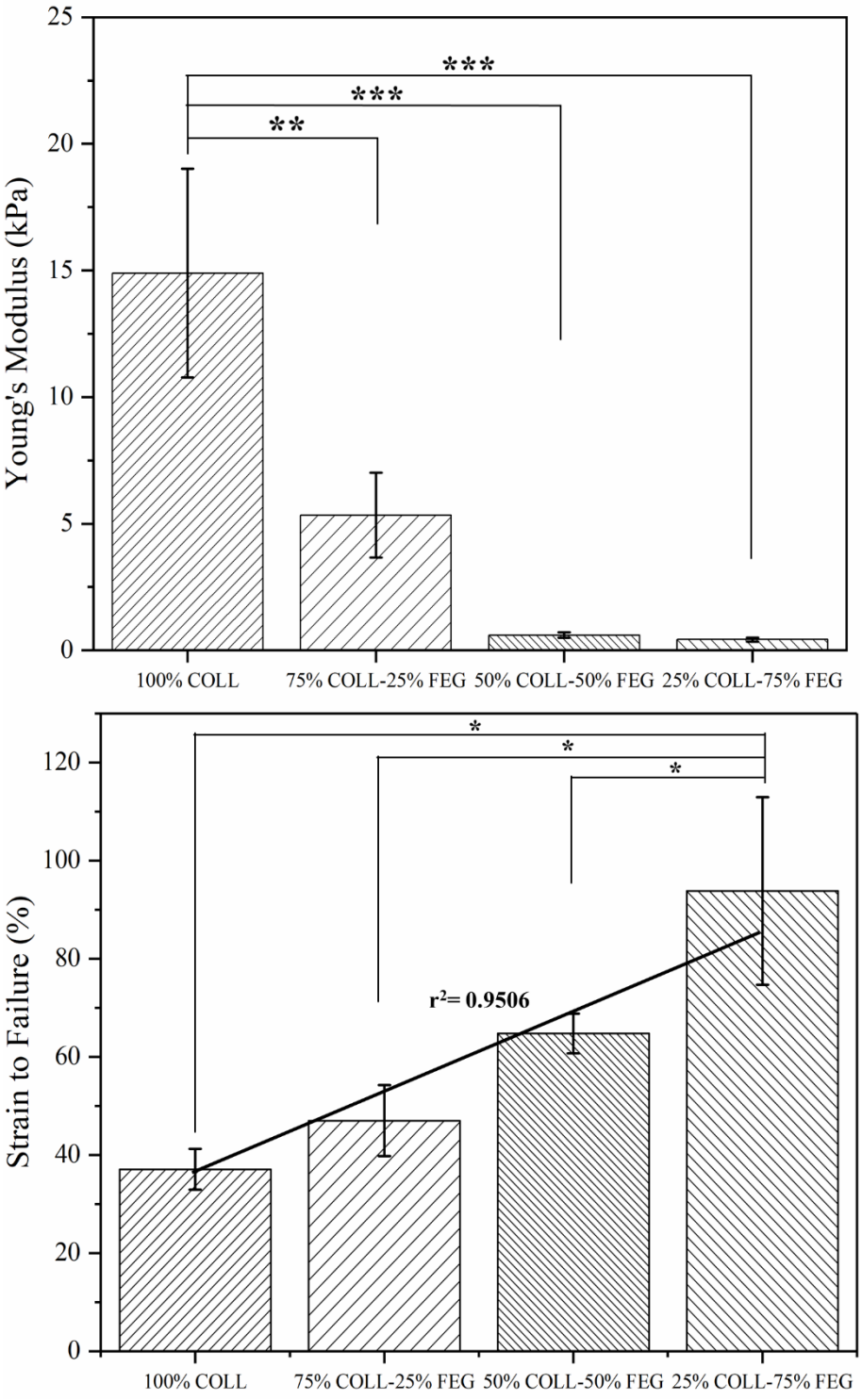

Figure 5.7: Young's modulus [top] and strain at failure [bottom] for 100% collagen, 75% collagen-25% FEG, 50% collagen- 50% FEG and 25% collagen-75% FEG scaffolds. Strain-to-failure shows a dependence to the concentration of FEG with a strong linear trend and a coefficient of determination (r^2) of 0.9506. where *p<0.05, **p<0.005, ***p<0.0005 and n≥3.

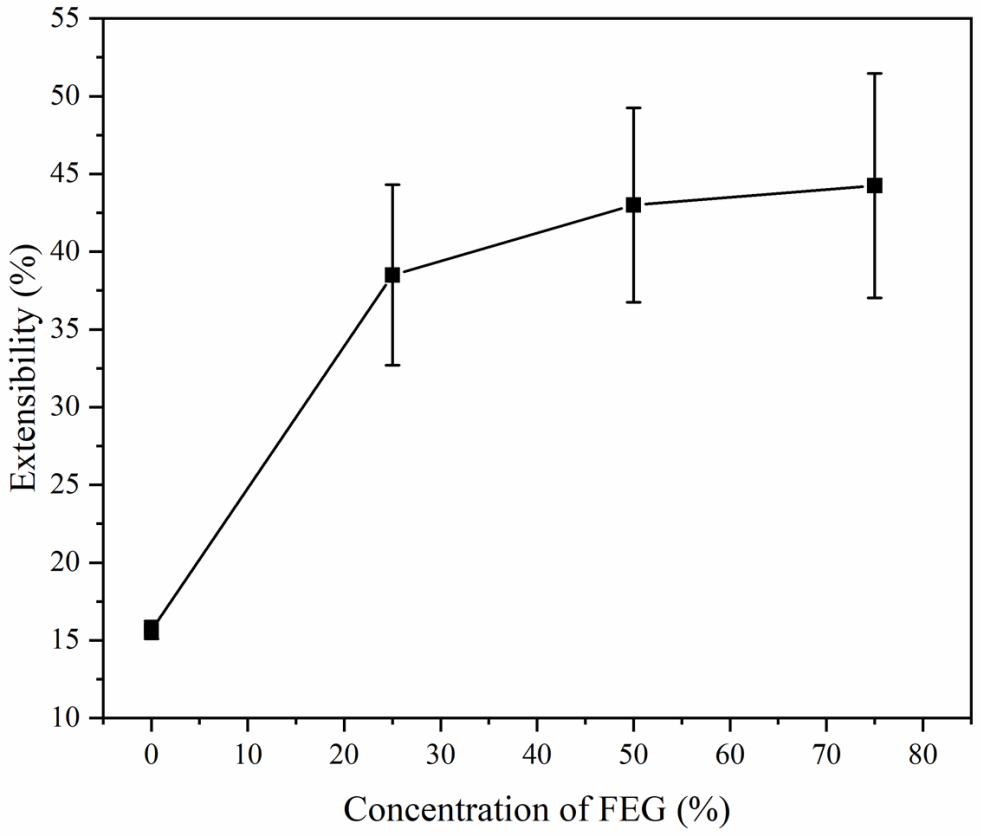

Figure 5.8: Extensibility of composite scaffolds as a function of concentration of fibrillar elastin gel (FEG) where after 25% substitution, no significant difference was observed.

The viscoelastic properties of cross-linked scaffolds measured using rheometry are presented in Fig.5.9. For all scaffolds there was no interaction between the storage and loss modulus at all frequencies, however, the response was dependent on frequency suggesting the scaffolds behave as physically cross-linked gels. For scaffolds, it was found that the substitution of collagen for FEG resulted in a very elastic response, where the loss factor was very low at lower frequencies and increased at higher frequencies. The resilience was determined using the loss factor and was found to increase significantly as the concentration of FEG increased. For all parameters measured, it was found that there was no significant difference between 50C-50E to 25C-75E. The substitution of 50% collagen resulted in a significant decrease in the

loss factor, suggesting the presence of FEG resulted in more elastic scaffolds. These factors were compared for all samples at a frequency of 1Hz as it is the frequency of normal heart rate, the results have been presented in Fig.5.10 and Table 5.2. It was found that the both the storage modulus and loss factor exhibited very strong negative linear trends where the substitution of collagen resulted in a significant decrease in both the storage modulus and loss factor as the r^2 value was 0.950 and 0.8703, respectively. These results suggest that the ability of the scaffolds to store energy increased as the concentration of FEG increased, resulting in a more energetically efficient system. It was found that the resilience showed a strong positive linear trend as the concentration of FEG increased with an r^2 value of 0.9080.

As the data was collected in the linear viscoelastic region (5% strain), E_T be determined using the following relationship: $E_T = 2G' (1+\nu)$, where ν is the Poisson's ratio and it is assumed to be 0.2 for gels. The results are shown in Table 5.2 and can be compared to the moduli determined from tensile testing directly. These results follow a similar trend to those found by tensile testing where a significant decrease in the modulus with the substitution of collagen was observed and no significant difference between 50C-50E and 25C-75E.

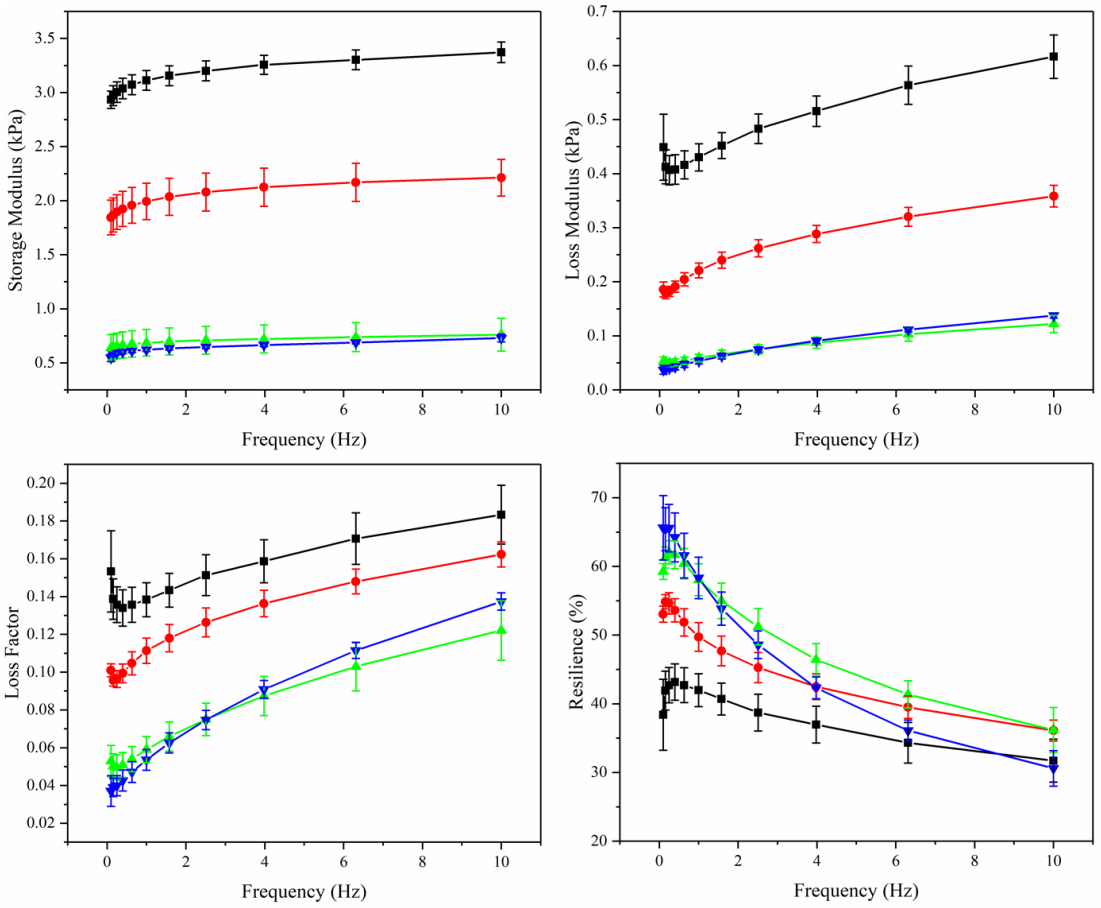

Figure 5.9: Viscoelastic properties measured using dynamic frequency sweeps at 0.1-10 Hz at 37°C for ■ 100% collagen, ● 75% collagen-25% FEG, ▲ 50% collagen- 50% FEG and ▼25% collagen-75% FEG scaffolds, n=3.

Table 5.2: Viscoelastic properties for all compositions measured at a frequency of 1 Hz and temperature of 37°C.

Composition	Storage Modulus (kPa)	Loss Modulus (kPa)	Loss Factor	Resilience (%)	Young's Modulus (kPa)*
100% COL	3.2 ± 0.09	0.5 ± 0.02	0.1 ± 0.009	40.7 ± 2.4	9.3 ± 0.3
75% COL-25% FEG	2.0 ± 0.2	0.2 ± 0.01	0.1 ± 0.007	49.7 ± 2.1	6.0 ± 0.5
50% COL-50% FEG	0.7 ± 0.1	0.06 ± 0.007	0.09 ± 0.006	58.0 ± 2.3	2.1 ± 0.4
25% COL-75% FEG	0.6 ± 0.02	0.05 ± 0.006	0.09 ± 0.008	58.3 ± 3.0	1.9 ± 0.05

**Young's modulus determined using the relationship E= 2G' (1+v), where v=0.2.*

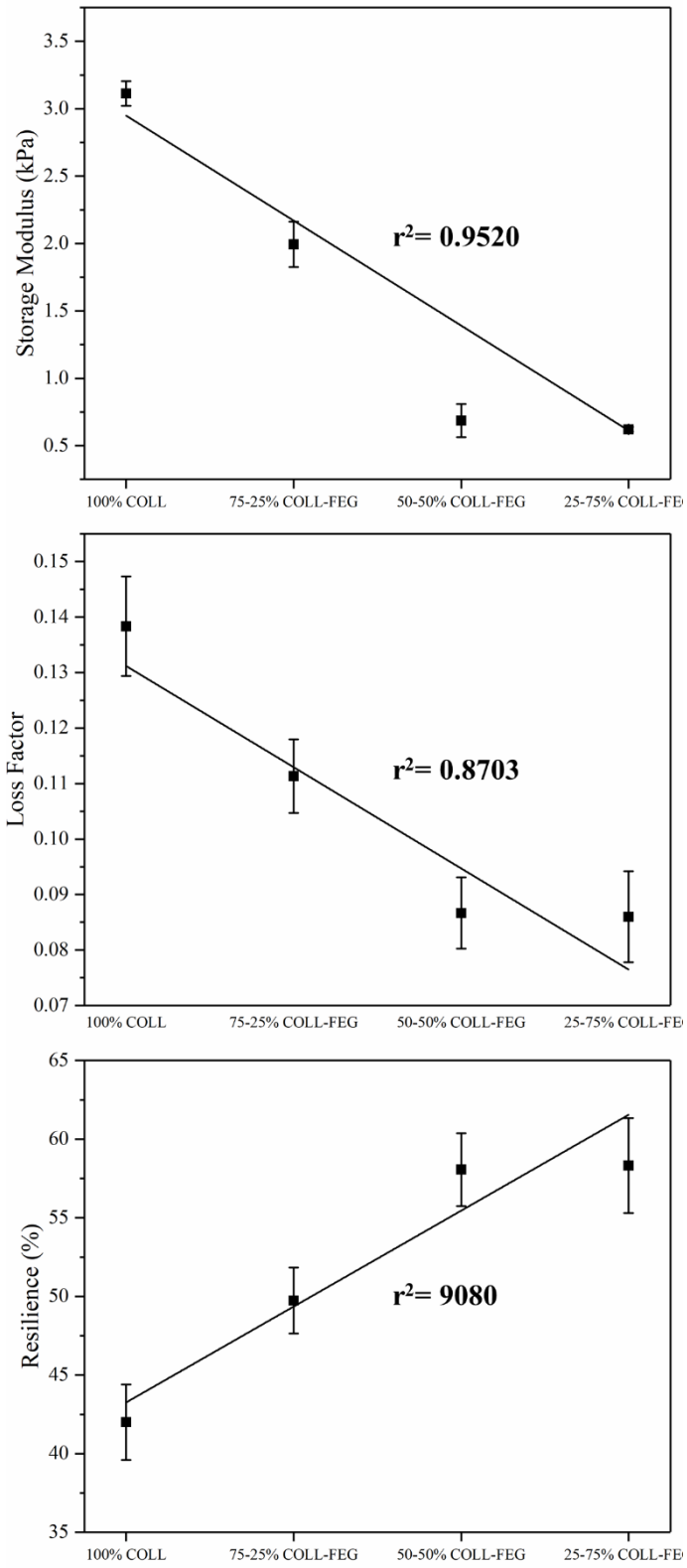

Figure 5.10: Viscoelastic properties for all compositions measured at a frequency of 1 Hz and temperature of 37°C showing the coefficient of determination (r^2), n=3

The tri-layers were tested under tension to understand the contribution of each layer, including coll-HA samples, to the overall bulk mechanical properties. Fig.5.11 shows representative stress-strain graphs for all individual compositions compared to the tri-layer. It was found that E_T of the tri-layer was not significantly different to 100C and coll-HA samples, suggesting that these two layers dominate the mechanical response of tri-layers in tension. Additionally, there was no significant difference in the strain-to-failure of tri-layers as they matched the response of 100C samples very closely with no significant difference. Coll-HA samples exhibited a high strain-to-failure with no significant difference compared to 50C-50E samples suggesting these scaffolds were more compliant than 100C and tri-layer samples. Tri-layer samples were also cultured with cells and tested under tension after 14 days, these results have been presented in Chapter 6.

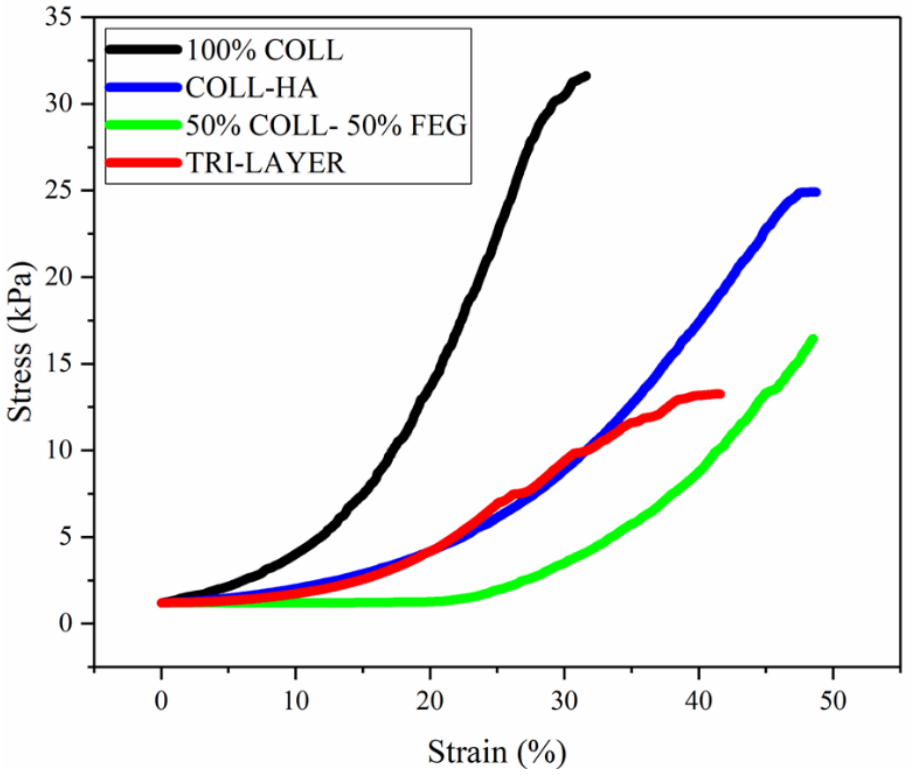

Figure 5.11: Representative stress-strain response of 100% collagen, coll-HA, 50% collagen- 50% FEG tri-layer scaffolds under tension.

Table 5.3: Summary of tensile testing results for all scaffold compositions.

Composition	Low Strain Modulus (kPa)	High Strain Modulus (kPa)	Extensibility (%)	Strain-to-Failure (%)
100% FEG CROSS-LINKED	0.4 ± 0.1 15.1 ± 0.9[a]	21.0 ± 1.2	47.0 ± 18.2	101.0 ± 21.5
100% COL	14.9 ± 4.1	93.1 ± 1.6	15.7 ± 0.6	37.1 ± 4.1
75% COL-25% FEG	5.3 ± 1.7	67.1 ± 5.8	38.5 ± 5.8	47.0 ± 7.2
50% COL-50% FEG	0.6 ± 0.1	70.6 ± 3.7	43.0 ± 6.2	64.8 ± 4.0
25% COL-75% FEG	0.4 ± 0.08	43.6 ± 8.7	44.2 ± 7.2	93.8 ± 19.1
COL-HA	6.9 ± 4.4	55.0 ± 20.1	25.0 ± 7.1	58 ± 12.5
TRI-LAYER (NON-SEEDED)	10.2 ± 4.9	82.9 ± 6.4	17.5 ± 5.4	35.4 ± 5.2

[a]*Measured at 40% strain.*

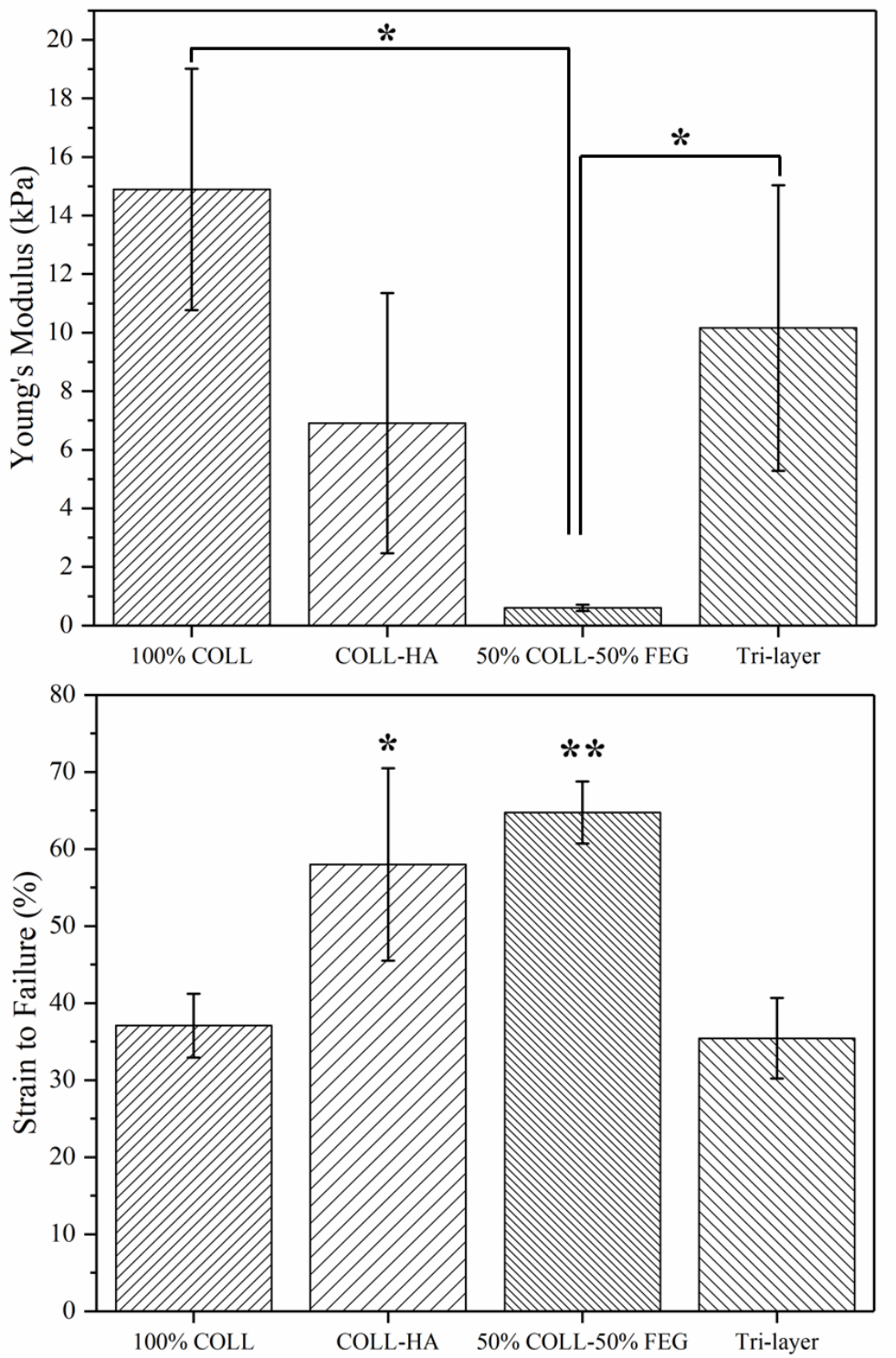

Figure 5.12: Young's modulus (E) [top] and strain at failure [bottom] for 100% collagen, coll-HA, 50% collagen- 50% FEG and tri-layer scaffolds, where *p<0.05, **p<0.005 and n≥3.

The mechanical properties of each layer making up the tri-layer were compared to the tri-layer by a self-deflection test in the hydrated state as a three-point bending test would not be suitable for these samples. It was found that the tri-layer was significantly stiffer than all the individual layers in bending mode, with a 5-fold increase in E_B compared to 100C and coll-HA samples and an 8-fold increase compared to the 50C-50E samples (Fig.5.17). There was no significant different between 100%collagen and coll-HA layers, however, it was found that the 50C-50E samples were significantly more compliant in bending than the other layers, which were over 1.5-fold stiffer (Table 5.3). The tri-layers were tested with (WC) and against curvature (AC) to see if they mimic the bending characteristics of native heart valves. It was found that the tri-layers were significantly stiffer against curvature than with curvature with a 1.3-fold increase in E_B. These results imply the 50C-50E layer contributes to the increased compliance with curvature in bending mode.

Table 5.4: Bending modulus for 100% collagen, coll-HA, 50% collagen- 50% FEG and tri-layer scaffolds with and against curvature, n=3.

Composition	Bending Modulus, E_B (kPa)
100% COL	6.8 ± 2.1
COL-HA	9.3 ± 3.6
50% COL-50% FEG	4.5 ± 0.5
TRI-LAYER WC	34.6 ± 4.8
TRI-LAYER AC	44.8 ± 3.3

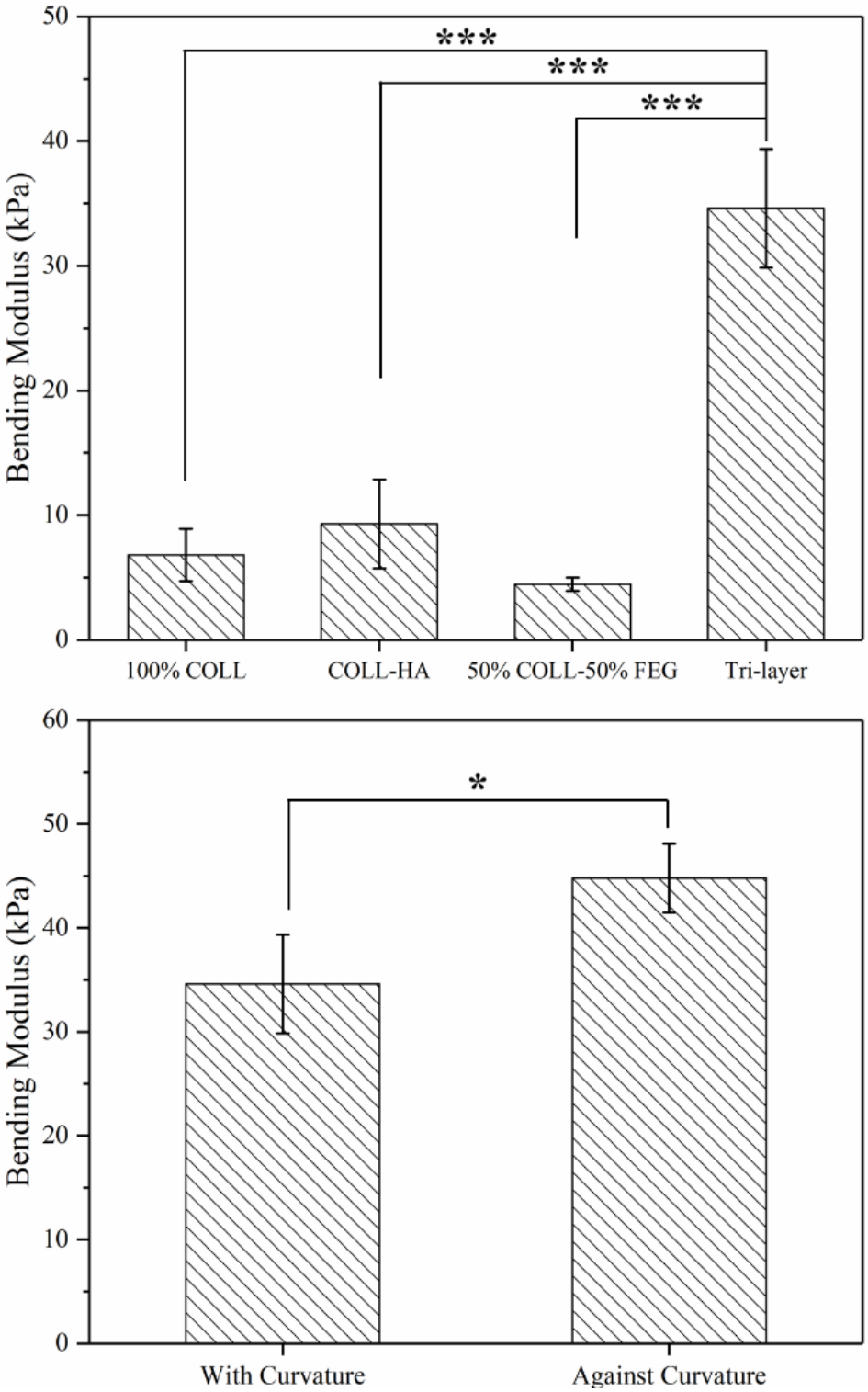

Figure 5.13: Bending modulus for 100% collagen, coll-HA, 50% collagen- 50% FEG and tri-layer scaffolds (top) and tri-layers with and against curvature (bottom), where *p<0.05, ***p<0.0005 and n=3.

5.4. Discussion

Mechanical testing of the scaffolds confirmed the non-linear deformation characteristics of FEG-based and collagen-based scaffolds which matches that of HVs. The typical behaviour of elastomeric foams under compression and tension was observed as follows. In compression (Fig.5.14a), three major zones are observed: a linear elastic region (pore-edge bending) which occurs between 5-10% strain, a collapse plateau (pore wall buckling) due to the rotation of struts and a densification regime (complete pore collapse) [378]. In comparison, in tension (Fig.5.14b), two zones were observed, these are the linear elastic region which is controlled by pore-edge bending and occurs at similar strains to compression and cell wall alignment in the direction of the applied load [379].

E_C of cross-linked scaffolds was found to be higher than that of uncross-linked scaffolds. This result is directly related to the change in pore characteristics observed post-cross-linking FEG. In cross-linked samples a 1.2-fold decrease in the aspect ratio and a 1.4-fold decrease in the average pore size was observed which accounts for the improved $E_{C.}$ It has been shown experimentally that a decrease in the aspect ratio results in a decrease in pore size as the lamellar spacing reduces and forms a structure closer to a honeycomb which has superior mechanical properties [380]. On the other hand, for composite scaffolds a decrease in E_C was observed compared to 100C scaffolds. This result occurs due to the difference in the rheological properties of the scaffolds where a lower viscosity was found with an increase in FEG content which in turn affected the pore characteristics as discussed in Section 4.4.1.1.

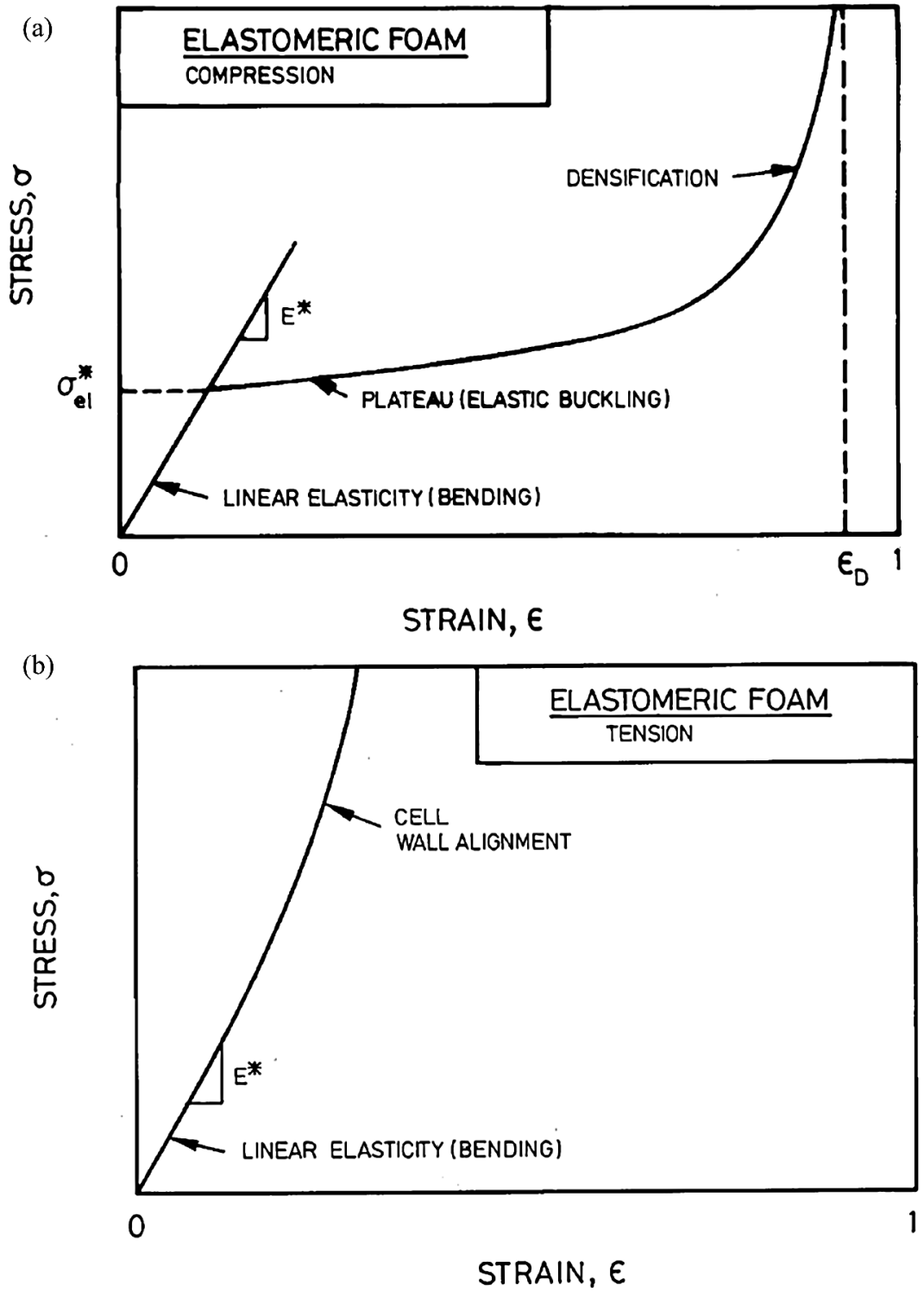

Figure 5.14: Typical stress-strain curves for open-cell elastomeric foams in (a) compression and (b) tension [379].

An interesting trend was observed amongst the composite scaffolds where the average E_C increased as the content of FEG increased. This could be associated with the significant decrease in pore size observed for 25C-75E samples which also increased the pore wall thickness. This decrease in wall thickness with the contraction of FEG post-cross-linking results in a decrease in the effective surface area.

The effective cross-link density (v_e) and associated molecular weight between cross-links (M_c) was determined using the mechanical testing data and the following relationship [381]:

$$v_e = \frac{E\emptyset^{-\frac{1}{3}}}{3RT} \qquad \text{(Equation 5.4)}$$

$$M_C = \frac{\rho^*}{v_e} \qquad \text{(Equation 5.6)}$$

where E, is the Young's modulus; ϕ, is the volume fraction; R, is the gas constant; T, is the temperature and ρ^* is the density of the scaffold. The results are summarised in Table 5.5 and agree with the findings from the swelling data presented in 4.4.2. A 3.3-fold increase in the cross-linking density of FEG-based scaffolds was observed as shown previously. The collagen-FEG composites show poor cross-linking with increase in the FEG content which results in physical interactions between collagen and FEG.

Table 5.5: Summary of the effective cross-linking density (v_e) and molecular weight between cross-links (Mc) calculated from the volume fraction (ϕ) and Young's modulus (E_T).*Compressive modulus (E_C) was used for these samples.

Sample	E_T	ϕ	v_e	M_c
100% FEG UNCROSS-LINKED	1.1 ± 0.1*	0.15	0.0003	309.4
100% FEG CROSS-LINKED	6.7 ± 1.2*	0.22	0.001	55.5
100% COL	14.9 ± 4.1	0.02	0.007	2.2
75% COL-25% FEG	5.3 ± 1.7	0.02	0.002	6.3
50% COL-50% FEG	0.6 ± 0.1	0.05	0.0002	97.7
25% COL-75% FEG	0.4 ± 0.08	0.06	0.0001	184.2

E_T and E_C were of the same order of magnitude; however, E_T was found to be higher than E_C for collagen scaffolds. A possible reasoning for this could be that in tension the pores experience pore wall stretching which does not take place in compression. This has been explained by Chen using the following relationships [240]:

$$\frac{E_T}{E_S} = 2\left(\frac{1-\emptyset}{3}\frac{\rho^*}{\rho_s}\right)^3 + 4\left(\frac{\emptyset}{3}\frac{\rho^*}{\rho_s}\right)^2 + \frac{1-\emptyset}{3}\frac{\rho^*}{\rho_s} \qquad \text{(Equation 5.7)}$$

$$\frac{E_C}{E_S} = 2\left(\frac{1-\emptyset}{3}\frac{\rho^*}{\rho_s}\right)^3 + 4\left(\frac{\emptyset}{3}\frac{\rho^*}{\rho_s}\right)^2 \qquad \text{(Equation 5.8)}$$

where E_S is the Young's modulus of the solid material, ϕ is the volume fraction, ρ^* is the density of the scaffold and ρ_s is the density of the solid. Equation 5.7 has three terms for the Young's modulus: the first term is for pore wall bending, the second term for pore edge bending and the third term is for pore wall stretching. As can be seen from Equation 5.8, the third term for pore wall stretching is absent and a term for pore wall buckling is not accounted for due to its negligible effects on the E_C. The simplified model in Fig.5.15 shows the difference in the deformation mechanism in tension and compression for an individual pore. As it is know from microstructural analysis that when collagen is substituted for FEG, the pores contain more secondary pores (voids),

it can postulated that the pore wall stretching has a smaller effect than pore wall and edge bending, hence E_C is larger for the composites.

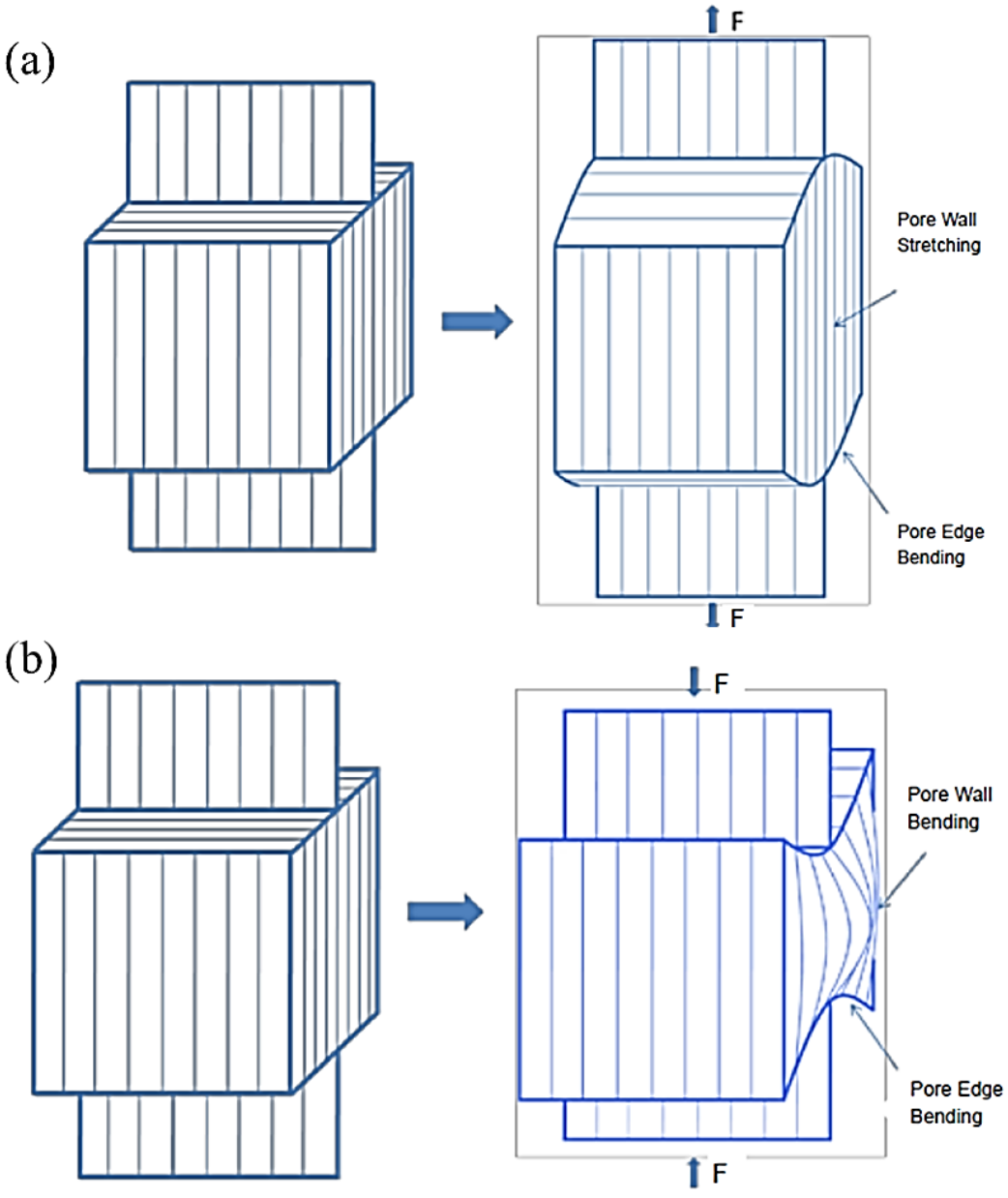

Figure 5.15: Simplified diagram showing the mechanism of deformation for an individual pore of a porous structure in (a) tension and (b) compression [175].

Experimental evidence shows that the mechanical properties of a scaffold should not change if the relative density is kept constant [148]. However, a significant difference in the mechanical properties of collagen-FEG composites was observed at the same relative density. This can be explained by the modulus of collagen and elastin which are 1.2GPa [382] and 1.1MPa [42], respectively. The solid modulus of elastin is significantly lower than collagen and explains why the mechanical properties vary significantly with incremental changes in the composition. E_T obtained for the composites showed a significant decrease with an increase in the concentration of FEG. At higher FEG content the mechanical response followed FEG only scaffolds more closely, i.e. a low E_T, high extensibility, and high strain-to-failure. The high strain-to-failure could also be due to a decrease in the collagen content, this is especially true for the high strain modulus which is double that of 100%FEG, however, the extensibility is associated closely with the presence of FEG as there was no significant effect of FEG content.

The aim of incorporating FEG in the scaffolds was to increase their extensibility and strain-to-failure of scaffolds to mimic the deformation characteristics of the ventricularis (elastin-rich) layer. In the ventricularis, extensibility can be in the range of 30-60% [84], [85]. The results presented in Section 5.3 show that the substitution of collagen for FEG significantly increased both the extensibility and strain-to-failure of both FEG-only scaffolds and composite scaffolds. It was found that even small substitutions of FEG was sufficient to increase the extensibility up to ~40% and the strain-to-failure increased in a concentration dependent manner. The tensile characteristics of collagen-FEG composites matched that of valves closely where a region of low strain and high strain that corresponds to the extension of FEG and

collagen, respectively, was observed. In tension, FEG molecules which are in the contracted state, extend when a tensile force is applied This contracted state can be associated with the higher extensibility of FEG as they are present in the scaffold as coiled or folded fibres which extend upon the application of a stress. The FEG is only responsible for accommodating the force at low strain, after full extension (extensibility), the collagen molecules take over as shown in Fig.5.16.

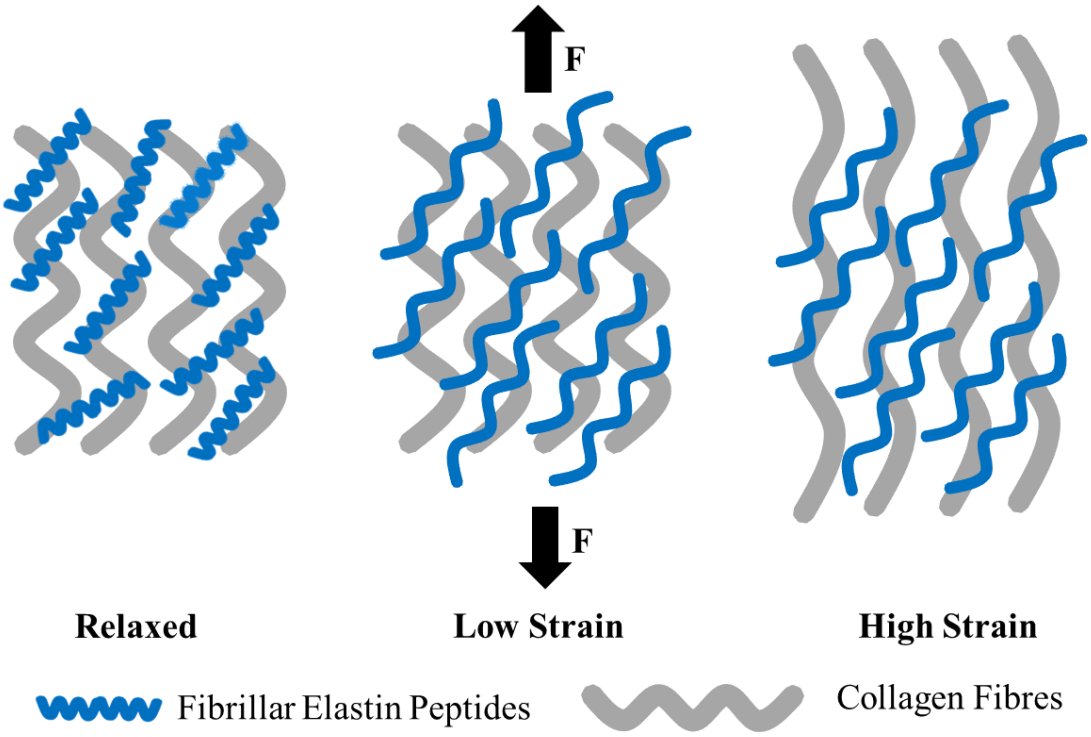

Figure 5.16: Behaviour of collagen-FEG composites in tension. Initially, fibres of both FEG and collagen are in the relaxed state and folded. As the force (F) is applied, the FEG fibres unfold first at low strains (<20%), as more force is applied, the limit of the FEG is reached and the force is transferred to the collagen fibres which extend until the sample fractures.

Mimicking the deformation characteristics of elastin in terms of its extensibility is a major achievement. Scaffolds to date that have employed elastin variants have shown no significant effect of the addition or substitution of bovine elastin to collagen as summarised in Table 5.6. The mechanical properties for elastin only scaffolds are

limited to soluble elastin as insoluble elastin is highly insoluble and cannot be used to design monolithic scaffolds. It was found that scaffolds were significantly more compliant and had a strain-to-failure that was closer to that of natural elastin (150%) [42]. Additionally, composites prepared from insoluble bovine neck ligament showed poor interaction with collagen and resultant mechanical properties. Equine insoluble elastin showed better mechanical properties (35-150%) that are comparable to collagen-FEG composites. However, as this source of elastin is not commercially available for use, it is limited in supply. The high extensibility of scaffolds composed from equine elastin is associated with its high shrinkage of 56% [236], which is comparable to that of FEG. There is a very strong correlation between volumetric contraction and the strain-to-failure of collagen-FEG scaffolds as shown in Fig.5.17 which suggests the contraction of FEG plays a significant role in its mechanical properties.

Table 5.6: Comparison of strain-to-failure and extensibility of natural elastin-based scaffolds.

Sample	Strain-to-Failure (%)	Ref
FEG, 3%wt/v	101	This study
α-elastin, 20%wt/v	1*	[211]
Tropoelastin and α-elastin, 100mg/ml	27.5-81.9	[208]
Collagen-FEG, 1%wt/v	47-94	This study
Type I soluble collagen (rat tendon) and ELPs, 2.5 mg/ml and 100 mg/ml ELPs	38.5	[231]
Type I collagen and α-elastin blends, 20 mg/ml and 10wt%	33	[232]
Type I collagen and insoluble or α-elastin, 1% wt/v	8-21	[233]
Type I soluble collagen and insoluble or α-elastin, 200 mg/ml (60:40)	13-15[a]	[234]
Type I collagen and insoluble elastin, 0.5% wt/v collagen and 10, 35 or 100wt% elastin	37-43	[229]
Type I collagen and insoluble elastin (equine)	35-150	[235]–[237]

**Dry sample, [a]Yield Strain.*

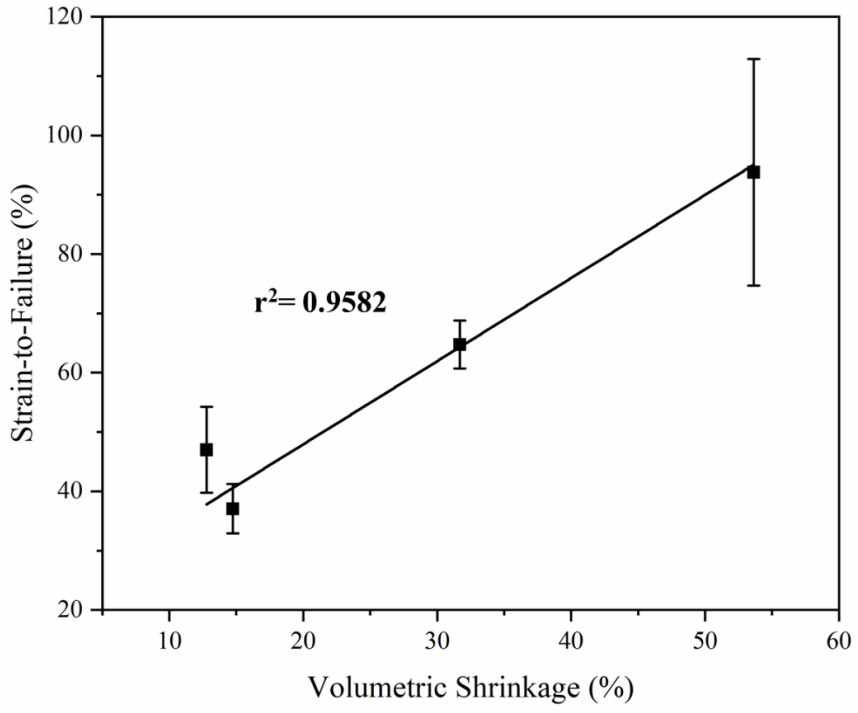

Figure 5.17: The dependence of volumetric shrinkage on the strain-to-failure of composite scaffolds shows a strong linear trend with a coefficient of determination (r^2) of 0.9582.

The results of this work suggest that FEG is more "interactive" than currently available commercial forms of elastin as it exhibited good interaction with collagen and mechanical properties that mimic the deformation characteristics of elastin. FEG exhibits properties closer to polymeric elastin and scaffolds with continuous distribution were fabricated as it could be manipulated to produce various suspensions. An important characteristic of elastin that could not be studied extensively in this work is the loss of energy of FEG-based scaffolds and their resilience. This is a very important parameter for valves as they experience repetitive loading. Preliminary rheology experiments were conducted which showed a decrease in the loss factor with increase in FEG content (Fig.5.10), implying that less energy was lost (lower hysteresis) by scaffolds containing higher concentrations of FEG. However, these samples were tested at low strain and further work is required to confirm this result at higher (at least 40%) strains. An experiment that was of interest but could not be conducted involved compression testing where samples are compressed to different levels of strain and released to measure the change in height and equate this to the resilience as shown by Mercuri *et al* [383]. It is highly recommended for future work on FEG-based scaffolds as it can also determine its potential as a material with "shape memory" properties which can be paired with catheters used to implant prosthetic valves.

The single layers (100C, coll-HA and 50C-50E) that form the tri-layers all exhibited non-linear deformation characteristics independently and as a composite. Tri-layers behaved similarly to the collagen layer, in terms of the modulus (10.2±4.9kPa) and strain-to-failure (35.4±5.2%) as it is the stiffest layer. The tri-layers prepared in this thesis would be suitable templates for cell seeding as a softer matrix (~6-14 kPa) is

preferred to emulate the mechanical properties of healthy heart valves [86], [141]. The addition of the 50C-50E layer did not improve the extensibility of scaffolds as the collagen layer dominated the mechanical properties. This was to be expected for a laminated structure as the stiffest layer dominates as it experiences the highest stress whereas the strain is continuous throughout the tri-layer [384]. The flexural response differed to that in tension as the tri-layer scaffolds exhibited a significantly higher E_B compared to the single compositions (4-8-fold). It is postulated that this was due to inhomogeneous swelling of the scaffolds as the 50C-50E layer was geometrically constrained by the other layers and therefore the swelling response was dominated by the 100C layer (Fig.5.18). The mismatch in swelling did not result in any observable tearing or poor integration at the interface of scaffolds and was negligible in tri-layers. Bending anisotropy (higher modulus against curvature) occurs due to the difference in the mechanical properties of the top (100C) and bottom (50C-50E) layers. When loaded WC, 100C is in compression whilst 50C-50E is in tension and vice versa when loaded AC. As E_T is lower for 50C-50E compared to 100E samples, E_B is lower WC and higher AC. The bending anisotropy ratio of tri-layers was shown to be in good agreement with that of native valves (1.3-fold vs. 1.4-fold) [385]. Although the mechanical properties of the tri-layer scaffolds designed in this work do not match that of native valves, the deformation characteristics were emulated. The tri-layer scaffolds could provide a good template for future *in vitro* work as they mimic the composition of native valves closely. However, further work on aligning of the elastin rich layer would be recommended to mimic the anisotropic properties of valves in the circumferential and radial directions.

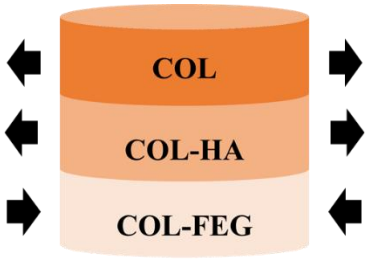

Figure 5.18: Constrained swelling due to layered structure where 100% collagen (COL) and the collagen-hyaluronic acid (COL-HA) layers swell (expand) and the 50%collagen-50%FEG (COL-FEG) layer contracts.

5.5. Summary

The aim of this chapter was to study the mechanical properties of scaffolds fabricated in Section 4.2.1. The main findings include:

- FEG-based scaffolds showed a 6-fold increase in the compressive moduli by cross-linking, implying that the mechanical properties of FEG can be tailored. In tension, it was found that FEG-based scaffolds mimicked the deformation characteristics of native elastin, which are a high strain-to-failure and a low Young's modulus.
- Collagen-FEG scaffolds exhibited non-linear deformation and a strong correlation between the content of FEG and the strain-to-failure. It was found that low concentrations of FEG (~25%) was sufficient to improve extensibility significantly compared to scaffolds without FEG. Preliminary work has shown a strong correlation between the content of FEG and decrease in loss factor, implying it plays a role in minimising energy loss.
- Anisotropic bending characteristics of tri-layer scaffolds were shown by self-deflection where the bending modulus was significantly higher against

curvature as seen in native valves. In tension, tri-layer scaffolds were dominated by the collagen rich layer in terms of their Young's modulus and strain-to-failure.

6

Biological Properties of Scaffolds

6.1. Introduction

This chapter will focus on assessing the effect of the composition of scaffolds on the cellular response of induced pluripotent stem cell derived cardiomyocytes (iPSC-CMs). iPSC-CMs were chosen as they are a mixed population of cells containing cardiomyocytes (CMs) and non-cardiomyocytes (NCMs) [386]. NCMs include fibroblasts, smooth muscle cells (SMCs) and endothelial cells that are also found in the cardiac lineage as summarised in Fig.6.1. Differentiation of iPSCs to CMs involves activation of the Wnt-β-catenin pathway which is involved in forming endocardial cushions that are also essential for heart valve development [387]. As mentioned in Section 2.2.2.4. valvular-interstitial cells (VICs) are also a mixed population of cells that are comprised of fibroblasts and SMCs and therefore iPSC-CMs could potentially be applicable as a cell source. Scaffolds prepared as described in Section 4.2.1. will be sterilised (Section 6.2.2.) and seeded with iPSC-CMs to study the effect of the different compositions on the cellular response. Properties of interest include the scaffolds metabolic activity, cell adhesion, gene expression and differentiation as well as cell morphology which will be discussed in Section 6.3. and 6.4.

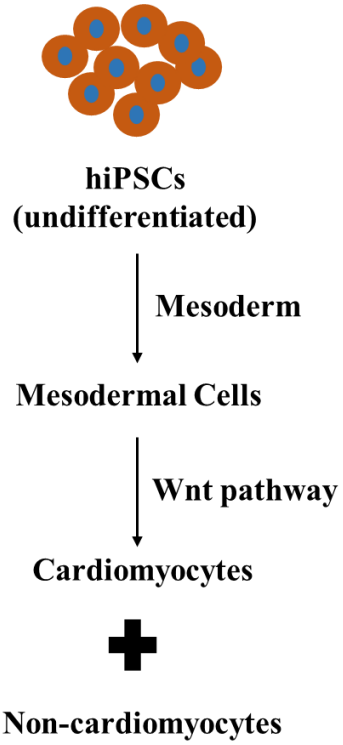

Figure 6.1: Pathway for differentiation of human induced pluripotent stem cells (hiPSCs) to hiPSC-derived cardiomyocytes and non-cardiomyocytes.

6.2. Materials & Methods

6.2.1. hiPSC Cell Culture and Differentiation

Human induced Pluripotent Stem Cells (hiPSCs) were cultured and differentiated following Lopez *et al's* protocol by either Dr. Colleen Lopez or Ujang Purnama. [388]. hiPSCs removed from liquid nitrogen and defrosted by running under warm tap water. The pellet was immediately resuspended in 10mL of Dulbecco's Phosphate Buffered Saline (DPBS, Sigma Aldrich, UK) and centrifuged (Heraeus Megafuge 8R Centrifuge, Thermo Fisher Scientific, UK) for 4mins at 1300rpm. The supernatant was discarded, and the pellet was resuspended in mTeSR™ media (Stemcell Technologies) containing rock inhibitor (RI, Merck Chemicals Ltd) and plated on a Matrigel (Corning) coated T25 flask. Matrigel was diluted with DMEM/F12 (Gibco).

The hiPSCs were differentiated according to the protocol reported by Lian *et al* [389], [390]. hiPSCs were cultured until 90% confluent before being dissociated and plated on a flask coated with reduced factor (RF) Matrigel (1:100µL) and incubated in the normoxic (21% O_2, 5% CO_2) incubator. After 24 hrs (Day -1), RF Matrigel (1:200µL) was added to mTeSR™ media and incubated in the hypoxia incubator (5% O_2, 5% CO_2). The following day (Day 0), the media was changed to Roswell Park Memorial Institute (RPMI) 1640 (Gibco), containing 1% B27 minus Insulin (Gibco), 12µM CHIR99201 (Stratech Scientific Ltd), 10ngmLs^{-1} Activin A (RD Systems Europe Ltd) and 1/200 RF Matrigel. On day 1, the media was changed to RPMI 1640, containing 1% B27 minus Insulin. On day 3, half of the media was changed to RPMI, containing 1% B27 minus Insulin and 10µM IWP4 (Tebu-bio, final concentration of IWP4 in medium is 5µM). On day 5, the medium was changed again to RPMI, containing 1% B27 minus Insulin. On day 7, the media was changed to RPMI, containing 1% B27 Complete (Gibco), and the plates were cultured under normoxia. From this point onwards, the medium was replenished every two-three days. The cells were harvested for seeding on day 15 as described in section 6.2.3.

6.2.2. Scaffold Sterilisation

After fabrication and miniaturisation as described in section 4.2.1., the scaffolds were transferred to vials containing 100% ethanol and placed inside the hood where sterilisation continued in well plates. Tri-layer scaffolds were also sterilised for evaluation of their tensile properties. The scaffolds were submerged in 70% ethanol for three washes lasting 30 mins, ensuring they were placed in wells containing fresh ethanol each time. The scaffolds were transferred to wells containing DPBS and washed a further three times to remove residual ethanol. The scaffolds were then

placed in RPMI with B27 supplement and antibiotics (P/S containing 100UmLs^{-1} penicillin, 0.1mgmLs^{-1} streptomycin and 0.25µgmLs^{-1} amphotericin B, Sigma Aldrich, UK), until required for cell seeding.

6.2.3. Cell Dissociation and Scaffold Seeding

At day 15, flasks containing cells were removed from the incubator and examined for confluency using an EVOS microscope (Life Technologies, Thermo Fisher Scientific, UK). The media in the flasks was discarded and the cells were rinsed with DPBS twice. 3-4 mL TrypLE™ Express Enzyme (Thermo Fisher Scientific, UK) was added to the flask and incubated at 37°C for 10mins. The flask was removed, and the solution was pipetted to dislodge cells adhered to the surface of the flask. The mixture was transferred to a conical containing three times more DPBS and centrifuged at 1300rpm for 4mins at 22°C to obtain a pellet. The supernatant was discarded, and the pellet was resuspended in media. 10µl of the cell suspension was mixed with 10µl of 0.4% Trypan Blue stain (Invitrogen by Thermo Fisher Scientific, UK) and was pipetted into a Countess™ Cell Counting Chamber Slides (Invitrogen by Thermo Fisher Scientific, UK) and inserted into a Countess™ Automated Cell Counter (Invitrogen by Thermo Fisher Scientific, UK). The remaining cell suspension was centrifuged again and diluted with media containing RI (10 µM Y-27632, Merck Chemicals Ltd) (1: 1000µl).

Once the cells were dissociated, the scaffolds were removed from the RPMI media and placed on autoclaved filter paper for 1 min until dehydrated. Once dehydrated, scaffolds were placed individually in a 96 well plate using tweezers and 50µl of the cell suspension containing 500000 cells was loaded on the scaffold, this resulted in instant rehydration. The well plate containing the scaffolds was placed in the normoxic incubator for 2-3 hrs. 200µl of RPMI + B27 complete media with P/S was loaded onto

the scaffolds and placed in the incubator. The media was changed every other day without changing the plate, except when studying the viability as mentioned below.

6.2.4. Cell Viability

The viability of the cells was monitored over 7 (1, 4 and 7 days) or 18 (1, 4, 7, 10, 14 and 18) days using an AlamarBlue® (AB) assay (Thermo Fisher Scientific, UK) as per the manufacturer's protocol. AB reagent was added to the media (1µL:10mL) to create a stock solution. 200µL of the solution was added to a new 96 well plate and the scaffolds were transferred to the plate using tweezers. The plate was incubated at 37°C for 4hrs. Positive or negative controls were prepared by incubating 1mL of the solution at 90°C in a heat block (Dri-Block® DB-3, Techne, UK) or in the fridge (4°C) for 4hrs, respectively. After 4hrs, 100µL of each sample, including the controls, was transferred to another 96 well plate. Media was added to the plate containing the scaffolds and placed in the incubator. The fluorescence was measured at 544/590 nm in a Microplate Photometer (FLUOstar Omega, BMG Labtech). This method quantifies cell viability by comparing fluorescence emitted after reduction of the reagent from resazurin to resorufin of the sample to the control:

$$\%\ \text{AB Reduction} = \frac{\text{Sample} - \text{Negtative Control}}{\text{Positive Control} - \text{Negative Control}} \times 100 \quad \text{(Equation 6.1)}$$

The plate was changed with the media every other day to avoid false positive results as the reagent reduces as the cells continue to metabolise.

6.2.5. Cell Attachment

The attachment of cells was determined on day 1 using the AB assay as an indicator of cell number, as the fluorescence is proportional to the number of cells. This method was only used for the FEG based scaffolds, both uncross-linked and cross-linked. The

proportion of cells attached was determined by comparing the fluorescence of cell seeded scaffolds to the fluorescence of cells remaining in the well. Scaffolds were placed in wells containing fresh media supplemented with AB regent and placed in the incubator. The wells from which scaffolds were removed were washed with PBS twice and the media mixture was added and also placed in the incubator. After 4hrs, the samples were removed, and the fluorescence was measured relative to control samples as described in section 6.2.4. To determine the proportion of cells attached the following equation was used:

$$\%\ \text{Cell Attachment} = \frac{\%\ \text{AB reduction (scaffold)}}{\%\ \text{AB reduction (scaffold)} + \ \%\ \text{AB reduction (well)}} \times 100 \qquad \text{(Equation 6.2)}$$

The number of cells attached for the remaining scaffolds (collagen-based and composites) were determined using the cell counter. Scaffolds were removed and placed in new wells containing fresh media on day 1. 10µl of the cell suspension was taken from the wells which the composites were initially removed and mixed with 10µl of Trypan Blue reagent before being read in the cell counter as described in section 6.2.3. The number of cells attached was determined using the following equation:

$$\%\ \text{Cell Attachement} = \frac{\text{Total number of cells} - \text{Detached cells}}{\text{Total number of cells}} \times 100 \qquad \text{(Equation 6.3)}$$

6.2.6. Real-time quantitative polymerase chain reaction (qPCR)

6.2.6.1. mRNA Isolation

Messenger Ribonucleic acid (mRNA) was extracted from monolayer cells at day 15 (after differentiation), which were the control group, they were dissociated as above, and mRNA was extracted from the pellet of cells. For scaffolds, a minimum of three scaffolds were taken at a time to maximise the quantity of mRNA isolated either at

days 7 or 14. Scaffolds were placed in a RNase- free microcentrifuge tube, 500µL of TRIzol™ reagent (Thermo Fisher Scientific, UK) was added and the scaffolds were disintegrated into fragments using a clean micro-pestle. For cells only, the TRIzol was added to the pellet and pipetted repeatedly for 1min, it was then left on ice until mRNA was isolated. The disintegrated scaffolds were centrifuged (Eppendorf™ Microcentrifuge, 5415C, Thermo Fisher Scientific, UK) for 4mins at 12000x*g*, the supernatant was removed and placed in a clean RNase free tube and placed on ice. A further 500µl of TRIzol was added to the pellet and the procedure was repeated, placing the new supernatant in the same tube as the first. The samples were left on ice whilst other samples were disintegrated in the same manner. mRNA was isolated using the Qiagen RNeasy® Mini Kit (Qiagen, UK) according to the manufacturer's protocol with the addition of a DNase step to obtain a purer mRNA sample. 700µL of 100% ethanol was added to the supernatant and it was agitated slowly, the mixture was left on ice for 5mins to allow any residual fragments to sink to the bottom of the tube. The mixture was transferred to a RNeasy Mini spin column and centrifuged for 15secs at 10000x*g*. The flow through solution was discarded and any remaining mixture was transferred to the column. The column was then washed with 350µL RW1 buffer and centrifuged again for 15secs. 80µL of DNase (RNase-Free DNase, Qiagen, UK) was added to the column and left for 15mins at room temperature. The column was washed again with RW1 buffer as above and washed further with RPE buffer before the mRNA was eluted using 33µL of RNase free water. The isolated mRNA was stored at -20°C until required for further testing. All work surfaces were cleaned with RNaseZAP™ (Sigma Aldrich, U.K.) prior to RNA extraction. NanoDrop UV spectrometry (NanoDrop™ Lite, Thermo Fisher Scientific, UK) was used to measure the

concentration of mRNA. mRNA samples were vortexed (Vortex-Genie 2, Scientific Industries Inc.) for 10secs prior to reading and RNase free water was used as a blank control. mRNA with a concentration above 15ng/µL and A260/A280 between 1.9 and 2.1 was used.

6.2.6.2. cDNA Analysis

The mRNA was converted into complementary deoxyribonucleic acid (cDNA) using a High Capacity cDNA Reverse Transcriptase Kit (Applied Biosystems, Thermo Fisher Scientific, UK). The isolated mRNA was mixed with RT random primers, RT buffer, MultiScribe Reverse Transcriptase enzyme, deoxynucleotide triphosphate (dNTP) mix and RNase free water, according to the manufacturer's protocol to produce a total volume of 20µL per reaction. The reaction mixtures were then incubated in a SensoQuest Basic Thermal Labcycler (SensoQuestGeneFlow) which ran the following procedure: 10min at 25°C, 120min at 37°C, and 5min at 85°C. The cDNA was then removed and stored in the fridge (4°C) until required for qPCR.

6.2.6.3. qPCR Reaction and Data Analysis

The genes of interest are listed in Table 6.1. qPCR was performed using the *Power*SYBR® Green PCR Master Mix (Applied Biosystems, Thermo Fisher Scientific, UK) method. A total of 10µL was used per reaction, this was composed of 7.5µL master mix: 5µL SYBR® Green reagent, 1.5µL RNase free water and 1µL primers (both forward and reverse), which was loaded on to a 96 well qPCR plate (MicroAmp Fast, Applied Biosystems, China) from one side, the plate was reversed and loaded with 2.5µL of cDNA. The plate was sealed using a MicroAmp™ Optical Adhesive Film (Applied Biosystems, Thermo Fisher Scientific, UK) before being

centrifuged for 4mins at 4400rpm to collect the reaction mixture at the bottom of the plate. The plate was then inserted in the StepOnePlus™ Real-Time PCR System (Applied Biosystems by Thermo Fisher Scientific, UK). The method used was a two-step cycle with 40 cycles in total, the settings for each stage is shown in Table 6.1.

Table 6.1: qPCR run method

Stage	Time (s)	Temperature (°C)
Holding (polymerase activation)	600	95
Cycling (denaturation)	15	95/60
Melt Curve (annealing/extension)	30	60

A common method for quantifying relative gene expression is the $2^{-\Delta\Delta CT}$ method proposed by Livak and Schmittgen [391]. It involves comparing an experimental group to a control group, which in this case is monolayer cells differentiated up to day 15. The cycle threshold (C_T) is measured real-time, it equates to the number of cycles required for the fluorescent signal of a sample to exceed the background signal (set as the threshold). To normalise the mRNA between sample types, a control gene, also known as a housekeeping gene (HKG) is used. The C_T of each target gene (TG) for the experimental group is normalised twice, once against the HKG and then against the control group. The steps involved in determining the fold change are as follows:

1) Calculate the average C_T of the TG as well as the HKG
2) Calculate ΔC_T: $\Delta C_T = C_T(TG) - C_T(HKG)$
3) Calculate $\Delta\Delta C_T$: $\Delta\Delta C_T = \Delta C_T(\text{experimental group}) - \Delta C_T(\text{control group})$
4) Calculate the relative fold change: $2^{-\Delta\Delta C_T}$

Table 6.2: Primers for genes of interest.

Target Gene	Sequence	Description	Ref
TATA-box binding protein (TBP)	TGACCCAGCATCACTGTTTCTT (FW) CAAGCCCTGAGCGTAAGGTG (RV)	Housekeeping gene	[392]
Collagen, type I	CCGCCGCTTCACCTACAGC (FW) TTTTGTATTCAATCACTGTCTTGCC (RV)	ECM gene	[393]
Elastin	CTGGAATTGGAGGCATCG (FW) TCCTGGGACACCAACTAC (RV)	ECM gene	[394]
Lysyl Oxidase (LOX)	GCATACAGGGCAGATGTCAGA (FW) TTGGCATCAAGCAGGTCATAG (RV)	Enzyme for cross-linking	[395]
Fibrillin-1 (FIB-1)	GGAACGTGAAGGAAACCAGA (FW) GGCAAATGGGGACAATACAC (RV)	ECM gene	[396]
Hyaluronan Synthase-2 (HAS-2)	AGCCTTCAGAGCACTGGGACGA (FW) ACAGATGAGGCTGGGTCAAGCA (RV)	ECM gene	[397]
α-smooth muscle actin (α-SMA)	TTCAATGTCCCAGCCATGTA (FW) CCAGATCCAGACGCATGAT (RV)	Marker for myofibroblasts	[398]
Vimentin	GAGAACTTTGCCGTTGAAGC (FW) TGGTATTCACGAAGGTGACG (RV)	Marker for fibroblasts	[399]
Cardiac muscle troponin T (TNNT-2)	GACAGAGCGGAAAAGTGGGA (FW) CTCCTTGGCCTTCTCCCTC (RV)	Marker for cardiomyocytes	[400]

Forward sequence (FW) and reverse sequence (RV). All primers were Homo sapien variants.

6.2.7. Total DNA Isolation & Quantification

To determine the total deoxyribonucleic acid (DNA) of cells seeded on scaffolds, the *Quick*-DNA™ Miniprep Plus Kit (Cambridge Bioscience, UK) was used. Scaffolds were prepared and seeded as mentioned above. DNA was isolated from cells seeded on scaffolds on day 1 or day 14 using the manufacturer's protocol with the addition of an RNase step to obtain purer DNA. Scaffolds were placed in a microcentrifuge tube

with 95µL RNase free water, 95µL solid tissue buffer and 10µL of Proteinase K, the samples were vortexed for 10secs and then incubated at 55°C in a heat block for 3hrs, ensuring to agitate it every hour. The samples were removed from the heat block and centrifuged at 12000x*g* for 1min, the supernatant was transferred to a new RNase free tube. 20µL RNase A (from PureLink™ Genomic DNA Mini Kit, Thermo Fisher Scientific, UK) with a concentration of 20mg/µL was added to each tube and incubated at 37°C in a water bath for 10mins. The samples were removed, and 440µL Genomic Binding buffer was added to the supernatant and vortexed for 10secs. The mixture was transferred to a Zymo-Spin™ IIC-XL Column and centrifuged for 1min, the flow through was discarded and washed as stated in the manufacturer's protocol. The DNA was eluted with 50µL of DNA elution buffer and used immediately. NanoDrop UV spectrometry was used to quantify the DNA, where the elution buffer was used as a blank control.

6.2.8. Immunocytochemistry & SEM

Monolayer cells and cells on scaffolds at day 7 or 14 were both studied by immunocytochemistry. For monolayers, cells were dissociated as above and re-seeded on glass slides placed in a 24 well plate and allowed to grow confluent for 24hrs. Cells on slides and scaffolds are both fixed with 4% paraformaldehyde in PBS (PFA, Thermo Fisher Scientific) for 10mins at room temperature and washed in DPBS. Samples are permeabilised with 0.5% Triton®X-100 (MP Biomedicals, Thermo Fisher Scientific) for 10mins at room temperature and washed again with DPBS. Blocking buffer (DPBS + 1% Bovine Serum Albumin + 0.05% Triton X-100) was added to the samples to reduce background from the samples and left for 1hr at room temperature. The samples were incubated with 50µL diluted primary antibodies

according to Table 6.3, where slides were incubated for 24hrs and scaffolds for 48 hrs at 4°C. The samples were washed again with DPBS at least three times, then incubated with 50µL secondary antibodies (Table 6.4) for either 1hr at room temperature for slides or 48hrs at 4°C for scaffolds, all samples were left in the dark during this period. Samples were then washed with DPBS again and stained with DAPI (Invitrogen™, Thermo Fisher Scientific, UK) with a dilution of 1/5000µL in DPBS for 2hrs for scaffolds or 1/10000µL in DPBS for 10mins for slides. All samples were washed in DPBS and scaffolds were stored at 4°C as they were until required for imaging, slides were mounted with 50:50 glycerol (Sigma Aldrich, UK): DPBS and stored in the dark at 4°C. Images were taken using the Olympus Fluoview FV1000 Confocal Laser Scanning Microscope at the Dunn School of Pathology, University of Oxford. All images were taken using the 60X objective lens. Monolayer samples were imaged by Ujang Purnama and all scaffolds were imaged by the author. Images were processed on ImageJ.

Scanning Electron Microscopy (SEM) was used to study the morphology of cells seeded on scaffolds using the Zeiss EVO MA10 as described in section 4.2.2. Scaffolds were fixed with 4% PFA for 30mins at room temperature and washed with deionised water before being frozen at -20 °C and freeze-dried. They were then mounted on stubs and sputter coated with 4nm platinum using the Leica ACE600 Coater (Leica Biosystems, UK) at a rate of 0.11nm/s.

Table 6.3: Primary antibodies used for immunocytochemistry

Primary Antibody	Source	Dilution
Monoclonal Anti-α-Actinin (Sarcomeric)	Sigma Aldrich	1:500
Recombinant Anti-alpha smooth muscle Actin (α-SMA) antibody	Abcam	1:100
Vimentin	Abcam	1:200
DAPI	Life Technologies	1:5000

Table 6.4: Secondary antibodies used for immunocytochemistry

Secondary Antibody	Source	Dilution
Alexa Fluor®-488 donkey anti-rabbit	Invitrogen by Thermo Fisher Scientific	1:200
Alexa Fluor®-594 donkey anti-mouse	Invitrogen by Thermo Fisher Scientific	1:200

6.2.9. Mechanical Testing

Mechanical testing was performed on tri-layer samples on day 14 of culture, scaffolds were prepared as mentioned in section 6.2.2-3. and tested using wet tensile testing as described in Section 5.2.1. Cell seeded scaffolds were compared to non-seeded scaffolds.

6.3. Results

6.3.1. hiPSC Cell Culture & Differentiation

hiPSC derived cardiomyocytes (hiPSC-CMs) are a phenotypically mixed population of cells as it is challenging to obtain a batch of pure CMs, it usually requires treatment to metabolically select the cell-type of interest. The cells used in this study were 73% cardiomyocytes as shown by flow cytometry [400]. The remaining non-cardiomyocyte (NCM) cells are either fibroblasts, SMCs, or endothelial cells. Immunocytochemistry was used to stain and image NCM and CM cells to confirm the presence of the mixed population. Fig.6.2 shows the cells used were positive for vimentin (fibroblast marker), sacromeric actinin (cardiomyocyte marker) and alpha-smooth muscle actin (α-SMA-marker for SMCs and myofibroblasts). As the cell type of interest for heart valves is myofibroblasts, the key distinction between SMCs and myofibroblasts is the presence of unique microfilament bundles (stress fibres) which were not observed in these samples.

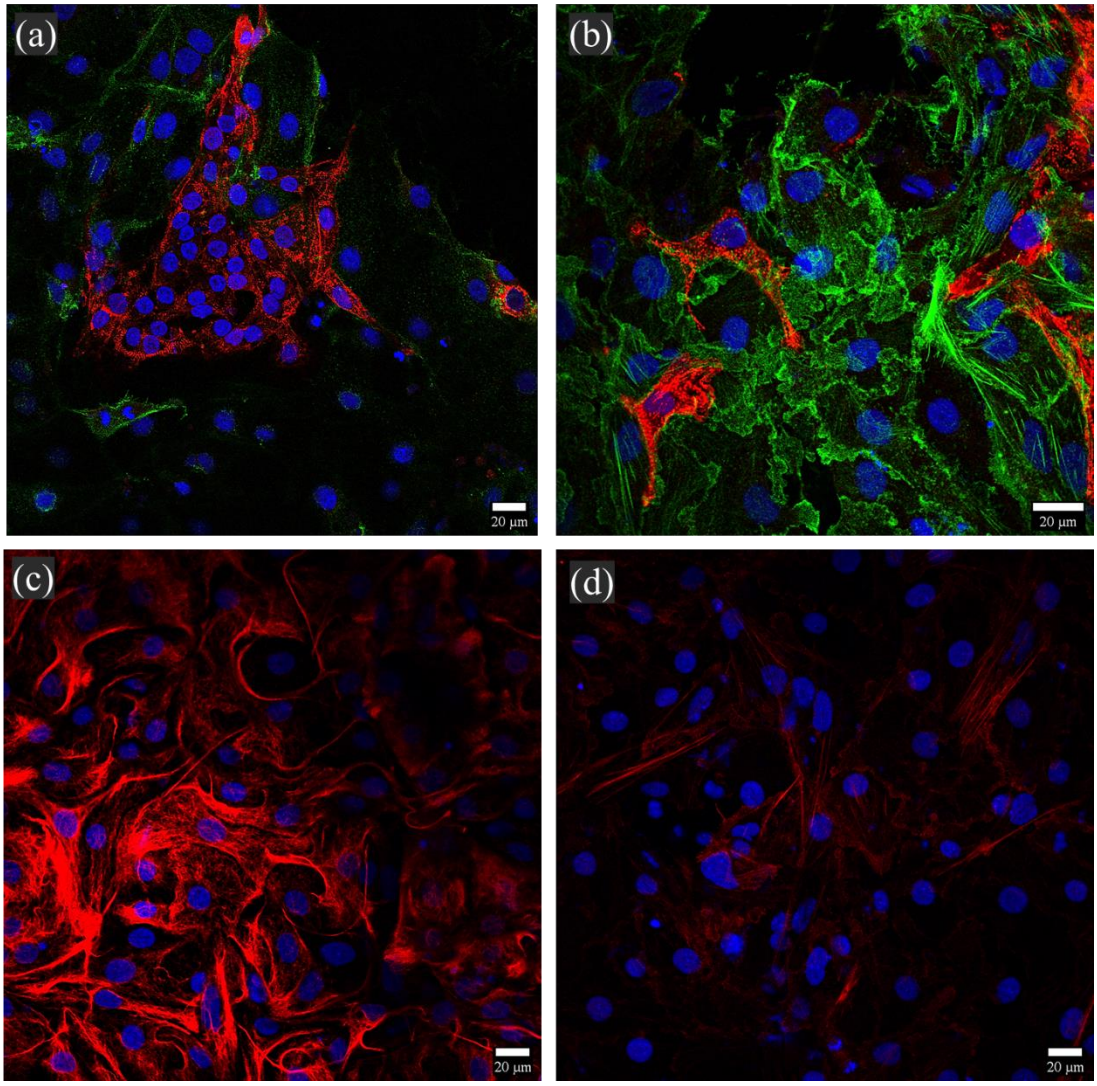

Figure 6.2: Laser scanning confocal images of monolayer cells stained for sacromeric actinin (red) and vimentin (green) in (a) and (b), α-smooth muscle actin (red) in (c) and (d) and DAPI in blue for all images to mark the nuclei of cells.

6.3.2. Cell Viability

hiPSC-CMs were cultured on FEG-based scaffolds and the metabolic activity was studied over a 7-day period. Fig.6.3 shows the results for FEG-based scaffolds compared to a control grown in a 96-well tissue culture plate. It was found on day 1, the cells were very metabolically active on the tissue culture plate compared to both the uncross-linked and cross-linked scaffolds. However, after 4 days of culture, the

metabolic activity of cells seeded on the culture plate dropped significantly, whereas cells on the scaffolds showed no significant difference. Fig.6.4 and Table 6.5 show the metabolic activity of the hiPSC-CMs culture on all samples normalised to the response on day 1. Overall, the cross-linked scaffold performed the best as there was a significant decrease in the metabolic activity of both the control and uncross-linked scaffolds after day 7, whereas the cross-linked sample maintained the viability of the cells over a 7-day period with no significant difference in the metabolic response.

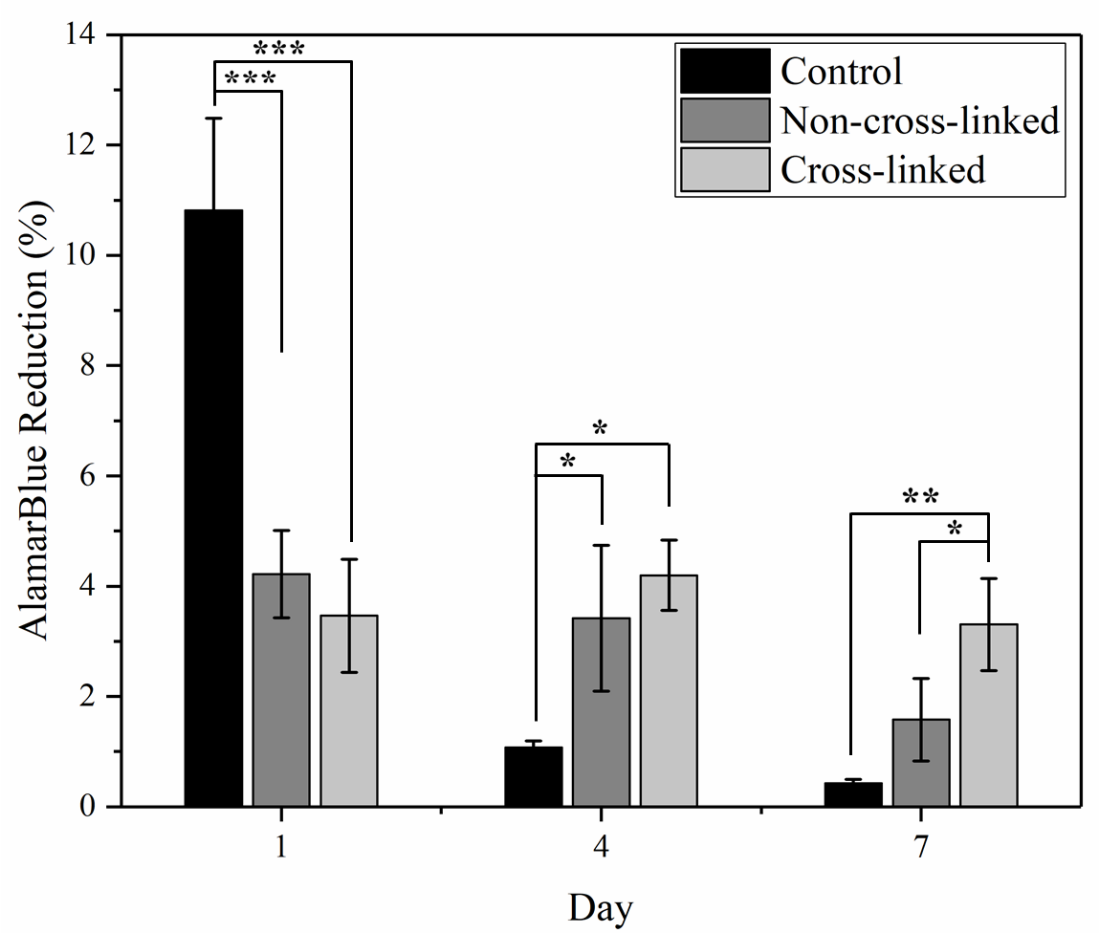

Figure 6.3: AlamarBlue assay results showing metabolic activity of hiPSC-derived cardiomyocytes over a 7-day period on monolayers (control sample) compared to uncross-linked FEG and cross-linked FEG samples, where *p<0.05, **p<0.005 and ***p<0.0005, n=4.

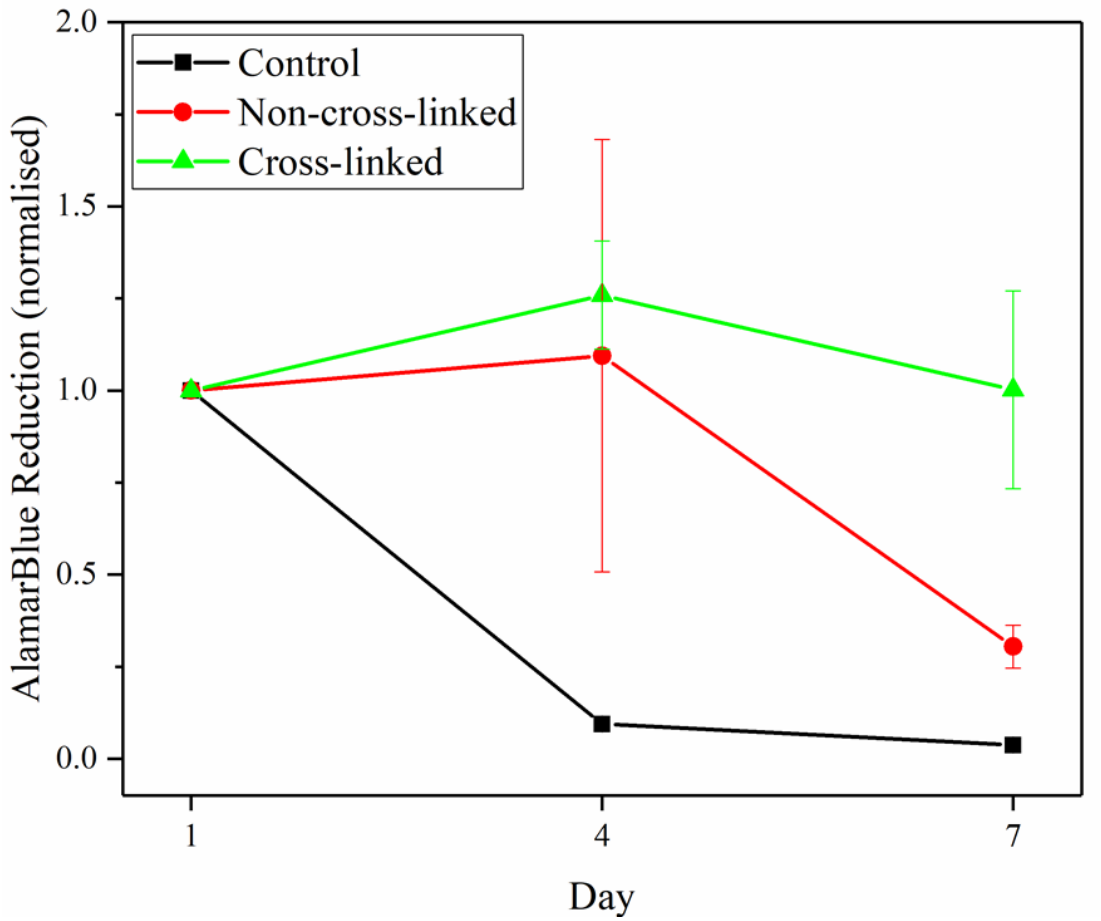

Figure 6.4: AlamarBlue assay results normalised at day 1 for all samples to show the change in metabolic activity of hiPSC-CMs on a control sample compared to FEG uncross-linked and cross-linked samples.

Table 6.5: AlamarBlue assay results for FEG-based scaffolds

Composition	AlamarBlue Reduction (normalised at day 1)	
	Day 4	Day 7
Control	0.1 ± 0.02	0.04 ± 0.002***
Uncross-linked	1.1 ± 0.6	0.3 ± 0.1***
Cross-linked	1.3 ± 0.1	1.0 ± 0.3

*Normalised to response at day 1, where ***p<0.0005.*

The viability of collagen-FEG based composites was also studied using the AB assay over an 18-day period (Fig.6.5). It was found that the substitution of collagen for FEG significantly affected the metabolic activity of the hiPSC-CMs from day 1 to day 10 where 100C scaffolds had the highest metabolic activity. After day 10, there was no significant difference in the samples containing more FEG, they were found to metabolise significantly more than 100C scaffolds by day 18.

Table 6.6 and Fig.6.6 represent the AB response normalised to day 1. For 100C and 75C-25E scaffolds, there was no significant difference in the metabolic activity of the hiPSC-CMs after day 7, however, the activity remained consistent at a 2.6-fold or 3.0-fold increase for 100C or 75C-25E, respectively, from day 7 onwards up to day 14, suggesting the cells were viable and metabolising. When more than 50% of the collagen was substituted for FEG there was a significant increase in the metabolic activity after day 14 where 50C-50E and 25C-75E had a 4.0-fold increase in the metabolic activity compared to day 1.

Table 6.6: AlamarBlue assay results for collagen-FEG scaffolds

Composition	**AlamarBlue Reduction (normalised at day 1)**				
	Day 4	**Day 7**	**Day 10**	**Day 14**	**Day 18**
100% COL	1.7 ± 0.1	2.6 ± 0.4	2.6 ± 0.2	2.9 ± 0.3	2.4 ± 0.1
75% COL-25% FEG	2.0 ± 0.6	3.1 ± 0.7	2.8 ± 0.5	3.3 ± 0.9	3.5 ± 0.7*
50% COL-50% FEG	0.7 ± 0.2*	1.2 ± 0.3**	2.9 ± 0.3	4.3 ± 0.4*	4.0 ± 0.6***
25% COL-75% FEG	1.6 ±0.4	0.8 ± 0.1**	1.8 ± 0.4*	3.2 ± 0.6	3.3 ± 0.3
25% COL-75% FEG	1.7 ± 0.1	2.6 ± 0.4	2.6 ± 0.2	2.9 ± 0.3	2.4 ± 0.1

*Normalised to response of composite samples at day 1, where *p<0.05, **p<0.005 and ***p<0.0005 for samples compared to 100% COL.*

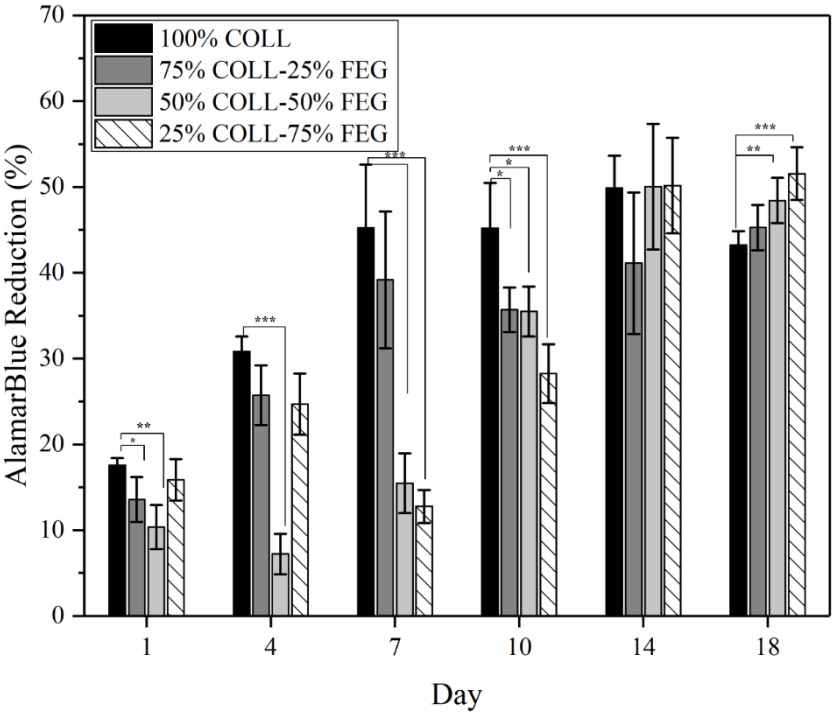

Figure 6.5: AlamarBlue assay results showing metabolic activity of hiPSC-derived cardiomyocytes over an 18-day period on cross-linked collagen-FEG based scaffolds, where *p<0.05, **p<0.005 and ***p<0.0005, n=4.

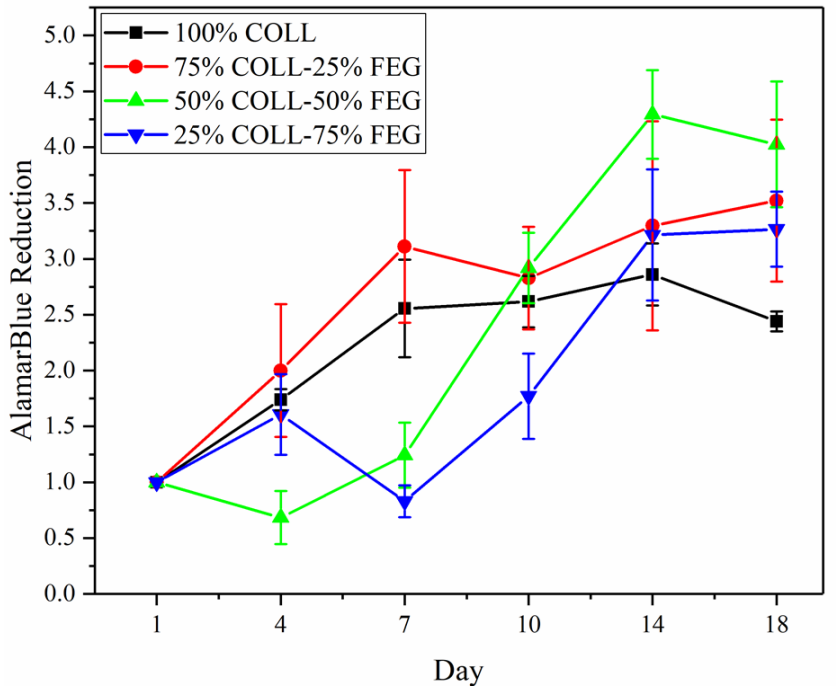

Figure 6.6: AlamarBlue assay results normalised at day 1 for 100% collagen, 75% collagen-25% FEG, 50% collagen-50% FEG and 25% collagen-75% FEG. Graph shows the change in metabolic activity of hiPSC-CMs over an 18-day period.

As 50C-50E was chosen as the composition for the ventricularis of the heart valve, its metabolic activity was compared to 100C and coll-HA which would simulate the fibrosa and spongiosa layer of the heart valve, respectively. Fig.6.7 presents the metabolic activity data measured using the AB assay over an 18-day period. It was found that cells seeded on 100C scaffolds were metabolising significantly higher than cells seeded on the other variants at day 1. However, after day 4, cells seeded on coll-HA samples metabolise significantly more than the other compositions and continue to metabolise significantly up to day 14. The normalised data has been presented in Fig.6.8 and Table 6.7. Fig.6.8 shows that cells on coll-HA samples metabolised more than both of the other compositions throughout the 18-day period. Cells on coll-HA samples metabolised up to 5-fold higher compared to day 1 which was significantly higher than all other compositions on day 14. By day 18, cells seeded on 100C scaffolds had the lowest metabolic activity at 2.4-fold higher compared to day 1, whereas it was 4.1-fold and 4.0-fold higher for cells seeded on coll-HA and 50C-50E scaffolds respectively.

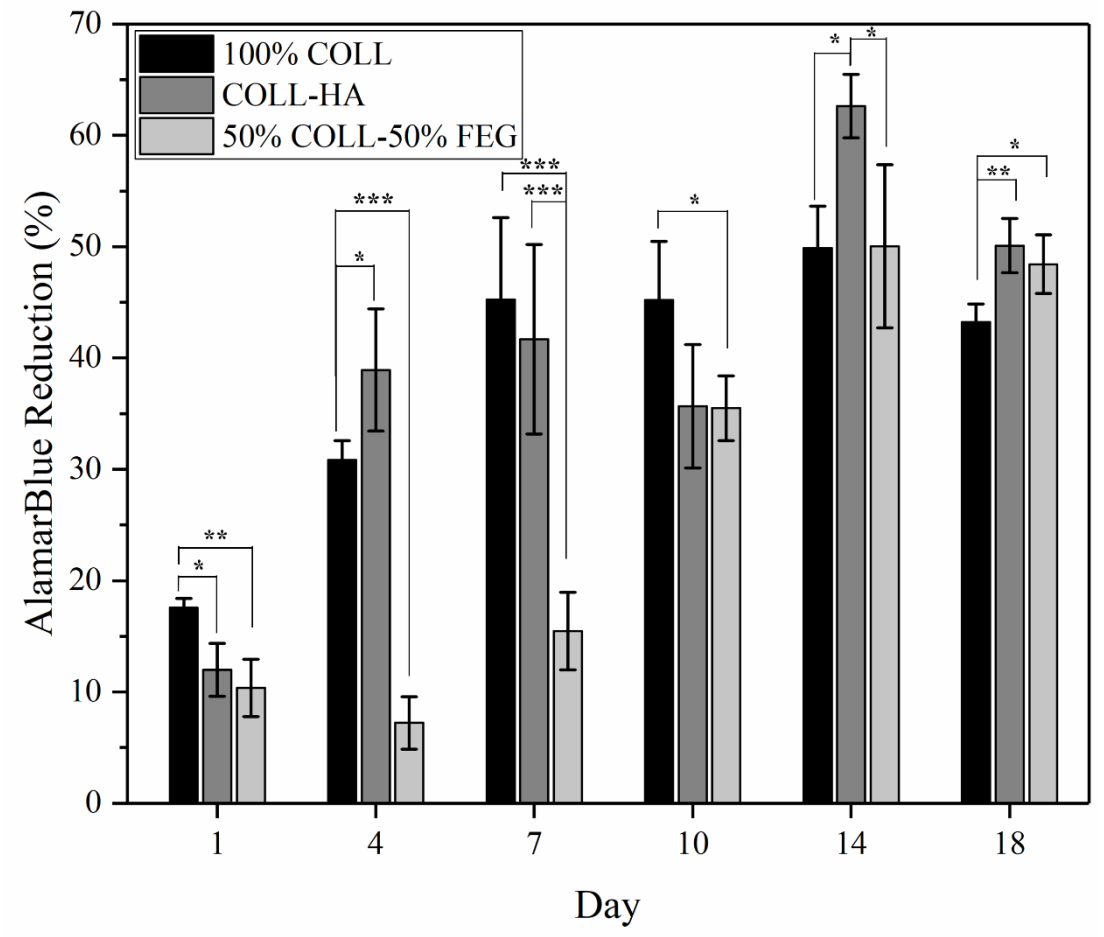

Figure 6.7: AlamarBlue assay results showing metabolic activity of hiPSC-derived cardiomyocytes over an 18-day period on 100% collagen, coll-HA and 50% coll-50% FEG scaffolds, where *p<0.05, **p<0.005 and ***p<0.0005, n=4.

Table 6.7: AlamarBlue assay results for 100% collagen, coll-HA and 50% coll-50% FEG scaffolds

Composition	AlamarBlue Reduction (normalised at day 1)				
	Day 4	Day 7	Day 10	Day 14	Day 18
100% COL	1.7 ± 0.1	2.6 ± 0.4	2.6 ± 0.2	2.9 ± 0.3	2.4 ± 0.1
COL-HA	3.1 ± 0.7**	3.5 ± 0.6*	3.0 ± 0.7	5.0 ± 0.8**	4.1 ± 0.7*
50% COL-50% FEG	0.7 ± 0.2*	1.2 ± 0.3*	2.9 ± 0.3	4.3 ± 0.4*	4.0 ± 0.6*

*Normalised to response at day 1, where *p<0.05 and **p<0.005.*

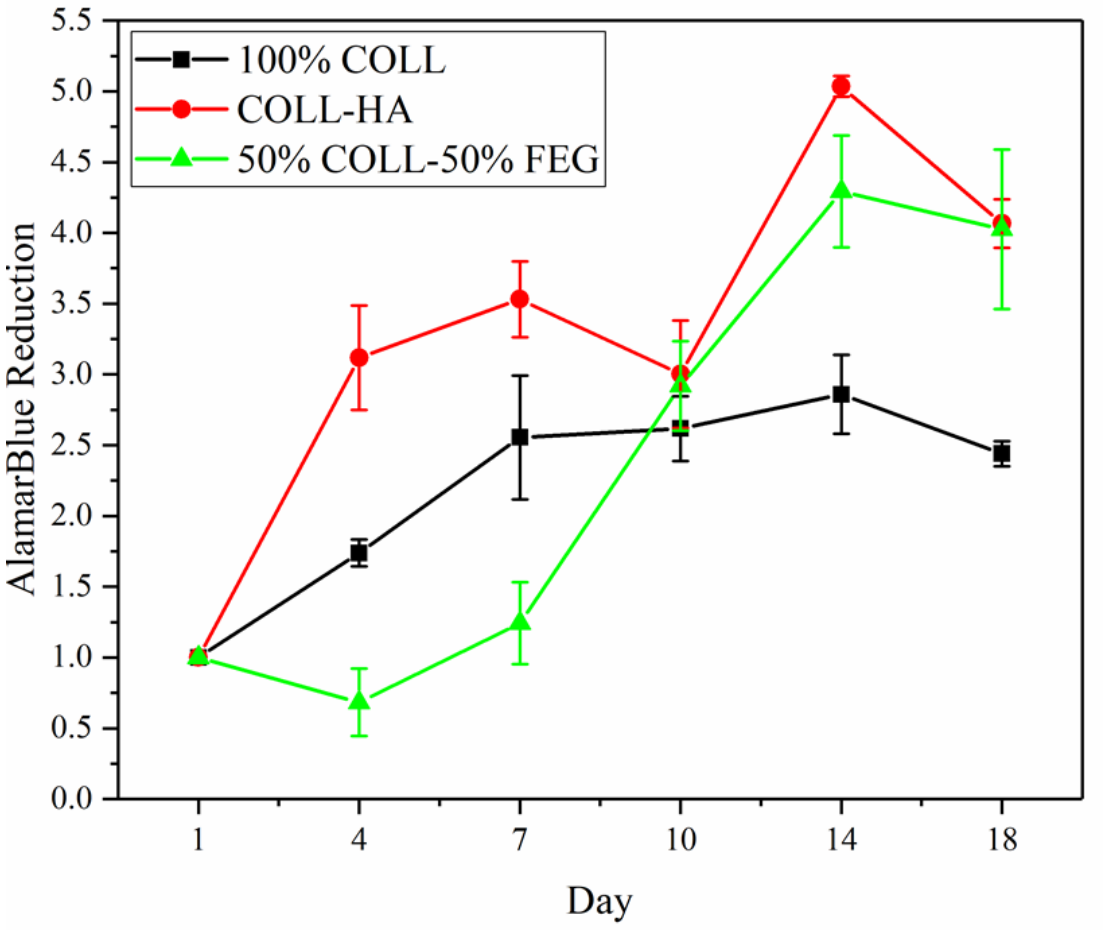

Figure 6.8: AlamarBlue assay results normalised at day 1 for 100% collagen, coll-HA and 50% coll-50% FEG samples to show the change in metabolic activity of hiPSC-CMs over an 18-day period.

6.3.3. Cell Attachment

Cell attachment for all compositions was measured on day 1. It was found that all scaffolds promoted the attachment of cells. Fig.6.9 shows the results for FEG based scaffolds, where there was no significant difference between the samples on day 1. Uncross-linked and cross-linked FEG had an attachment of 55±5% and 55±15%, respectively.

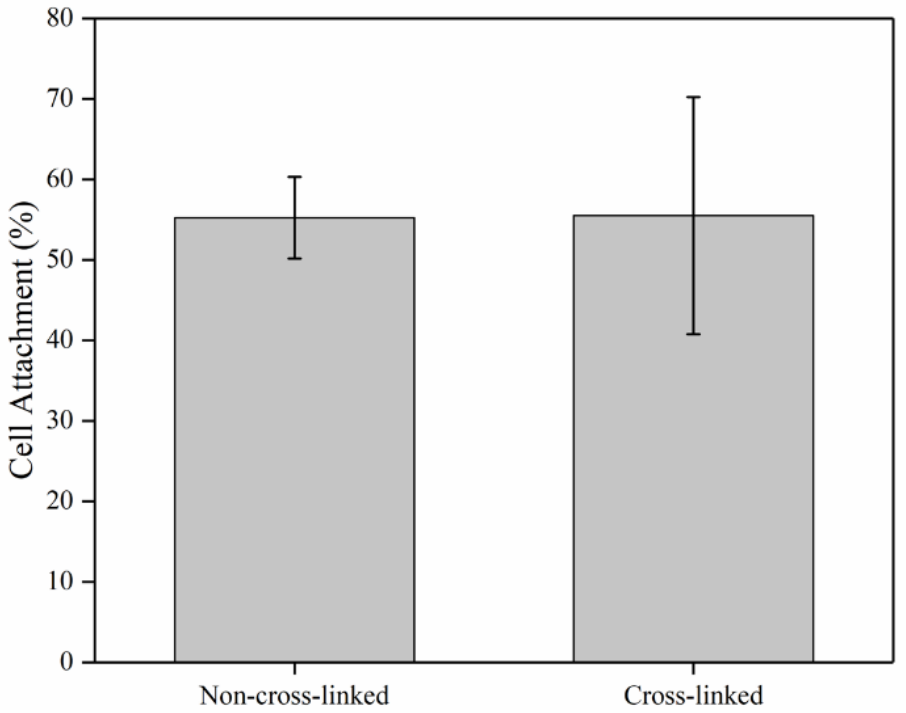

Figure 6.9: Attachment of cells at day for uncross-linked and cross-linked FEG-based scaffolds, measured using AlamarBlue assay as an indirect method, n=4.

Fig.6.10 shows the cell attachment for the composites, there was a significant difference when the concentration of FEG was over 50% only, although all samples resulted in an attachment of over 98%. Fig.6.11 compares coll-HA to 100C and 50C-50E, it was found there was no significant difference between coll-HA and the other variants.

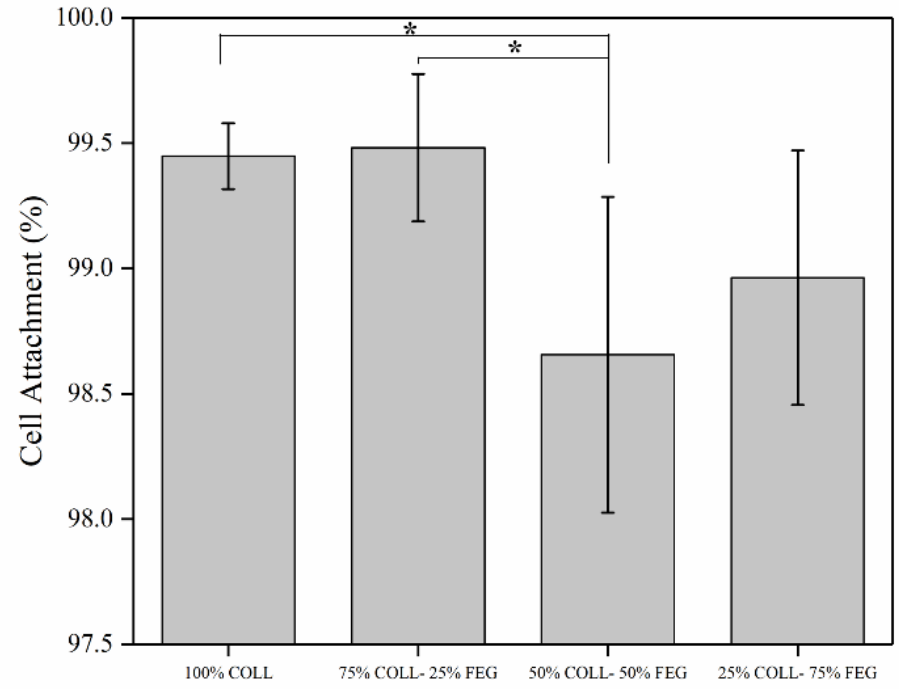

Figure 6.10: Attachment of cells at day 1 for 100% collagen, 75% collagen-25% FEG, 50% collagen- 50% FEG and 25% collagen-75% FEG scaffolds, measured using a cell counter, *p<0.05, n=6.

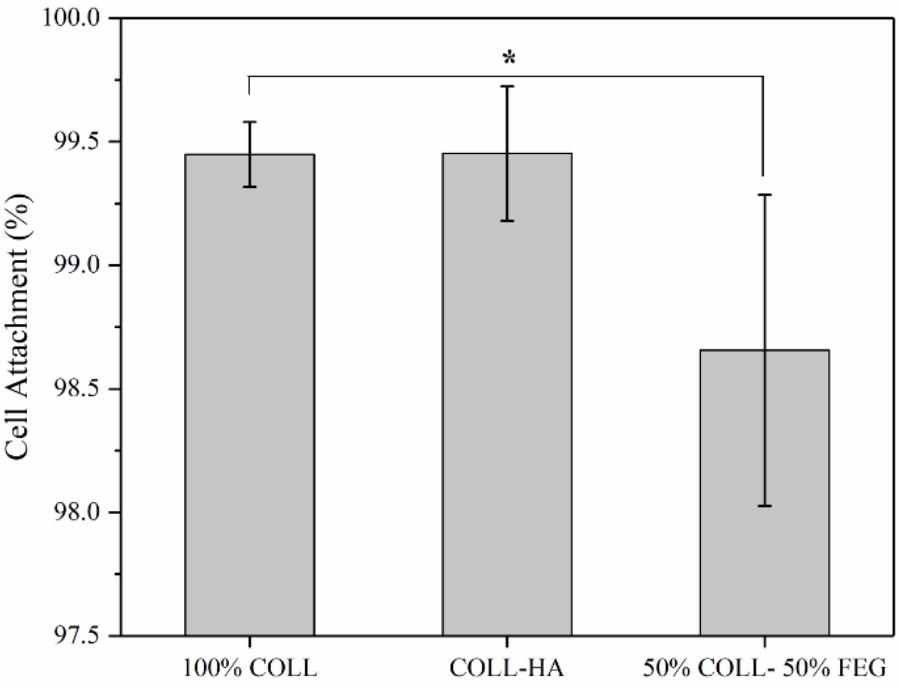

Figure 6.11: Attachment of cells at day 1 for 100% collagen, coll-HA and 50% collagen- 50% FEG scaffolds, measured using a cell counter, *p<0.05, n=6.

6.3.4. Real-time quantitative polymerase chain reaction (qPCR)

qPCR was used to understand the effect of the composition of scaffolds on the relative gene expression of hiPSC-CMs after culturing the cells for 14 days. These samples were compared to monolayer scaffolds directly after 15 days of differentiation with no further culturing. The first group of genes of interest were ECM markers, the expression of collagen type I (COL), elastin (ELA), fibrillin-1 (FIB-1) and lysyl oxidase (LOX) by hiPSC-CMs seeded on 100C scaffolds were compared to collagen-FEG composites. Fig.6.12 shows the effect of the composition on each gene of interest. It was found that COL gene was expressed significantly more in scaffolds compared to monolayer cells. Additionally, when comparing between scaffolds, there was a significant decrease in the expression of COL as the concentration of collagen reduced and FEG increased in the scaffolds. At day 14, there was a 33±5-fold increase in the expression of COL, whereas it was 7±0.5-fold, 6±0.3-fold and 13±0.8-fold for 75C-25E, 50C-50E and 25C-75E scaffolds, respectively. The expression of ELA was significantly higher than monolayer samples for all compositions except 100C. It was found that the replacement of collagen for FEG resulted in a significant increase in the expression of elastin by the hiPSC-CMs as it was 6±2-fold and 3±4-fold in 50C-50E and 25C-75E scaffolds, respectively, compared to 1.0±0.1-fold and 1.5±0.7-fold in 100C and 75C-25E, respectively.

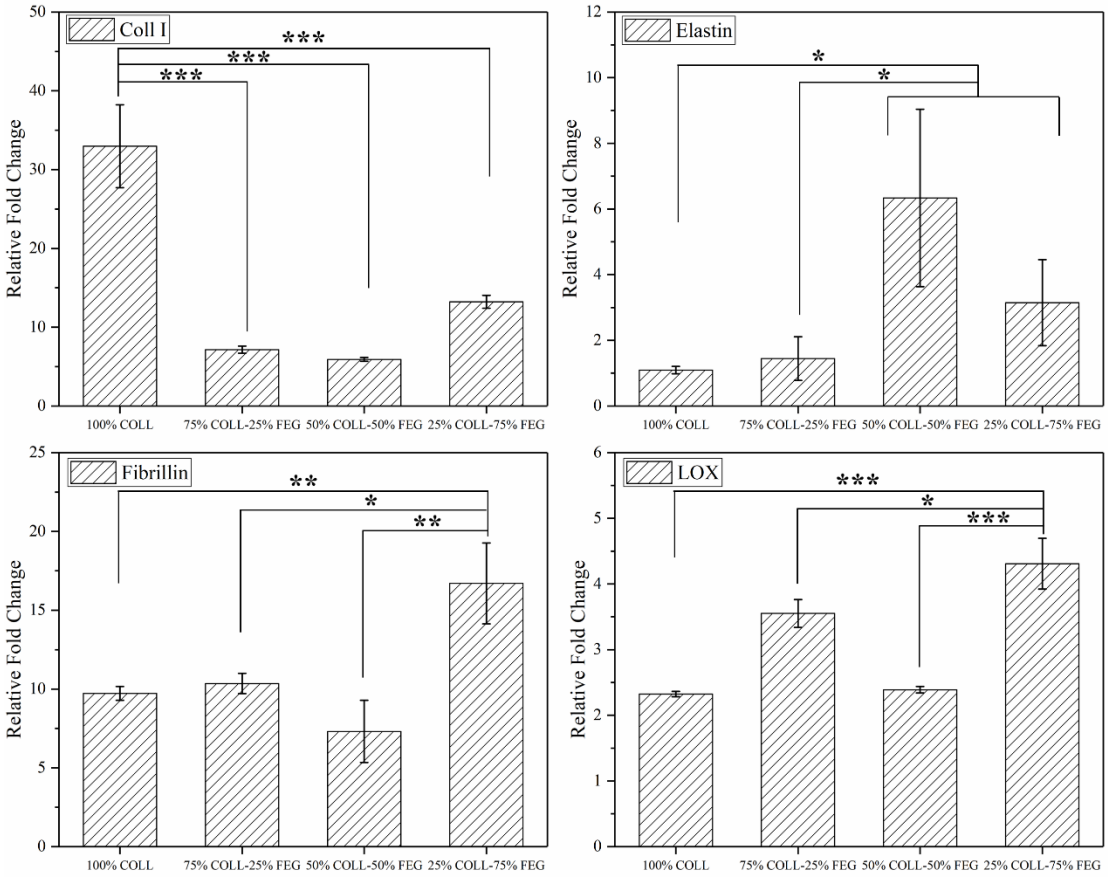

Figure 6.12: Relative expression of collagen type I, elastin, fibrillin and LOX after 14-days of culturing hiPSC-CMs on 100% collagen, 75% collagen-25% FEG, 50% collagen- 50% FEG and 25% collagen-75% FEG scaffolds in comparison to monolayer samples at day 0, *p<0.05, **p<0.005 and ***p<0.0005, n=3.

It was found that hiPSC-CMs expressed significantly higher levels of FIB-1 when seeded on any of the scaffolds compared to monolayers. Additionally, when comparing between the scaffolds, the substitution of collagen for FEG resulted in a significant increase in the expression of FIB-1 when there was 75% collagen replacement, resulting in a 17±3-fold increase in FIB-1 expression. It was also found that the expression of LOX was upregulated significantly in all scaffold compositions compared to monolayers. For scaffolds, it was also found that a significant

upregulation was only observed when 75% of collagen was replaced with FEG where a fold change of 4±0.4 was observed.

The second group of genes of interest were cell markers to understand the effect of the composition of scaffolds on the multiple phenotypes present within hiPSC-CMs. For these genes, 100C, coll-HA and 50C-50E scaffolds were used to emulate the fibrosa, spongiosa and ventricularis, respectively. The expression of vimentin (marker for fibroblasts), α-SMA (marker for myofibroblasts) and TNNT-2 (marker for cardiomyocytes) as well as ECM markers COL, ELA and HAS-2 (marker for hyaluronic acid) were studied at days 7 and 14 and compared to monolayers at day 0 (Fig.6.13).

The expression of vimentin was significantly higher in the scaffold compositions at both days 7 and 14 compared to monolayer samples. On day 7, 100C scaffolds had a significantly higher upregulation of vimentin compared to the other scaffold types. However, by day 14, the cells seeded on both coll-HA and 50C-50E scaffolds expressed higher levels of vimentin. The relative fold change for each gene has been presented in Table 6.8 and the normalised data has been presented in Table 6.9.

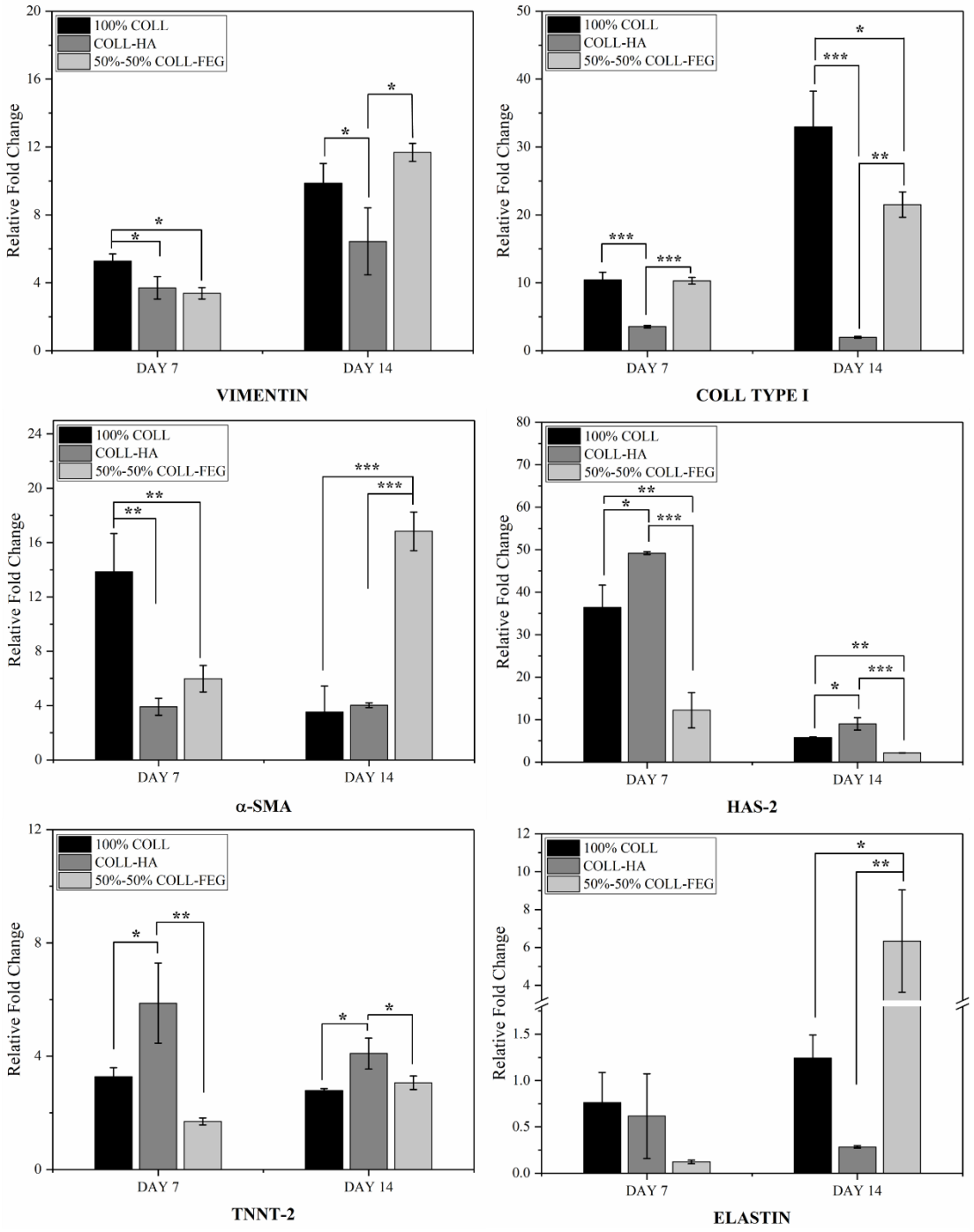

Figure 6.13: Relative expression of vimentin, alpha-smooth muscle actin (α-SMA), TNNT-2, collagen type I, HAS-2 and elastin by hiPSC-CMs when seeded on 100% collagen, coll-HA and 50% collagen- 50% FEG scaffolds were compared on days 7 and 14 to monolayer samples at day 0, *p<0.05, **p<0.005 and ***p<0.0005, n=3.

Table 6.8: : Relative gene expression by hiPSC-CMs seeded on 100% collagen, coll-HA or 50% collagen-50% FEG scaffolds

Day	Gene	Relative Fold Change		
		100% COL	COL-HA	50% COL-50% FEG
7	Vimentin	5.3 ± 0.4	3.7 ± 0.3	3.4 ± 0.7
	α-SMA	13.9 ± 2.8	3.9 ± 0.6	6.0 ± 0.7
	TNNT-2	3.3 ± 0.3	5.9 ± 1.4	1.7 ± 0.1
	Collagen type I	10.4 ± 1.1	3.6 ± 0.2	10.3 ± 0.5
	HAS-2	32.2 ± 4.6	43.5 ± 0.3	10.8 ± 3.7
	Elastin	0.8 ± 0.3	0.6 ± 0.5	0.1 ± 0.02
14	Vimentin	9.9 ± 1.2	6.4 ± 0.5	11.7 ± 2.0
	α-SMA	3.5 ± 1.9	4.0 ± 0.2	16.8 ± 1.4
	TNNT-2	2.8 ± 0.1	4.1 ± 0.5	3.1 ± 0.2
	Collagen type I	33.0 ± 5.3	2.0 ± 0.1	21.5 ± 1.9
	HAS-2	10.7 ± 0.6	7.9 ± 1.3	1.9 ± 0.02
	Elastin	1.2 ± 0.2	0.3 ± 0.01	6.3 ± 2.7

*Samples were compared on days 7 and 14 to monolayer samples at day 0, *p<0.05, **p<0.005 and ***p<0.0005, n=3*

Table 6.9: Relative gene expression by hiPSC-CMs when seeded on 100% collagen, coll-HA and 50% collagen-50% FEG scaffolds

Gene	Relative Fold Change (normalised to day 7)		
	100% COL	COL-HA	50% COL-50% FEG
Vimentin	1.9**	1.7**	3.5**
α-SMA	0.3*	1.0*	2.8***
TNNT-2	0.9	0.7	1.8**
Collagen type I	3.2**	0.6***	2.1**
HAS-2	0.2**	0.2**	0.2***
Elastin	1.6	0.5	51.6*

*Normalised at day 7 to compare difference in fold-change, *p<0.05, **p<0.005 and ***p<0.0005, n=3.*

Amongst the three compositions, after 14 days of culturing, 50C-50E upregulated the expression of vimentin the most with a fold change of 3.5 in comparison to 1.9 and 1.7-fold for 100C and coll-HA, respectively. Similarly, α-SMA was expressed significantly higher in the scaffolds compared to monolayers. On day 7, there was a significant upregulation of α-SMA by 100C scaffolds compared to the other variants. However, by day 14, there was a significant change in the expression of α-SMA, where the cells on the 100C scaffolds downregulated the expression of α-SMA, coll-HA maintained the same levels of expression, but cells seeded on 50C-50E scaffolds significantly upregulated the expression of α-SMA by 2.8-fold. The expression of TNNT-2 was also significantly higher by cells seeded on scaffolds compared to monolayer samples. On day 7, coll-HA samples promoted the expression of cardiomyocyte cells the most, with a significant difference compared to the other two scaffold types. The same trend was observed on day 14, and there was no significant difference between days 7 and 14 for 100C and coll-HA samples, however, there was a significant upregulation of TNNT-2 by cells seeded on 50C-50E scaffolds, although it was insignificant compared to the other two samples.

The expression of COL was significantly higher in cells seeded on scaffolds compared to monolayers for all sample types. There was no significant difference between 100C and 50C-50E scaffolds at day 7, however, cells seeded on coll-HA scaffolds expressed significantly lower levels of COL. Additionally, by day 14, cells seeded on coll-HA samples expressed lower levels of COL, resulting in a downregulation. Both 100C and 50C-50E scaffolds resulted in continued upregulation of COL on day 14, where cells on 100C had a 3.2-fold upregulation and cells on 50C-50E had a 2.1-fold upregulation. HAS-2 expression was significantly higher in all the scaffold compositions compared to monolayers on both days 7 and 14. On day 7, cells on coll-HA samples had a significant upregulation of HAS-2 compared to both 100C and 50C-50E. Although, 50C-50E promoted the upregulation of HAS-2, it was significantly lower than both 100C and coll-HA scaffolds. The same trend was observed on day 14, however, the fold change was significantly lower suggesting the expression of HAS-2 was downregulated by day 14 for all compositions as they all downregulated by 0.2-fold. The final ECM marker of interest was ELA, it was found on day 7, there was no significant difference in the expression of ELA between monolayers and cells seeded on all types of scaffolds, except for 50C-50E scaffolds which had significantly lower expression of elastin compared to monolayers. This was also true for cells seeded on 100C scaffolds, however, for coll-HA, there was a significant downregulation compared to cells in monolayers. For cells seeded on 50C-50E scaffolds there was a significant increase in the upregulation of elastin at day 14, where a fold change of 51.6 was observed.

6.3.5. Total DNA Quantification

Fig.6.14 presents the results for the DNA concentration for each composition. On day 1, cells seeded on 100C have the highest concentration of DNA, whereas there is no significant difference between the other two compositions. The same relationship is observed on day 14 where 100C scaffolds result in the highest DNA concentration. However, when comparing between days 1 and 14, there is a significant decrease in the concentration of DNA at day 14 compared to day 1 for all compositions (Table 6.10).

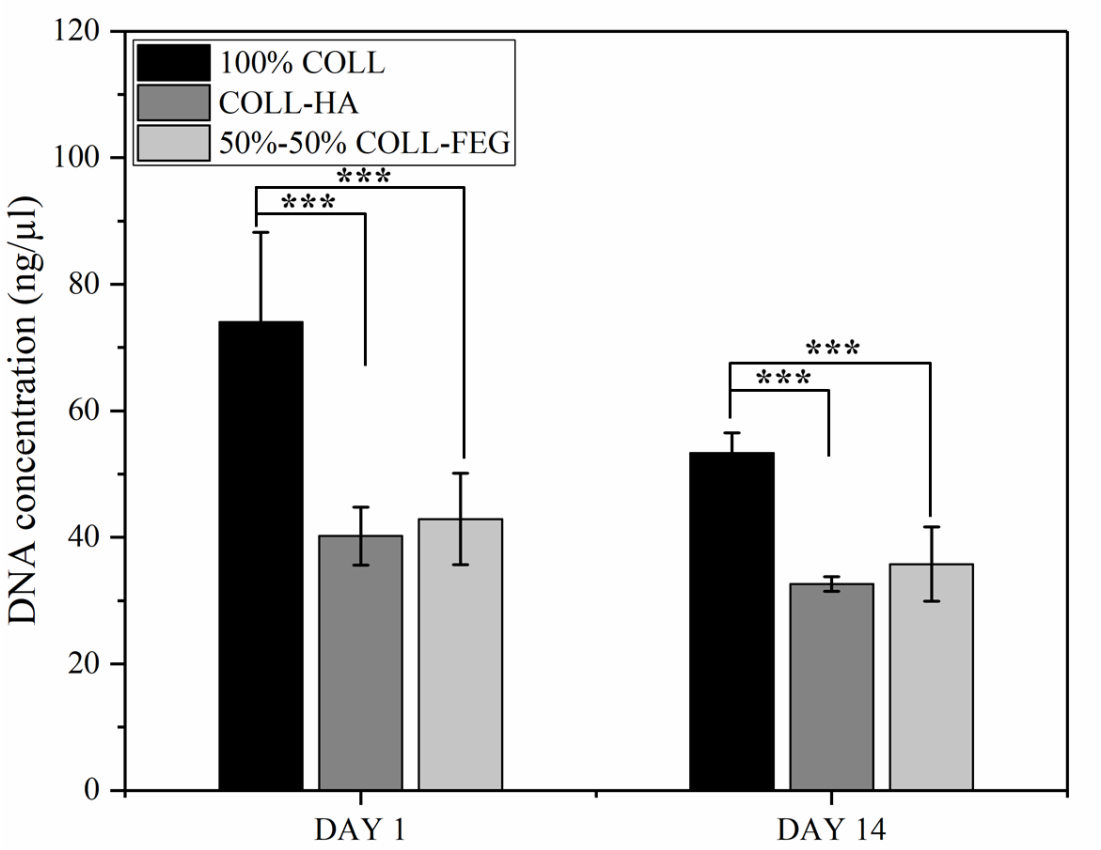

Figure 6.14: Concentration of DNA isolated from iPSC-CMs seeded on 100% collagen, coll-HA and 50% collagen-50% FEG scaffolds at day 1 and day 14, where ***p<0.0005, n=3.

Table 6.10: Concentration of DNA isolated on day 1 and day 14

Composition	DNA concentration (ng/µl)	
	Day 1	**Day 14**
100% COL	74 ± 14	53 ± 3***
COL-HA	40 ± 5	32 ± 1***
50% COL-50% FEG	42 ± 7	36 ± 6*

*where *p<0.05***p<0.0005, n=3.*

6.3.6. SEM & Immunocytochemistry

SEM was used to understand the interaction between the scaffolds and cells. FEG-based scaffolds were imaged after 7 days of culture (Fig.6.15). SEM images revealed that cells were able to attach to the scaffolds, suggesting that the FEG-based scaffolds are biocompatible. Although efforts were made to seed single cells on scaffolds, it appeared that the cells were clustered. Collagen-FEG composites which were seeded for 14 days were also imaged using SEM (Fig.6.16). It was also found that cells adhered to the surface of the scaffolds for all compositions. 100C scaffolds also contained cells that clustered as well as projections from the cells as observed with FEG based scaffolds. Additionally, coll-HA scaffolds were also studied with SEM after 14 days of culturing (Fig.6.17).

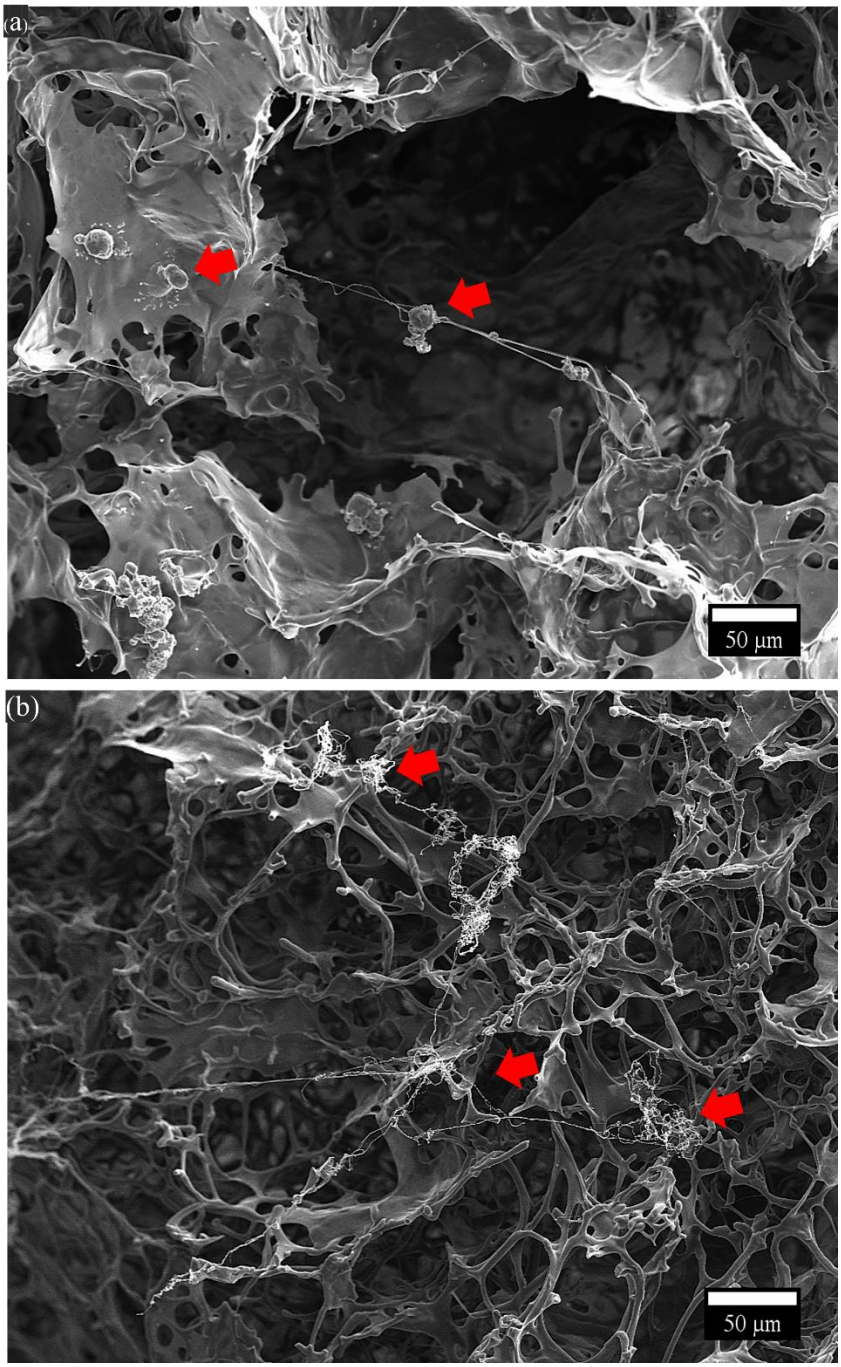

Figure 6.15: SEM images of iPSC-CMs seeded scaffolds at day 7 showing (a) uncross-linked FEG and (b) cross-linked FEG scaffolds. Cells have been marked with red arrows.

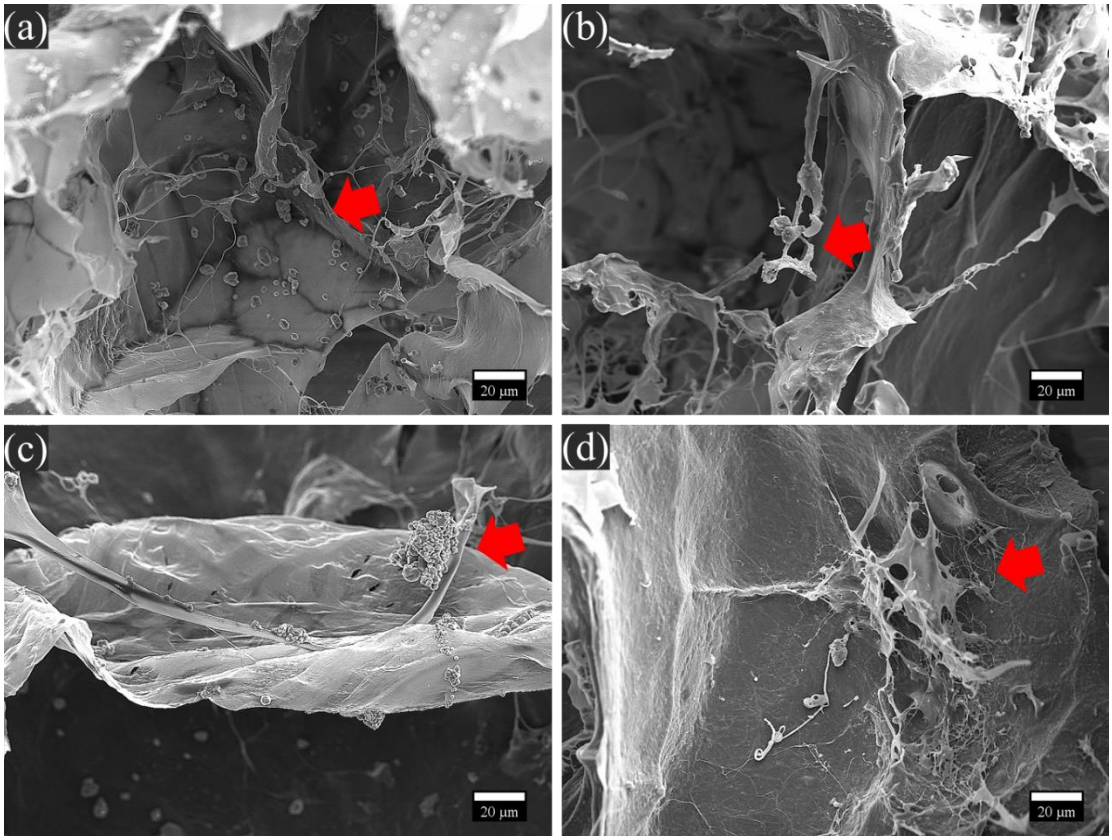

Figure 6.16: SEM images of iPSC-CMs seeded cross-linked scaffolds at day 14 showing (a) 100% collagen (b) 75% collagen-25% FEG, (c) 50% collagen-50% FEG and (d) 25% collagen and 75% FEG. Cells have been marked with a red arrow.

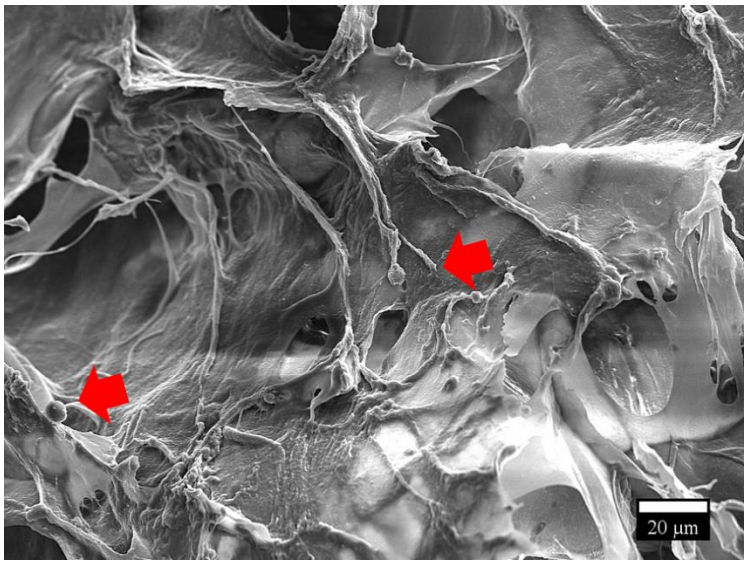

Figure 6.17: SEM image of iPSC-CMs seeded on a coll-HA scaffold at day 14. Cells have been marked with red arrows.

In addition to SEM imaging, immunocytochemistry was used to stain for particular proteins in cells as markers for cell type. Vimentin (marker for fibroblasts) and α-SMA (marker for myofibroblasts) were of interest as they are non-cardiomyocytes that have similarities to VICs. Additionally, as α-SMA is often used as a marker for SMCs, it was important to observe this marker as myofibroblasts appear as stress fibres. Confocal images have been presented in Fig.6.18, cells were observed in all samples, further confirming successful adhesion of cells throughout the culture period. All samples imaged stained positive for both vimentin and α-SMA, suggesting both fibroblasts as well as myofibroblasts were present.

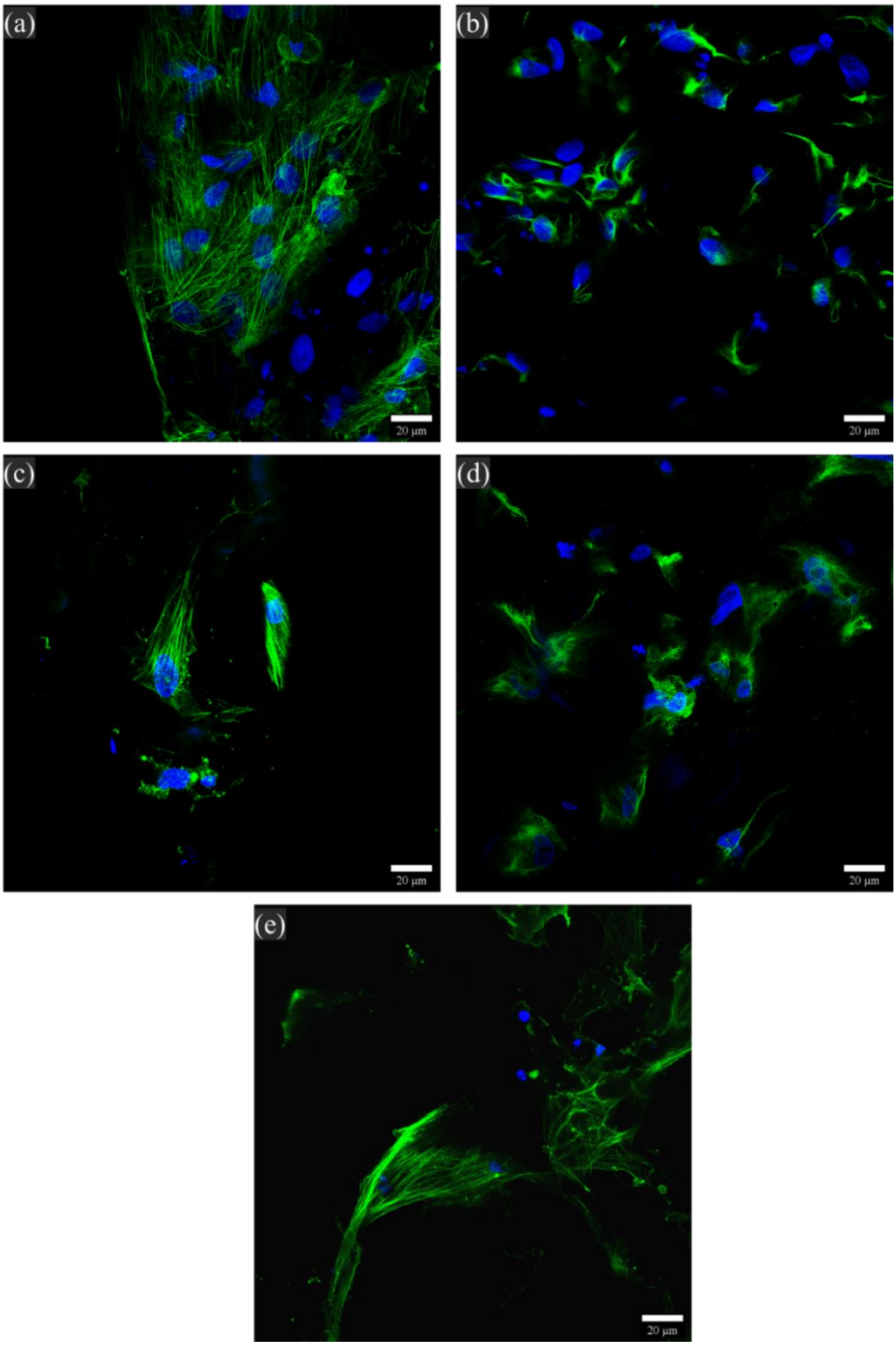

Figure 6.18: Laser scanning confocal images of scaffolds seeded with iPSC-CMs stained for α-smooth muscle actin (green) in (a) 100% collagen, (c) 50% collagen-50% FEG, (e) coll-HA and vimentin (green) in (b) 100% collagen (d) 50% collagen- 50% FEG scaffolds after 14 days of culture. DAPI in blue for all images to mark the nuclei of cells. All images were taken under the 60X objective lens.

6.3.7. Tensile Properties of Tri-layers

Results for the tensile test are presented in Fig.6.19, it was found that *in vitro* culture had no significant effect of culture on the Young's modulus. However, the strain-to-failure and extensibility of tri-layer scaffolds was 1.5-fold higher after culture (Table 6.11).

Table 6.11: Summary of tensile properties of non-seeded tri-layers and seeded tri-layers.

Composition	Young's Modulus (kPa)	Extensibility (%)	Strain-to-failure (%)
TRI-LAYER (NON-SEEDED)	10.2 ± 4.9	17.5 ± 5.4	35.4 ± 5.2
TRI-LAYER (SEEDED)	27.9 ± 14.8	27.0 ± 3.5	52.6 ± 1.3

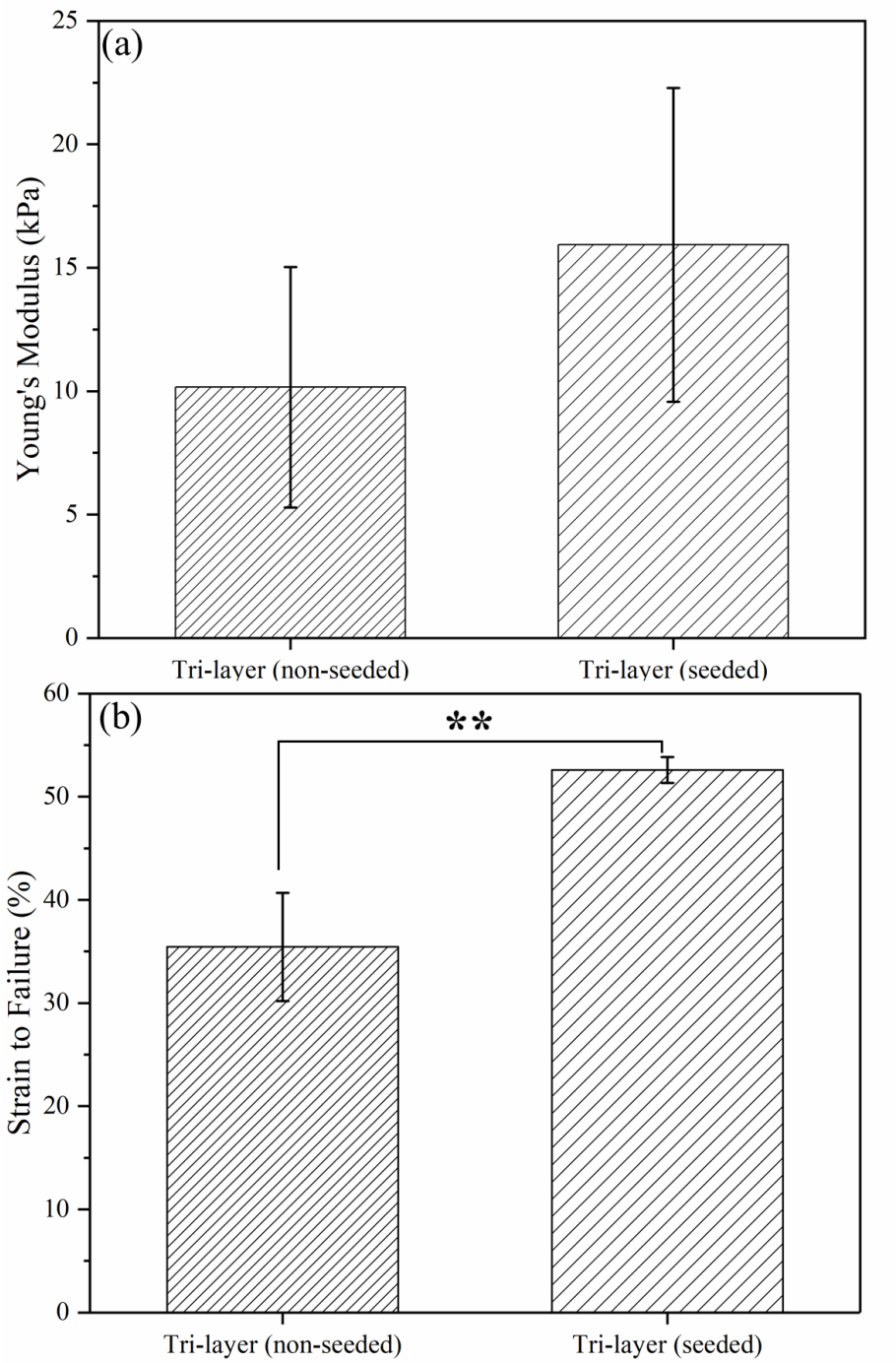

Figure 6.19: Tensile test results for tri-layers with and without cell culture. Seeded cells were cultured for 14 days with hiPSC-CMs. Results show (a) the Young's modulus and (b) the strain to failure.

6.4. Discussion

6.4.1. Cell Attachment & Viability

The bioactivity of a scaffold is dependent on multiple factors associated with its physical, biochemical, and biomechanical properties [401]. The physical properties include its porosity, pore size, the interconnectivity of pores and the density of available ligands (cell binding sites) [344], [345]. The cell attachment results suggest that FEG contains cell binding sites as cellular adhesion was observed and therefore suggests that these sites are composed of hydrophobic residues as they were not hydrolysed. This finding agrees with the literature as elastin-like-polypeptides (ELPs) which are hydrophobic oligomers and α-elastin have been shown to be chemotactic [402], [403]. Elastin contains elastin-binding protein (EBP) complexes which act as receptors for cells [9], [404]. EBPs have been shown to bind to hydrophobic residues of ELPs (VGVAPG) and stimulate a cellular response [405]. Additionally, no significant difference in cell attachment was observed between uncross-linked and cross-linked samples, implying that the cross-linking sites (which are composed of hydrophilic residues) and the cell-binding sites are different.

The viability of iPSC-CMs on FEG-based scaffolds was lower compared to other compositions, but significantly better than the control group. This is an unusual result as cells are cultured in 2D environments. A possible explanation for this could be the high cell density (10000 cells/µl) used in a 96 well-plate and the absence of any coating which is normally applied during cell differentiation. This could have caused overcrowding and poor adhesion to the plate of cells resulting in a weak response. The results suggest cells seeded on cross-linked scaffolds had a higher metabolic activity

and therefore viability. A possible reason for this could be the low stiffness of uncross-linked scaffolds which resulted in contraction due its inability to sustain the forces exerted by cells which can be of the order of 1nN for fibroblasts [406]. However, the local stiffness of scaffolds is expected to be significantly higher as the solid modulus of elastin is 1.1MPa [42]. It is surprising that FEG supported cell adhesion as it is an extremely hydrophobic protein and cells are known to be more conducive on hydrophilic surfaces as they can spread their cytoskeleton to form focal adhesions [407]–[409]. However, as discussed in Section 4.4.2, FEG based scaffolds absorb significantly more solvent (380-560%) compared to natural elastin (46%) which suggests it is more hydrophilic than polymeric elastin. FEGs inherently cross-linked and fibrillar nature makes it a better choice than synthetic variants that do not resemble the parent protein as "naked" soluble peptides have been shown to be unsuitable for cell attachment and require functionalisation [410]. Additionally, polymeric elastin has also been shown to limit cell viability due to its poor solvent interactivity and therefore unavailability of buried hydrophobic residues [175], [229], [233]. The steady cell viability and initial adhesion of cells on FEG scaffolds shows that it is a biocompatible material, however, the pores are too small for cell growth and infiltration, and therefore were not studied further [411].

Collagen-FEG composites and coll-HA scaffolds showed significantly higher cell attachment compared to FEG-only scaffolds. The method used to determine cell attachment for both scaffold types is not directly comparable as one involved the reduction of AB which assumes the fluorescence of a sample is proportional to the number of cells, and the other involved determining the relative percentage of cells detached via a digital cell counter. As the compositions of collagen-FEG and coll-HA

composites had the same relative density they can be compared to each other. It was found that all scaffolds showed an attachment of over 98% of cells. However, there was a higher variation in the results at higher concentrations of FEG (above 50%), implying that multiple factors are involved and could have affected cell attachment.

Each of the materials studied have unique ligands that associate with different cell-surface receptors. As mentioned above, elastin has EBPs which provide sites for adhesion. Conversely, collagen has unique arginine-glycine-aspartic acid (RGD) peptides which mediate cellular adhesion by integrins including $\alpha_1\beta_1$ and $\alpha_2\beta_1$ [412]. As collagen was present in all the collagen-FEG composites, it is likely to contribute to the response for all samples. Therefore, the higher cell attachment is due to the presence of both collagen and FEG and their independent binding sites. The reasoning for higher variation includes the increase in hydrophobicity of scaffolds as shown by the decrease in water-uptake ratio previously, as well as the change in the pore characteristics of samples with a higher concentration of FEG. The pore size of 50C-50E is significantly larger than 100C which means that the surface area-to-volume ratio (SA/V) is lower due to the following relationship (for a tetrakaidecahedral unit cell), where d is the average pore size and the relative density is taken as 1% [344]:

$$\frac{SA}{V} = \frac{1.015}{d} \qquad \text{(Equation 6.4)}$$

A lower SA/V means there is an increase in distance between cells and therefore a decrease in the density of cell binding ligands resulting in poorer cell adhesion. The large variation in 25C-75E scaffolds can be explained by the significantly higher SA/V ratio of 2.3-fold compared to 100C and the significantly lower swelling ratio which results in contraction. The interaction between these two parameters resulted in the

variation in the cell adhesion and no significant difference compared to 100C or 50C-50E.

DNA quantification was used to assess the cell attachment on day 1 and 14 as it has been shown to be a more conclusive method [413]. The similarity between coll-HA and 50C-50E scaffolds in terms of DNA content could be due to increase in hydrophobicity of coll-HA scaffolds as HA was functionalised by cross-linking it to collagen. The modification of HA is essential as it is naturally soluble in water and highly negatively charged which makes it non-conducive for cell attachment in the unmodified state [188]. DNA content decreased on day 14 for all samples and metabolic activity plateaued after day 10 for 100C whereas it continued to rise for coll-HA and 50C-50E. A possible reasoning for this is that the cells seeded on the scaffolds were at different stages of the cell cycle and were activated at different time points. The sudden increase at day 10 implies that one of the subpopulation of cells, which include fibroblasts and SMCs may be growing during this stage. This reasoning could also be extended to the composites which showed low metabolic activity up to day 10 and sudden increase thereafter.

6.4.2. Expression of Layer-Specific Markers

The remaining discussion will consider the gene expression of cell markers on 100C, 50C-50E and coll-HA scaffolds. qPCR results revealed the expression of fibroblasts, α-SMA and TNNT-2 genes on both days 7 and 14. Overall, normalisation of the day 14 results revealed an upregulation of vimentin on all scaffolds, the upregulation of α-SMA on coll-HA and 50C-50E and the upregulation of TNNT-2 on 50C-50E only. Vimentin is the marker for fibroblasts and is the dominant cell type of VICs that remains quiescent. α-SMA is the marker for SMCs and myofibroblasts, of which the

latter is hypothesised to be upregulated during injury or disease to promote remodelling [414]. TNNT-2 is the marker for cardiomyocytes, the cell-type which has the lowest abundance in VICs [73]. The results suggest that the scaffold compositions studied promote the maturation of non-CM cells significantly more than that of CMs. In valves, quiescent fibroblasts are characterised by a high expression of vimentin and low expression of α-SMA as seen with 100C and coll-HA in comparison to the 2.8-fold increase in 50C-50E [415]. Similar to the results, in valves, a greater proportion of α-SMA is found in the radial (elastin rich) layer [243], [416]. The relationship between α-SMA and the stiffness of a substrate is not clear as some studies have shown a higher stiffness promotes the activation of VICs whereas others have reported the opposite effect [180], [375], [417]. The effect of the composition, in particular the presence of FEG, a form of elastin, can offer a better explanation. Elastin has been shown to promote a contractile phenotype of SMCs which also explains the low metabolic activity observed up to day 7 [229], [240], [418]. 100C scaffolds showed upregulation of α-SMA on day 7 and a significant downregulation on day 14, implying that cells on the scaffolds changed from a contractile (quiescent) to synthetic (proliferative) state [419]. A similar response has been shown by Yamamoto *et al* who reported collagen templates promoted a synthetic phenotype and elastin promoted a contractile phenotype [420].

Contractile cells have a flat and elongated shape, which is similar to that observed by LSCM [421], [422]. Spreading of cells and the presence of filaments were observed by LSCM, however, cells appeared more rounded in SEM images for all compositions. A similar round morphology was observed for hiPSCs by Dattola *et al* [423]. It has been shown that softer substrates result in more round morphology of fibroblasts which

may explain why such a morphology is observed [424]. FEG-only scaffolds showed long nanofibrous projections from the cells, suggesting that new ECM may have been formed. The LSCM results suggest that the α-SMA corresponds to myofibroblasts as organised stress-fibres appear, however, quantification of the fibres could not be carried out as representative images could not be normalised. The activation of myofibroblasts is not necessarily a disadvantage as it also occurs in the embryonic state, however, it can become detrimental if prolonged activation is not controlled or reverted. Although the results imply activation of α-SMA to myofibroblasts, it is important to note its non-specificity and therefore confirmation via another marker such as desmin would be required to validate these results.

Tensile testing conducted on tri-layer scaffolds showed a significant improvement in the extensibility and strain-to-failure after 14 days of culturing. It was found that the scaffolds had decreased in thickness but maintained their length. Total cell-mediated contraction of 38.4±5.6% was observed after 14 days of culture. Cell-mediated contraction occurs due to stress exerted by cells on the matrix resulting in a strain which is detected by cells in the vicinity [425]. It is likely that the presence of FEG and its effect on the stiffness of scaffolds has resulted in mechanical contractility as it activates the contractile phenotype of SMCs (shown by the expression of α-SMA). An increase in strain-to-failure post culturing has been reported for collagen-elastin composites, although a decrease in the Young's modulus was observed, which was not the case in this study [234]. Although no significant contraction was observed in monolithic scaffolds except for coll-HA, the contraction of natural scaffolds is a recurring problem. The contraction of scaffolds could be a major drawback of these scaffolds as they intend to eventually replace a diseased valve and therefore shrinkage

after implantation is undesirable. A possible method to overcome this is to account for the shrinkage as the results from this thesis suggest the contraction of FEG is correlated to its unique mechanical properties (Section 5.3.) and associated cellular response as discussed above.

The gene expression of monolayers reveals the need to control of the composition of scaffolds to direct the gene expression of cells. Layer-specific ECM expression was found where the collagen layer (fibrosa) expressed the most COL, coll-HA layer (spongiosa) expressed the most HAS-2 and the 50C-50E layer (ventricularis) expressed the most ELA. The expression of COL has been extensively studied and has been shown be upregulated by multiple compositions [129], [169], [245], [426]–[428]. The importance of HAS-2 is often overlooked, it is essential for valvulogenesis and the first molecule that is synthesised during heart development and gives rise to the synthesis of other ECM molecules [47]. Unlike the findings of this work, Puperi *et al* showed no significant difference in the expression of HAS-2 between HA-based scaffolds and synthetic controls [181]. A possible explanation can be the preparation of scaffolds as leaching of HA from the coll-HA scaffolds is likely as well as its degradation as shown by the SEM images. The layer-specific upregulation of ECM markers by the composition of tri-layers is significant as tri-layers composed of synthetic polymers have not been able to emulate this feature, and it shows why it is important to mimic the composition of valves to guide the cellular response [243], [244].

The *in vitro* work carried out in this thesis is not extensive to be able to make any conclusions about the applicability of iPSC-CMs as a potential source of cells for heart valve tissue engineering. Further work would be necessary to determine its

applicability and direct comparisons of VICs and the cells isolated from scaffolds after culture would be required to confirm any correlations. The tri-layer scaffolds as they stand would not be suitable for application in valve tissue engineering and mechanical conditioning to increase their stiffness would be compulsory.

6.4.3. Expression of Elastogenic Markers

Gene expression is the first step required for protein expression and therefore being able to stimulate a gene is very important. Elastogenesis is imperative for a functional scaffold as the absence of elastin results in stenosis and abnormal mechanical functionality of valves [422]. Elastin synthesis is a major bottleneck in tissue engineering and has been a persistent challenge as it is difficult to replicate [64]. Methods to improve elastogenesis have included the use of biochemical signals and scaffolds where the composition and degradation of the scaffold promotes elastogenesis as reviewed by Sivaraman *et al* [429]. The expression of tropoelastin on its own is insufficient to form mature elastic fibres, elastogenesis associated genes include ELA, FIB-1, and LOX. FIB-1 is an essential glycoprotein that forms the template for tropoelastin deposition and LOX is an enzyme which cross-links extracellular molecules such as collagen and elastin *in vivo* to form mature fibres, its deficiency has been associated with disorganised ECM [187], [430].

Correlations between the physical and mechanical properties of collagen-FEG composites and the resultant gene expression could not be found except for the ELA gene. It can be proposed that the decrease in stiffness and increase in compliance, promotes an increase in the expression of ELA with no significant difference between 50C-50E and 25C-75E. Crapo and Wang reported a similar response where they showed increase in elastin expression on substrates with lower stiffness compared to

those with higher stiffness, however, the differing fabrication technique and material properties restrict direct comparison [431].

The expression of ELA can be associated with the presence of FEG as it is significantly lower for 100C scaffolds. The expression of LOX and FIB-1 do not show any concentration dependence and was highest for 25C-75E and can therefore be associated with its physical properties (smaller pore size and consequent high SA/V ratio). The expression of these markers has been compared to studies found in the literature in Table 6.12. The key takeaways from this are that 3D environments are better suited for elastogenesis than 2D and that FEG offers a good platform to study elastogenesis and can provide a template for future work. Future research questions would need to address protein expression as the next step from gene expression and assess the maturity of elastic fibres as well as the effect of biomechanical conditioning which has shown to significantly increase the expression of elastin [63], [432], [433].

Table 6.12: Gene expression of elastogenesis markers

Sample	Cell type	Culture Period (days)	Fold Change			Ref
			FIB-1	ELA	LOX	
Collagen-FEG	hiPSC-CMs	14	16.7	2.4	3.1	This study
Collagen-GAG-Fibrin and Tropoelastin	hVSMCs	3-14	1.4	1.3	1.2	[434]
PEGdma/PLA	hiPSC-SMCs	30	1.0	1.0	1.0	[432]
PEGdma/PLA*	hiPSC-SMCs	30	1.5	45.0	1.5	[432]
PGS-PCL	VICs	21	-	1.0	-	[435]

*Samples compared to 25%collagen-75%FEG at day 14 of culture with iPSC-CMs. FIB-1=fibrillin-1, ELA=elastin and LOX=lysyl oxidase. *Mechanically conditioned.*

6.5. Summary

The aim of this chapter was to study the cellular response of iPSC-CMs on FEG-based, collagen-based, coll-HA and tri-layer scaffolds. The main findings include:

- FEG was shown to be biocompatible and supported adhesion of iPSC-CMs in both uncross-linked and cross-linked samples with no significant difference between them, implying that the cell binding sites, and cross-linking sites are independent.
- The substitution of FEG for collagen did not show any significant effect on the cell adhesion, however, it was found that for FEG-rich scaffolds (>50%), the metabolic activity of cells was slower than collagen-rich scaffolds (<50%) up to day 10. The slower initial response has been suggested to be associated with the contractile phenotype of α-SMA which is promoted by the presence of FEG.
- Monolithic scaffolds (100C, coll-HA and 50C-50E) that were proposed to form tri-layer scaffolds showed the maturation of non-cardiomyocyte cells as well as layer specific expression of COL, HAS-2 and ELA depending on the composition of the layer. Tensile testing of tri-layers showed no significant difference in Young's modulus after culturing for 14 days but found a significant increase of 1.5-fold in the strain-to-failure.
- The expression of elastogenesis associated markers was found to be significantly higher in samples containing the highest concentration of FEG due to the composition and higher surface area-to-volume ratio. The expression of ELA was found to be have a strong correlation with the content of FEG

present. The results were encouraging and suggest that FEG could be used as a template to study elastogenesis.

7

Thesis Summary & Future Work

7.1. Thesis Summary

Heart valve tissue engineering (HVTE) offers great promise as a technique to overcome the limitations of currently available prostheses. Scaffolds provide a platform that can control cellular responses and promote the synthesis of new extracellular matrix (ECM) molecules to replace diseased tissues. A recurring impediment in HVTE is the mimicking of the non-linear deformation characteristics of the valves and the synthesis of new elastin by cells, both of which determine the potential functionality of a replacement valve. This is in part due to the limitations of the functionality of the materials available and their insufficient capacity to promote elastogenesis by cells. A potential method to overcome this is to incorporate exogenous forms of elastin in scaffolds for HVTE as shown in this thesis (summarised in Fig.7.1.).

Commercially available forms of natural elastin consist to two types, polymeric and soluble. Both of these forms have been experimentally shown to be limited as biomaterials as they are unable to be processed into constructs when polymeric and do not emulate the mechanical characteristics of elastin (a high strain-to-failure and resilience) when soluble [436], [437]. Chapter 3 aimed to address the poor processability of natural elastin by devising a method to synthesise a novel form of elastin. The discovery of the material came from multiple attempts by the author to modify natural elastin to a “processable” form that was also structurally intact (i.e. not completely fragmented). Rheological characterisation of the material revealed its gel-like properties and its fibrillar microstructure was shown by scanning electron microscopy (SEM), which led to the name fibrillar elastin gel (FEG). Fourier transform infrared spectroscopy (FT-IR) suggested that the gelation occurred due to the loss of

α-helices by hydrolysis which gave rise to intermolecular interactions between the remaining β-sheets. The gel has been suggested to be a result of the increased interactions between and within β-sheets which led to its aggregation and the appearance of a gel. FEG was found to exhibit pH-sensitivity and showed high water-uptake at pH's of 2.7 and 12.1 where polymer-solvent interactions were highest due to ionisation of its functional groups. FEG's pH-sensitivity and therefore improved solubility in such conditions make it possible to manipulate the material into multiple forms.

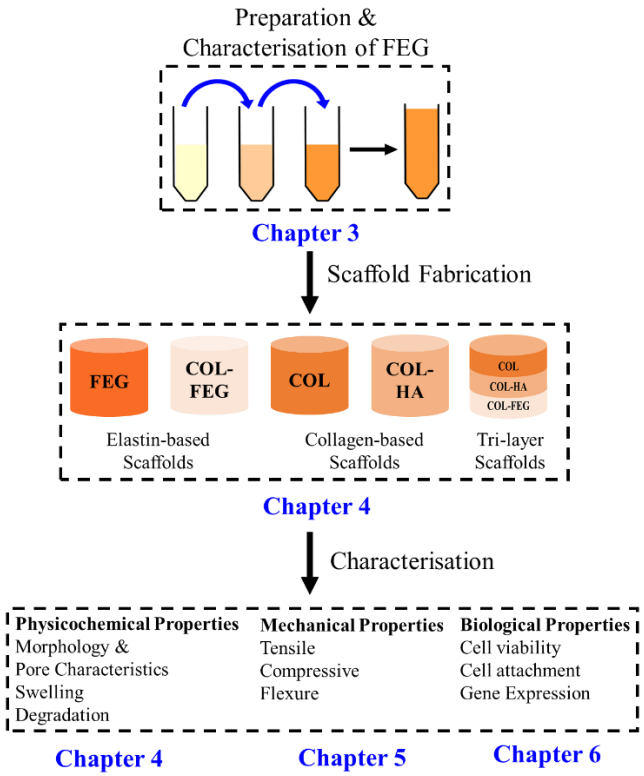

Figure 7.1: Summary of thesis. Chapter 3 described a method for isolation a novel fibrillar elastin gel (FEG) which was prepared from polymeric elastin and characterised to propose a model for the mechanism of gelation. The material was applied to manufacture scaffolds of various compositions, including a tri-layer scaffold that mimicked the composition of native valves in Chapter 4. This chapter also characterised the pore characteristics and swelling and degradation behaviour of scaffolds. Chapters 5 and 6 characterised the bulk mechanical properties and the *in vitro* cell response of induced pluripotent stem cell-derived cardiomyocytes, respectively.

Chapter 4 explored the potential application of FEG in scaffolds independently as well as in composites with collagen which were used to fabricate tri-layer scaffolds that mimic the composition of heart valves. Freeze-casting was chosen as the method to fabricate scaffolds as it offers high porosity. This is the first study to use freeze-casting as a fabrication technique for elastin-only scaffolds as natural elastin has poor polymer-solvent interactions and therefore obtaining a suspension for freeze-casting is extremely challenging. Processing parameters such as the relative density and freezing temperature were studied and 3%wt/v and -20°C were chosen for further experiments as they offered the highest pore size (46-63μm) and porosity (94%). By taking advantage of the pH-sensitivity of both FEG and collagen it was possible to prepare suspensions of multiple compositions with pore sizes ranging between 52-143μm. Swelling studies showed FEG exhibited thermosensitivity and had a negative temperature dependence with an inverse transition temperature (ITT) at 30°C. It was found that above the ITT, FEG displayed higher hydrophobicity and poorer interaction with the swelling media whereas below the ITT, FEG was more hydrophilic and exhibited improved polymer-solvent interactions compared to native elastin. FEG's sensitivity to pH and temperature dominated in collagen-FEG composites as collagen could not support its structure and scaffolds displayed higher contraction with the increase in FEG content. It was also shown that FEG was biodegradable and its resistance to degradation could be tailored by cross-linking.

The mechanical properties of FEG-based, collagen-FEG-based and tri-layer scaffolds were studied in Chapter 5. It was shown that all scaffolds exhibited a non-linear deformation response, akin to heart valves. FEG-only scaffolds were tested in compression and tension. It was found that cross-linking was effective as the

compressive modulus increased by 6-fold and showed a 3-fold increase in the cross-linking density. In tension, FEG-only scaffolds exhibited a high strain-to-failure of 101% which is significantly higher than scaffolds reported to date containing natural forms of elastin. Collagen-FEG composites showed an increase in strain-to-failure from 37% to 94% as the concentration of FEG increased from 0% to 75%. Composite scaffolds exhibited a mechanical response that was similar to 100C at higher concentrations of collagen and closer to 100%FEG at higher concentrations of FEG, implying that the mechanical response was dominated by the modulus of the solid materials and not the relative density (which was kept constant). The properties of tri-layer scaffolds in tension were dominated by the collagen-rich layer as it was the stiffest layer, and the addition of a FEG-rich layer had no significant effect on strain-to-failure as it is continuous in laminated structures. In bending, anisotropy of 1.3-fold was found when comparing scaffolds with and against curvature, implying the tri-layers follow similar bending characteristics as native valves which have an anisotropy of 1.4-fold.

The cellular response of induced pluripotent stem cell-derived cardiomyocytes (iPSC-CMs) was studied in Chapter 6. FEG-based, coll-HA and collagen-FEG-based scaffolds were assessed for cell attachment and viability, all scaffold compositions were found to be biocompatible and able to support the metabolic activity of iPSC-CMs. Scaffolds containing FEG exhibited slow initial metabolic activity up to day 10 in comparison to 100C and coll-HA, this has been suggested to be due to stimulation of a contractile phenotype of the cells due to the presence of FEG. The gene expression of elastogenesis associated markers (ELA, FIB-1, and LOX) were evaluated for collagen-FEG composites and were found to be significantly upregulated in scaffolds

containing the highest concentration of FEG. The increase in metabolic activity of monolithic scaffolds that form each layer of the tri-layer scaffolds (100C, coll-HA, and 50C-50E) was suggested to be associated with the maturation of non-cardiomyocytes (NCMs) such as fibroblasts, smooth muscle cells and/or myofibroblasts. The gene expression for NCMs was upregulated in these compositions and it was found that the expression of layer-specific ECM markers was dominated by the composition of the scaffold. The tri-layer scaffolds provide a good template for future work on scaffolds for heart valve tissue engineering where elastogenesis can also be promoted by the addition of FEG.

7.2. Future Work

A major shortcoming of the work conducted during this thesis is the absence of complete characterisation of cell penetration throughout the thickness of scaffolds. Future work that would be recommended immediately as a follow up study would be to evaluate the depth penetration of cells using imaging and potentially incorporating a method to promote penetration as cells were seeded statically. A potential method to achieve an even distribution of cells would be to dynamically load the cells by rotating the scaffolds in cell suspension. In terms of scaffolds for HVTE, future work could entail using a bottom up approach to take advantage of FEG's self-assembly (coacervation) properties to produce scaffolds that have improved interaction at the molecular level, which will in turn improve the mechanical properties and the resistance to degradation.

The robustness of the tri-layer scaffolds need to be assessed in terms of resistance to fatigue and delamination at the interface as valves function in a highly dynamic

environment. As the constructs fabricated during this work do not fulfil the full mechanical range required for valves, either a method to improve the mechanical properties of the scaffolds designed would need to be developed or biomechanical conditioning would be required. Biomechanical conditioning has been shown to improve the mechanical properties of scaffolds and will be a key step in determining the applicability of the tri-layer scaffolds fabricated in this thesis for HVTE [438]. Studies have shown that biomechanical conditioning often leads to fibrotic tissue as materials and cells do not promote elastogenesis, therefore it would be particularly interesting to study the effect of FEG on a cells ability to synthesise mature elastin in static and dynamic conditions [439]. Biomechanical conditioning can be conducted on rectangular scaffolds as used in this study or structures that mimic the anatomy of heart valves and/or the aortic root in particular can be fabricated by freeze-casting for future *in vivo* studies as experimentally shown by Brougham *et al* [440].

As well as improving the mechanical properties, studies that evaluate the quality of the tissue generated in terms of its histology, quantity and cross-linking density will need to be conducted as the quantity of cross-links (hydroxylysyl pyridinoline for collagen and desmosine for elastin) have been shown to be related to the stiffness [84]. An important aspect that was not addressed during this research is if FEG has any effect on calcification, this is particularly important for HVTE as biological prostheses undergo calcification. This parameter can be evaluated by studying the gene expression of specific markers for calcification (alkaline phosphatase and osteocalcin) as well as staining for calcium deposits [441].

Additionally, the modified form of elastin developed provides a platform for the application of FEG in other areas of biomedical research such as drug delivery where

FEG's "smart" properties (pH- and thermo-sensitivity) would be particularly advantageous [442]. Extension of the material into other connective tissues is also possible as elastin is present in tissues including the skin, lungs, and blood vessels where elastin synthesis is a limiting factor. In addition to applications of the material, the processable form of elastin offers the advantage to be employed by other conventional fabrication techniques such as electrospinning [10], [443].

References

[1] W. H. O. (WHO), "Cardiovascular diseases (CVDs) Fact Sheet," 2017. http://www.who.int/mediacentre/factsheets/fs317/en/ (accessed Sep. 18, 2017).

[2] R. C. Osorio, F. Solano de Freitas Souza, M. Novaes de Andrade, B. Câmara de Freitas, and A. R. Durães, "Valvular Heart Diseases - Epidemiology and New Treatment Modalities," *Interventional Cardiology Journal*, vol. 2, no. 1, pp. 1–11, 2016, doi: 10.21767/2471-8157.100012.

[3] J. Chikwe, Y. P. Chiang, N. N. Egorova, S. Itagaki, and D. H. Adams, "Survival and Outcomes Following Bioprosthetic vs Mechanical Mitral Valve Replacement in Patients Aged 50 to 69 Years," *Americal Medical Association*, vol. 313, no. 14, p. 1435, 2015, doi: 10.1001/jama.2015.3164.

[4] A. Mol, A. I. P. M. Smith, C. V. C. Bouten, and F. P. T. Baaijens, "Tissue engineering of heart valves: Advances and current challenges," *Expert Review of Medical Devices*, vol. 6, no. 3, pp. 259–275, 2009, doi: 10.1586/erd.09.12.

[5] I. Vesely, "The role of elastin in aortic valve mechanics," *Journal of Biomechanics*, vol. 31, no. 2, pp. 115–123, 1997, doi: 10.1016/S0021-9290(97)00122-X.

[6] T. C. Lee *et al.*, "The effect of elastin damage on the mechanics of the aortic valve," *Journal of Biomechanics*, vol. 34, no. August 2000, pp. 203–210, 2001.

[7] E.-H. Ismail *et al.*, "Long-term outcomes after autograft versus homograft aortic root replacement in adults with aortic valve disease: a randomised controlled trial," *The Lancet*, vol. 376, no. 9740, pp. 524–531, 2010.

[8] J. Usprech, W. L. K. Chen, and C. A. Simmons, "Heart valve regeneration: The need for systems approaches," *Wiley Interdisciplinary Reviews: Systems Biology and Medicine*, vol. 8, no. 2, pp. 169–182, 2016, doi: 10.1002/wsbm.1329.

[9] W. F. Daamen, J. H. Veerkamp, J. C. M. van Hest, and T. H. van Kuppevelt, *Elastin as a biomaterial for tissue engineering*, vol. 28, no. 30. 2007.

[10] G. C. Yeo, B. Aghaei-Ghareh-Bolagh, E. P. Brackenreg, M. A. Hiob, P. Lee, and A. S. Weiss, "Fabricated Elastin," *Advanced Healthcare Materials*, vol. 4, no. 16, pp. 2530–2556, 2015, doi: 10.1002/adhm.201400781.

[11] T. Brade, L. S. Pane, A. Moretti, K. R. Chien, and K. L. Laugwitz, "Embryonic heart progenitors and cardiogenesis.," *Cold Spring Harbor perspectives in medicine*, vol. 3, no. 10, pp. 1–17, 2013, doi: 10.1101/cshperspect.a013847.

[12] G. J. Tortora and B. Derrickson, "The Cardiovascular System: The Heart," in *Volume 2: Principles of Anatomy & Physiology, Maintenance and Continuity of the Human Body*, 13th ed., John Wiley & Sons, Inc, 2011, pp. 757–765.

[13] M. Sylva, M. J. B. van den Hoff, and A. F. M. Moorman, “Development of the human heart,” *American Journal of Medical Genetics, Part A*, vol. 164, no. 6, pp. 1347–1371, 2014, doi: 10.1002/ajmg.a.35896.

[14] J. Hjortnaes *et al.*, “Valvular interstitial cells suppress calcification of valvular endothelial cells,” *Atherosclerosis*, vol. 242, no. 1, pp. 251–260, 2015, doi: 10.1016/j.atherosclerosis.2015.07.008.

[15] S. Zucker, “Cardiac Jelly and Its Roles in Heart Development,” *The science journal of the Lander College of Arts and Sciences*, vol. 4, no. 4, pp. 23–29, 2011, [Online]. Available: https://touroscholar.touro.edu/cgi/viewcontent.cgi?referer=https://www.google.co.uk/&httpsredir=1&article=1164&context=sjlcas.

[16] M. D. Combs and K. E. Yutzey, “Heart valve development: Regulatory networks in development and disease,” *Circulation Research*, vol. 105, no. 5, pp. 408–421, 2009, doi: 10.1161/CIRCRESAHA.109.201566.

[17] M. Lockhart, E. Wirrig, A. Phelps, and A. Wessells, “Extracellular Matrix and Heart Development,” *Birth Defects Res A Clin Mol Teratol*, vol. 91, no. 6, pp. 535–550, 2011, doi: 10.1002/bdra.20810.Extracellular.

[18] A. Vlaming *et al.*, “Atrioventricular Valve Development: New Perspectives on an Old Theme,” *Differentiation*, vol. 84, no. 1, pp. 103–116, 2012, doi: 10.1523/JNEUROSCI.5473-10.2011.Loss.

[19] S. E. Lindsey and J. T. Butcher, “The cycle of form and function in cardiac valvulogenesis,” *Aswan Heart Centre Science & Practice Series*, vol. 2011, no. 2, p. 10, 2011, doi: http://dx.doi.org/10.5339/ahcsps.2011.10.

[20] A. D. Person, S. E. Klewer, and R. B. Runyan, “Cell biology of cardiac cushion development,” *International Review of Cytology*, vol. 243, pp. 287–335, 2005, doi: 10.1016/S0074-7696(05)43005-3.

[21] J. T. Butcher and R. R. Markwald, “Valvulogenesis: the moving target,” *Philosophical Transactions of the Royal Society B*, vol. 362, pp. 1489–1503, 2007, doi: 10.1098/rstb.2007.2130.

[22] J. v. Barnett and J. S. Desgrosellier, “Early events in valvulogenesis: A signaling perspective,” *Birth Defects Research Part C - Embryo Today: Reviews*, vol. 69, no. 1, pp. 58–72, 2003, doi: 10.1002/bdrc.10006.

[23] M. Misfeld and H.-H. Sievers, “Heart valve macro- and microstructure,” *Philosophical Transactions of the Royal Society B: Biological Sciences*, vol. 362, no. 1484, pp. 1421–1436, 2007, doi: 10.1098/rstb.2007.2125.

[24] E. I. Charitos and H.-H. Sievers, “Anatomy of the aortic root: implications for valve-sparing surgery.,” *Annals of cardiothoracic surgery*, vol. 2, no. 1, pp. 53–6, 2013, doi: 10.3978/j.issn.2225-319X.2012.11.18.

[25] E. I. Charitos and H.-H. Sievers, “Anatomy of the aortic root: implications for valve-sparing surgery.,” *Annals of cardiothoracic surgery*, vol. 2, no. 1, pp. 53–6, 2013, doi: 10.3978/j.issn.2225-319X.2012.11.18.

[26] M. J. Underwood, G. el Khoury, D. Deronck, D. Glineur, and R. Dion, “The aortic root: structure, function, and surgical reconstruction,” *Heart*, vol. 83, pp. 376–380, 2000.

[27] I. Tilea, H. Suciu, B. Tilea, C. M. Tatar, M. M. Ispas, and R. C. Serban, “Anatomy and Function of Normal Aortic Valvular Complex,” in *Calcific aortic valve disease*, E. Aikawa, Ed. InTech, 2013, pp. 31–55.

[28] M. Loukas, E. Bilinsky, S. Bilinsky, C. Blaak, R. S. Tubbs, and R. H. Anderson, “The anatomy of the aortic root,” *Clinical Anatomy*, vol. 27, no. 5, pp. 748–756, 2014, doi: 10.1002/ca.22295.

[29] R. McKay and D. N. Ross, “Primary repair and autotransplantation of cardiac valves,” *Annu Rev Med*, vol. 44, pp. 181–188, 1993, doi: 10.1146/annurev.me.44.020193.001145.

[30] Y. Missirlis and C. D. Armeniades, “Ultrastructure of the human aortic valve,” *Acta anat*, vol. 98, pp. 199–205, 1977.

[31] P. E. Hammer, C. A. Pacak, R. D. Howe, and P. J. del Nido, “Straightening of curved pattern of collagen fibers under load controls aortic valve shape,” *Journal of Biomechanics*, vol. 47, no. 2, pp. 341–346, 2014, doi: 10.1016/j.jbiomech.2013.11.032.

[32] C. E. Eckert *et al.*, “On the biomechanical role of glycosaminoglycans in the aortic heart valve leaflet,” *Acta Biomaterialia*, vol. 9, no. 1, pp. 4653–4660, 2013, doi: 10.1016/j.actbio.2012.09.031.

[33] K. Murata, “Acidic glycosaminoglycans in human heart valves,” *Journal of Molecular and Cellular Cardiology*, vol. 13, no. 3, pp. 281–292, 1981, doi: 10.1016/0022-2828(81)90316-3.

[34] D. Wiltz *et al.*, “Extracellular Matrix Organization, Structure, and Function,” in *Calcific aortic valve disease*, E. Aikawa, Ed. InTech, 2013, pp. 3–30.

[35] I. Vesely, “The role of elastin in aortic valve mechanics,” *Journal of Biomechanics*, vol. 31, no. 2, pp. 115–123, 1997, doi: 10.1016/S0021-9290(97)00122-X.

[36] D. M. Ibrahim, A. Kakarougkas, and N. K. Allam, “Recent advances on electrospun scaffolds as matrices for tissue-engineered heart valves,” *Materials Today Chemistry*, vol. 5, pp. 11–23, 2017, doi: 10.1016/j.mtchem.2017.05.001.

[37] V. R. Sherman, W. Yang, and M. A. Meyers, “The materials science of collagen,” *Journal of the Mechanical Behavior of Biomedical Materials*, vol. 52, pp. 22–50, 2015, doi: 10.1016/j.jmbbm.2015.05.023.

[38] M. D. Shoulders and R. T. Raines, “Collagen Structure and Stability,” *Annu Rev Biochem*, vol. 78, pp. 929–958, 2010, doi: 10.1146/annurev.biochem.77.032207.120833.COLLAGEN.

[39] W. G. Cole, D. Chan, A. J. Hickeyt, and D. E. L. Wilckent, “Collagen composition of normal and myxomatous human mitral heart valves,” *Biochem. J*, vol. 219, pp. 451–460, 1984, doi: 10.1042/bj2190451.

[40] V. Ottani, D. Martini, M. Franchi, A. Ruggeri, and M. Raspanti, “Hierarchical structures in fibrillar collagens,” *Micron*, vol. 33, no. 7–8, pp. 587–596, 2002, doi: 10.1016/S0968-4328(02)00033-1.

[41] S. Ricard-Blum and F. Ruggiero, “The collagen superfamily: From the extracellular matrix to the cell membrane,” *Pathologie Biologie*, vol. 53, no. 7, pp. 430–442, 2005, doi: 10.1016/j.patbio.2004.12.024.

[42] J. Gosline, M. Lillie, E. Carrington, P. Guerette, C. Ortlepp, and K. Savage, “Elastic proteins: biological roles and mechanical properties,” *Philosophical Transactions of the Royal Society B: Biological Sciences*, vol. 357, no. 1418, pp. 121–132, 2002, doi: 10.1098/rstb.2001.1022.

[43] R. Mecham, *The Extracellular Matrix: An Overview*, vol. 1. 2011.

[44] V. Physiology, *Advances in Heart Valve Biomechanics*. 2018.

[45] T. C. Laurent, “Biochemistry of hyaluronan.,” *Acta oto-laryngologica. Supplementum*, vol. 442, no. 3, pp. 7–24, 1987, doi: 10.3109/00016488709102833.

[46] R. D. Price, M. G. Berry, and H. A. Navsaria, “Hyaluronic acid: the scientific and clinical evidence,” *Journal of Plastic, Reconstructive and Aesthetic Surgery*, vol. 60, no. 10, pp. 1110–1119, 2007, doi: 10.1016/j.bjps.2007.03.005.

[47] T. D. Camenisch *et al.*, “Disruption of hyaluronan synthase-2 abrogates normal cardiac morphogenesis and hyaluronan- mediated transformation of epithelium to mesenchyme,” *The Journal of Clinical Investigation*, vol. 106, no. 3, pp. 349–360, 2000.

[48] J. Butany and M. J. Collins, “Analysis of prosthetic cardiac devices: A guide for the practising pathologist,” *Journal of Clinical Pathology*, vol. 58, no. 2, pp. 113–124, 2005, doi: 10.1136/jcp.2004.020271.

[49] M. G. Giro and J. M. Davidson, “Elastin,” in *Study of Repair Processes in Inflammation*, vol. 163, no. 1983, 1988, pp. 656–673.

[50] L. Sandberg, N. Soskel, and J. Leslie, “Elastin Structure, Biosynthesis, and Relation to Disease States,” *The New England Journal of Medicine*, vol. 304, no. 10, pp. 566–579, 1981.

[51] M. Akagawa and K. Suyama, “Mechanism of formation of elastin crosslinks,” *Connective Tissue Research*, vol. 41, no. 2, pp. 131–141, 2000, doi: 10.3109/03008200009067665.

[52] C. M. Halabi and R. P. Mecham, “Elastin purification and solubilization,” in *Methods in Cell Biology*, 1st ed., vol. 143, Elsevier Inc., 2018, pp. 207–222.

[53] C. A. J. Hoeve, “The Elastic Properties of Elastin,” *Biopolymers*, vol. 13, pp. 677–686, 1974, doi: 10.1021/ja01557a016.

[54] T. Weis-Fogh and S. O. Andersen, “New molecular model for the long-range elasticity of elastin,” *Nature*, vol. 227, pp. 718–721, 1970, doi: 10.1038/227718a0.

[55] W. R. Gray, L. B. Sandberg, and J. A. Foster, “Molecular Model for Elastin Structure and Function,” *Nature*, vol. 246, no. 21/28, pp. 461–466, 1973.

[56] D. W. Urry, “Studies on the conformation and interaction of elastin.,” in *Arterial mesenchyme and arteriosclerosis.*, Adv Exp Med Biol., 1974, pp. 211–43.

[57] B. Li and V. Daggett, “Molecular basis for the extensibility of elastin,” *Journal of Muscle Research and Cell Motility*, vol. 23, pp. 561–573, 2002, doi: https://doi.org/10.1023/A:1023474909980.

[58] M. G. W. Liu *et al.*, “A comparison of the mechanical and structural properties of fibrin fibers with other protein fibers,” *Cell Biochem Biophys*, vol. 49, no. 3, pp. 165–181, 2007, doi: 10.1007/s12013-007-9001-4.A.

[59] B. B. Aaron and J. M. Gosline, “Elastin as a random-network elastomer: A mechanical and optical analysis of single elastin fibers,” *Biopolymers*, vol. 20, no. 6, pp. 1247–1260, 1981, doi: 10.1002/bip.1981.360200611.

[60] L. Gotte, M. Mammi, and G. Pezzin, “Scanning electron microscope observations on elastin,” *Connective Tissue Research*, vol. 1, no. 1, pp. 61–67, 1972, doi: 10.3109/03008207209152057.

[61] S. D. Shapiro, S. K. Endicott, M. A. Province, J. A. Pierce, and E. J. Campbell, “Marked longevity of human lung parenchymal elastic fibers deduced from prevalence of D-aspartate and nuclear weapons-related radiocarbon,” *Journal of Clinical Investigation*, vol. 87, no. 5, pp. 1828–1834, 1991, doi: 10.1172/JCI115204.

[62] C. B. Saitow, S. G. Wise, A. S. Weiss, J. J. Castellot, and D. L. Kaplan, “Elastin biology and tissue engineering with adult cells,” *Biomolecular Concepts*, vol. 4, no. 2, pp. 173–185, 2013, doi: 10.1515/bmc-2012-0040.

[63] M. Votteler *et al.*, “Elastogenesis at the onset of human cardiac valve development.,” *Development (Cambridge, England)*, vol. 140, no. 11, pp. 2345–53, 2013, doi: 10.1242/dev.093500.

[64] A. Patel, B. Fine, M. Sandig, and K. Mequanint, “Elastin biosynthesis: The missing link in tissue-engineered blood vessels,” *Cardiovascular Resea*, vol. 71, pp. 40–49, 2006, doi: 10.1016/j.cardiores.2006.02.021.

[65] F. Opitz *et al.*, “Tissue engineering of aortic tissue: Dire consequence of suboptimal elastic fiber synthesis in vivo,” *Cardiovascular Research*, vol. 63, no. 4, pp. 719–730, 2004, doi: 10.1016/j.cardiores.2004.05.002.

[66] N. V. Bhagavan and H. Chung-Eun, “Connective Tissue : Fibrous and Nonfibrous Proteins and Proteoglycans,” in *Essentials of Medical Biochemistry With Clinical Cases*, 2nd ed., Elsevier, 2015, pp. 119–136.

[67] B. Vrhovski and A. S. Weiss, “Biochemistry of tropoelastin,” *Eur. J. Biochem*, vol. 258, pp. 1–18, 1998, doi: https://doi.org/10.1046/j.1432-1327.1998.2580001.x.

[68] I. El-Hamamsy, A. H. Chester, and M. H. Yacoub, “Cellular regulation of the structure and function of aortic valves,” *Journal of Advanced Research*, vol. 1, no. 1, pp. 5–12, 2010, doi: 10.1016/j.jare.2010.02.007.

[69] M. S. Sacks and A. P. Yoganathan, “Heart valve function: a biomechanical perspective.,” *Philosophical transactions of the Royal Society of London. Series B, Biological sciences*, vol. 362, no. 1484, pp. 1369–91, 2007, doi: 10.1098/rstb.2007.2122.

[70] J. T. Butcher, C. a Simmons, and J. N. Warnock, “Review: Mechanobiology of the aortic heart valve.,” *The Journal of heart valve disease*, vol. 17, no. 1, pp. 62–73, 2008, doi: 10.1371/JOURNAL.PONE.0084433.

[71] E. Rabkin-Aikawa, M. Farber, M. Aikawa, and F. J. Schoen, “Dynamic and reversible changes of interstitial cell phenotype during remodeling of cardiac valves,” *Journal of Heart Valve Disease*, vol. 13, no. 5, pp. 841–847, 2004.

[72] A. Roy, N. Brand, and M. Yacoub, “Molecular characterization of interstitial cells isolated from human heart valves,” *J Heart Valve Dis*, vol. 9, pp. 459–464, 2000.

[73] N. J. Brand, A. Roy, G. Hoare, A. Chester, and M. H. Yacoub, “Cultured interstitial cells from human heart valves express both specific skeletal muscle and non-muscle markers,” *International Journal of Biochemistry and Cell Biology*, vol. 38, no. 1, pp. 30–42, 2006, doi: 10.1016/j.biocel.2005.06.018.

[74] C. S. Elangbam, “Drug-induced valvulopathy: An update,” *Toxicologic Pathology*, vol. 38, no. 6, pp. 837–848, 2010, doi: 10.1177/0192623310378027.

[75] A. Alexopoulos, N. Michelakakis, and H. Papadaki, “Pathophysiologic Mechanisms of Age – Related Aortic Valve Calcification,” in *Aortic Stenosis - Etiology, Pathophysiology and Treatment*, 2011, pp. 33–46.

[76] A. H. Chester, I. El-Hamamsy, J. T. Butcher, N. Latif, S. Bertazzo, and M. H. Yacoub, “The living aortic valve: From molecules to function,” *Global Cardiology Science and Practice*, vol. 2014, no. 1, p. 11, 2014, doi: 10.5339/gcsp.2014.11.

[77] M. A. Gomel, R. Lee, and K. J. Grande-allen, “Comparing the Role of Mechanical Forces in Vascular and Valvular Calcification Progression,” vol. 5, no. January, pp. 1–14, 2019, doi: 10.3389/fcvm.2018.00197.

[78] R. M. Buchanan and M. S. Sacks, “Interlayer Micromechanics of the Aortic Heart Valve Leaflet,” *Biomechanics and Modeling in Mechanobiology*, vol. 13, no. 4, pp. 813–826, 2014, doi: 10.1038/jid.2014.371.

[79] M. S. Sacks, W. David Merryman, D. E. Schmidt, W. D. Merrryman, and D. E. Schmidt, “On the biomechanics of heart valve function,” *Journal of Biomechanics*, vol. 42, no. 12, pp. 1804–1824, 2009, doi: 10.1016/j.jbiomech.2009.05.015.

[80] S. Korossis, “Structure-Function Relationship of Heart Valves in Health Health and and Disease Disease,” in *Structural Insufficiency Anomalies in Cardiac Valves*, Kaan Kirali, Ed. InTechOpen, 2018, pp. 1–38.

[81] N. T. Saidy *et al.*, “Biologically Inspired Scaffolds for Heart Valve Tissue Engineering via Melt Electrowriting,” *Small*, vol. 15, no. 24, pp. 1–15, 2019, doi: 10.1002/smll.201900873.

[82] A. Hasan *et al.*, “Biomechanical properties of native and tissue engineered heart valve constructs,” *Journal of Biomechanics*, vol. 47, no. 9, pp. 1949–1963, 2014, doi: 10.1016/j.jbiomech.2013.09.023.

[83] R. L. Li *et al.*, “Mechanical considerations for polymeric heart valve development: Biomechanics, materials, design and manufacturing,” *Biomaterials*, vol. 225, no. September, p. 119493, 2019, doi: 10.1016/j.biomaterials.2019.119493.

[84] A. Balguid *et al.*, “The role of collagen cross-links in biomechanical behavior of human aortic heart valve leaflets - Relevance for tissue engineering,” *Tissue Engineering*, vol. 13, no. 7, pp. 1501–1511, 2007, doi: 10.1089/ten.2006.0279.

[85] I. Vesely and R. Noseworthy, “Micromechanics of the Fibrosa and the Ventricularis in Aortic Valve Leaflets,” *Journal of Biomechanics*, vol. 25, no. 1, pp. 101–113, 1992.

[86] S. Hinderer *et al.*, “Engineering of a bio-functionalized hybrid off-the-shelf heart valve,” *Biomaterials*, vol. 35, no. 7, pp. 2130–2139, 2014, doi: 10.1016/j.biomaterials.2013.10.080.

[87] D. Mozaffarian *et al.*, *Heart Disease and Stroke Statistics--2017 Update: A Report From the American Heart Association*, vol. 131. 2017.

[88] B. Iung and A. Vahanian, “Epidemiology of acquired valvular heart disease,” *Canadian Journal of Cardiology*, vol. 30, no. 9, pp. 962–970, 2014, doi: 10.1016/j.cjca.2014.03.022.

[89] N. M. Rajamannan *et al.*, “Calcific aortic valve disease: Not simply a degenerative process: A review and agenda for research from the national heart and lung and blood institute aortic stenosis working group,” *Circulation*, vol. 124, no. 16, pp. 1783–1791, 2011, doi: 10.1161/CIRCULATIONAHA.110.006767.

[90] R. B. Hinton *et al.*, “Extracellular matrix remodeling and organization in developing and diseased aortic valves,” *Circulation Research*, vol. 98, no. 11, pp. 1431–1438, 2006, doi: 10.1161/01.RES.0000224114.65109.4e.

[91] R. A. Manji, A. H. Menkis, B. Ekser, and D. K. C. Cooper, “Porcine bioprosthetic heart valves: The next generation,” *American Heart Journal*, vol. 164, no. 2, pp. 177–185, 2012, doi: 10.1016/j.ahj.2012.05.011.

[92] J. J. Thaden, V. T. Nkomo, and M. Enriquez-Sarano, “The Global Burden of Aortic Stenosis,” *Progress in Cardiovascular Diseases*, vol. 56, no. 6, pp. 565–571, 2014, doi: 10.1016/j.pcad.2014.02.006.

[93] R. Manji, B. Ekser, A. Menkis, and D. K. C. Cooper, “Bioprosthetic Heart Valves of the Future,” *Xenotransplantation*, vol. 21, no. 1, pp. 1–10, 2014, doi: 10.1111/xen.12080.BIOPROSTHETIC.

[94] S. P. Hoestrup and B. Weber, “Biological heart valves A technology on the verge of another breakthrough?,” *European Heart Journal*, vol. 36, pp. 1005–1011, 2015, doi: 10.1093/eurheartj/ehv055.

[95] A. M. Matthews, “The development of the Starr-Edwards heart valve.,” *Texas Heart Institute journal*, vol. 25, no. 4, pp. 282–293, 1998.

[96] W. Vongpatanasin, D. Hillis, and R. a. Lange, “Prosthetic Heart Valves,” *N Engl J Med*, vol. 335, no. 6, pp. 407–416, 1996.

[97] K. Mendelson and F. J. Schoen, “Heart valve tissue engineering: Concepts, approaches, progress, and challenges,” *Annals of Biomedical Engineering*, vol. 34, no. 12, pp. 1799–1819, 2006, doi: 10.1007/s10439-006-9163-z.

[98] W. W. Angell and J. D. Angell, “Porcine valves,” *Progress in cardiovascular diseases*, vol. 23, no. 2, pp. 141–166, 1980, doi: 0033-0620(80)90009-2 [pii].

[99] R. A. Manji, W. Lee, and D. K. C. Cooper, “Xenograft bioprosthetic heart valves: Past, present and future,” *International Journal of Surgery*, vol. 23, pp. 280–284, 2015, doi: 10.1016/j.ijsu.2015.07.009.

[100] A. L. Y. Nachlas, S. Li, and M. E. Davis, “Developing a Clinically Relevant Tissue Engineered Heart Valve-A Review of Current Approaches,” *Advanced*

Healthcare Materials, vol. 1700918, p. 1700918, 2017, doi: 10.1002/adhm.201700918.

[101] F. J. Schoen and R. J. Levy, "Tissue heart valves: current challenges and future research perspectives.," *Journal of biomedical materials research*, vol. 47, no. 4, pp. 439–65, 1999, doi: 10.1002/(SICI)1097-4636(19991215)47:4<439::AID-JBM1>3.0.CO;2-O.

[102] K. Z. Konakci *et al.*, "Alpha-Gal on bioprostheses: Xenograft immune response in cardiac surgery," *European Journal of Clinical Investigation*, vol. 35, no. 1, pp. 17–23, 2005, doi: 10.1111/j.1365-2362.2005.01441.x.

[103] R. A. Manji *et al.*, "Glutaraldehyde-fixed bioprosthetic heart valve conduits calcify and fail from xenograft rejection," *Circulation*, vol. 114, no. 4, pp. 318–327, 2006, doi: 10.1161/CIRCULATIONAHA.105.549311.

[104] J. H. BOWES and R. H. KENTEN, "Some observations on the amino acid distribution of collagen, elastin and reticular tissue from different sources.," *The Biochemical journal*, vol. 45, no. 3, pp. 281–285, 1949, doi: 10.1042/bj0450281.

[105] N. Vyavahare, M. Ogle, F. J. Schoen, and R. J. Levy, "Elastin calcification and its prevention with aluminum chloride pretreatment," *American Journal of Pathology*, vol. 155, no. 3, pp. 973–982, 1999, doi: 10.1016/S0002-9440(10)65197-8.

[106] M. T. Bailey, S. Pillarisetti, H. Xiao, and N. R. Vyavahare, "Role of elastin in pathologic calcification of xenograft heart valves," *Journal of Biomedical Materials Research - Part A*, vol. 66, no. 1, pp. 93–102, 2003, doi: 10.1002/jbm.a.10543.

[107] P. H. Schoof *et al.*, "Degeneration of the pulmonary autograft: An explant study," *Journal of Thoracic and Cardiovascular Surgery*, vol. 132, no. 6, pp. 1426–1432, 2006, doi: 10.1016/j.jtcvs.2006.07.035.

[108] Y. Lei, Y. Xia, and Y. Wang, "The tropoelastin and lysyl oxidase treatments increased the content of insoluble elastin in bioprosthetic heart valves," *Journal of Biomaterials Applications*, vol. 33, no. 5, pp. 1–10, 2018, doi: 10.1177/0885328218807077.

[109] H. A. Alhadrami, R. U. R. Syed, A. A. Zahid, R. Ahmed, S. Hasan, and A. Hasan, "Structure and Rheological Properties of Bovine Aortic Heart Valve and Pericardium Tissue: Implications in Bioprosthetic and Tissue-Engineered Heart Valves," *Journal of Healthcare Engineering*, 2019, doi: 10.1155/2019/3290370.

[110] Y. S. Morsi, "Biomaterials Charactetization," in *Tissue Engineering of the Aortic Heart Valve: Fundamentals and Developments*, Nova Science Publishers, Inc., 2012, pp. 44–50.

[111] Humacyte, “Humacyte,” 2020. https://humacyte.com/ (accessed Sep. 23, 2020).

[112] D. Macgrogan, G. Luxán, A. Driessen-Mol, C. Bouten, F. Baaijens, and J. L. de La Pompa, “How to make a heart valve: From embryonic development to bioengineering of living valve substitutes,” *Cold Spring Harbor Perspectives in Medicine*, vol. 4, no. 11, pp. 1–24, 2014, doi: 10.1101/cshperspect.a013912.

[113] D. Sengupta, S. D. Waldman, and S. Li, “From in vitro to in situ tissue engineering,” *Annals of Biomedical Engineering*, vol. 42, no. 7, pp. 1537–1545, 2014, doi: 10.1007/s10439-014-1022-8.

[114] M. Scleicher, H. P. Wendel, O. Fritze, and U. A. Stock, “In vivo tissue engineering of heart valves: Evolution of a novel concept,” *Regenerative Medicine*, vol. 4, no. 4, pp. 613–619, 2009, doi: 10.2217/rme.09.22.

[115] V. L. T. Ballard and J. M. Edelberg, “Stem cells and the regeneration of the aging cardiovascular system,” *Circulation Research*, vol. 100, no. 8, pp. 1116–1127, 2007, doi: 10.1161/01.RES.0000261964.19115.e3.

[116] N. A. Gude, K. M. Broughton, F. Firouzi, and M. A. Sussman, “Cardiac ageing: extrinsic and intrinsic factors in cellular renewal and senescence,” *Nature Reviews Cardiology*, vol. 15, no. 9, pp. 523–542, 2018, doi: 10.1038/s41569-018-0061-5.

[117] O. M. J. A. Stassen, D. E. P. Muylaert, C. V. C. Bouten, and J. Hjortnaes, “Current Challenges in Translating Tissue-Engineered Heart Valves,” *Current Treatment Options in Cardiovascular Medicine*, vol. 19, no. 9, p. 71, 2017, doi: 10.1007/s11936-017-0566-y.

[118] S. Abdulghani and G. R. Mitchell, “Biomaterials for in situ tissue regeneration: A review,” *Biomolecules*, vol. 9, no. 11, 2019, doi: 10.3390/biom9110750.

[119] J. Kluin *et al.*, “In situ heart valve tissue engineering using a bioresorbable elastomeric implant – From material design to 12 months follow-up in sheep,” *Biomaterials*, vol. 125, pp. 101–117, 2017, doi: 10.1016/j.biomaterials.2017.02.007.

[120] S. Jana, R. Tranquillo, and A. Lerman, “Cells for tissue engineering of cardiac valves,” *Journal of tissue engineering and regenerative medicine*, vol. 10, pp. 804–824, 2016, doi: 10.1002/term.

[121] T. Shinoka *et al.*, “Tissue engineering heart valves: Valve leaflet replacement study in a lamb model,” *Annals of Thoracic Surgery*, vol. 60, no. 6S, pp. S513–S516, 1995, doi: 10.1016/0003-4975(95)00733-4.

[122] D. Hoffman-Kim *et al.*, “Comparison of three myofibroblast cell sources for the tissue engineering of cardiac valves,” *Tissue Engineering*, vol. 11, no. 1–2, pp. 288–301, 2005, doi: 10.1089/ten.2005.11.288.

[123] G. Zund *et al.*, “The in vitro construction of a tissue engineered bioprosthetic heart valve,” *European Journal of Cardio-thoracic Surgery*, vol. 11, no. 3, pp. 493–497, 1997, doi: 10.1016/S1010-7940(96)01005-6.

[124] A. J. E. Appleton, C. T. G. Appleton, D. R. Boughner, and K. A. Rogers, “Vascular smooth muscle cells as a valvular interstitial cell surrogate in heart valve tissue engineering,” *Tissue Engineering - Part A*, vol. 15, no. 12, pp. 3889–3897, 2009, doi: 10.1089/ten.tea.2009.0031.

[125] J. T. Butcher and R. M. Nerem, “Porcine Aortic Valve Interstitial Cells in Three-Dimensional Culture: Comparison of Phenotype with Aortic Smooth Muscle Cells,” *Journal of Heart Valve Disease*, vol. 13, no. 3, pp. 479–485, 2004.

[126] M. Rothenburger *et al.*, “In vitro modelling of tissue using isolated vascular cells on a synthetic collagen matrix as a substitute for heart valves,” *Thoracic and Cardiovascular Surgeon*, vol. 49, no. 4, pp. 204–209, 2001, doi: 10.1055/s-2001-16108.

[127] A. Bader *et al.*, “Tissue engineering of heart valves - Human endothelial cell seeding of detergent acellularized porcine valves,” *European Journal of Cardio-thoracic Surgery*, vol. 14, no. 3, pp. 279–284, 1998, doi: 10.1016/S1010-7940(98)00171-7.

[128] K. Sang-Soo *et al.*, “Tissue Engineering of Heart Valves In Vivo Using Bone Marrow-derived Cells,” *Arifical Organs*, vol. 30, no. 7, pp. 554–557, 2006, doi: 10.1111/j.1525-1594.2006.00258.x.

[129] F. Colazzo *et al.*, “Extracellular matrix production by adipose-derived stem cells: Implications for heart valve tissue engineering,” *Biomaterials*, vol. 32, no. 1, pp. 119–127, 2011, doi: 10.1016/j.biomaterials.2010.09.003.

[130] R. Sodian *et al.*, “Use of Human Umbilical Cord Blood-Derived Progenitor Cells for Tissue-Engineered Heart Valves,” *Annals of Thoracic Surgery*, vol. 89, no. 3, pp. 819–828, 2010, doi: 10.1016/j.athoracsur.2009.11.058.

[131] D. Y. Cheung, B. Duan, and J. T. Butcher, “Current Progress in Tissue Engineering of Heart Valves: Multiscale Problems, Multiscale Solutions,” *Expert Opin Biol Ther*, vol. 15, no. 8, pp. 1155–1172, 2015, doi: 10.1038/nbt.3121.ChIP-nexus.

[132] K. Takahashi and S. Yamanaka, “Induction of Pluripotent Stem Cells from Mouse Embryonic and Adult Fibroblast Cultures by Defined Factors,” *Cell*, vol. 126, no. 4, pp. 663–676, 2006, doi: 10.1016/j.cell.2006.07.024.

[133] A. G. Efthymiou, G. Chen, M. Rao, G. Chen, and M. Boehm, “Self-renewal and cell lineage differentiation strategies in human embryonic stem cells and induced pluripotent stem cells,” *Expert Opinion on Biological Therapy*, vol. 14, no. 9, pp. 1333–1344, 2014, doi: 10.1517/14712598.2014.922533.

[134] D. L. Simpson *et al.*, “Engineering patient-specific valves using stem cells generated from skin biopsy specimens,” *Annals of Thoracic Surgery*, vol. 98, no. 3, pp. 947–954, 2014, doi: 10.1016/j.athoracsur.2014.04.075.

[135] A. L. Y. Nachlas, S. Li, R. Jha, M. Singh, C. Xu, and M. E. Davis, “Human iPSC-derived mesenchymal stem cells matured into valve interstitial-like cells using PEGDA hydrogels,” *Acta Biomaterialia*, vol. 71, pp. 235–46, 2018.

[136] T. Neri *et al.*, “Human pre-valvular endocardial cells derived from pluripotent stem cells recapitulate cardiac pathophysiological valvulogenesis,” *Nature Communications*, vol. 10, no. 1, pp. 1–14, 2019, doi: 10.1038/s41467-019-09459-5.

[137] C. V. C. Bouten, P. Y. W. Dankers, A. Driessen-Mol, S. Pedron, A. M. A. Brizard, and F. P. T. Baaijens, “Substrates for cardiovascular tissue engineering.,” *Advanced drug delivery reviews*, vol. 63, no. 4–5, pp. 221–41, 2011, doi: 10.1016/j.addr.2011.01.007.

[138] I. Bružauskaitė, D. Bironaitė, E. Bagdonas, and E. Bernotienė, “Scaffolds and cells for tissue regeneration: different scaffold pore sizes—different cell effects,” *Cytotechnology*, vol. 68, no. 3, pp. 355–369, 2016, doi: 10.1007/s10616-015-9895-4.

[139] C. M. Murphy and F. J. O’Brien, “Understanding the effect of mean pore size on cell activity in collagen-glycosaminoglycan scaffolds,” *Cell Adhesion and Migration*, vol. 4, no. 3, pp. 377–381, 2010, doi: 10.4161/cam.4.3.11747.

[140] M. Namdari and A. Eatemadi, “Nanofibrous bioengineered heart valve—Application in paediatric medicine,” *Biomedicine and Pharmacotherapy*, vol. 84, pp. 1179–1188, 2016, doi: 10.1016/j.biopha.2016.10.058.

[141] H. Wang, S. M. Haeger, A. M. Kloxin, L. A. Leinwand, and K. S. Anseth, “Redirecting valvular myofibroblasts into dormant fibroblasts through light-mediated reduction in substrate modulus,” *PLoS ONE*, vol. 7, no. 7, 2012, doi: 10.1371/journal.pone.0039969.

[142] S. Jana, A. Lerman, and R. D. Simari, “In vitro model of a fibrosa layer of a heart valve,” *ACS Applied Materials and Interfaces*, vol. 7, no. 36, pp. 20012–20020, 2015, doi: 10.1021/acsami.5b04805.

[143] H. Wang, M. W. Tibbitt, S. J. Langer, L. A. Leinwand, and K. S. Anseth, “Hydrogels preserve native phenotypes of valvular fibroblasts through an elasticity-regulated PI3K/AKT pathway,” *Proceedings of the National Academy of Sciences of the United States of America*, vol. 110, no. 48, pp. 19336–19341, 2013, doi: 10.1073/pnas.1306369110.

[144] S. A. Sell, P. S. Wolfe, K. Garg, J. M. McCool, I. A. Rodriguez, and G. L. Bowlin, “The use of natural polymers in tissue engineering: A focus on

electrospun extracellular matrix analogues," *Polymers*, vol. 2, no. 4, pp. 522–553, 2010, doi: 10.3390/polym2040522.

[145] Q. P. Pham, U. Sharma, and A. G. Mikos, "Electrospinning of polymeric nanofibers for tissue engineering applications: A review," *Tissue Engineering*, vol. 12, no. 5, pp. 1197–1211, 2006, doi: 10.1089/ten.2006.12.1197.

[146] J. Nam, Y. Huang, S. Agarwal, and J. Lannutti, "Materials Selection and Residual Solvent Retention in Biodegradable Electrospun Fibers," *Journal of Applied Polymer Science*, vol. 107, pp. 1557–1554, 2008, doi: 10.1002/app.

[147] S. Deville, "Freeze-casting of porous biomaterials: Structure, properties and opportunities," *Materials*, vol. 3, no. 3, pp. 1913–1927, 2010, doi: 10.3390/ma3031913.

[148] B. A. Harley, J. H. Leung, E. C. C. M. Silva, and L. J. Gibson, "Mechanical characterization of collagen-glycosaminoglycan scaffolds," *Acta Biomaterialia*, vol. 3, no. 4, pp. 463–474, 2007, doi: 10.1016/j.actbio.2006.12.009.

[149] U. G. K. Wegst, M. Schecter, A. E. Donius, and P. M. Hunger, "Biomaterials by freeze casting," *Philosophical Transactions of the Royal Society A: Mathematical, Physical and Engineering Sciences*, vol. 368, no. 1917, pp. 2099–2121, 2010, doi: 10.1098/rsta.2010.0014.

[150] A. Hasan, S. Soliman, F. el Hajj, Y. Tseng, and H. C. Yalcin, "Fabrication and In Vitro Characterization of a Tissue Engineered PCL-PLLA Heart Valve," *Scientific Reports*, vol. 8, no. 8187, pp. 1–13, 2018, doi: 10.1038/s41598-018-26452-y.

[151] G. S. Offeddu, J. C. Ashworth, R. E. Cameron, and M. L. Oyen, "Multi-scale mechanical response of freeze-dried collagen scaffolds for tissue engineering applications," *Journal of the Mechanical Behavior of Biomedical Materials*, vol. 42, pp. 19–25, 2015, doi: 10.1016/j.jmbbm.2014.10.015.

[152] D. Schmidt, U. A. Stock, and S. P. Hoerstrup, "Tissue engineering of heart valves using decellularized xenogeneic or polymeric starter matrices," *Philosophical transactions of the Royal Society of London. Series B, Biological sciences*, vol. 362, no. June, pp. 1505–12, 2007, doi: 10.1098/rstb.2007.2131.

[153] M. C. VeDepo, M. S. Detamore, R. A. Hopkins, and G. L. Converse, "Recellularization of decellularized heart valves: Progress toward the tissue-engineered heart valve," *Journal of Tissue Engineering*, vol. 8, p. 204173141772632, 2017, doi: 10.1177/2041731417726327.

[154] H. Baraki *et al.*, "Orthotopic replacement of the aortic valve with decellularized allograft in a sheep model," *Biomaterials*, vol. 30, no. 31, pp. 6240–6246, 2009, doi: 10.1016/j.biomaterials.2009.07.068.

[155] N. Grabow *et al.*, “Mechanical and structural properties of a novel hybrid heart valve scaffold for tissue engineering,” *Artificial Organs*, vol. 28, no. 11, pp. 971–979, 2004, doi: 10.1111/j.1525-1594.2004.00007.x.

[156] J. Liao, E. M. Joyce, and M. S. S. Ã, “Effects of decellularization on the mechanical and structural properties of the porcine aortic valve leaflet,” *Biomaterials*, vol. 29, pp. 1065–1074, 2008, doi: 10.1016/j.biomaterials.2007.11.007.

[157] Q. Chen, S. Liang, and G. A. Thouas, “Elastomeric biomaterials for tissue engineering,” *Progress in Polymer Science*, vol. 38, no. 3–4, pp. 584–671, 2013, doi: 10.1016/j.progpolymsci.2012.05.003.

[158] S. Jana, B. J. Tefft, D. B. Spoon, and R. D. Simari, “Scaffolds for tissue engineering of cardiac valves,” *Acta Biomaterialia*, vol. 10, no. 7, pp. 2877–2893, 2014, doi: 10.1016/j.actbio.2014.03.014.

[159] E. Fallahiarezoudar, M. Ahmadipourroudposht, A. Idris, and N. Mohd Yusof, “A review of: Application of synthetic scaffold in tissue engineering heart valves,” *Materials Science and Engineering C*, vol. 48, pp. 556–565, 2015, doi: 10.1016/j.msec.2014.12.016.

[160] Y. Xue, V. Sant, J. Phillippi, and S. Sant, “Biodegradable and biomimetic elastomeric scaffolds for tissue-engineered heart valves,” *Acta Biomaterialia*, vol. 48. Acta Materialia Inc., pp. 2–19, 2017, doi: 10.1016/j.actbio.2016.10.032.

[161] W. D. Merryman *et al.*, “Correlation between heart valve interstitial cell stiffness and transvalvular pressure: Implications for collagen biosynthesis,” *American Journal of Physiology - Heart and Circulatory Physiology*, vol. 290, no. 1, pp. 224–231, 2006, doi: 10.1152/ajpheart.00521.2005.

[162] B. Dhandayuthapani, Y. Yoshida, T. Maekawa, and D. S. Kumar, “Polymeric scaffolds in tissue engineering application: A review,” *International Journal of Polymer Science*, vol. 2011, no. ii, 2011, doi: 10.1155/2011/290602.

[163] E. Solheim, B. Sudmann, G. Bang, and E. Sudmann, “Biocompatibility and effect on osteogenesis of poly(ortho ester) compared to poly(DL-lactic acid),” *Journal of Biomedical Materials Research*, vol. 49, no. 2, pp. 257–263, 2000, doi: 10.1002/(SICI)1097-4636(200002)49:2<257::AID-JBM15>3.0.CO;2-5.

[164] R. S. Walton, D. D. Brand, and J. T. Czernuszka, “Influence of telopeptides, fibrils and crosslinking on physicochemical properties of Type i collagen films,” *Journal of Materials Science: Materials in Medicine*, vol. 21, no. 2, pp. 451–461, 2010, doi: 10.1007/s10856-009-3910-2.

[165] R. Parenteau-Bareil, R. Gauvin, and F. Berthod, “Collagen-based biomaterials for tissue engineering applications,” *Materials*, vol. 3, no. 3, pp. 1863–1887, 2010, doi: 10.3390/ma3031863.

[166] K. S. Silvipriya, K. Krishna Kumar, A. R. Bhat, B. Dinesh Kumar, A. John, and P. Lakshmanan, "Collagen: Animal sources and biomedical application," *Journal of Applied Pharmaceutical Science*, vol. 5, no. 3, pp. 123–127, 2015, doi: 10.7324/JAPS.2015.50322.

[167] U. Cheema, M. Ananta, and V. Mudera, "Collagen: applications of a natural polymer in regenerative medicine," in *Regenerative Medicine and Tissue Engineering*, InTechOpen, 2011, pp. 288–300.

[168] B. Chevallay and D. Herbage, "Collagen-based biomaterials as 3D scaffold for cell cultures: applications for tissue engineering and gene therapy," *Medical & Biological Engineering & Computing*, vol. 38, no. 2, pp. 211–218, 2000, doi: 10.1007/BF02344779.

[169] P. M. Taylor, E. Sachlos, S. A. Dreger, A. H. Chester, J. T. Czernuszka, and M. H. Yacoub, "Interaction of human valve interstitial cells with collagen matrices manufactured using rapid prototyping," *Biomaterials*, vol. 27, no. 13, pp. 2733–2737, 2006, doi: 10.1016/j.biomaterials.2005.12.003.

[170] S. Dreger *et al.*, "Potential for synthesis and degradation of extracellular matrix proteins by valve interstitial cells seeded onto collagen scaffolds.," *Tissue engineering*, vol. 12, no. 9, pp. 2533–40, 2006, doi: 10.1089/ten.2006.12.2533.

[171] M. Rothenburger, W. Völker, P. Vischer, B. Glasmacher, H. H. Scheld, and M. Deiwick, "Ultrastructure of proteoglycans in tissue-engineered cardiovascular structures," *Tissue Engineering*, vol. 8, no. 6, pp. 1049–1056, 2002, doi: 10.1089/107632702320934146.

[172] M. Rothenburger *et al.*, "Tissue engineering of heart valves: Formation of a three-dimensional tissue using porcine heart valve cells," *ASAIO Journal*, vol. 48, no. 6, pp. 586–591, 2002, doi: 10.1097/00002480-200211000-00003.

[173] Y. Shi and I. Vesely, "Fabrication of Mitral Valve Chordae by Directed Collagen Gel Shrinkage," *Tissue Engineering*, vol. 9, no. 6, pp. 1233–1242, 2003, doi: 10.1089/10763270360728143.

[174] Y. Shi, R. Iyer, A. Soundararajan, D. Dobkin, and I. Vesely, "Collagen-based tissue engineering as applied to heart valves," in *Annual International Conference of the IEEE Engineering in Medicine and Biology - Proceedings*, 2005, vol. 7 VOLS, pp. 4912–4915, doi: 10.1109/iembs.2005.1615574.

[175] Q. Chen, A. Bruyneel, K. Clarke, C. Carr, and J. Czernuszka, "Collagen-Based Scaffolds for Potential Application of Heart Valve Tissue Engineering," *Journal of Tissue Science & Engineering*, vol. S11, pp. 3–8, 2012, doi: 10.4172/2157-7552.s11-003.

[176] B. Kim and D. J. Mooney, "Scaffolds for Engineering Smooth Muscle Under Cyclic Mechanical Conditioning," *J Biomech Eng*, vol. 122, no. 3, pp. 210–215, 2000.

[177] D. Pezzoli *et al.*, “Fibronectin promotes elastin deposition, elasticity and mechanical strength in cellularised collagen-based scaffolds,” *Biomaterials*, vol. 180, pp. 130–142, 2018, doi: 10.1016/j.biomaterials.2018.07.013.

[178] I. G. de Torre and M. Alonso, “Elastin-Based Materials : Promising Candidates for Cardiac Tissue Regeneration,” *Frontiers in Bioengineering and Biotechnology*, vol. 8, no. 657, pp. 1–20, 2020, doi: 10.3389/fbioe.2020.00657.

[179] M. N. Collins and C. Birkinshaw, “Hyaluronic acid based scaffolds for tissue engineering - A review,” *Carbohydrate Polymers*, vol. 92, no. 2, pp. 1262–1279, 2013, doi: 10.1016/j.carbpol.2012.10.028.

[180] B. Duan, L. Hockaday, E. Kapetanovic, K. Kang, and J. T. Butcher, “Stiffness and Adhesivity Control Aortic Valve Interstitial Cell Behavior within Hyaluronic Acid Based Hydrogels,” *Acta Biomaterialia*, vol. 9, no. 8, pp. 7640–7650, 2013, doi: 10.1161/CIRCULATIONAHA.110.956839.

[181] D. S. Puperi, R. W. O. Connell, Z. E. Punske, Y. Wu, J. L. West, and K. J. Grande-allen, “Hyaluronan Hydrogels for a Biomimetic Spongiosa Layer of Tissue Engineered Heart Valve Sca ff olds,” *Biomacromolecules*, vol. 17, pp. 1766–1775, 2016, doi: 10.1021/acs.biomac.6b00180.

[182] K. S. Masters, D. N. Shah, L. A. Leinwand, and K. S. Anseth, “Crosslinked hyaluronan scaffolds as a biologically active carrier for valvular interstitial cells,” *Biomaterials*, vol. 26, no. 15, pp. 2517–2525, 2005, doi: 10.1016/j.biomaterials.2004.07.018.

[183] A. Ramamurthi and I. Vesely, “Evaluation of the matrix-synthesis potential of crosslinked hyaluronan gels for tissue engineering of aortic heart valves,” *Biomaterials*, vol. 26, pp. 999–1010, 2005, doi: 10.1016/j.biomaterials.2004.04.016.

[184] C. R. Kothapalli and A. Ramamurthi, “Copper nanoparticle cues for biomimetic cellular assembly of crosslinked elastin fibers,” *Acta Biomaterialia*, vol. 5, no. 2, pp. 541–553, 2009, doi: 10.1016/j.actbio.2008.09.004.

[185] C. R. Kothapalli, P. M. Taylor, R. T. Smolenski, M. H. Yacoub, and A. Ramamurthi, “Transforming growth factor beta 1 and hyaluronan oligomers synergistically enhance elastin matrix regeneration by vascular smooth muscle cells,” *Tissue Engineering - Part A*, vol. 15, no. 3, pp. 501–511, 2009, doi: 10.1089/ten.tea.2008.0040.

[186] L. Venkataraman and A. Ramamurthi, “Induced elastic matrix deposition within three-dimensional collagen scaffolds,” *Tissue Engineering - Part A*, vol. 17, no. 21–22, pp. 2879–2889, 2011, doi: 10.1089/ten.tea.2010.0749.

[187] C. Kothapalli and A. Ramamurthi, “Lysyl Oxidase Enhances Elastin Synthesis and Matrix Formation by Vascular Smooth Muscle Cells,” *J Tissue Eng REgen Med.*, vol. 3, no. 8, pp. 655–661, 2009, doi: 10.1038/jid.2014.371.

[188] A. Ramamurthi and I. Vesely, “Ultraviolet light-induced modification of crosslinked hyaluronan gels,” *J Biomed Mater Res A*, vol. 66, no. 2, pp. 317–329, 2002.

[189] M. D. Brigham *et al.*, “Mechanically Robust and Bioadhesive Collagen and Photocrosslinkable Hyaluronic Acid Semi-Interpenetrating Networks,” *Tissue Engineering - Part A*, vol. 15, no. 7, pp. 1646–1653, 2009.

[190] S. Suri and C. E. Schmidt, “Photopatterned collagen-hyaluronic acid interpenetrating polymer network hydrogels,” *Acta Biomaterialia*, vol. 5, no. 7, pp. 2385–2397, 2009, doi: 10.1016/j.actbio.2009.05.004.

[191] R. Nazir, A. Bruyneel, C. Carr, and J. Czernuszka, “Collagen type I and hyaluronic acid based hybrid scaffolds for heart valve tissue engineering,” *Biopolymers*, vol. 110, no. 8, pp. 1–13, 2019, doi: 10.1002/bip.23278.

[192] R. Nazir, “Development and Characterisation of Collagen type I and Hyaluronic Acid (HA) based Interlaced Scaffolds for Tissue Engineered Heart Valves (TEHVs).”

[193] W. F. Daamen, T. Hafmans, J. H. Veerkamp, and T. H. van Kuppevelt, “Comparison of five procedures for the purification of insoluble elastin,” *Biomaterials*, vol. 22, no. 14, pp. 1997–2005, 2001, doi: 10.1016/S0142-9612(00)00383-5.

[194] B. C. Starcher and M. J. Galione, “Purification and Comparison of Elastins Animal Species from Different Animal Species,” *Analytical Biochem*, vol. 74, pp. 441–447, 1976.

[195] W. F. Daamen, T. Hafmans, J. H. Veerkamp, and T. H. van Kuppevelt, “Comparison of five procedures for the purification of insoluble elastin,” *Biomaterials*, vol. 22, pp. 1997–2005, 2001.

[196] R. P. Mecham, “Methods in Elastic Tissue Biology: Elastin Isolation and Purification,” *Methods*, vol. 45, no. 1, pp. 32–41, 2008, doi: https://doi.org/10.1016/j.ymeth.2008.01.007.

[197] S. M. Partridge, “Elastin, Biosynthesis and Structure,” *Gerontologia*, vol. 15, pp. 85–100, 1969.

[198] A. B. T.-M. in E. Light, “[46] Partial acid hydrolysis,” in *Enzyme Structure*, vol. 11, Academic Press, 1967, pp. 417–420.

[199] G. S. Adair, H. F. Davis, and S. M. Partridge, “A Soluble protein derived from elastin,” *Nature*, vol. 167, no. 4250. p. 605, 1951, doi: 10.1038/167605a0.

[200] S. M. Partridge, H. F. Davis, and G. S. Adair, “The Chemistry of Connective Tisses 2. Soluble proteins derived from partial hydrolysis of elastin,” *The Biochemical Journal*, vol. 61, no. 1, pp. 11–21, 1955, doi: ttps://doi.org/10.1042/bj0610011.

[201] T. J. Bowen, “Physical studies on a soluble protein obtained by the degradation of elastin with urea,” *Biochem J.*, vol. 55, no. 5, pp. 766–768, 1953, doi: 10.1097/00000441-194420740-00023.

[202] M. Jacob and W. Hornebeck, “Isolation and characterisation of insoluble and kappa-elastins,” *Methods of connective tissue research*, vol. 4, pp. 92–129, 1985.

[203] D. A. Hall, “The reaction between elastase and elastic tissue, 1. the substrate,” *Biochemistry*, vol. 59, no. 1953, pp. 459–470, 1955.

[204] S. G. Wise, S. M. Mithieux, and A. S. Weiss, “Engineered Tropoelastin and Elastin-Based Biomaterials,” in *Advances in Protein Chemistry and Structural Biology*, vol. 78, 2009, pp. 1–24.

[205] N. Annabi, S. M. Mithieux, G. Camci-Unal, M. R. Dokmeci, A. S. Weiss, and A. Khademhosseini, “Elastomeric recombinant protein-based biomaterials,” *Biochemical Engineering Journal*, vol. 77, pp. 110–118, 2013, doi: 10.1016/j.bej.2013.05.006.

[206] N. Annabi, S. M. Mithieux, E. A. Boughton, A. J. Ruys, A. S. Weiss, and F. Dehghani, “Synthesis of highly porous crosslinked elastin hydrogels and their interaction with fibroblasts in vitro,” *Biomaterials*, vol. 30, no. 27, pp. 4550–4557, 2009, doi: 10.1016/j.biomaterials.2009.05.014.

[207] N. Annabi, S. M. Mithieux, A. S. Weiss, and F. Dehghani, “The fabrication of elastin-based hydrogels using high pressure CO2,” *Biomaterials*, vol. 30, no. 1, pp. 1–7, 2009, doi: 10.1016/j.biomaterials.2008.09.031.

[208] N. Annabi, S. M. Mithieux, A. S. Weiss, and F. Dehghani, “Cross-linked open-pore elastic hydrogels based on tropoelastin, elastin and high pressure CO2,” *Biomaterials*, vol. 31, no. 7, pp. 1655–1665, 2010, doi: 10.1016/j.biomaterials.2009.11.051.

[209] J. B. Leach, J. B. Wolinsky, P. J. Stone, and J. Y. Wong, “Crosslinked α-elastin biomaterials: Towards a processable elastin mimetic scaffold,” *Acta Biomaterialia*, vol. 1, no. 2, pp. 155–164, 2005, doi: 10.1016/j.actbio.2004.12.001.

[210] J. Araujo *et al.*, “Processing and characterization of α-elastin electrospun membranes,” *Applied Physics A: Materials Science and Processing*, vol. 115, no. 4, pp. 1291–1298, 2014, doi: 10.1007/s00339-013-7984-9.

[211] M. Li, M. J. Mondrinos, M. R. Gandhi, F. K. Ko, A. S. Weiss, and P. I. Lelkes, “Electrospun protein fibers as matrices for tissue engineering,” *Biomaterials*, vol. 26, pp. 5999–6008, 2005, doi: 10.1016/j.biomaterials.2005.03.030.

[212] K. Trabbic-Carlson, L. A. Setton, and A. Chilkoti, “Swelling and mechanical behaviors of chemically cross-linked hydrogels of elastin-like polypeptides,” *Biomacromolecules*, vol. 4, no. 3, pp. 572–580, 2003, doi: 10.1021/bm025671z.

[213] M. K. McHale, L. A. Setton, and A. Chilkoti, “Synthesis and in Vitro Evaluation of Enzymatically Cross-Linked Elastin-Like Polypeptide Gels for Cartilaginous Tissue Repair,” *Tissue Engineering*, vol. 11, no. 12, pp. 1768–1779, 2005, doi: https://doi.org/10.1089/ten.2005.11.1768.

[214] Y. N. Zhang *et al.*, “A Highly Elastic and Rapidly Crosslinkable Elastin-Like Polypeptide-Based Hydrogel for Biomedical Applications,” *Advanced Functional Materials*, vol. 25, no. 30, pp. 4814–4826, 2015, doi: 10.1002/adfm.201501489.

[215] J. Raphel, A. Parisi-Amon, and S. C. Heilshorn, “Photoreactive elastin-like proteins for use as versatile bioactive materials and surface coatings,” *Journal of Materials Chemistry*, vol. 22, no. 37, pp. 19429–19437, 2012, doi: 10.1039/c2jm31768k.

[216] L. Nivison-Smith and A. S. Weiss, “Alignment of human vascular smooth muscle cells on parallel electrospun synthetic elastin fibers,” *Journal of Biomedical Materials Research - Part A*, vol. 100 A, no. 1, pp. 155–161, 2012, doi: 10.1002/jbm.a.33255.

[217] S. M. Mithieux, J. E. J. Rasko, and A. S. Weiss, “Synthetic elastin hydrogels derived from massive elastic assemblies of self-organized human protein monomers,” *Biomaterials*, vol. 25, no. 20, pp. 4921–4927, 2004, doi: 10.1016/j.biomaterials.2004.01.055.

[218] S. M. Mithieux, S. G. Wise, M. J. Raftery, B. Starcher, and A. S. Weiss, “A model two-component system for studying the architecture of elastin assembly in vitro,” *Journal of Structural Biology*, vol. 149, pp. 282–289, 2005, doi: 10.1016/j.jsb.2004.11.005.

[219] J. Rnjak, Z. Li, P. K. M. Maitz, S. G. Wise, and A. S. Weiss, “Primary human dermal fibroblast interactions with open weave three-dimensional scaffolds prepared from synthetic human elastin,” *Biomaterials*, vol. 30, no. 32, pp. 6469–6477, 2009, doi: 10.1016/j.biomaterials.2009.08.017.

[220] J. Rnjak-Kovacina *et al.*, “Tailoring the porosity and pore size of electrospun synthetic human elastin scaffolds for dermal tissue engineering,” *Biomaterials*, vol. 32, no. 28, pp. 6729–6736, 2011, doi: 10.1016/j.biomaterials.2011.05.065.

[221] K. A. McKenna *et al.*, “Mechanical property characterization of electrospun recombinant human tropoelastin for vascular graft biomaterials,” *Acta Biomaterialia*, vol. 8, no. 1, pp. 225–233, 2012, doi: 10.1016/j.actbio.2011.08.001.

[222] D. L. Nettles, A. Chilkoti, and L. A. Setton, “Applications of elastin-like polypeptides in tissue engineering,” *Advanced Drug Delivery Reviews*, vol. 62, no. 15, pp. 1479–1485, 2010, doi: 10.1016/j.addr.2010.04.002.

[223] X. Wang, M. S. Ali, and C. M. R. Lacerda, “A Three-Dimensional Collagen-Elastin Scaffold for Heart Valve Tissue Engineering,” *Bioengineering*, vol. 5, no. 69, pp. 1–12, 2018, doi: 10.3390/bioengineering5030069.

[224] N. Annabi, A. Fathi, S. M. Mithieux, A. S. Weiss, and F. Dehghani, “Fabrication of porous PCL/elastin composite scaffolds for tissue engineering applications,” *The Journal of Supercritical Fluids*, vol. 59, pp. 157–167, 2011, doi: 10.1016/j.supflu.2011.06.010.

[225] J. Rnjak-Kovacina *et al.*, “Electrospun synthetic human elastin:collagen composite scaffolds for dermal tissue engineering,” *Acta Biomaterialia*, vol. 8, no. 10, pp. 3714–3722, 2012, doi: 10.1016/j.actbio.2012.06.032.

[226] D. Boland, Eugene, “Electrospinning collagen and elastin: preliminary vascular tissue engineering,” *Frontiers in Bioscience*, vol. 9, no. 1–3, p. 1422, 2004, doi: 10.2741/1313.

[227] S. M. Mithieux, S. G. Wise, and A. S. Weiss, “Tropoelastin - A multifaceted naturally smart material,” *Advanced Drug Delivery Reviews*, vol. 65, no. 4, pp. 421–428, 2013, doi: 10.1016/j.addr.2012.06.009.

[228] D. v. Bax *et al.*, “Fundamental insight into the effect of carbodiimide crosslinking on cellular recognition of collagen-based scaffolds.,” *Acta Biomaterialia*, 2016, doi: 10.1016/j.actbio.2016.11.059.

[229] A. J. Ryan and F. J. O’Brien, “Insoluble elastin reduces collagen scaffold stiffness, improves viscoelastic properties, and induces a contractile phenotype in smooth muscle cells,” *Biomaterials*, vol. 73, pp. 296–307, 2015, doi: 10.1016/j.biomaterials.2015.09.003.

[230] Y. Garcia, N. Hemantkumar, R. Collighan, M. Griffin, J. C. Rodriguez-Cabello, and A. Pandit, “In vitro characterization of a collagen scaffold enzymatically cross-linked with a tailored elastin-like polymer,” *Tissue Engineering - Part A*, vol. 15, no. 4, pp. 887–899, 2009, doi: 10.1089/ten.tea.2008.0104.

[231] V. A. Kumar *et al.*, “Acellular vascular grafts generated from collagen and elastin analogs,” *Acta Biomaterialia*, vol. 9, no. 9, pp. 8067–8074, 2013, doi: 10.1016/j.actbio.2013.05.024.

[232] S. Minardi *et al.*, “Biomimetic collagen / elastin meshes for ventral hernia repair in a rat model,” *Acta Biomaterialia*, vol. 50, pp. 165–177, 2017, doi: 10.1016/j.actbio.2016.11.032.

[233] D. v Bax, H. E. Smalley, R. W. Farndale, S. M. Best, and R. E. Cameron, “Cellular response to collagen-elastin composite materials,” *Acta Biomaterialia*, vol. 86, pp. 158–170, 2019, doi: 10.1016/j.actbio.2018.12.033.

[234] T. U. Nguyen, C. A. Bashur, and V. Kishore, “Impact of elastin incorporation into electrochemically aligned collagen fibers on mechanical properties and

smooth muscle cell phenotype," *Biomedical Materials (Bristol)*, vol. 11, no. 2, p. 25008, 2016, doi: 10.1088/1748-6041/11/2/025008.

[235] W. F. Daamen *et al.*, "Preparation and evaluation of molecularly-defined collagen-elastin-glycosaminoglycan scaffolds for tissue engineering," *Biomaterials*, vol. 24, no. 22, pp. 4001–4009, 2003, doi: 10.1016/S0142-9612(03)00273-4.

[236] L. Buttafoco *et al.*, "First steps towards tissue engineering of small-diameter blood vessels: preparation of flat scaffolds of collagen and elastin by means of freeze drying," *Journal of Biomedical Materials Research - Part B Applied Biomaterials*, vol. 77, no. 2, pp. 357–368, 2006, doi: 10.1002/jbm.b.30444.

[237] L. Buttafoco, P. Engbers-Buijtenhuijs, A. A. Poot, P. J. Dijkstra, I. Vermes, and J. Feijen, "Physical characterization of vascular grafts cultured in a bioreactor," *Biomaterials*, vol. 27, no. 11, pp. 2380–2389, 2006, doi: 10.1016/j.biomaterials.2005.10.017.

[238] N. Annabi, A. Fathi, S. M. Mithieux, P. Martens, A. S. Weiss, and F. Dehghani, "The effect of elastin on chondrocyte adhesion and proliferation on poly (e-caprolactone)/elastin composites," *Biomaterials*, vol. 32, no. 6, pp. 1517–1525, 2011, doi: 10.1016/j.biomaterials.2010.10.024.

[239] L. Buttafoco *et al.*, "Electrospinning of collagen and elastin for tissue engineering applications," *Biomaterials*, vol. 27, no. 5, pp. 724–734, 2006, doi: 10.1016/j.biomaterials.2005.06.024.

[240] Q. Chen, "Collagen-Based Scaffolds for Heart Valve Tissue Engineering," 2013.

[241] M. E. Tedder, A. Simionescu, J. Chen, J. Liao, and D. T. Simionescu, "Assembly and testing of stem cell-seeded layered collagen constructs for heart valve tissue engineering.," *Tissue engineering. Part A*, vol. 17, no. 1–2, pp. 25–36, 2011, doi: 10.1089/ten.tea.2010.0138.

[242] H. Tseng *et al.*, "Fabrication and Mechanical Evaluation of Anatomically-Inspired Quasilaminate Hydrogel Structures with Layer-Specific Formulations," *Ann Biomed Eng*, vol. 41, no. 2, pp. 398–407, 2013, doi: 10.1161/CIRCULATIONAHA.110.956839.

[243] S. Jana and A. Lerman, "Behavior of valvular interstitial cells on trilayered nanofibrous substrate mimicking morphologies of heart valve leaflet," *Acta Biomaterialia*, vol. 85, pp. 142–156, 2019, doi: 10.1016/j.actbio.2018.12.005.Behavior.

[244] S. Jana, F. Franchi, and A. Lerman, "Trilayered tissue structure with leaflet-like orientations developed through in vivo tissue engineering," *Biomedical Materials (Bristol)*, vol. 15, no. 1, 2020, doi: 10.1088/1748-605X/ab52e2.

[245] B. Duan, E. Kapetanovic, L. A. Hockaday, and J. T. Butcher, “3D Printed Trileaflet Valve Conduits Using Biological Hydrogels and Human Valve Interstitial Cells,” *Acta Biomaterialia*, vol. 10, no. 5, pp. 1836–1846, 2014, doi: 10.1038/jid.2014.371.

[246] Q. Chen, A. Bruyneel, C. Carr, and J. Czernuszka, “Trilayer scaffold with cardiosphere-derived cells for heart valve tissue engineering,” *Journal of Biomedical Materials Research - Part B Applied Biomaterials*, vol. 108, no. 3, pp. 729–737, 2020, doi: 10.1002/jbm.b.34427.

[247] S. M. Partridge and L. Temperature, “The Chemistry of Connective Tissues 3. Composition of The Soluble Proteins Derived From Elastin,” *The Biochemical Journal*, vol. 6, pp. 600–607, 1956.

[248] H. B. Henninger, C. J. Underwood, S. J. Romney, G. L. Davis, and J. A. Weiss, “Effect of elastin digestion on the quasi-static tensile response of medial collateral ligament,” *Journal of Orthopaedic Research*, vol. 31, no. 8, pp. 1226–1233, 2013, doi: 10.1002/jor.22352.

[249] B. Smith, “Fundamentals of Fourier Transform Infrared Spectroscopy,” in *CRC Press*, Second., Taylor & Francis Group, 2011, pp. 1–17.

[250] J. Wang, Y. Su, F. Jia, and H. Jin, “Characterization of casein hydrolysates derived from enzymatic hydrolysis,” *Chemistry Central Journal*, vol. 7, no. 1, pp. 1–8, 2013, doi: 10.1186/1752-153X-7-62.

[251] H. Jiang, W. Su, P. T. Mather, and T. J. Bunning, “Rheology of highly swollen chitosan/polyacrylate hydrogels,” *Polymer*, vol. 40, no. 16, pp. 4593–4602, 1999, doi: 10.1016/S0032-3861(99)00070-1.

[252] J. C. Cameselle, J. Meireles Ribeiro, and A. Sillero, “Derivation and use of a formula to calculate the net charge of acid-base compounds. Its application to amino acids, proteins and nucleotides,” *Biochemical Education*, vol. 14, no. 3, pp. 131–136, 1986, doi: 10.1016/0307-4412(86)90176-7.

[253] R. Mercadé-Prieto, R. J. Falconer, W. R. Paterson, and D. I. Wilson, “Swelling and dissolution of β-lactoglobulin gels in alkali,” *Biomacromolecules*, vol. 8, no. 2, pp. 469–476, 2007, doi: 10.1021/bm060553n.

[254] K. J. Payne and A. Veis, “Fourier Transform IR Spectroscopy of Collagen and GelatinSolutions: Deconvolution of the Amide I Band for Conformational Studies,” *Biopolymers*, vol. 27, no. 11, pp. 1749–1760, 1988, doi: 10.1002/bip.360271105.

[255] M. C. Popescu, C. Vasile, and O. Craciunescu, “Structural analysis of some soluble elastins by means of FT-IR and 2D IR correlation spectroscopy,” *Biopolymers*, vol. 93, no. 12, pp. 1072–1084, 2010, doi: 10.1002/bip.21524.

[256] X. Hu, D. Kaplan, and P. Cebe, “Determining beta-sheet crystallinity in fibrous proteins by thermal analysis and infrared spectroscopy,” *Macromolecules*, vol. 39, no. 18, pp. 6161–6170, 2006, doi: 10.1021/ma0610109.

[257] S. Cai and B. R. Singh, “Identification of β-turn and random coil amide III infrared bands for secondary structure estimation of proteins,” *Biophysical Chemistry*, vol. 80, no. 1, pp. 7–20, 1999, doi: 10.1016/S0301-4622(99)00060-5.

[258] C. Stani, L. Vaccari, E. Mitri, and G. Birarda, “FTIR investigation of the secondary structure of type I collagen: New insight into the amide III band,” *Spectrochimica Acta - Part A: Molecular and Biomolecular Spectroscopy*, vol. 229, pp. 1–7, 2020, doi: 10.1016/j.saa.2019.118006.

[259] N. Bouklas and R. Huang, “Swelling kinetics of polymer gels: Comparison of linear and nonlinear theories,” *Soft Matter*, vol. 8, no. 31, pp. 8194–8203, 2012, doi: 10.1039/c2sm25467k.

[260] J. M. Gosline, “The temperature-dependent swelling of elastin,” *Biopolymers*, vol. 17, no. 3, pp. 697–707, 1978, doi: 10.1002/bip.1978.360170312.

[261] E. G. Cleary and W. J. Cliff, “The Substructure of Elastin,” *Experimental and Molecular Pathology*, vol. 28, no. 2, pp. 227–246, 1978, doi: https://doi.org/10.1016/0014-4800(78)90054-0.

[262] B. A. Cox, B. C. Starcher, and D. W. Urry, “Coacervation of a-elastin results in fiber formation,” *Bioehirnica et Biophysica Acta*, vol. 317, pp. 209–213, 1973.

[263] D. Volpin, D. Urry, B. Cox, and L. Gotte, “Optical Diffraction Of Tropoelastin And a-Elastin Coacervates,” *Biochimica et Biophysica Acta*, vol. 439, pp. 253–258, 1976.

[264] L. Gotte, D. Volpin, R. W. Horne, and M. Mammi, “Electron microscopy and optical diffraction of elastin,” *Micron*, vol. 7, pp. 95–102, 1976.

[265] L. Gotte, M. G. Giro, D. Volpin, and R. W. Horne, “The ultrastructural organization of elastin,” *Journal of Ultrasructure Research*, vol. 46, pp. 23–33, 1974, doi: 10.1016/S0022-5320(74)80019-5.

[266] D. P. Thornhill, “Separation of a series of chromophores and fluorophores present in elastin,” *Biochemical Journal*, vol. 147, no. 2, pp. 215–219, 1975, doi: 10.1042/bj1470215.

[267] Z. Deyl, K. Macek, M. Adam, and Vancikova, “Studies on the chemical nature of elastin fluorescence,” *Biochimica et Biophysica Acta*, vol. 625, no. 2, pp. 248–254, 1980, doi: 10.1016/0005-2795(80)90288-3.

[268] D. H. Tinker, R. B. Rucker, and A. L. Tappel, “Variation of elastin fluorescence with method of preparation: Determination of the major fluorophore of fibrillar

elastin," *Connective Tissue Research*, vol. 11, no. 4, pp. 299–308, 1983, doi: 10.3109/03008208309004862.

[269] Y. Wang, J. Hahn, and Y. Zhang, "Mechanical Properties of Arterial Elastin with Water Loss," *Journal of Biomechanical Engineering*, vol. 140, no. 4, pp. 1–8, 2018, doi: 10.1115/1.4038887.

[270] M. Mammi, L. Gotte, and G. Pezzin, "Evidence for order in the structure of α-elastin," *Nature*, vol. 220, pp. 371–373, 1968, doi: 10.1038/220371b0.

[271] L. Debelle *et al.*, "The secondary structure and architecture of human elastin," *European Journal of Biochemistry*, vol. 258, no. 2, pp. 533–539, 1998, doi: 10.1046/j.1432-1327.1998.2580533.x.

[272] L. Debelle and A. J. P. Alix, "The structures of elastins and their function," *Biochimie*, vol. 81, no. 10, pp. 981–994, 1999, doi: 10.1016/S0300-9084(99)00221-7.

[273] E. A. Foegeding and J. P. Davis, "Food protein functionality: A comprehensive approach," *Food Hydrocolloids*, vol. 25, no. 8, pp. 1853–1864, 2011, doi: 10.1016/j.foodhyd.2011.05.008.

[274] L. Debelle *et al.*, "Bovine elastin and κ-elastin secondary structure determination by optical spectroscopies," *Journal of Biological Chemistry*, vol. 270, no. 44, pp. 26099–26103, 1995, doi: 10.1074/jbc.270.44.26099.

[275] C. Jung, "Insight into protein structure and protein-ligand recognition by Fourier transform infrared spectroscopy," *Journal of Molecular Recognition*, vol. 13, no. 6, pp. 325–351, 2000, doi: 10.1002/1099-1352(200011/12)13:6<325::AID-JMR507>3.0.CO;2-C.

[276] G. T. Meng and C. Y. Ma, "Fourier-transform infrared spectroscopic study of globulin from Phaseolus angularis (red bean)," *International Journal of Biological Macromolecules*, vol. 29, pp. 287–294, 2001, doi: 10.1016/S0141-8130(01)00178-7.

[277] V. Serrano, W. Liu, and S. Franzen, "An Infrared Spectroscopic Study of the Conformational Transition of Elastin-Like Peptides," *Biophysical Journal*, vol. 93, no. 7, pp. 2429–2435, 2007, doi: 10.1529/biophysj.106.100594.

[278] J. Kong and S. Yu, "Fourier transform infrared spectroscopic analysis of protein secondary structures," *Acta Biochimica et Biophysica Sinica*, vol. 39, no. 8, pp. 549–559, 2007, doi: 10.1111/j.1745-7270.2007.00320.x.

[279] T. Lefèvre and M. Subirade, "Molecular differences in the formation and structure of fine-stranded and particulate β-lactoglobulin gels," *Biopolymers*, vol. 54, no. 7, pp. 578–586, 2000, doi: https://doi.org/10.1002/1097-0282(200012)54:7<578::AID-BIP100>3.0.CO;2-2.

[280] G. M. Kavanagh, A. H. Clark, and S. B. Ross-Murphy, “Heat-induced gelation of globular proteins: Part 3. Molecular studies on low pH β-lactoglobulin gels,” *International Journal of Biolo*, vol. 28, no. 1, pp. 41–50, 2000, doi: 10.1016/S0141-8130(00)00144-6.

[281] B. Shivu, S. Seshadri, J. Li, K. A. Oberg, V. N. Uversky, and A. L. Fink, “Distinct β-sheet structure in protein aggregates determined by ATR-FTIR spectroscopy,” *Biochemistry*, vol. 52, no. 31, pp. 5176–5183, 2013, doi: 10.1021/bi400625v.

[282] B. R. Singh, D. B. DeOliveira, F.-N. Fu, and M. P. Fuller, “Fourier transform infrared analysis of amide III bands of proteins for the secondary structure estimation,” *Biomolecular Spectroscopy III*, vol. 1890, pp. 47–55, 1993, doi: 10.1117/12.145242.

[283] M. Jackson, L. P. ing Choo, P. H. Watson, W. C. Halliday, and H. H. Mantsch, “Beware of connective tissue proteins: Assignment and implications of collagen absorptions in infrared spectra of human tissues,” *BBA - Molecular Basis of Disease*, vol. 1270, no. 1, pp. 1–6, 1995, doi: 10.1016/0925-4439(94)00056-V.

[284] S. Ikeda and F. E. Allen, “Measurement of Gel Rheology: Dynamic Tests,” *Current Protocols in Food Analytical Chemistry*, vol. 7, no. 1, p. H3.2.1-9, 2003.

[285] G. Kavanaugh and S. Ross-Murphy, “Rheological Characterisation Polymer Gels,” *Prog. Polym. Sci.*, vol. 23, pp. 533–562, 1998.

[286] L. D. Muiznieks, S. A. Jensen, and A. S. Weiss, “Structural changes and facilitated association of tropoelastin,” *Archives of Biochemistry and Biophysics*, vol. 410, no. 2, pp. 317–323, 2003, doi: 10.1016/S0003-9861(02)00719-1.

[287] A. M. Tamburro, V. Guantieri, and D. Daga Gordini, “Synthesis and structural studies of a pentapeptide sequence of elastin. Poly (val-gly-gly-leu-gly),” *Journal of Biomolecular Structure and Dynamics*, vol. 10, no. 3, pp. 441–454, 1992, doi: 10.1080/07391102.1992.10508661.

[288] R. J. Kerekes, “Rhology of fibre suspensions in papermaking: An overview of recent research,” *Nordic Pulp and Paper Research Journal*, vol. 21, no. 5, pp. 100–114, 2006, doi: https://doi.org/10.3183/npprj-2006-21-05-p598-612.

[289] A. Sugawara-Narutaki *et al.*, “Rheology of dispersions of high-aspect-ratio nanofibers assembled from elastin-like double-hydrophobic polypeptides,” *International Journal of Molecular Sciences*, vol. 20, no. 24, 2019, doi: 10.3390/ijms20246262.

[290] R. J. Kerekes and C. J. Schell, “Characterization of fibre flocculation regimes by a crowding factor,” *Journal of Pulp and Paper Science*, vol. 18, no. 1, pp. 32–38, 1992.

[291] P. R. Sharma *et al.*, "High Aspect Ratio Carboxycellulose Nanofibers Prepared by Nitro-Oxidation Method and Their Nanopaper Properties," *ACS Applied Nano Materials*, vol. 1, no. 8, pp. 3969–3980, 2018, doi: 10.1021/acsanm.8b00744.

[292] P. M. L. Janssen and M. Periasamy, "Determinants of Frequency Dependent Contraction and Relaxation of Mammalian Myocardium," *J Mol Cell Cardiol.*, vol. 43, no. 5, pp. 523–531, 2007.

[293] H. Betre, L. A. Setton, D. E. Meyer, and A. Chilkoti, "Characterization of a genetically engineered elastin-like polypeptide for cartilaginous tissue repair," *Biomacromolecules*, vol. 3, no. 5, pp. 910–916, 2002, doi: 10.1021/bm0255037.

[294] D. Xu, D. Asai, A. Chilkoti, and S. L. Craig, "Rheological properties of cysteine-containing elastin-like polypeptide solutions and hydrogels," *Biomacromolecules*, vol. 13, no. 8, pp. 2315–2321, 2012, doi: 10.1021/bm300760s.

[295] K. Nagapudi *et al.*, "Viscoelastic and mechanical behavior of recombinant protein elastomers," *Biomaterials*, vol. 26, no. 23, pp. 4695–4706, 2005, doi: 10.1016/j.biomaterials.2004.11.027.

[296] J. T. Cirulis, F. W. Keeley, and D. F. James, "Viscoelastic properties and gelation of an elastin-like polypeptide," *Journal of Rheology*, vol. 53, no. 5, pp. 1215–1228, 2009, doi: 10.1122/1.3177005.

[297] Y. Zhao, H. Su, L. Fang, and T. Tan, "Superabsorbent hydrogels from poly(aspartic acid) with salt-, temperature- and pH-responsiveness properties," *Polymer*, vol. 46, no. 14, pp. 5368–5376, 2005, doi: 10.1016/j.polymer.2005.04.015.

[298] G. R. Mahdavinia, A. Pourjavadi, H. Hosseinzadeh, and M. J. Zohuriaan, "Modified chitosan 4. Superabsorbent hydrogels from poly(acrylic acid-co-acrylamide) grafted chitosan with salt- and pH-responsiveness properties," *European Polymer Journal*, vol. 40, no. 7, pp. 1399–1407, 2004, doi: 10.1016/j.eurpolymj.2004.01.039.

[299] H. Sage, "Structure-function relationships in the evolution of elastin," *Journal of Investigative Dermatology*, vol. 79, pp. 146–153, 1982, doi: 10.1038/jid.1982.27.

[300] S. Dogu, M. Kilic, and O. Okay, "Collapse of acrylamide-based polyampholyte hydrogels in water," *Journal of Applied Polymer Science*, vol. 113, no. 3, pp. 1375–1382, 2009, doi: 10.1002/app.30081.

[301] E. Su and O. Okay, "Polyampholyte hydrogels formed via electrostatic and hydrophobic interactions," *European Polymer Journal*, vol. 88, pp. 191–204, 2017, doi: 10.1016/j.eurpolymj.2017.01.029.

[302] F. G. Donnan, “The theory of membrane equilibria,” *Chemical Reviews*, vol. 1, no. 1, pp. 73–90, 1924, doi: 10.1021/cr60001a003.

[303] M. Quesada-Pérez, J. A. Maroto-Centeno, J. Forcada, and R. Hidalgo-Alvarez, “Gel swelling theories: the classical formalism and recent approaches,” *Soft Matter*, vol. 7, no. 22, pp. 10536–10547, 2011, doi: 10.1039/c1sm06031g.

[304] F. Horkay and P. Basser, “Ionic and pH Effects on the Osmotic Properties and Structure of Polyelectrolyte Gels,” *Journal of Polymer Science: Part B: Polymer Physics*, vol. 46, pp. 2803–2810, 2008.

[305] P. J. Flory, “Phase Equilibria in Polymer Systems,” in *Principles of Polymer Chemistry*, Cornell University Press, Ithaca, NY, 1953, pp. 576–584.

[306] J. D. Willott, B. A. Humphreys, T. J. Murdoch, S. Edmondson, G. B. Webber, and E. J. Wanless, “Hydrophobic effects within the dynamic pH-response of polybasic tertiary amine methacrylate brushes,” *Physical Chemistry Chemical Physics*, vol. 17, no. 5, pp. 3880–3890, 2015, doi: 10.1039/c4cp05292g.

[307] S. Morozova and M. Muthukumar, “Electrostatic effects in collagen fibril formation,” *Journal of Chemical Physics*, vol. 149, no. 16, 2018, doi: 10.1063/1.5036526.

[308] R. Schroeder, A. A. Rudov, L. A. Lyon, W. Richtering, A. Pich, and I. I. Potemkin, “Electrostatic Interactions and Osmotic Pressure of Counterions Control the pH-Dependent Swelling and Collapse of Polyampholyte Microgels with Random Distribution of Ionizable Groups,” *Macromolecules*, vol. 48, no. 16, pp. 5914–5927, 2015, doi: 10.1021/acs.macromol.5b01305.

[309] K. Urayama, T. Kawamura, and S. Kohjiya, “Elastic modulus and equilibrium swelling of networks crosslinked by end-linking oligodimethylsiloxane at solution state,” *Journal of Chemical Physics*, vol. 105, no. 11, pp. 4833–4840, 1996, doi: 10.1063/1.472320.

[310] F. Horkay and D. C. Lin, “Mapping the local osmotic modulus of polymer gels,” *Langmuir*, vol. 25, no. 15, pp. 8735–8741, 2009, doi: 10.1021/la900103j.

[311] H. Li, X. D. Chen, and R. Mercadé-Prieto, “Elastic modulus and equilibrium swelling of stranded and particulate protein hydrogels at acid pH,” *Food Hydrocolloids*, vol. 71, pp. 168–175, 2017, doi: 10.1016/j.foodhyd.2017.05.008.

[312] K. Joanna, P. Michał, and P. Anna, “Osmotic Properties of Polysaccharides Solutions,” in *Solubility of Polysaccharides*, 2017, pp. 23–43.

[313] A. H. Clark, G. M. Kavanagh, and S. B. Ross-Murphy, “Globular protein gelation- Theory and experiment,” *Food Hydrocolloids*, vol. 15, no. 4–6, pp. 383–400, 2001, doi: 10.1016/S0268-005X(01)00042-X.

[314] A. D. Drozdov and J. deClaville Christiansen, “The effects of pH and ionic strength on equilibrium swelling of polyampholyte gels,” *International Journal of Solids and Structures*, vol. 110–111, pp. 192–208, 2017, doi: 10.1016/j.ijsolstr.2017.01.028.

[315] G. Nisato, J. P. Munch, and S. J. Candau, “Swelling, structure, and elasticity of polyampholyte hydrogels,” *Langmuir*, vol. 15, no. 12, pp. 4236–4244, 1999, doi: 10.1021/la981027n.

[316] M. Betz, J. Hörmansperger, T. Fuchs, and U. Kulozik, “Swelling behaviour, charge and mesh size of thermal protein hydrogels as influenced by pH during gelation,” *Soft Matter*, vol. 8, no. 8, pp. 2477–2485, 2012, doi: 10.1039/c2sm06976h.

[317] A. Shalviri, Q. Liu, M. J. Abdekhodaie, and X. Y. Wu, “Novel modified starch-xanthan gum hydrogels for controlled drug delivery: Synthesis and characterization,” *Carbohydrate Polymers*, vol. 79, no. 4, pp. 898–907, 2010, doi: 10.1016/j.carbpol.2009.10.016.

[318] C. Yan and D. J. Pochan, “Rheological properties of peptide-based hydrogels for biomedical and other applications,” *Chemical Society Reviews*, vol. 39, no. 9, pp. 3528–3540, 2010, doi: 10.1039/b919449p.

[319] M. Langton and A. M. Hermansson, “Fine-stranded and particulate gels of β-lactoglobulin and whey protein at varying pH,” *Topics in Catalysis*, vol. 5, no. 6, pp. 523–539, 1992, doi: 10.1016/S0268-005X(09)80122-7.

[320] J. F. Zayas and J. F. Zayas, “Gelling Properties of Proteins,” in *Functionality of Proteins in Food*, Berlin: Springer Berlin Heidelberg, 1997, pp. 310–366.

[321] E. A. Foegeding, “Food biophysics of protein gels: A challenge of nano and macroscopic proportions,” *Food Biophysics*, vol. 1, no. 1, pp. 41–50, 2006, doi: 10.1007/s11483-005-9003-y.

[322] A. F. Allain, P. Paquin, and M. Subirade, “Relationships between conformation of β-lactoglobulin in solution and gel states as revealed by attenuated total reflection Fourier transform infrared spectroscopy,” *International Journal of Biological Macromolecules*, vol. 26, no. 1, pp. 337–344, 1999, doi: 10.1016/S0141-8130(99)00104-X.

[323] N. H. Grant and K. C. Robbinst, “An Elastin Gel,” *Nature*, vol. 185, p. 320, 1960.

[324] X. Yu *et al.*, “Controlling the structural organization of regenerated bone by tailoring tissue engineering scaffold architecture,” *Journal of Materials Chemistry*, vol. 22, no. 19, pp. 9721–9730, 2012, doi: 10.1039/c2jm30332a.

[325] J. A. Burdick, C. Chung, X. Jia, M. A. Randolph, and R. Langer, “Controlled degradation and mechanical behavior of photopolymerized hyaluronic acid

networks," *Biomacromolecules*, vol. 6, no. 1, pp. 386–391, 2005, doi: 10.1021/bm049508a.

[326] J. Mudassir and N. M. Ranjha, "Dynamic and equilibrium swelling studies: Crosslinked pH sensitive methyl methacrylate-co-itaconic acid (MMA-co-IA) hydrogels," *Journal of Polymer Research*, vol. 15, no. 3, pp. 195–203, 2008, doi: 10.1007/s10965-007-9159-x.

[327] S. M. H. Bukhari, S. Khan, M. Rehanullah, and N. M. Ranjha, "Synthesis and Characterization of Chemically Cross-Linked Acrylic Acid/Gelatin Hydrogels: Effect of pH and Composition on Swelling and Drug Release," *International Journal of Polymer Science*, vol. 2015, 2015, doi: 10.1155/2015/187961.

[328] J. A. Wieland, T. L. Houchin-Ray, and L. D. Shea, "Non-viral vector delivery from PEG-hyaluronic acid hydrogels," *Journal of Controlled Release*, vol. 120, no. 3, pp. 233–241, 2007, doi: 10.1016/j.jconrel.2007.04.015.

[329] M. N. Collins and C. Birkinshaw, "Investigation of the Swelling Behavior of Crosslinked Hyaluronic Acid Films and Hydrogels Produced Using Homogeneous Reactions," *Journal of Applied Polymer Science*, vol. 109, pp. 923–931, 2008, doi: 10.1002/app.

[330] C. F. Chi, Z. H. Cao, B. Wang, F. Y. Hu, Z. R. Li, and B. Zhang, "Antioxidant and functional properties of collagen hydrolysates from Spanish mackerel skin as influenced by average molecular weight," *Molecules*, vol. 19, no. 8, pp. 11211–11230, 2014, doi: 10.3390/molecules190811211.

[331] M. Shah, P. Y. Hsueh, G. Sun, H. Y. Chang, S. M. Janib, and J. A. MacKay, "Biodegradation of elastin-like polypeptide nanoparticles," *Protein Science*, vol. 21, no. 6, pp. 743–750, 2012, doi: 10.1002/pro.2063.

[332] K. H. Gustavson, *The chemistry and reactivity of collagen*. New York: Academic Press, 1956.

[333] C. Dong and Y. Lv, "Application of collagen scaffold in tissue engineering: Recent advances and new perspectives," *Polymers*, vol. 8, no. 2, pp. 1–20, 2016, doi: 10.3390/polym8020042.

[334] J. H. BOWES and R. H. KENTEN, "The swelling of collagen in alkaline solutions; swelling in solutions of univalent bases.," *The Biochemical Journal*, vol. 46, no. 5, pp. 524–529, 1950, doi: 10.1042/bj0460524.

[335] J. H. Highberger, "The Isoelectric Point of Collagen," *Journal of the American Chemical Society*, vol. 61, no. 9, pp. 2302–2303, 1939, doi: 10.1021/ja01878a010.

[336] W. Friess and M. Schlapp, "Effects of processing conditions on the rheological behavior of collagen dispersions," *European Journal of Pharmaceutics and Biopharmaceutics*, vol. 51, no. 3, pp. 259–265, 2001, doi: 10.1016/S0939-6411(01)00136-9.

[337] M. Tamaddon, R. S. Walton, D. D. Brand, and J. T. Czernuszka, "Characterisation of freeze-dried type II collagen and chondroitin sulfate scaffolds," *Journal of Materials Science: Materials in Medicine*, vol. 24, no. 5, pp. 1153–1165, 2013, doi: 10.1007/s10856-013-4882-9.

[338] G. Lai, Y. Li, and G. Li, "Effect of concentration and temperature on the rheological behavior of collagen solution," *International Journal of Biological Macromolecules*, vol. 42, no. 3, pp. 285–291, 2008, doi: 10.1016/j.ijbiomac.2007.12.010.

[339] F. van den Berg, "Extracellular matrix," in *Fascia: The Tensional Network of the Human Body*, R. Schleip, T. W. Findley, C. Leon, and P. A. Huijing, Eds. Churchill Livingstone: Elsevier Ltd., 2012, pp. 165–170.

[340] W. Grut, J. Edwards, and E. J. Evans, "Scanning electron microscopy of freeze-dried aortic elastin," *Journal of Microscopy*, vol. 110, no. 3, pp. 271–275, 1977, doi: 10.1111/j.1365-2818.1977.tb00037.x.

[341] Q. L. Loh and C. Choong, "Three-dimensional scaffolds for tissue engineering applications: role of porosity and pore size.," *Tissue engineering. Part B, Reviews*, vol. 19, no. 6, pp. 485–502, 2013, doi: 10.1089/ten.TEB.2012.0437.

[342] K. M. Pawelec, A. Husmann, S. M. Best, and R. E. Cameron, "Ice-templated structures for biomedical tissue repair: From physics to final scaffolds," *Applied Physics Reviews*, vol. 1, no. 2, 2014, doi: 10.1063/1.4871083.

[343] M. G. Haugh, C. M. Murphy, and F. J. O. Brien, "Novel Freeze-Drying Methods to Produce a Range of Collagen–Glycosaminoglycan Scaffolds with Tailored Mean Pore Sizes," *Tissue Engineering: Part C*, vol. 16, no. 5, pp. 887–893, 2010.

[344] F. J. O'Brien, B. A. Harley, I. v. Yannas, and L. J. Gibson, "The effect of pore size on cell adhesion in collagen-GAG scaffolds," *Biomaterials*, vol. 26, no. 4, pp. 433–441, 2005, doi: 10.1016/j.biomaterials.2004.02.052.

[345] C. M. Murphy, M. G. Haugh, and F. J. O'Brien, "The effect of mean pore size on cell attachment, proliferation and migration in collagen-glycosaminoglycan scaffolds for bone tissue engineering," *Biomaterials*, vol. 31, no. 3, pp. 461–466, 2010, doi: 10.1016/j.biomaterials.2009.09.063.

[346] D. A. Wahl, E. Sachlos, C. Liu, and J. T. Czernuszka, "Controlling the processing of collagen-hydroxyapatite scaffolds for bone tissue engineering," *Journal of Materials Science: Materials in Medicine*, vol. 18, no. 2, pp. 201–209, 2007, doi: 10.1007/s10856-006-0682-9.

[347] C. Körber, G. Rau, M. D. Cosman, and E. G. Cravalho, "Interaction of particles and a moving ice-liquid interface," *Journal of Crystal Growth*, vol. 72, no. 3, pp. 649–662, 1985, doi: 10.1016/0022-0248(85)90217-9.

[348] S. Deville, “Freeze-casting of porous ceramics: A review of current achievements and issues,” *Advanced Engineering Materials*, vol. 10, no. 3, pp. 155–169, 2008, doi: 10.1002/adem.200700270.

[349] T. Waschkies, R. Oberacker, and M. J. Hoffmann, “Investigation of structure formation during freeze-casting from very slow to very fast solidification velocities,” *Acta Materialia*, vol. 59, no. 13, pp. 5135–5145, 2011, doi: 10.1016/j.actamat.2011.04.046.

[350] S. Deville, E. Saiz, and A. P. Tomsia, “Ice-templated porous alumina structures,” *Acta Materialia*, vol. 55, no. 6, pp. 1965–1974, 2007, doi: 10.1016/j.actamat.2006.11.003.

[351] W. D. Callister and D. G. Rethwisch, *Materials Science and Engineering*, Eighth. John Wiley & Sons, Inc, 2010.

[352] W. L. Li, K. Lu, and J. Y. Walz, “Freeze casting of porous materials: Review of critical factors in microstructure evolution,” *International Materials Reviews*, vol. 57, no. 1, pp. 37–60, 2012, doi: 10.1179/1743280411Y.0000000011.

[353] X. Xie, Y. Zhou, H. Bi, K. Yin, S. Wan, and L. Sun, “Large-range control of the microstructures and properties of three-dimensional porous graphene,” *Scientific Reports*, vol. 3, pp. 1–6, 2013, doi: 10.1038/srep02117.

[354] L. Qian and H. Zhang, “Controlled freezing and freeze drying: A versatile route for porous and micro-/nano-structured materials,” *Journal of Chemical Technology and Biotechnology*, vol. 86, no. 2, pp. 172–184, 2011, doi: 10.1002/jctb.2495.

[355] Y. Zhang, K. Zhou, Y. Bao, and D. Zhang, “Effects of rheological properties on ice-templated porous hydroxyapatite ceramics,” *Materials Science and Engineering C*, vol. 33, no. 1, pp. 340–346, 2013, doi: 10.1016/j.msec.2012.08.048.

[356] D. Ghosh, N. Dhavale, M. Banda, and H. Kang, “A comparison of microstructure and uniaxial compressive response of ice-templated alumina scaffolds fabricated from two different particle sizes,” *Ceramics International*, vol. 42, no. 14, pp. 16138–16147, 2016, doi: 10.1016/j.ceramint.2016.07.131.

[357] R. Young and P. Lovell, *Introduction to Polymers*, Third. New York: CRC Press, Taylor & Francis Group, 2011.

[358] C. Gao, X. Hu, Y. Hong, J. Guan, and J. Shen, “Photografting of poly(hydroxylethyl acrylate) onto porous polyurethane scaffolds to improve their endothelial cell compatibility,” *J Biomater Sci Polym Ed*, vol. 14, no. 9, pp. 937–50, 2003.

[359] J. M. Gosline and C. J. French, “Dynamic mechanical properties of elastin,” *Biopolymers*, vol. 18, no. 8, pp. 2091–2103, 1979, doi: 10.1002/bip.1979.360180818.

[360] M. Rizwan *et al.*, “pH sensitive hydrogels in drug delivery: Brief history, properties, swelling, and release mechanism, material selection and applications,” *Polymers*, vol. 9, no. 4, 2017, doi: 10.3390/polym9040137.

[361] A. S. Hoffman, “Hydrogels for biomedical applications,” *Advanced Drug Delivery Reviews*, vol. 64, no. SUPPL., pp. 18–23, 2012, doi: 10.1016/j.addr.2012.09.010.

[362] S. Gallagher, L. Florea, K. J. Fraser, and D. Diamond, “Swelling and shrinking properties of thermo-responsive polymeric ionic liquid hydrogels with embedded linear pNIPAAM,” *International Journal of Molecular Sciences*, vol. 15, no. 4, pp. 5337–5349, 2014, doi: 10.3390/ijms15045337.

[363] M. R. Guilherme, R. da Silva, A. F. Rubira, G. Geuskens, and E. C. Muniz, “Thermo-sensitive hydrogels membranes from PAAm networks and entangled PNIPAAm: Effect of temperature, cross-linking and PNIPAAm contents on the water uptake and permeability,” *Reactive and Functional Polymers*, vol. 61, no. 2, pp. 233–243, 2004, doi: 10.1016/j.reactfunctpolym.2004.06.004.

[364] M. A. Ward and T. K. Georgiou, “Thermoresponsive polymers for biomedical applications,” *Polymers*, vol. 3, no. 3, pp. 1215–1242, 2011, doi: 10.3390/polym3031215.

[365] L. Klouda and A. Mikos, “Thermoresponsive hydrogels in biomedical applications - a review,” *Eur J Pharm Biopharm*, vol. 68, no. 1, pp. 34–45, 2008, doi: 10.1016/j.ejpb.2007.02.025.Thermoresponsive.

[366] N. T. Southall, K. A. Dill, and A. D. J. Haymet, “A view of the hydrophobic effect,” *Journal of Physical Chemistry B*, vol. 106, no. 3, pp. 521–533, 2002, doi: 10.1021/jp015514e.

[367] B. Widom, P. Bhimalapuram, and K. Koga, “The hydrophobic effect,” *Physical Chemistry Chemical Physics*, vol. 5, no. 15, pp. 3085–3093, 2003, doi: 10.1039/b304038k.

[368] D. W. Urry, “Elastic biomolecular machines,” *Scientific American*, vol. 272, no. 1, pp. 64–69, 1995, doi: 10.1038/scientificamerican0195-64.

[369] D. W. Urry and T. M. Parker, “Mechanics of elastin: molecular mechanism of biological elasticity and its relationship to contraction,” *Mechanics of Elastic Biomolecules*, vol. 1, pp. 543–559, 2003, doi: 10.1007/978-94-010-0147-2_14.

[370] S. Perticaroli, G. Ehlers, N. Jalarvo, J. Katsaras, and J. D. Nickels, “Elasticity and Inverse Temperature Transition in Elastin,” *Journal of Physical Chemistry Letters*, vol. 6, no. 20, pp. 4018–4025, 2015, doi: 10.1021/acs.jpclett.5b01890.

[371] Y. Cho, Y. Zhang, T. Christensen, L. B. Sagle, A. Chilkoti, and P. S. Cremer, "Effects of hofmeister anions on the phase transition temperature of elastin-like polypeptides," *Journal of Physical Chemistry B*, vol. 112, no. 44, pp. 13765–13771, 2008, doi: 10.1021/jp8062977.

[372] A. Pourjavadi and M. Kurdtabar, "Collagen-based highly porous hydrogel without any porogen: Synthesis and characteristics," *European Polymer Journal*, vol. 43, no. 3, pp. 877–889, 2007, doi: 10.1016/j.eurpolymj.2006.12.020.

[373] A. Pourjavadi, M. Kurdtabar, and H. Ghasemzadeh, "Salt- and pH-resisting collagen-based highly porous hydrogel," *Polymer Journal*, vol. 40, no. 2, pp. 94–103, 2008, doi: 10.1295/polymj.PJ2007042.

[374] Q. Lu, K. Ganesan, D. T. Simionescu, and N. R. Vyavahare, "Novel porous aortic elastin and collagen scaffolds for tissue engineering," *Biomaterials*, vol. 25, no. 22, pp. 5227–5237, 2004, doi: 10.1016/j.biomaterials.2003.12.019.

[375] H. Ma, A. R. Killaars, F. W. DelRio, C. Yang, and K. S. Anseth, "Myofibroblastic activation of valvular interstitial cells is modulated by spatial variations in matrix elasticity and its organization," *Biomaterials*, vol. 131, pp. 131–144, 2017, doi: 10.1016/j.biomaterials.2017.03.040.

[376] N. Latif *et al.*, "Modulation of human valve interstitial cell phenotype and function using a fibroblast growth factor 2 formulation," *PLoS ONE*, vol. 10, no. 6, pp. 1–19, 2015, doi: 10.1371/journal.pone.0127844.

[377] D. T. Simionescu, J. Chen, M. Jaeggli, B. Wang, and J. Liao, "Form Follows Function: Advances in Trilayered Structure Replication for Aortic Heart Valve Tissue Engineering," *Journal of healthcare engineering*, vol. 3, no. 2, pp. 179–202, 2012, doi: 10.1260/2040-2295.3.2.179.

[378] L. J. Gibson and M. F. Ashby, *The mechanics of foams: basic results*. 2014.

[379] L. J. Gibson, "Biomechanics of cellular solids," *Journal of Biomechanics*, vol. 38, no. 3, pp. 377–399, 2005, doi: 10.1016/j.jbiomech.2004.09.027.

[380] P. M. Hunger, A. E. Donius, and U. G. K. Wegst, "Structure-property-processing correlations in freeze-cast composite scaffolds," *Acta Biomaterialia*, vol. 9, no. 5, pp. 6338–6348, 2013, doi: 10.1016/j.actbio.2013.01.012.

[381] Z. Lin, W. Wu, J. Wang, and X. Jin, "Swelling behaviors, tensile properties and thermodynamic interactions in APS/HEMA copolymeric hydrogels," *Frontiers of Materials Science in China*, vol. 1, no. 4, pp. 427–431, 2007, doi: 10.1007/s11706-007-0078-x.

[382] C. M. Pollock and R. E. Shadwick, "Relationship between body mass and biomechanical properties of limb tendons in adult mammals," *American Journal of Physiology - Regulatory Integrative and Comparative Physiology*, vol. 266, no. 3 35-3, 1994, doi: 10.1152/ajpregu.1994.266.3.r1016.

[383] J. Mercuri, C. Addington, R. Pascal, S. Gill, and D. Simionescu, “Development and initial characterization of a chemically stabilized elastin-glycosaminoglycan-collagen composite shape-memory hydrogel for nucleus pulposus regeneration,” *Journal of Biomedical Materials Research - Part A*, vol. 102, no. 12, pp. 4380–4393, 2014, doi: 10.1002/jbm.a.35104.

[384] B. J. Goodno and J. M. Gere, *Mechanics of Materials*, Nineth. Cengage Learning, 2017.

[385] W. D. Merryman, H. Y. Shadow Huang, F. J. Schoen, and M. S. Sacks, “The effects of cellular contraction on aortic valve leaflet flexural stiffness,” *Journal of Biomechanics*, vol. 39, no. 1, pp. 88–96, 2006, doi: 10.1016/j.jbiomech.2004.11.008.

[386] X. Lian *et al.*, “Robust cardiomyocyte differentiation from human pluripotent stem cells via temporal modulation of canonical Wnt signaling,” *Proceedings of the National Academy of Sciences of the United States of America*, vol. 109, no. 27, 2012, doi: 10.1073/pnas.1200250109.

[387] S. Gessert and M. Kühl, “The multiple phases and faces of Wnt signaling during cardiac differentiation and development,” *Circulation Research*, vol. 107, no. 2, pp. 186–199, 2010, doi: 10.1161/CIRCRESAHA.110.221531.

[388] C. A. Lopez *et al.*, “Physiological and pharmacological stimulation for in vitro maturation of substrate metabolism in human induced pluripotent stem cell-derived cardiomyocytes,” *Scientific Reports*, vol. 11, no. 1, pp. 1–13, 2021, doi: 10.1038/s41598-021-87186-y.

[389] X. Lian *et al.*, “Directed cardiomyocyte differentiation from human pluripotent stem cells by modulating Wnt/β-catenin signaling under fully defined conditions,” *Nature Protocols*, vol. 8, no. 1, pp. 162–175, 2013, doi: 10.1038/nprot.2012.150.

[390] X. Lian, J. Zhang, K. Zhu, T. J. Kamp, and S. P. Palecek, “Insulin inhibits cardiac mesoderm, not mesendoderm, formation during cardiac differentiation of human pluripotent stem cells and modulation of canonical Wnt signaling can rescue this inhibition,” *Stem Cells*, vol. 31, no. 3, pp. 447–457, 2013, doi: 10.3174/ajnr.A1256.Functional.

[391] K. J. Livak and T. D. Schmittgen, “Analysis of Relative Gene Expression Data Using Real- Time Quantitative PCR and the 2-ΔΔCT Method,” *Methods*, vol. 25, pp. 402–408, 2001, doi: 10.1006/meth.2001.1262.

[392] R. Tjitro *et al.*, “Modeling the function of TATA box binding protein in trascriptional changes induced by HIV-1 tat in innate immune cells and the effects of methamphetamine exposure,” *Frontiers in Immunology*, vol. 10, pp. 1–20, 2019, doi: 10.3389/fimmu.2018.03110.

[393] L. Zuo, J. Zhang, and X. Xu, “Combined Application of Bevacizumab and Mitomycin C or Bevacizumab and 5-Fluorouracil in Experimental Glaucoma Filtration Surgery,” *Journal of Ohthalmology*, pp. 1–13, 2018.

[394] N. A. M. Bax, M. H. van Marion, B. Shah, M. Goumans, C. V. C. Bouten, and D. W. J. van der Schaft, “Matrix production and remodeling capacity of cardiomyocyte progenitor cells during in vitro differentiation,” *Journal of Molecular and Cellular Cardiology*, vol. 53, pp. 497–508, 2012, doi: 10.1016/j.yjmcc.2012.07.003.

[395] J. Xie *et al.*, “Up-regulation expressions of lysyl oxidase family in Anterior Cruciate Ligament and Medial Collateral Ligament fibroblasts induced by Transforming Growth Factor-Beta 1,” *International Orthopaeducs (SICOT)*, vol. 36, pp. 207–213, 2012, doi: 10.1007/s00264-011-1261-3.

[396] N. Yoshiba *et al.*, “Correlation between Fibrillin-1 Degradation and mRNA Downregulation and Myofibroblast Differentiation in Cultured Human Dental Pulp Tissue,” *Journal of Histochemistry & Cytochemistry*, vol. 63, no. 6, pp. 438–448, 2015, doi: 10.1369/0022155415580622.

[397] Y. Yung, L. Ophir, G. M. Yerushalmi, M. Baum, A. Hourvitz, and E. Maman, “HAS2-AS1 is a novel LH/hCG target gene regulating HAS2 expression and enhancing cumulus cells migration,” *Journal of Ovarian Research*, vol. 12, no. 1, pp. 1–7, 2019, doi: 10.1186/s13048-019-0495-3.

[398] S.-M. Yuan, “α-Smooth Muscle Actin and ACTA2 Gene Expressions in Vasculopathies,” *Braz J Cardiovasc Surg*, vol. 30, no. 6, pp. 644–649, 2015, doi: 10.5935/1678-9741.20150081.

[399] W. Wang, L. Dong, B. Zhao, J. U. N. Lu, and Y. Zhao, “E - cadherin is downregulated by microenvironmental changes in pancreatic cancer and induces EMT,” *Oncology Reports*, vol. 40, pp. 1641–1649, 2018, doi: 10.3892/or.2018.6528.

[400] C. A. Lopez *et al.*, “Physiological and pharmacological stimulation for in vitro maturation of substrate metabolism in hiPS-derived cardiomyocytes,” *Submitted to Scientific Reports*, 2021.

[401] I. Levental, P. C. Georges, and P. A. Janmey, “Soft biological materials and their impact on cell function,” *Soft Matter*, vol. 3, no. 3, pp. 299–306, 2007, doi: 10.1039/b610522j.

[402] J. F. Almine *et al.*, “Elastin-based materials,” *Chemical Society Reviews*, vol. 39, no. 9, pp. 3371–3379, 2010, doi: 10.1039/b919452p.

[403] S. Ito, S. Ishimaru, and S. E. Wilson, “Effect of coacervated α-elastin on proliferation of vascular smooth muscle and endothelial cells,” *Angiology*, vol. 49, no. 4, pp. 289–297, 1998, doi: 10.1177/000331979804900407.

[404] L. Robert, “Cell-elastin interaction and signaling,” *Pathologie Biologie*, vol. 53, no. 7, pp. 399–404, 2005, doi: 10.1016/j.patbio.2004.12.020.

[405] S. Tajima, H. Wachi, Y. Uemura, and K. Okamoto, “Modulation by elastin peptide VGVAPG of cell proliferation and elastin expression in human skin fibroblasts,” *Archives of Dermatological Research*, vol. 289, no. 8, pp. 489–492, 1997, doi: 10.1007/s004030050227.

[406] T. M. Freyman, I. v. Yannas, R. Yokoo, and L. J. Gibson, “Fibroblast contraction of a collagen-GAG matrix,” *Biomaterials*, vol. 22, no. 21, pp. 2883–2891, 2001, doi: 10.1016/S0142-9612(01)00034-5.

[407] Y. Arima and H. Iwata, “Effect of wettability and surface functional groups on protein adsorption and cell adhesion using well-defined mixed self-assembled monolayers,” *Biomaterials*, vol. 28, no. 20, pp. 3074–3082, 2007, doi: 10.1016/j.biomaterials.2007.03.013.

[408] J. M. Goddard and J. H. Hotchkiss, “Polymer surface modification for the attachment of bioactive compounds,” *Progress in Polymer Science (Oxford)*, vol. 32, no. 7, pp. 698–725, 2007, doi: 10.1016/j.progpolymsci.2007.04.002.

[409] P. Parhi, A. Golas, and E. A. Vogler, *Role of proteins and water in the initial attachment of mammalian cells to biomedical surfaces: A review*, vol. 24, no. 5. 2010.

[410] A. Nicol, D. Channe Gowda, and D. W. Urry, “Cell adhesion and growth on synthetic elastomeric matrices containing ARG-GLY–ASP–SER-,” *Journal of Biomedical Materials Research*, vol. 26, pp. 393–413, 1992, doi: 10.1002/jbm.820260309.

[411] Y. C. Chiu *et al.*, “The role of pore size on vascularization and tissue remodeling in PEG hydrogels,” *Biomaterials*, vol. 32, no. 26, pp. 6045–6051, 2011, doi: 10.1016/j.biomaterials.2011.04.066.

[412] C. G. Knight, L. F. Morton, A. R. Peachey, D. S. Tuckwell, R. W. Farndale, and M. J. Barnes, “The collagen-binding a-domains of integrins α1/β1 and α2/β1 recognize the same specific amino acid sequence, GFOGER, in native (triple-helical) collagens,” *Journal of Biological Chemistry*, vol. 275, no. 1, pp. 35–40, 2000, doi: 10.1074/jbc.275.1.35.

[413] L. P. Silva, P. L. Lorenzi, P. Purwaha, V. Yong, D. H. Hawke, and J. N. Weinstein, “Measurement of DNA concentration as a normalization strategy for metabolomic data from adherent cell lines,” *Analytical Chemistry*, vol. 85, no. 20, pp. 9536–9542, 2013, doi: 10.1021/ac401559v.

[414] T. Horne *et al.*, “Dynamic Heterogeneity of the Heart Valve Interstitial Cell Population in Mitral Valve Health and Disease,” *Journal of Cardiovascular Development and Disease*, vol. 2, no. 3, pp. 214–232, 2015, doi: 10.3390/jcdd2030214.

[415] A. C. Liu, V. R. Joag, and A. I. Gotlieb, “The emerging role of valve interstitial cell phenotypes in regulating heart valve pathobiology,” *American Journal of Pathology*, vol. 171, no. 5, pp. 1407–1418, 2007, doi: 10.2353/ajpath.2007.070251.

[416] N. Latif, P. Sarathchandra, A. H. Chester, and M. H. Yacoub, “Expression of smooth muscle cell markers and co-activators in calcified aortic valves,” *European Heart Journal*, vol. 36, no. 21, pp. 1335–1345, 2015, doi: 10.1093/eurheartj/eht547.

[417] C. M. Kirschner, D. L. Alge, S. T. Gould, and K. S. Anseth, “Clickable, photodegradable hydrogels to dynamically modulate valvular interstitial cell phenotype,” *Advanced Healthcare Materials*, vol. 3, no. 5, pp. 649–657, 2014, doi: 10.1002/adhm.201300288.

[418] S. K. Karnik *et al.*, “A critical role for elastin signaling in vascular morphogenesis and disease,” *Development*, vol. 130, no. 2, pp. 411–423, 2003, doi: 10.1242/dev.00223.

[419] S. S. M. Rensen, P. A. F. M. Doevendans, and G. J. J. M. van Eys, “Regulation and characteristics of vascular smooth muscle cell phenotypic diversity,” *Netherlands Heart Journal*, vol. 15, no. 3, pp. 100–108, 2007.

[420] M. Yamamoto, K. Yamamoto, and T. Noumura, “Type I collagen promotes modulation of cultured rabbit arterial smooth muscle cells from a contractile to a synthetic phenotype,” *Experimental Cell Research*, vol. 204, no. 1. pp. 121–129, 1993, doi: 10.1006/excr.1993.1016.

[421] R. B. Vernon, T. F. Lane, J. C. Angello, and H. Sage, “Adhesion, shape, proliferation, and gene expression of mouse Leydig cells are influenced by extracellular matrix in vitro,” *Biol Reprod*, vol. 44, no. 1, pp. 157–170, 1991.

[422] A. Kapelouzou, L. Tsourelis, L. Kaklamanis, D. Degiannis, N. Kogerakis, and D. v. Cokkinos, “Serum and tissue biomarkers in aortic stenosis,” *Global Cardiology Science and Practice*, vol. 2015, no. 4, p. 49, 2015, doi: 10.5339/gcsp.2015.49.

[423] E. Dattola *et al.*, “Development of 3D PVA scaffolds for cardiac tissue engineering and cell screening applications,” *RSC Advances*, vol. 9, no. 8, pp. 4246–4257, 2019, doi: 10.1039/C8RA08187E.

[424] JR. ROBERT J. PELHAM and Y.-L. WANG, “Cell locomotion and focal adhesions are regulated by substrate flexibility,” *Proceedings of the National Academy of Sciences*, vol. 94, pp. 13661–13665, 1997.

[425] D. E. Discher, P. Janmey, and Y. L. Wang, “Tissue cells feel and respond to the stiffness of their substrate,” *Science*, vol. 310, no. 5751, pp. 1139–1143, 2005, doi: 10.1126/science.1116995.

[426] N. Masoumi *et al.*, “Tri-layered elastomeric scaffolds for engineering heart valve leaflets,” *Biomaterials*, vol. 35, no. 27, pp. 7774–7785, 2014, doi: 10.1016/j.biomaterials.2014.04.039.

[427] T. C. Flanagan, B. Wilkins, A. Black, S. Jockenhoevel, T. J. Smith, and A. S. Pandit, “A collagen-glycosaminoglycan co-culture model for heart valve tissue engineering applications,” *Biomaterials*, vol. 27, no. 10, pp. 2233–2246, 2006, doi: 10.1016/j.biomaterials.2005.10.031.

[428] N. Masoumi, K. L. Johnson, M. C. Howell, and G. C. Engelmayr, “Valvular interstitial cell seeded poly(glycerol sebacate) scaffolds: Toward a biomimetic in vitro model for heart valve tissue engineering,” *Acta Biomaterialia*, vol. 9, no. 4, pp. 5974–5988, 2013, doi: 10.1016/j.actbio.2013.01.001.

[429] B. Sivaraman, C. A. Bashur, and A. Ramamurthi, “Advances in biomimetic regeneration of elastic matrix structures,” *Drug Delivery and Translational Research*, vol. 2, no. 5, pp. 323–350, 2012, doi: 10.1007/s13346-012-0070-6.

[430] H. Zhang, W. Hu, and F. Ramirez, “Developmental expression of fibrillin genes suggests heterogeneity of extracellular microfibrils,” *Journal of Cell Biology*, vol. 129, no. 4, pp. 1165–1176, 1995, doi: 10.1083/jcb.129.4.1165.

[431] P. M. Crapo and Y. Wang, “Physiologic compliance in engineered small-diameter arterial constructs based on an elastomeric substrate,” *Biomaterials*, vol. 31, no. 7, pp. 1626–1635, 2010, doi: 10.1016/j.biomaterials.2009.11.035.

[432] J. H. Eoh *et al.*, “Enhanced elastin synthesis and maturation in human vascular smooth muscle tissue derived from induced-pluripotent stem cells,” *Acta Biomaterialia*, vol. 52, pp. 49–59, 2017, doi: 10.1016/j.actbio.2017.01.083.

[433] M. Wanjare, N. Agarwal, and S. Gerecht, “Biomechanical strain induces elastin and collagen production in human pluripotent stem cell-derived vascular smooth muscle cells,” *American Journal of Physiology - Cell Physiology*, vol. 309, no. 4, pp. C271–C281, 2015, doi: 10.1152/ajpcell.00366.2014.

[434] A. Gonz, F. R. Almeida-gonz, F. J. O. Brien, A. S. Weiss, and C. M. Brougham, “A step closer to elastogenesis on demand ; Inducing mature elastic fibre deposition in a natural biomaterial scaffold,” *Materials Science & Engineering C*, vol. 120, pp. 1–12, 2021, doi: 10.1016/j.msec.2020.111788.

[435] M. Eslami, G. Javadi, N. Agdami, and M. A. Shokrgozar, “Expression of COLLAGEN 1 and ELASTIN genes in mitral valvular interstitial cells within microfiber reinforced hydrogel,” *Cell Journal*, vol. 17, no. 3, pp. 478–488, 2015, doi: 10.22074/cellj.2015.22.

[436] J. Rnjak-Kovacina, W. F. Daamen, D. Orbanić, J. C. Rodríguez-Cabello, and A. S. Weiss, “Elastin Biopolymers,” *Comprehensive Biomaterials II*, vol. 2, pp. 412–437, 2017, doi: 10.1016/B978-0-12-803581-8.10187-0.

[437] A. M. J. Coenen, K. v. Bernaerts, J. A. W. Harings, S. Jockenhoevel, and S. Ghazanfari, “Elastic materials for tissue engineering applications: Natural, synthetic, and hybrid polymers,” *Acta Biomaterialia*, vol. 79, pp. 60–82, 2018, doi: 10.1016/j.actbio.2018.08.027.

[438] Y. Lei, S. Masjedi, and Z. Ferdous, “A study of extracellular matrix remodeling in aortic heart valves using a novel biaxial stretch bioreactor,” *Journal of the Mechanical Behavior of Biomedical Materials*, vol. 75, no. March, pp. 351–358, 2017, doi: 10.1016/j.jmbbm.2017.07.041.

[439] S. Parvin Nejad, M. C. Blaser, J. P. Santerre, C. A. Caldarone, and C. A. Simmons, “Biomechanical conditioning of tissue engineered heart valves: Too much of a good thing?,” *Advanced Drug Delivery Reviews*, vol. 96. Elsevier B.V., pp. 161–175, 2016, doi: 10.1016/j.addr.2015.11.003.

[440] C. M. Brougham *et al.*, “Freeze-Drying as a Novel Biofabrication Method for Achieving a Controlled Microarchitecture within Large, Complex Natural Biomaterial Scaffolds,” *Advanced Healthcare Materials*, vol. 6, no. 21, pp. 1–7, 2017, doi: 10.1002/adhm.201700598.

[441] K. J. Rodriguez, L. M. Piechura, and K. S. Masters, “Regulation of valvular interstitial cell phenotype and function by hyaluronic acid in 2-D and 3-D culture environments,” *Matrix Biology*, vol. 30, no. 1, pp. 70–82, 2011, doi: 10.1016/j.matbio.2010.09.001.

[442] J. C. Rodríguez-Cabello, F. J. Arias, M. A. Rodrigo, and A. Girotti, “Elastin-like polypeptides in drug delivery,” *Advanced Drug Delivery Reviews*, vol. 97, pp. 85–100, 2016, doi: 10.1016/j.addr.2015.12.007.

[443] D. Miranda-Nieves and E. L. Chaikof, “Collagen and Elastin Biomaterials for the Fabrication of Engineered Living Tissues,” *ACS Biomaterials Science & Engineering*, p. acsbiomaterials.6b00250, 2016, doi: 10.1021/acsbiomaterials.6b00250.